Magnetic Ordering at the Nanoscale

Habilitationsschrift

vorgelegt von

Olena (E.Y.) Vedmedenko

aus Lugansk

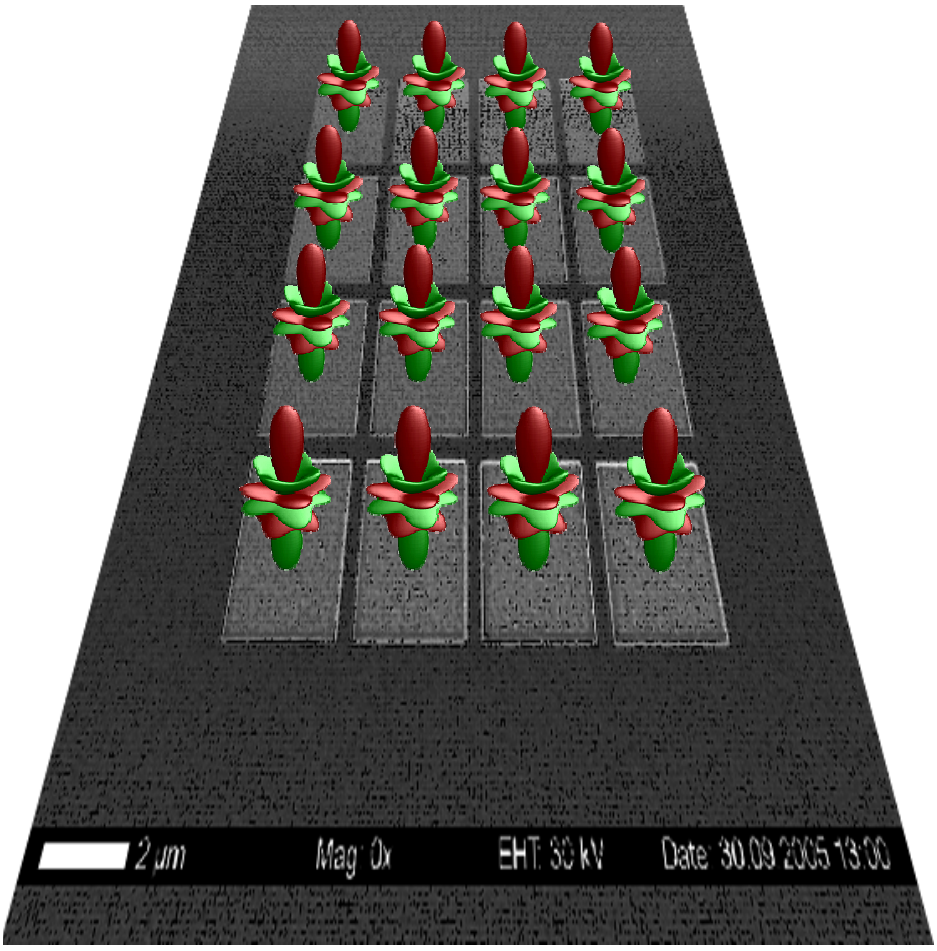

Hamburg, 2006

Magnetic Ordering at the Nanoscale

Habilitationsschrift

vorgelegt von
Olena (E.Y.) Vedmedenko
aus Lugansk

Hamburg
2006

Preface

The work presented here concerns theoretical aspects of magnetism in many different systems of reduced dimensions including two-dimensional films, frustrated magnets, magnetic nanoparticles and their arrays. This report summarizes investigations performed by me and my co-workers at the University of Hamburg, the Max-Planck Institute for Microstructure Physics and the University of Paris VII. Its intention is to give a comprehensive overview on the main areas of my scientific activity in the last 7 years, which are Magnetic Ordering of the Spin Reorientation Transition, Anisotropic Orientation of Magnetic Domain Walls, Magnetostatic properties of Nanoarrays and Magnetism in Quasicrystals. The report is structured as follows:

- In the first part, the main ideas behind the work and a summary of the most important results are given. The interconnections between different topics are highlighted;

- The second part contains a selection of 19 manuscripts, which have been already published or are in press. The aim of this section is to give deeper information on the issues presented in the first part. Therefore, the papers are referenced correspondingly to the Chapters of the first part;

- The appendix contains a full list of my scientific publications and patents to give a complete overview on my activities.

Acknowledgements

Most part of the investigations has been based on the closest collaboration with experimental groups. Therefore I like to thank all collaborators of the groups of Prof. Dr. R. Wiesendanger, Prof. Dr. H. P. Oepen and Prof. Dr. J. Kirschner involved in the results.

First of all I would like to thank Prof. Dr. R. Wiesendanger for the opportunity to write this habilitation within his group at the Institute of Applied Physics and for his steady support in many difficult situations, for fruitful discussions and spirit of innovation concerning the scientific research. I am grateful to Prof. J. Kirschner for his enthusiasm in the scientific work, many helpful comments and the courage to begin completely new topics like magnetism in quasicrystals. I thank Prof. Dr. H. P. Oepen for many-hours, hot debates, which helped me to find a thread in difficult scientific problems.

I like to acknowledge important contributions of the Ph.D. work of Dr. N. Mikuszeit, his helpful critics and cooperativeness. I have had longtime pleasure to work and discuss the results with Dr. S. Pütter and Dr. R. Frömter. I have learned a lot from the efficient and many-sided activity of Dr. A. Kubetzka, Dr. M. Bode and Dr. K. von Bergmann. I am especially grateful to Dr. O. Pietzsch for his courageous work with AlMnPd quasicrystal and his friendly being. Furthermore I enjoy the nice working atmosphere in this group.

My thank goes also to D. Stickler, Dr. D. Sander, Prof. Dr. W. Wulfhekel, Dipl. Phys. J. Hoyer, Dipl. Phys. H. Stillrich, Dipl. Phys. M. Wiggers, Dr. F. Porrati, Dr. W. Lutzke, Dr. H. F. Ding, Dipl. Phys. S. Krause, Dipl. Phys. L. Berbil-Bautista, and Dr. J. Chen for discussions. I have got important hints from Dr. D. Görlitz, Prof. Dr. J. Kötzler, Prof. Dr. D. Grundler, Prof. Dr. D. Heitmann. I thank Prof. Dr. W. Hansen for giving me an opportunity to work in the "Graduierten Kolleg". Prof. Dr. R. Anton, Prof. Dr. J.-B. Suck have opened for me many experimental aspects of aperiodic substances. I thank Dr. E. Uhrig and Dr. S. Jenks for preparation of quasicrystalline samples and Dr. M. Scheffer for introduction into the programming of quasicrystalline tilings.

My special thanks go to Dr. A. Ghazali and Prof. Dr. J.-C. Lévy who introduced me the world of magnetism. I gratefully acknowledge fruitful discussions with Dr. Y. Millev, Prof. Dr. U. Gradmann, Dr. D. Berkov, Prof. Dr. E. Bauer, Prof. A. Lichtenstein, and Prof. Dr. D. Pfankuche. I thank for theoretical explanations of Prof. Dr. M. Baake and Dr. U. Grimm. I find very valuable collaboration with Jr. Prof. Dr. S. Heinze and Dr. P. Ferriani.

My thank goes to Ms. P. Roth, Ms. U. Brenger, Ms. B. Truppe, Mr. B. Kellershof, Mr. R. Schlüter, Mr. A. Pusskeppel and Ms. A. Beese for technical support.

Hamburg, April 2006

Elena Y. Vedmedenko

Contents

Chapter 1

Introduction

The configuration of magnetization on all length scales is one of the central questions of magnetism as it determines macroscopic properties of a magnet. Whilst in the past the broader scientific issues have concerned magnetic structuring on a microscopic scale, in the context of recent developments in the field of nanoscience magnetic configurations on the nanoscale have become increasingly important.

The rapid rise of the scientific research on ever-smaller magnets is due to the appearance over the past 10 years of a collection of new experimental techniques that have made manipulation and construction of objects at the nanoscale possible. Some of these experimental methods, such as scanning tunneling microscopy with polarization analysis and magnetic force microscopy have created new capabilities for characterizing nanostructures. The application of new and extraordinary experimental tools to systems of reduced dimensionality has created an urgent need for a quantitative and qualitative understanding of matter at the atomic scale. An additional motivation for the investigation of nanomagnetic ordering is its increasing importance for its application in sensors, logic devices and in data storage.

Many new problems, that are not characteristic of bulk materials, arise at the nanoscale. These new problems generate many questions. Such as: what is the role of frustrating spin arrangements for the stability and hysteretic properties of two-dimensional magnets and nanoparticles; what are the size- and the temperature-dependent properties of nanomagnets; what is the role of the structural disorder for the magnetic ordering in nanoobjects and which effects may arise due to the discrete nature of matter? Theoretically, these questions can be effectively studied by model Hamiltonian methods or within analytical approaches. One of the best investigative tools based on model Hamiltonians to solve these stochastic optimization problems are Monte-Carlo methods. They are particularly good for realistically evaluating all kinds of transition probabilities and the effects of entropy. Since magnetic ordering at nanoscale is driven by entropy as well as by energy, Monte-Carlo calculations are really essential for describing magnetization configurations on the nanoscale. Modern classical Monte-Carlo schemes are able to describe large systems consisting of many ten thousands of atoms. The method naturally incorporates long-range dipolar inter-

actions, effects of the atomic lattice, the temperature and the entropy. In combination with analytical calculations, and experimental evidence, the Monte-Carlo treatment is a powerful tool for the description of magnetic ordering in magnets of reduced dimensionality.

Outline

This work presents a systematic theoretical study of the influence of the competing interactions, discrete atomic structure, temperature, geometrical frustration and the finite sample size on the magnetic ordering in nanostructures. The basic methods used in this work are; extended Monte-Carlo numerical simulations, analytical calculations of magnetostatic moments of nanoparticles based on the fundamental theory of electrostatics, numerical and analytical calculations of magnetostatic energies and demagnetizing factors of nanoplatelets, and phenomenological approaches concerning the calculation of the ground state magnetic configurations. The corresponding theoretical procedures are presented at the beginning of each of the four main sections of the manuscript.

Chapter 2 is devoted to the theoretical description of the magnetic structure of the Spin Reorientation Transition in nanometer thin films and of nanosize structures. After a short introduction to the theoretical methods thickness-driven magnetization reorientation is discussed in the framework of the first- and second-order uniaxial magnetic anisotropy approximation. The correspondence between theory and recent experimental advances on the spin reorientation transition is then analyzed. It is shown that the discrete nature of an atomic lattice may lead to the size-driven reorientation of magnetization in nanoparticles, *i*.e. the magnetization direction can be changed by shrinking the lateral size, keeping the thickness fixed. It is predicted that the critical size of the reorientation can be very large compared to the film thickness. It is demonstrated that the shape anisotropy of a nanomagnet can be divided into the discrete and the continuum contributions. A compact formula is derived for the demagnetization factors and the dipolar magnetostatic anisotropy energy density for a saturated (zero-susceptibility) continuum ferromagnet, possessing the shape of a right circular cylinder of any geometric ratio $k = d/t$.

In the third Chapter the orientation of domain walls in magnetic nanowires is discussed. In mesoscopic crystals the orientation of magnetic domain walls is usually determined by the competition between the magnetocrystalline and shape anisotropy. An isotropic exchange interaction cannot affect the global wall orientation in bulk crystals of cubic symmetry. It is demonstrated that in nanostructures of a few monolayer thickness the magnetic anisotropy and the magnetostatic energy play a minor role for the wall orientation. In case of low-symmetry objects the orientation of domain walls is mainly determined by the discreteness of the atomic lattice structure and by the exchange energy. The reduced symmetry of the film surface and the distortion of the atomic structure due to the pseudomorphic growth of nanoobjects can often lead

to the orientational dependency of the exchange tensor and, hence, to the anisotropy in the orientation of domain walls. Correlations of the theoretical results and recent experiments on magnetic nanoordering are given.

The theoretical study of the magnetostatically interacting nanoarrays is presented in Chapter 4. The multipole moments and multipole-multipole interactions of uniformly polarized particles have been calculated based on the fundamental theory of electrostatics. The polarization may have its origin in magnetization or ferroelectricity or be an intrinsic property of molecules. It is demonstrated that, depending on the geometry of the particles, the higher order interactions can be comparable to, or even stronger than, the dipole-dipole interaction. The higher order moments give rise to an additional energy contribution in arrays of close packed polarized nanoparticles. The influence of particle aspect ratios as well as array periodicity is discussed. The low-temperature stable states and the magnetization reversal of realistic two-dimensional nanoarrays with dipolar, and higher-order magnetostatic interactions are studied theoretically. For a general geometry of the multipole-multipole interaction energy a Hamiltonian in spherical coordinates has been introduced into the Monte Carlo scheme. It is demonstrated that higher-order interactions considerably change the dipolar ground states of in-plane magnetized arrays favoring collinear configurations. The multipolar interactions lead to enhancement or decrease of the coercivity in arrays with in-plane or out-of-plane magnetization.

Theoretical advances in the description of the magnetic ordering and its stability in two-dimensional quasiperiodic tilings with strongly localized magnetic moments are presented in Chapter 5. It is demonstrated that the combination of the magnetic frustration and the quasiperiodic order of atoms leads to noncollinear ground states. Experimental and theoretical evidence for the possibility of a new phase, in which stable, magnetically ordered subtilings coexist with highly frustrated, glass-like regions is given.

Chapter 2

Magnetic Ordering of the Spin Reorientation Transition in Nanostructures

2.1 Introduction

A classification of experimentally available magnetic structures may be given in terms of the dimensionality modulation: three-dimensional systems (3D), like bulk materials or thin films; two-dimensional systems (2D), like surfaces, ultrathin films and multilayers; one-dimensional systems (1D), like nanowires; and so-called zero-dimensional materials with all three dimensions on the nanometer scale like small atomic clusters or nanoparticle arrays. With decreasing dimensionality of a magnetic object new factors determining the magnetic ordering come into play.

One of the very interesting effects one observes in ultra-thin 2D ferromagnetic films and 1D nanoparticles is a reorientation of the spontaneous magnetization by varying either the film thickness or the temperature. For not too thin films the magnetization generally is in-plane due to the shape anisotropy originating from the dipole interaction. On the other hand in very thin films this may change due to various competing anisotropy energies of structural, magnetoelastic or magnetostatic origin. Broken atomic symmetry at the surfaces of a film, or absent in the ideal crystal strain induced distortion, often leads to uniaxial anisotropy energies favoring a perpendicular to the film plane magnetization [1]. Over the last decade the investigation of the Spin Reorientation Transition (SRT) in ultrathin films has been a vivid field in basic research. A good collection of literature on the theory of temperature-driven SRT can be found in [2]. To describe the thickness-driven SRT Monte Carlo simulations and analytical studies have been performed in first-order approximation of perpendicular magnetic anisotropy. In those investigations emphasis was put on the change of the magnetization orientation as a result of competing anisotropy and dipolar energies with temperature or thickness as a driving parameter [3–14]. Phase diagrams were

put forward and noncontinuous magnetization changes postulated [3, 4, 7]. The evolution of the magnetic microstructures was not explicitly studied in these numerical investigations. The configuration of magnetization, however, may strongly influence the details of the switching of the magnetization and thus the macroscopic behavior of the ferromagnet as it has been shown experimentally [15–19]. Therefore, the role of magnetic ordering is an important question for physics of the SRT.

In this review a survey will be given of recent theoretical advances in the study of the magnetic microstructure of SRT. The simulation technique will be introduced in the Section 2.2. Chapter 2.3 will be focused on the thickness dependent Spin Reorientation Transition in the first order perpendicular anisotropy approximation. Then, the effects of higher-order anisotropies will be analyzed (Chapter 2.4). The influence of the discrete structure of an atomic lattice on the nanomagnetic ordering and the size driven SRT will be discussed in the Chapter 2.5.

2.2 Simulation

2.2.1 Competing interactions

The ordering of magnetization is a cooperative effect made possible, below a critical temperature, by the interactions between the magnetic moments of the unpaired electrons throughout a solid. The magnetization configuration is influenced by many factors, some of the more important of which are spin value and dimensionality, the degree of structural and magnetic disorder, the temperature, and the presence of competing interactions.

The main energetic ingredient governing magnetic ordering is the quantum mechanical exchange interaction. Without going into details the exchange coupling between two neighboring magnetic ions will force the individual moments into parallel (ferromagnetic) or antiparallel (antiferromagnetic) alignment with their neighbors. It is very strong but short range, i.e. decreases rapidly as the ions (atoms) are separated. The direct exchange interaction in it simplest form can be described by the Heisenberg Hamiltonian containing a sum of the products of two variables, vector spins or operators belonging to the nearest-neighboring lattice sites

$$H_{exch} = \sum_{\langle i,j \rangle} J_i \bar{S}_i \cdot \bar{S}_j = \sum_{\langle i,j \rangle} J_i (\alpha (S_i^x S_j^x + S_i^y S_j^y) + \beta (S_i^z S_j^z)) \ , \tag{2.1}$$

where S^x, S^y, S^z are projections of either an operator $\bar{S}$ for a quantum system or of a vector $\vec{S}$ for a classical system. The case of $\alpha = 0$, $\beta = 1$ corresponds then to the Ising model, $\alpha = 1$, $\beta = 0$ - to the XY model and $\alpha = \beta = 1$ - to the Heisenberg model. For relatively high temperatures the magnetic ordering can be successfully described in the framework of the classical models. The main difference between the three classical cases is different number of available states. For magnetic systems of reduced dimensionality, where noncollinear magnetic states often appear, the Heisenberg model

has been chosen for the computations as a three dimensional Heisenberg vector of a unit length can have any orientation in 3D physical space.

The second energetic component which is always present in an ensemble of atomic magnetic moments (dipoles) is the dipolar interaction. It comes from the fact that every moment itself is a source of a magnetic field and can be aligned in the field of any other dipole and vice versa, i.e. the moments interact. The interaction Hamiltonian reads

$$H_{dip} = D \sum_{i,j} \left(\frac{\mathbf{S_i} \cdot \mathbf{S_j}}{r_{ij}^3} - 3 \frac{(\mathbf{S_i} \cdot \mathbf{r_{ij}}) (\mathbf{S_j} \cdot \mathbf{r_{ij}})}{r_{ij}^5} \right), \tag{2.2}$$

where r_{ij} is the distance between moments i and j and $D = \frac{\mu_0 g^2 \mu_B^2}{4\pi a^3}$ - the strength of the coupling with μ_0 - the permeability of the vacuum, g - Lande factor, μ_B - Bohr magneton and a - lattice constant. The strength of the dipolar interaction between two dipoles is only of order of few degree of Kelvin. However, because of the long-range character and the position dependence the dipolar interaction may significantly change a critical behavior and magnetic ground states.

The dipolar interaction is the source of the so-called shape anisotropy. The shape anisotropy of a finite body ($\triangle E_D$) is described by the demagnetizing tensor N: $\triangle E_D = N \cdot 2\pi M_S^2$, where M_S is the saturation magnetization and $2\pi M_S^2$ the shape anisotropy of the infinite continuous magnet. Neglecting the discrete nature of matter N can be analytically calculated for uniformly magnetized bodies like ellipsoids.

Another energetic component which is necessary for the appearance of SRT is the crystal anisotropy. Whatever the microscopic origin of crystal anisotropy is, following a phenomenological approach, one may express the anisotropy energy density as a function of the direction cosines (or sines) of the magnetization component along the anisotropy axis, because the anisotropy energy is invariant under magnetization reversal. In the case of ultrathin films with uniaxial anisotropy, the energy density is

$$K_1 sin^2(\theta) + K_2 sin^4(\theta) + K_3 sin^6(\theta) + K_3^1 sin^6(\theta) cos(6\phi) + ... \tag{2.3}$$

with θ and ϕ polar angles with respect to the direction of the anisotropy. The magnitude of anisotropy constants decreases rapidly with increasing order. However, as it will be demonstrated below, even weak higher order contributions may change a magnetic ground state of a system if the sign of a higher order term is different from that of the first order anisotropy constant.

2.2.2 Monte Carlo Simulations

As has been pointed in the Section 2.2.1, for relatively high temperatures a magnetic crystal can be successfully described by atomistic classical models. During the last years we could reach a considerable progress in the area of application of classical Monte-Carlo (MC) calculations to real magnetic systems [20–25]. Modern MC

computational schemes are able to describe large systems consisting of many tens thousands of atoms [23]. The long-range magnetostatic interactions and temperature can be incorporated into the model Hamiltonian with reasonable efforts. Since magnetic ordering is a complicated many-body problem driven by minimization of the total energy this method is extremely powerful for the description of ground state properties of magnets.

A large advantage of the MC approach is that in contrast to the micromagnetic scheme, where a magnetic material is represented by blocks of a continuous medium, a discrete lattice structure of a specific material can be introduced into the calculations. Introduction of lattice symmetry provides a unique opportunity to account for the effects arising from the discrete nature of matter. However, calculations with atomistic resolution are very computer power intensive, especially when long-range interactions are considered. In this case one needs the CPU time proportional to N^2 per one Monte Carlo (MC) step, where N is the number of spins. For studies of magnetic ordering in objects with reduced dimensionality the dipolar coupling plays an especially important role, as it can compete with the exchange interaction due to its long range character. Hence, it must be considered in calculations. This, however, means that large samples can be treated only with periodic boundary conditions in order to reduce the size of a sample to the size of the periodically repeated unit cell. Unfortunately, the periodic boundary conditions often cannot be addressed for nanostructures of finite dimension because of the non-periodicity of the magnetic structure. In addition, periodic boundaries in many cases can introduce artificial periodicity and other unwanted effects. To overcome these difficulties we have developed a scaling approach [21] which enables us to consider very large samples (up to $1\mu m$) with open boundary conditions which could not be introduced directly in an atomistic numerical computation. In this approach we introduce into the Hamiltonian an effective dimensionless parameter which permits to change the mesh of the calculation in dependence on specific objectives of the system.

This dimensionless parameter is defined mainly through the coupling constants of the exchange and the dipolar interaction $q = \frac{D}{J \cdot a^3}$ with the lattice parameter a. Without anisotropy and without external field, the scaling parameter a remains the only free variable: Different ratios D/J can be considered as issued from a single case with a given q value but with different effective lattice parameters a. Thus increasing the dipolar coupling D while keeping the exchange coupling J constant amounts to a mere increase of the effective lattice parameter a. In the usual $3d$ magnets, the ratio $\frac{D}{J \cdot a_0^3}$ is of the order of $10^{-3}...10^{-4}$, where a_0 is a typical atomic distance in metals. Thus, for $D/J = 0.1$, $a \approx 5a_0...10a_0$ and for $D/J = 1$, $a \approx 10a_0...20a_0$, i.e. the larger values of D/J correspond to the larger samples and the coarser calculation mesh. With this method one can look at the structures first with a coarser resolution which requires less CPU time and afterwards resolve the interesting places more accurately.

The figure 2.1 shows for example a 1 μm large platelet made from a soft magnetic material as Permalloy possessing several metastable magnetic vortices. Because the

mesh is large, the internal structure of a vortex cannot be resolved. If the structure is calculated with a finer factor q, one recognizes immediately that the core of the vortex has a significant out-of-plane component of magnetization (Fig. 2.2) what has been recently observed experimentally [26].

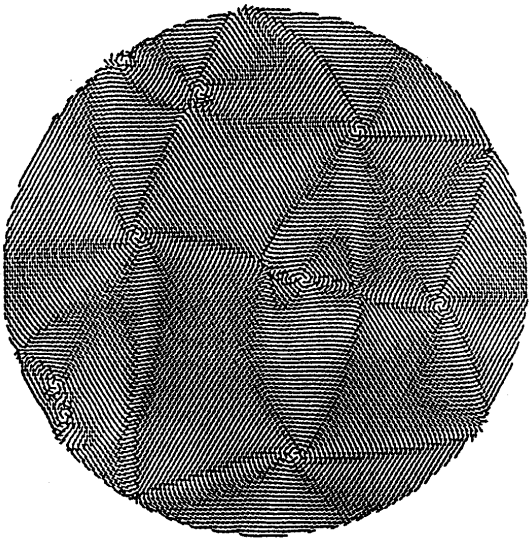

Figure 2.1: Top-view of a $1\mu m$ large soft magnetic platelet with several metastable vortex structures. The cores of the vortices cannot be resolved.

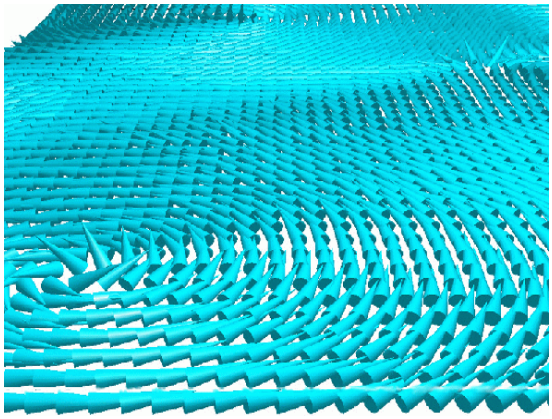

Figure 2.2: Perspective view of a portion of the same, but better resolved sample. The core of a vortex has a strong out-of-plane component of magnetization. The size of the core can be easily determined.

The MC program has been successfully applied for many structural phenomena such as magnetization reversal [20], domain or vortex formation [21, 22], and spin reorientation transitions [23–25]. We understand the work with this program as experimental investigations as the methodology is very similar to that of a real experiment. In the simulations we use magnetic parameters of real 2D systems which permit certain analogies to experimental results. The aim of the investigations lies not in the modelling of abstract, theoretical systems, but on the description of the real behavior of experimentally accessible magnets.

2.3 Spin Reorientation Transition in the first order anisotropy Approximation

In ultrathin films the configuration of magnetic moments, i.e. the magnetization configuration, is governed by the balance between dipolar and anisotropy energies. Due to the long-range order the dipolar energy is minimal when all magnetic moments compensate each other and the total magnetic charge is equal to zero (so-called pole

avoidance principle). In order to satisfy this minimum condition the dipolar energy pushes all spins into the film plane and distributes them evenly. The anisotropy energy, vice-versa, enforces spins to lie in some preferred directions. One experimental manifestation of the competition of these two energies is found in the thickness driven spin reorientation in Co/Au(111) films [17]. In the limit of small thickness the Co has a dominant perpendicular surface anisotropy which causes a perpendicular magnetization orientation. With increasing film thickness the dipolar energy becomes dominant and the magnetization turns into the film plane. One of the best known analytical treatment of spin reorientation in a one monolayer film is given in a paper by Yafet and Gyorgy [11]. The authors have made an extension of an old ansatz [14] introducing domain walls of finite width. In the analytical description Yafet and Gyorgy find that close to the transition point domain walls become larger than domains. In this state the whole film exhibits a wave-like phase. In the region where magnetostatic energy dominates their theory cannot make any predictions.

We have studied the same kind of reorientation transition by means of computer simulations of thin magnetic films [23]. The advantage of our method is that we can deal with the model Hamiltonian without limitations concerning the configuration of domains and domain walls as in Ref. [11]. We performed an extended Monte-Carlo treatment of a spin monolayer on a triangular lattice of 100×100 effective magnetic sites with three-component vector spins S of unit length $S = 1$. This corresponds to a surface orthogonal to the c axis of a *hcp* lattice or to the (111) surface of an fcc structure. The Hamiltonian of the problem includes exchange, dipolar interactions, and perpendicular anisotropy (see the Section 2.2.1).

We have performed simulations for three typical values of the ratio $1/q = \frac{J \cdot a^3}{D}$, namely $1/q = 10$, $1/q = 1$, and $1/q = 0$ (pure dipolar interactions with K_1 finite). In all simulations continuous transitions were found. We focus on the results for $1/q = 10$ as the scales for Co/Au(111) (5 nm mesh width and 500 nm sample size) are best adopted to the microstructures that appear in the spin reorientation transition.

The results are presented as a low-temperature phase diagram in Fig. 2.3. The averaged values of the vertical component S_z and the squared value S_z^2 of the magnetic moment versus f with $f = E_A/E_D$ as the ratio of perpendicular anisotropy energy E_A to the dipolar energy E_D. Usually the MC results are plotted as a function of K_1/E_D. As the behavior of the magnetic sample is governed by the total energy we find normalized energies more convenient. The magnetostatic energy is defined as the difference between the vertical single domain configuration and a stray field free vortex structure. This energy and the anisotropy energy is normalized with respect to the number of moments and used for calculating the f value given in Fig. 2.3. By this we avoid major effects of shape and size on the graph and obtain a generalized behavior of the spin reorientation in thin films. S_z and S_z^2 have been obtained from the simulations. While S_z^2 is proportional to the total amount of the structure with out-of-plane magnetization orientation, S_z reveals information about the occupation of the two vertical states of magnetization.

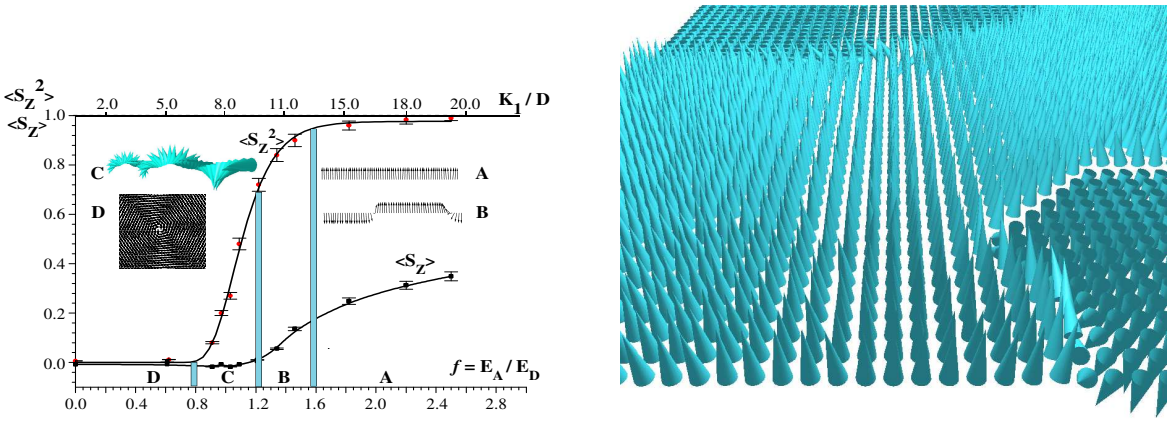

Figure 2.3: **(a)** Plot of S_z^2 and S_z versus f. S_z is the perpendicular component of magnetization and $f = E_A/E_D$ is the ratio of anisotropy energy to dipolar energy. The shaded areas separate the phases (A,B,C,D). The phases are characterized by the different microstructures, which are shown as insets in the diagram. The microstructures have been obtained for disk-shaped ($f \approx 1.46$) and rectangular samples ($f \approx 1.46$) of about 10200 vector spins on a triangular lattice for $k_BT/J \approx 0.01$. **(b)** Perspective view of an enlarged part of the phase B. For clarity, only one row out of two and one moment out of two in the row are drawn as cones.

Our results are in good agreement with the analytical model [11] within its range of validity. We obtain, however, a more precise picture of domain size and shape dependence on the ratio f, as no restrictions on admissible domain patterns were made. In the region where anisotropy energy dominates ($f > 1.4$) the size of out-of-plane domains is much larger than 500 nm limited by the size of our sample in the simulations. In the experiment [17] this kind of domains was found in very thin Co/Au(111) films (1...3.7 monolayers) with strong surface anisotropy. Fig. 2.3b represents the typical domain structure for the region $1.1 < f < 1.4$. The structure is characterized by small out-of-plane domains with narrow domain walls. The domain size decreases with the ratio f and reaches domain sizes of 300-400 nm for $f \approx 1.1$. Domains of this size were also found in a certain thickness range when a collapse of domain size was experimentally observed in annealed Co on Au(111) films. At the point $f \approx 1.1$ the total magnetization per spin is zero. This means that the magnetic moments are evenly oriented in all directions. Fig. 2.4a exhibits a relaxed MC magnetization configuration at the point where the dipolar energy is equal to the anisotropy energy $f = 1$.

It is almost the central point of the transition region from out-of-plane to in-plane configurations ($0.8 < f < 1.1$). Yafet and Gyorgy reached only $f = f_{min} \approx 0.99$ and predict there a purely two-dimensional wave-like profile of magnetization with macroscopic size of domain walls. We find the cosine-like profile at the same point (Fig. 2.4b). The profile and shape, however, is more complicated than the predicted 2d structure. Below $f \approx 1.2$ the domain walls become larger, as more and more magnetic moments

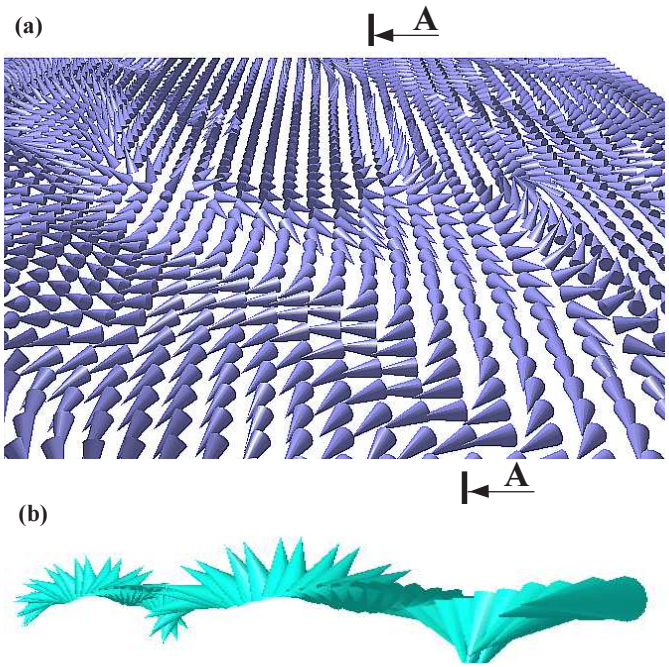

Figure 2.4: Top-view of a $1\mu m$ large soft magnetic platelet with several metastable vortex structures. The cores of the vortices cannot be resolved.

from the vertical magnetized domains are tilted. It is the beginning of the formation of vortices. At the point $f = 1$ walls meet each other and form a kind of spiral profile (Fig. 2.4b). The magnetization rotates in a helicoidal form along all three principal axes. The structure formed has been called the twisted phase. At this particular point the magnetic moments are evenly oriented in all directions, which is characteristic of the twisted configuration. This yields $S_z^2 = S_y^2 = S_x^2 = 1/3$ for a sample of infinite extension.

To analyze the stability of the twisted configuration its energy has been compared with several in-plane (vortex, single domain) and out-of-plane (with different periods of up and down domains) configurations for $f = 1$. The numerical values of the energies can be found in the Ref. [23]. The main conclusion is that at that particular point of the phase diagram the twisted configuration remains the one with the lowest energy among all considered magnetic states.

In conclusion, consideration of the magnetic microstructure reveals a continuous character of the SRT in ultrathin magnetic films with the perpendicular anisotropy. In first-order anisotropy approximation a continuous reorientation transition occurs from an out-of-plane magnetization to a vortex structure. A new phase, the twisted configuration, is found as an intermediate structure between these two states. At the point where the dipolar energy is equal to the perpendicular anisotropy energy the twisted configuration represents the minimum of the free energy.

2.4 Spin Reorientation Transition in the second order anisotropy Approximation

The importance of higher-order anisotropy contributions for the spin reorientation transition has been pointed out rather long time ago [27–29] and a phenomenological magnetic phase diagram in second-order anisotropy approximation has been postulated [27]. According to those investigations the reorientation can proceed either through

the canting of magnetization or through the state of coexisting local minima for the in-plane and the vertical magnetization.

The first option was quoted as a second-order transition or a continuous reorientation. A possible microstructure of those phase, however, has not been considered. The second kind of transition should proceed via states of "coexisting phases". The reorientation through this path is often classified as a discontinuous or first-order SRT. The classification is due to the assumptions or the models that are made to explain the flip of the moment. In the state of coexisting phases both orientations of magnetization have local minima. Hence, there is a possibility for the magnetization to be oriented along one or the other direction. Two models of occupation are commonly accepted leading to a discontinuous flip, i.e. the "Perfect Delay" and the "Maxwell" convention [30]. Initially in both models the magnetization occupies the state of the lowest minimum. In the first model the magnetization is believed to stay in that state until the corresponding minimum of the free energy is completely erased. The second model assumes that the orientation of magnetization is always determined by the lowest lying energy minimum. A sudden flop appears at the point where both minima have equal depth. Both models have been discussed in literature for zero temperature. In the common discussion of the discontinuous transition neither finite temperature nor any microstructure has been taken seriously into account.

2.4.1 The Phase Diagram

To clarify the question about the magnetic microstructure of the SRT in the second order anisotropy approximation we have recently performed a spatially resolved analysis of the magnetization reorientation in the framework of competing dipolar, first- and second-order contributions of the perpendicular anisotropy (see Chapter 2.2.1) for a given exchange coupling [24, 25]

$$\begin{aligned} H &= -J \sum_{<\mathbf{ij}>} \mathbf{S_i} \cdot \mathbf{S_j} + D \sum_{ij} \left(\frac{\mathbf{S_i} \cdot \mathbf{S_j}}{r_{ij}^3} - 3 \frac{(\mathbf{S_i} \cdot \mathbf{r_{ij}})(\mathbf{S_j} \cdot \mathbf{r_{ij}})}{r_{ij}^5} \right) \\ &\quad + K_1 \sum_i \sin^2\theta + K_2 \sum_i \sin^4\theta \quad . \end{aligned} \tag{2.4}$$

As in the previous Chapter the SRT will be discussed in the appropriate anisotropy space. For the sake of simplicity the diagram is given by K_1^{eff} - the difference between first-order anisotropy K_1 and demagnetizing energy density or shape anisotropy E_D - and the second-order anisotropy energy density K_2 (Fig. 2.5). Thus, K_1^{eff} takes the magneto-static energy contribution into account. E_D is taken as the magneto-static energy of an infinite film, i.e. $2\pi M_S^2$. We want, however, to strengthen that in the simulations the magneto-static energies are calculated exactly while the phase diagram helps to make the presentation of the findings clearer. For positive K_1^{eff} and K_2 vertical magnetization is favored while negative values cause an in-plane state (see Eq. 2.4).

In the region of "vertical" magnetization (Fig. 2.5), for positive K_1^{eff} and $K_2 > -\frac{1}{2}K_1^{eff}$, we find the following microstructure. For large K_1^{eff} the vertically magnetized

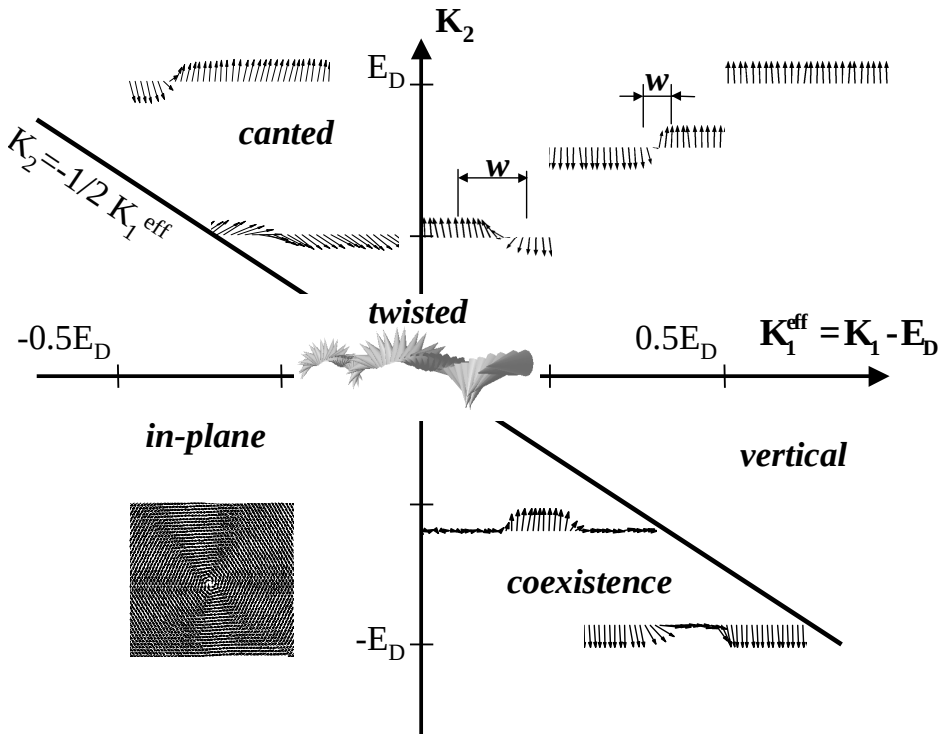

Figure 2.5: Micromagnetic phases of a monolayer of classical magnetic moments in the anisotropy space (second-order uniaxial anisotropy approximation) after Ref. [27, 31]. K_1^{eff} is the difference between first-order anisotropy and demagnetizing energy density $K_1^{eff} = K_1 - E_D$, K_2 is the second-order anisotropy density. The lines $K_2 = -\frac{1}{2}K_1^{eff}$ and $K_1^{eff} = 0$ separate vertical, canted, in-plane and coexistence phases (see text).

domains are very large. With K_1^{eff} decreasing the domain size shrinks and the domain walls become broader. This result is similar to the findings in first-order anisotropy approximation [11, 23]. If K_2 is large the domain size and the domain wall width are mainly determined by K_2. The trend is that the stronger the second-order anisotropy the narrower are the domain walls and the larger are the domains. In the close vicinity of $K_1^{eff} = 0$ with non-vanishing K_2 the wall width is finite in contrast to the infinite sinus-like profile of magnetization in the first order anisotropy approximation. This means that K_2 substitutes K_1 in the definition of wall width and energy. For $K_1^{eff} = 0$ and $K_2 = 0$ the twisted phase described in the Chapter 2.3 is formed.

For negative K_1^{eff} and $K_2 < -\frac{1}{2}K_1^{eff}$ (region "in-plane" in Fig. 2.5), the vertical magnetization vanishes and a complete in-plane orientation of the magnetic moments exists. To minimize the magneto-static energy vortex structures form as the magnetic anisotropy in the film plane was set to zero. In the "in-plane" region K_2 has only minor influences on the microstructure compared to the former situation with $K_1^{eff} > 0$.

In the following we will discuss situations where the microstructure is strongly dominated by the interplay of K_1^{eff} and K_2.

2.4.2 Canted Phase

At first for $K_1^{eff} < 0$ and $K_2 > -\frac{1}{2}K_1^{eff}$ (inset "canted" in Fig. 2.5) the negative K_1^{eff} competes with the positive K_2. The energy minimization requires canting of the magnetization to the film normal [10, 27–29, 31, 32]. In fact we find the canting of magnetic moments in the simulation (Fig. 2.5). The vertical component of magnetization changes continuously from 1 at $K_1^{eff} = 0$ to zero at $K_2 \approx -\frac{1}{2}K_1^{eff}$. In the literature this phase is called "cone-state" as it is generally assumed that the canted magnetic moments are distributed uniformly on a perimeter of the base of a cone with no preferred direction of the in-plane components. We find, however, that the canted magnetic moments form domains with in-plane components oriented along the principal directions in the lattice plane although the in-plane anisotropy was set to zero. The principal axes of the triangular lattice become the in-plane easy-axes of magnetization due to the dipolar interaction [33]. We may conclude that in the canted phase the ferromagnetic system is already affected by negligibly small in-plane anisotropies. The in-plane anisotropy causes the appearance of domains with magnetization components along distinct in-plane directions.

A top-view of the domain structure in the canted regime is presented in the Fig. 2.6. In Fig. 2.6(a) different shades of gray represent different orientations of the magnetic moments in the film plane. In Fig. 2.6(b) the different shades of gray give the up- and down- components of magnetization. The frequency distribution of the in-plane component of magnetization in the down-canted domains is given in Fig. 2.6(c). It demonstrates that two main in-plane orientations of the magnetization (around 240° and 120°) appear. For the vertical component the frequency histogram Fig. 2.6(d) reveals that the angle to the film normal is identical for all moments in the domains. The angle is equal to the value one obtains from the analytical treatment in case of $0 \leq -\frac{1}{2}\frac{K_1^{eff}}{K_2} \leq 1$, i.e. $\theta_M \approx \arcsin\sqrt{-\frac{K_1^{eff}}{K_2}}$. The small amount of deviating orientations is found in the domain walls. A three-dimensional representation of the magnetic moments is given in Fig. 2.6 (right). Hence, a continuous reorientation transition through the phase of canted domains occurs. In this region K_2 has a strong influence on the microstructure of magnetization.

2.4.3 Coexisting Phases

The third possible path for the reorientation of the magnetization proceeds via the forth quadrant of the anisotropy space ($K_1^{eff} > 0$, $K_2 < 0$).

In this region (inset "coexistence" in Fig. 2.5) we find that the average vertical component of magnetization goes gradually from almost unity above $K_2 = -\frac{1}{2} \cdot K_1^{eff}$ to zero at $K_1^{eff} = 0$. This continuous change of the magnetization component can lead

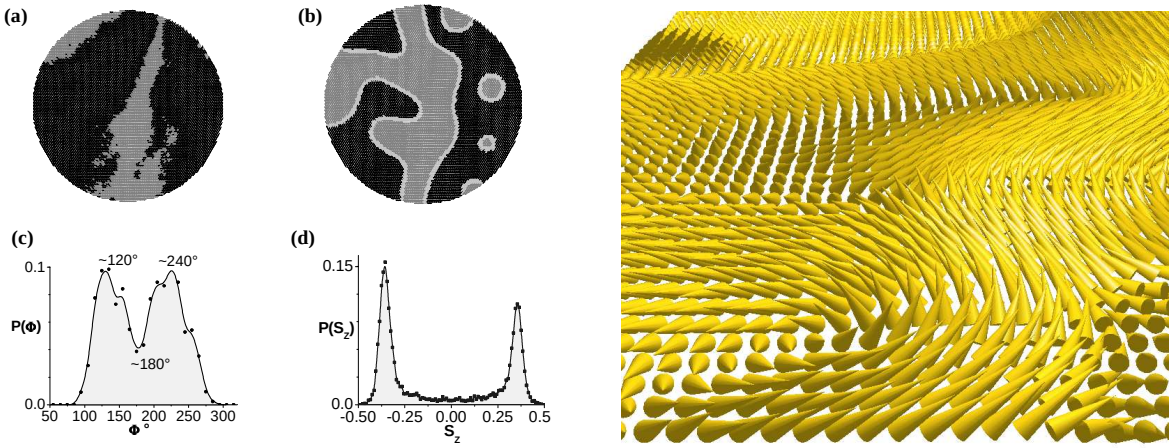

Figure 2.6: Top-view (left) and perspective view (right) of a portion the magnetic microstructure in the canted phase for $K_1^{eff} = -0.4E_D$, $K_2 = 0.65E_D$ and $k_BT/J = 0.05$. (**a**) shows a top-view of the microstructure. In this image the in-plane component of magnetization is coded in gray. Light-gray color gives the part of the sample with an in-plane component pointing mainly to left or right in the plane of drawing (azimuthal orientation of 0° or 180°). Dark-gray color indicates the regions having the in-plane components of magnetization at the angle of 60° or 240° to the horizontal within the plane of drawing. (**b**) gives the out-of-plane components of magnetization in the same sample. Dark and light-gray arrows represent canted-down and canted-up domains correspondingly. (**c**) exhibits the frequency distribution of the in-plane component of magnetization. The abscissa gives the angle of the magnetization to the horizontal within the plane of drawing. (**d**) displays the frequency distribution of the out-of-plane component of the magnetization. The abscissa gives the component of the magnetization along the normal.

to the erroneous conclusion that the reorientation proceeds via the canting of magnetization. The canting phase, however, does not exist in this part of the anisotropy space. We find in the simulation a magnetic microstructure that consists of domains magnetized perpendicular and in-plane, i.e. a coexistence of the two phases (histogram Fig. 2.7b). The domain walls cause the small amount of moments with deviating orientation. Hence, the very existence of two local minima in the free energy leads to the appearance of domains with vertical and in-plane orientation of magnetization. This result rules out the models discussed in literature for $T = 0$ K, i.e. "Perfect delay" and "Maxwell" convention [30].

In our simulations we find an increase/decrease of the in-plane/vertical domains size with decreasing K_1^{eff}. This means that the frequencies of population of the two phases of magnetization depend on the ratio K_1^{eff}/K_2. A top-view of the microstructures of the state of coexisting phases is presented in Fig. 2.8. Fig. 2.8(a) represents the situation where the vertical magnetization is favored which leads to the preponderance of vertically magnetized domains. On a first glance the in-plane domains could be misleadingly interpreted as walls. The magnetization profile, however, deviates completely from that of a domain wall. While in the wall a continuous tilting of the magnetiza-

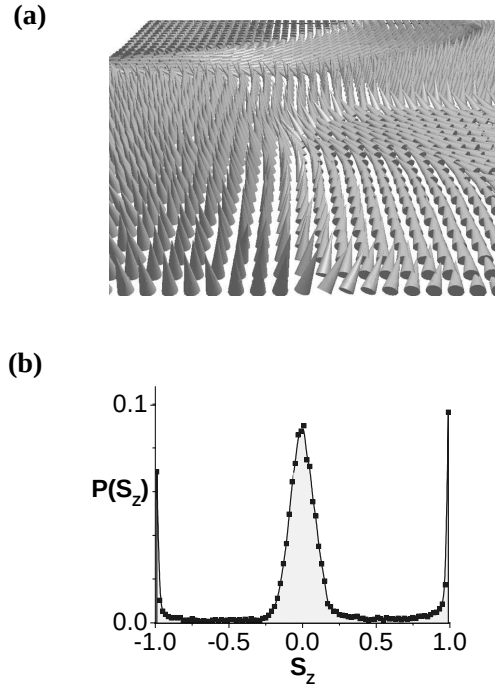

Figure 2.7: Microstructure of the state of coexisting phases for $K_1^{eff} = E_D$, $K_2 = -0.8E_D$ and $k_BT/J = 0.05$. (**a**) Perspective view of an enlarged part of the sample. For clarity only one row out of two and one moment out of two in the row are drawn as cones. (**b**) Frequency distribution of the magnetization orientation. The population frequency is given as a function of the magnetization component along the normal. The plot is generated from the simulation shown in *a*.

tion is expected we find that all spins lie in the film plane except for a thin region, i.e. wall, along the domain contours (Fig. 2.8a). The walls are not exactly described in our simulations as the mesh size is too large. If the in-plane orientation is more favorable (deeper minimum) an in-plane vortex-like structure appears (Fig. 2.8(b)). The vortex-structure is a consequence of minimization of the magneto-static energy as no in-plane anisotropy is assumed. The vertical domains remain in the core of the vortices and at the sample edges. Again the continuous transition between adjacent phases is achieved via the microstructure.

The multi-domain state of the coexisting phase transforms into a single domain state when the sample size is smaller than the typical domain size for a given K_1^{eff}/K_2. In that situation the ratio of K_1^{eff}/K_2 defines the probability to find the sample in a vertical or an in-plane magnetized single domain state. The domains with in-plane magnetization do not show vortex structure in small samples. The mono-domain configuration is energetically preferred as the gain in the dipolar energy is lower than the loss in the exchange energy for small structures.

In conclusion, a strong influence of the second-order perpendicular anisotropy on the microstructure of the spin reorientation transition is found. For $K_2 > 0$ the transition via a canted domain structure is established that yields the smooth, continuous connection between the vertical domain structure and the vortex structure with in-plane magnetization. For $K_2 < 0$ a continuous reorientation via a state of coexisting vertical and in-plane magnetized domains occurs. The sizes of the vertical and the in-plane domains depend on the ratio of K_1^{eff} and K_2. The spatial arrangement of the domains can change with time, while the frequency distribution of the in-plane and

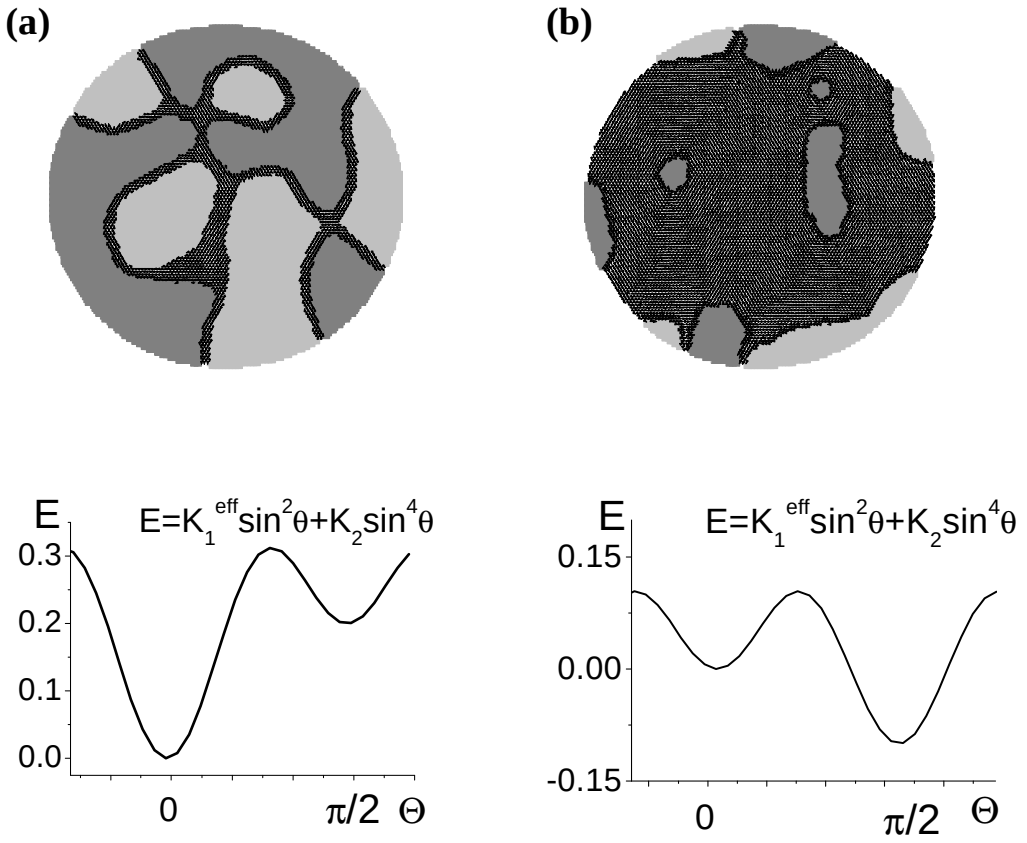

Figure 2.8: Top-view of the microstructure of the state of coexisting phases and corresponding energetic potential. Dark- and light-grey areas represent spin-up and spin-down domains correspondingly. Black arrows show the in-plane domains, $k_BT/J = 0.05$. In (**a**) the situation of a deeper minimum for the vertical phase ($K_2 = -0.8K_1^{eff}$) is shown. The region between the vertical domains are in-plane magnetized domains. (**b**) exhibits the microstructure for the situation that the energy minimum for the in-plane phase is deeper ($K_2 = -1.1K_1^{eff}$). Note that vertical domains remain at the edges and in the center of domains with "rotating" in-plane magnetization. They will shrink to the center of vortices found in the in-plane phase.

the vertical phases is invariable.

2.4.4 Theory versus Experiment

The experimental investigation of the SRT mechanism requires microscopic information about the magnetic domain structure. Different experimental techniques have been used for the imaging of magnetic domains within the SRT. These are photoelectron emission microscopy (PEEM) with x-ray magnetic circular dichroism (XMCD) [34], spin-polarized low-energy electron microscopy
(SPLEEM) [35, 36], scanning electron microscopy with polarization analysis (SEMPA) [16, 17, 37], magnetic force microscopy (MFM) [38], scanning tunneling microscopy

with spin polarization analysis (SPSTM) [39]. The different kinds of SRT have been also studied by surface integrating methods like magnetooptical Kerr microscopy (MOKE) [40, 41], magnetic torque magnetometry [42] or Brillouin light scattering (BLS) measurings [43].

The experimentally studied domain structures agree in many aspects with theoretical predictions. So, domains of sizes predicted in [23, 25] have been experimentally observed close to the reorientation transition in annealed Co/Au(111) films [16, 17, 37]. The borderlines of the phase of coexisting domains in the calculations are in good agreement with the experimentally defined borders of the "gray" zone of SRT in Co/Au(111) [37].

Experimental evidence of canted and coexisting domains predicted theoretically in the second order anisotropy approximation [24, 25] has been recently revealed in Co/Au(111)/W(110) and Fe-Co on Au(111) [35]. The coexisting domains have been also found in Fe grown on Cu/Si(111) [38]. The continuous rotation of the magnetization from out-of-plane to in-plane through the domain structure where the magnetization is canted has been reported for Cu/Ni/Ci/Si(001) films [42, 43].

2.5 Size-dependent Spin Reorientation Transition

Magnetism at small length scales has lately attracted considerable scientific attention. Interesting physical phenomena occur in magnets with all three dimensions on the nanometer scale. An array of such magnetic particles can potentially provide a huge gain in information storage density [44]. Hence, the understanding of the micromagnetic ordering in ultra-low-dimensional objects is of high significance for the fundamental physics of magnetic materials as well as for technological applications. The increased ratio of boundary to non-boundary atoms in such structures can lead to unusual physical phenomena.

2.5.1 The Shape Anisotropy of Nanoplatelets

The calculation of the shape anisotropy (see Chapter 2.2.1) has been performed for spheroidal or prismatic samples in the approximation of a continuum magnetization [45, 46]. The derived demagnetizing factors depend on a geometric ratio k, which is for example given by the thickness-to-diameter ratio L/t of the sample shape. In continuum approximation E_D deviates from unity only for structures where L and t are comparable.

It has been proposed that the model of a continuum magnetization is no longer valid when the film thickness is reduced to a few atomic layers [47, 48]. In this case the system is treated as a collection of discrete magnetic dipoles, which are arranged on a crystalline lattice. Calculations of the shape anisotropy have been performed for infinite large ultrathin films, and a deviation from the continuum magnetization model was found for films thinner than 16Å. The consideration of a discrete magnetization

yielded a reduced stray field energy for perpendicular magnetization of ultrathin films as compared to thick films, and the magnitude of deviation depends on the lattice type [47].

Recently, we have numerically calculated the shape anisotropy of structures with a limited lateral size [49]. Analytical approximations of the results [49] have been provided [50]. The platelets were discs of finite diameter L and thickness t on a discrete lattice. Diameter-to-thickness ratios $k = \frac{L}{t}$, ranging from 40 to 1000 with the thickness ranging from 1 to 6 monolayers as well as different crystal arrangements (sc[100], bcc[110], bcc[100], fcc[111], fcc[100], hcp[0001])were considered. The shape anisotropy (dipolar magnetic anisotropy energy) has been calculated as the difference between the dipolar energy of the vertical and the in-plane single domain state: $\tilde{E}_D = E_D(\perp) - E_D(\parallel)$.

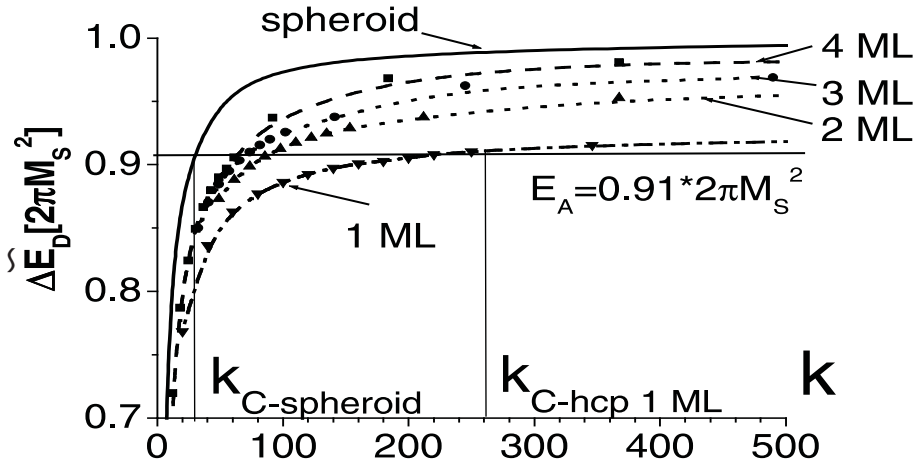

Figure 2.9: Numerically calculated demagnetizing energy density $\triangle\tilde{E}_D$ as a function of the dimensional aspect ratio $k = L/d$ for 1-4 monolayer films on a triangular lattice with *hcp* stacking. $\triangle\tilde{E}_D$ is normalized with respect to the demagnetizing energy in the continuum limit $2\pi M_S^2$. The straight horizontal line corresponds to the perpendicular magnetocrystalline anisotropy E_A. The dashed vertical lines denote the critical size k_C of the reorientation.

The results of the calculations for a triangular lattice with *hcp* stacking are shown in Fig. 2.9 as a function of $k = L/t$ for 1-4 ML thick films. The calculated energies are normalized with respect to $2\pi M_S^2$. For other lattices similar results were obtained.

The exact calculation of the dipolar sums deviates strongly from the magnetostatic energy obtained from the continuum ansatz (Fig. 2.9). Instead of a unique $\tilde{E}_D(L/t)$ function we obtain different curves for different sample thickness. Thus, the shape anisotropy of discs with diameters of several hundred lattice constants and a few atomic layers thickness (nanoplatelets), depends on both size L and thickness t, and not just simply on the ratio of the two parameters. For example, $\tilde{E}_D(L/t)$ of the platelet 100×1 on a *hcp* lattice is 1.2 times smaller than that of the platelet 300×3, although

$k = 100$ is the same for both objects. A remarkable result of those calculations is that the size effect already comes into play for rather large monolayer platelets of a few hundred atoms in diameter, and not only for situations where $L/t = 1$. For $t > 5$ ML $\tilde{E}_D(k,t)$ merges into $E_D = f(k)$. In all of these cases, the limit of infinite lateral dimensions was studied and the results of previous studies [47, 48, 51] have been retrieved.

A non-trivial step was then taken and the rather individual curves, corresponding to the different thicknesses at "fixed" structure, were normalized against the value for the dipolar magnetic anisotropy energy (MAE) $2\pi M_S^2$ of the laterally infinite sample. It was then established [49] that all these individual curves collapsed to a single, and thus universal, curve whose precise appearance depended on the ratio k of the cylindrical island only. This universal curve for the rescaled dipolar MAE was compared to the one for the dipolar MAE of an ellipsoid of revolution [49] and the disc [50] with the same aspect ratio in the continuum micromagnetic approximation (see, *e.g.*, Ref. [45]). Deviations were established and the conclusion was made that the dipolar sum can be separated into two contributions: thickness- and geometry-dependent parts. The geometry-dependent demagnetizing factors found by means of the discrete summation are identical to those found in continuum approximation [50]. It was pointed out that the combination of these two effects in nanoplatelets could be especially dramatic for ultrathin systems with a spin reorientation transition [49].

2.5.2 Spin Reorientation Transition

The magnetic anisotropy is a local property and constant for a given thickness. Thus, it can be represented by a straight line in Fig. 2.9. The intersection of $\tilde{E}_D(k,t)$ and E_A gives a critical length $L_C = k_C \cdot t$ where the magnetization orientation switches, i.e. reorientation appears. As the shape anisotropy in ellipsoid approximation deviates from unity only at $k \approx 1$ the reorientation can happen only at $L \approx t$ (Fig. 2.9). Thus, it is commonly assumed that the orientation of magnetization in structures with $L >> t$ depends only on the thickness and the temperature of the sample.

However, the shape anisotropy of nanoplatelets, according to the investigations [49, 50], is reduced for certain lattice symmetries. The reduction of $\tilde{E}_D(k,t)$ should lead to an enhancement of the effective perpendicular anisotropy $E_{eff} = E_A - \tilde{E}_D(k,t)$ with shrinking size and, hence, to the increase of the L_C. For certain range of E_A the critical size L_C of the reorientation can be very large compared to the film thickness.

Monte-Carlo simulations have been performed to check how the discreteness of the lattice reflects in the orientation of the magnetization [52]. In an extension of the earlier work [49], noncollinear spin states due to thermal disorder have been considered, and the temperature-driven magnetic reorientation is discussed in view of the different temperature dependence of dipolar and magnetic anisotropy energies.

The Hamiltonian of the problem includes exchange, dipolar interactions and perpendicular anisotropy of the first order: $\mathrm{H} = \xi_{ex} + \xi_D + \xi_A$. The ratio $D/J \approx 10^{-3}$ used in the calculations corresponds to real materials. Hence, no rescaling of the sample size

has been used. For the chosen D a single-domain magnetization configuration in the samples is expected. In that case the exchange energy for in-plane and out-of-plane configurations is identical and the magnetization orientation is fully described by the competition between E_D and E_A.

The low-temperature magnetic microstructure in samples of sizes $100a \leq L \leq 350a$, where a is the lattice parameter, have been investigated. Thus, the lateral size of the platelets has been chosen to be much larger than the thickness t ($L > 100t$). A wide range of the total anisotropy energy has been explored. Here the case where E_A is slightly smaller than $2\pi M_S^2$, i.e. $E_A \approx 0.9 \cdot 2\pi M_S^2$ is described. In the continuous ellipsoid approximation the selected sizes and anisotropy let expect any shape effects to become effective at $L_C \approx 20t$. Hence, in all calculated structures with $L > 100t$ an in- plane magnetization configuration should be expected.

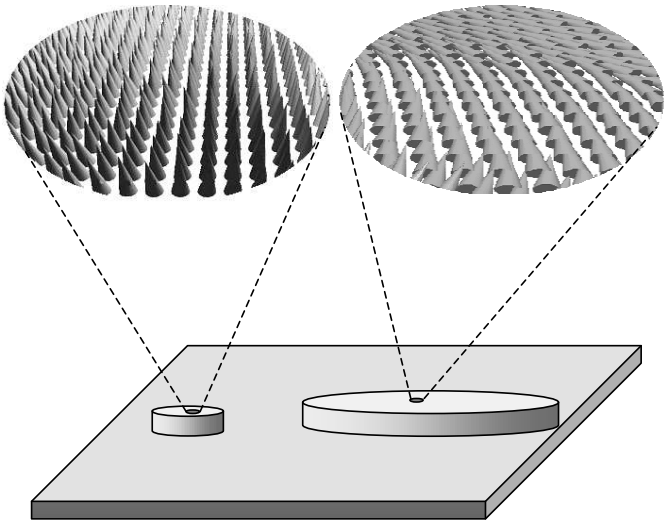

Figure 2.10: The low temperature magnetic microstructure of two discs on triangular lattice with, L_1=100 and L_2=330; $E_A = 0.9(2\pi M_S^2)$. The exchange, the anisotropy, the dipolar energy constants and the temperature are identical for both samples. For the sake of an appropriate representation a perspective view of an enlarged part of each sample is shown. For clarity, only one spin row out of two is drawn as cones. The smaller island has a vertical single-domain structure. The larger structure presents an in-plane single-domain magnetization configuration.

In contrast to the predictions made in the framework of the continuum approximation a vertical monodomain state in the case of objects with $L < 230t$ on a triangular lattice is found (Fig. 2.10, left). In case of $L > 300t$ an in-plane configuration of magnetization exists (Fig 2.10, right). For $230t < L < 300t$ structures with an intermediate values of vertical component of magnetization have been revealed. For the square lattice the results are completely different. We find for all structures with $L > 100t$ an in-plane single domain in accordance with the ellipsoid approximation.

By comparison with the triangular lattice we see that the critical size of the reorientation L_C depends on the type of the crystalline lattice. According to [49] the shape anisotropy of a triangular lattice with *hcp* or *fcc* stacking is strongly reduced, while $\tilde{E}_D(k,t)$ of a square lattice with *sc* stacking is almost equal to that of continuum. Thus, in contrast to the analytical assumption and in accordance with the numerical approach [49] the critical size of the reorientation L_C depends on the type of the crystalline lat-

tice and in some cases takes place far beyond the k-range deduced from the ellipsoid approximation. Another important conclusion is that the magnetization direction can change by shrinking the lateral size without changing parameters like thickness or temperature.

The demagnetizing and the anisotropy energy of non-collinear due to the thermal agitations MC configurations have been studied by taking advantage of the Monte-Carlo scheme that permits the introduction of temperature effects into the calculations in [52]. Fig. 2.11 gives $\tilde{E}_D(L)$ and $E_A(L)$ of platelets on a triangular lattice for strictly collinear and relaxed solutions.

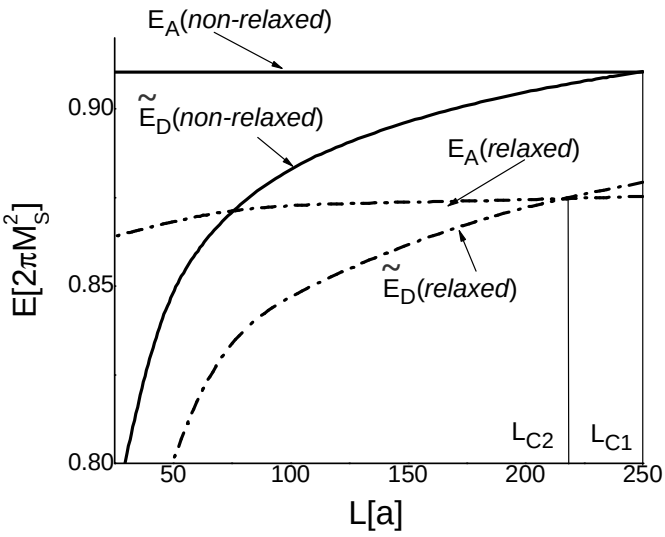

Figure 2.11: Comparison of the demagnetizing $\tilde{E}_D(k, L)$ and the anisotropy E_A energy of disc on a triangular lattice as a function of size for strictly collinear and relaxed solutions. All energetic parameters J, D, K_1 are identical in both cases. The energy is normalized with respect to $2\pi M_S^2$, $kT/J = 0.05$, $D/J = 10^{-3}$. The vertical lines denote the critical sizes L_{C1} and L_{C2} of the magnetization reorientation for collinear and non-collinear configurations

Generally, the dipolar and the anisotropy energy of the relaxed solution are smaller than those of the collinear case due to the thermal disorder. Interestingly, the anisotropy energy of the MC configurations is no longer a constant, but is size dependent. As a consequence L_C is shifted to smaller sizes with respect to the collinear case (Fig. 2.9). However, the critical size of the reorientation is still dependent on the lattice type and can be very large comparably to the thickness of the sample. This indicates that the size-dependence of the reorientation transition in discrete lattices is not due to the shape effect of the continuous model that depends on the ratio of the object dimensions. The effect found for the monolayer example may be even more pronounced in thicker samples due to the thickness dependence of the demagnetizing energy of a platelets on a discrete lattice [49].

For $E_A \approx \tilde{E}_D(continuum)$ the size-dependent reorientation of magnetization will appear only in the platelet on a square lattice. The magnetization of a nanoplatelet on a triangular lattice will be always out-of-plane as the maximal possible shape anisotropy of a sample is smaller $\tilde{E}_D(L \to \infty) \approx 0.91 \cdot 2\pi M_S^2$. The effective perpendicular anisotropy of a triangular lattice, however, will increase due to the shape and the lattice dependence of $\tilde{E}_D(k, t)$. This is sometimes erroneously interpreted as the increase of Perpendicular Magnetic Anisotropy with shrinking size, as $\tilde{E}_D(k, t)$ is commonly assumed to be constant. First experimental findings pointing into this

direction have been published recently [53].

In conclusion, we demonstrate that in laterally confined ultra-thin magnetic structures the magnetic behavior depends on the type of the lattice and the sample size. As a consequence, the spin reorientation transition in small platelets of identical shape on different lattices occur at different sizes for identical anisotropy energy. For $\tilde{E}_D(k,t) < \tilde{E}_D(L \to \infty)$ the reorientation from an in-plane configuration for larger sizes to an out-of-plane configuration below a critical size L_C occurs. L_C can be very large compared to the film thickness.We have shown that an enhancement of the effective perpendicular anisotropy E_{eff} can occur with shrinking size.

2.6 Dipolar Magnetic Anisotropy: Multiplicative separation of discrete and continuum contributions

To check previous numerical results concerning the separation of the total demagnetizing energy in the discrete and the continuum contribution the analytical formulae for the demagnetizing factors of circular cylinders has been derived [50]. New closed-form analytic expressions for the demagnetization factors $N_{\mathrm{axial}}(k)$ and $N_{\mathrm{diam}}(k) = \big[1 - N_{\mathrm{axial}}(k)\big]/2$ for the right circular cylinder in the usual micromagnetic sense, *i.e.* in the continuum limit of micromagnetism, have been obtained. The expression for $N_{\mathrm{axial}}(k)$ is listed below

$$N_{\mathrm{axial}}(k) = 1 + \frac{4}{3\pi}k - \frac{{}_2F_1(\frac{5}{2},\frac{1}{2};2;\frac{k^2}{1+k^2})}{\sqrt{1+k^2}} \quad . \tag{2.5}$$

There is no need to tabulate this function, because the hypergeometric Gauss function ${}_2F_1(a,b;c;z)$ is built-in into widely spread computer-algebra packages and is actually a shorthand notation for an infinite convergent series. In the context of very flat cylinders, as is the case for the ultrathin-film cylindrical platelets, large values of $k \gg 1$ are of interest. Although the relevant results based on calculations of the inductance of cylindrical coil have been available for quite some time now [54], the formula provided under Eq. 2.5 is the first time that the demagnetization factors of the saturated zero-susceptibility cylinders are expressed in terms of the hypergeometric function. Notably, it covers the whole range of possible values of k ($0 < k < \infty$); in particular, one does not need to examine separately the thin (long) as opposed to the flat (short) cylinder.

From this, we have obtained straightforwardly the dipolar magnetic anisotropy energy density (shape anisotropy) depending solely on the shape of the cylinder as specified by the geometric ratio $k = \frac{d}{t}$ = diameter to thickness. The expressions are superior to the usually quoted formulas in terms of the complete elliptic integrals. The

very important finding is that

$$\frac{\Delta E_{\mathrm{dipolar}}(\mathrm{discrete})}{X} = \Delta E_{\mathrm{dipolar}}(\mathrm{continuum}) = S(k) \tag{2.6}$$

to within a very high accuracy (the small deviations in the third digit of the discrete result are certainly a numerical artifact) in agreement with the numerical results [49]. Equivalently, the identity of the two quantities can be established by comparison of $\tilde{N}(k)$ and of $\left[3N_{\mathrm{axial}}(k) - 1\right]/2$. The function $S(k)$ is a universal function of the geometry ratio. At this stage, it has been proven that the following form holds for the discrete mesoscopic system:

$$\Delta E_{\mathrm{dipolar}}(\mathrm{discrete}) = X(\{\mathrm{lattice}\}, t)S(k)\frac{\mu_0 M_S^2}{2} \quad . \tag{2.7}$$

Altogether, it has been shown that the exact finite summation of the dipolar sums for an essentially discrete dipole lattice, as is encountered in experimental situations in ultrathin ferromagnetic platelets, leads to a clear delineation of the validity of the micromagnetic continuum ansatz and the quantitative way in which the discreteness of the lattice bears on the final result for the MAE density.

2.7 Summary

A microstructure of thickness- and size-driven spin reorientation transition in ultrathin films and nanostructures has been discussed. It has been demonstrated that the results of numerical Monte-Carlo investigations showed an astoundingly good correspondence with recent experiments and led to a microscopic understanding of the spin reorientation transition in the first- and the second-order magnetocrystalline anisotropy approximation.

It has been demonstrated that in first-order anisotropy approximation a continuous reorientation transition occurs from an out-of-plane magnetization to a vortex structure. At the point where the dipolar energy is equal to the perpendicular anisotropy energy a new phase, the twisted configuration represents the minimum of the free energy. The second-order perpendicular anisotropy strongly influences the microstructure of the spin reorientation transition. For $K_2 > 0$ a transition via a canted domain structure is established that yields a smooth, continuous connection between the vertical domain structure and the vortex structure with in-plane magnetization. For $K_2 < 0$ a continuous reorientation via a state of coexisting vertical and in-plane magnetized domains occurs. The sizes of the vertical and the in-plane domains depend on the ratio of K_1^{eff} and K_2. The spatial arrangement of the domains can change with time, while the frequency distribution of the in-plane and the vertical phases is invariable.

It has been shown by means of strict calculation of the dipolar lattice sums that the shape anisotropy of ultra-thin magnetic nanoplatelets differs from that of continuum ellipsoid- approximation. The superposition of thickness- and improved shape-effect

leads to a new phenomenon: size-dependent reorientation of magnetization. Critical size of the reorientation can be very large compared to the film thickness.

Chapter 3

Anisotropic Domain Walls in Magnetic Nanostructures with Perpendicular Anisotropy

3.1 Introduction

The microscopic and macroscopic physical properties of a magnet - hysteresis, magnetotransport and magnetooptical properties, excitation spectrum etc. - in many respects are determined by the configuration of magnetization [55–58]. Therefore, magnetic ordering on different length scales is one of the central questions of magnetism. Magnetic domains play an especially important role for the physics of magnetism. The understanding of the influence of the domain structure on the magnetic behavior in nanomagnets is of high significance for the fundamental physics of magnetic materials as well as for technological applications.

The size of domains in magnetic systems on all length scales is driven by the competition between the magnetocrystalline, the shape anisotropy, and the exchange energy. For given energetic parameters (and therefore a given domain size) a system may gain some additional energy which aligns the domain walls in one or in another crystallographic direction. The optimum orientation of domain walls in bulk materials is determined by the minimization of the magnetocrystalline and magnetostatic energy density [59]. As the walls in that case are planes a "wrong" orientation of a wall can lead to significant losses in the anisotropy energy and/or to significant stray fields. In laterally confined nanomagnets the magnetic shape anisotropy comes into play [60]. We take as example a thin rectangular magnetic sample shown in Fig. 3.1. If the density of domain walls is low the orientation of the walls is governed by a minimization of the total wall length, *i*.e., the walls should generally be oriented perpendicularly to the sides of a rectangle. If the wall density is high, the total length of the walls is almost identical for the longitudinal and the polar orientations. Therefore, the least energetically costly solution is to orient the domain walls either parallel to the long

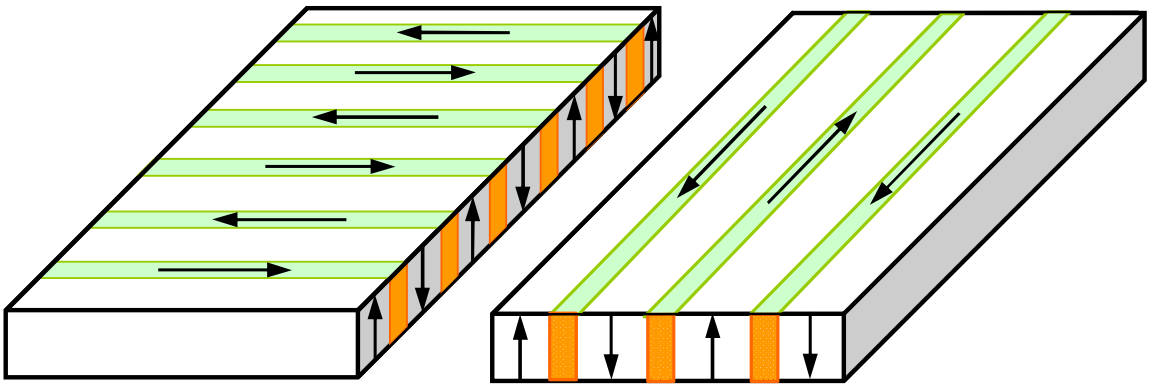

Figure 3.1: Schematic representation of two possible orientations of Bloch domain walls in a magnet of rectangular shape with perpendicular anisotropy for high wall density. The white regions are domains, the light grey regions - walls. The arrows give the orientation of magnetization. The dark grey areas denote uncompensated magnetic poles.

side of the rectangle, or concentrically. This is since such configurations will lead to a minimization of free magnetic poles on the sides of the sample [60] (see Fig. 3.1). Hence, as for high as for low wall density the orientation of domain walls is strongly dependent on the shape of a magnet. If the magnet as a whole will be rotated the domain walls should rotate together with it in order to preserve the relative orientation. An exciting question is whether the orientation of domain walls in the ultrathin film limit obeys the same principles?

3.2 Experiments

One experimentally accessible and, for future applications, very perspective geometrical shape is a so-called nanowire - a quasi one-dimensional structure of infinite length and lateral dimensions on the nanometer scale. The nanowire geometry is particularly advantageous for the investigation of the orientation of domain walls as it has very strong shape anisotropy, *i*.e., similarly to the previous example the walls should generally be oriented perpendicularly or parallel to the sides of a wire depending on the wall density. In many cases the wall density in turn can be tuned by the width of the wires [61]. The narrower the wires the lower the density of walls.

For many experimental systems, *e*.g. Fe/Cu(100), the shortest wall-path coincides with one of the crystallographic axes which makes it impossible to distinguish between the role of the lattice for the domain formation and other effects. Only if the shortest distance is different from all principal axes of a lattice can the mechanism underlying the orientation of the domain walls be revealed in case of a small wall density. A suitable and experimentally well-studied model system are double layer (DL) Fe nanowires on stepped W(110) [61, 62] being characterized by perpendicularly magne-

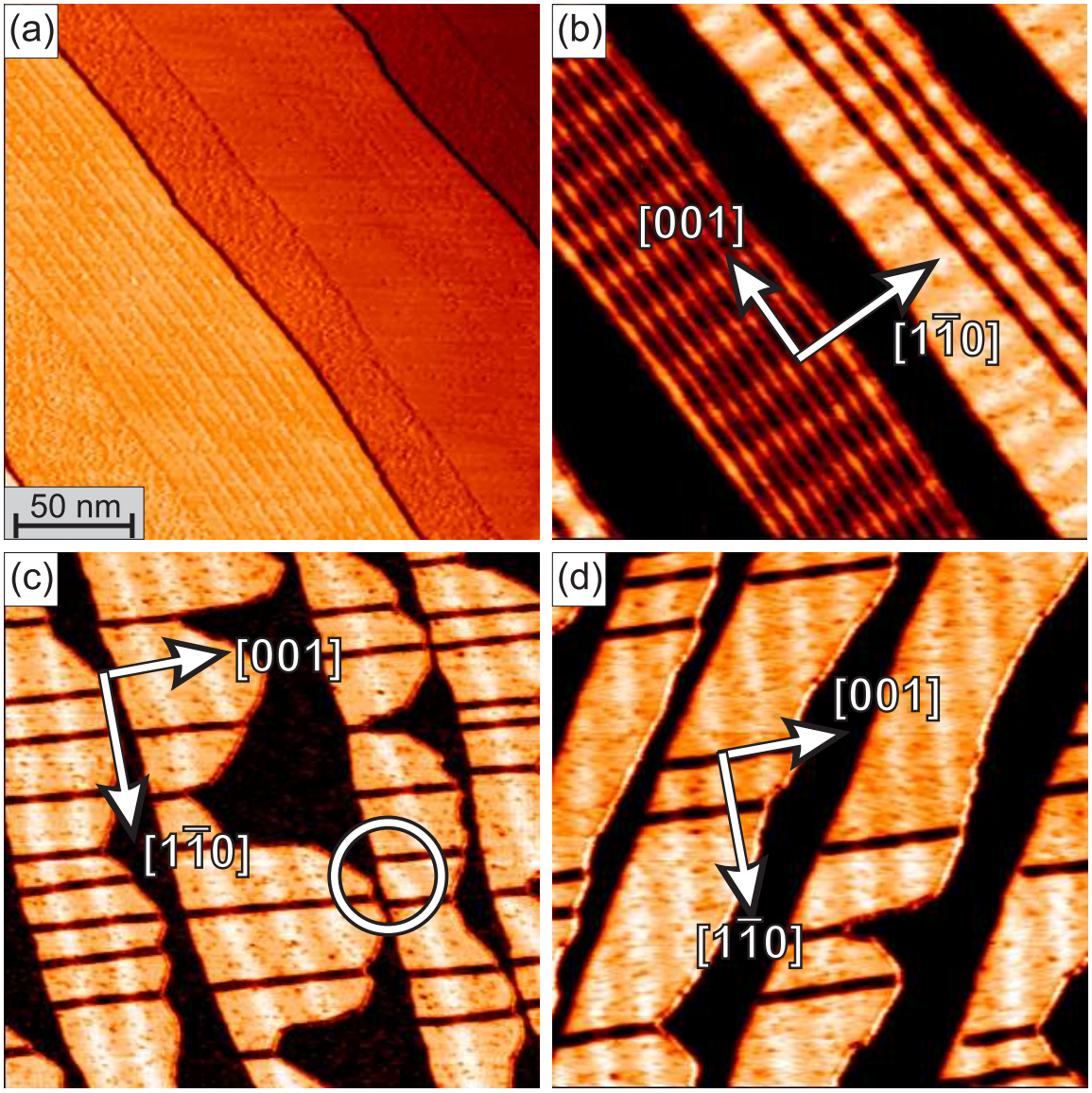

Figure 3.2: **(a)** Topography and **(b)-(d)** dI/dU maps of of 1.7 ML Fe/W(110) at different local miscut orientation. (a) and (b) were recorded simultaneously. The lateral scale is the same in all images. In all cases, domain walls (white lines) are oriented along [1$\bar{1}$0], regardless of the orientation of the nanowires. Parameters: $U = 5\,\mathrm{mV}$, $I = 0.5\,\mathrm{nA}$, $T = 75\,\mathrm{K}$ (b, c) and 120 K (d).

tized domains separated by domain walls. Fe/W(110) nanowires are extending along the substrate step edges. As the step edges of the W-surface can have different crystallographic orientations the spatial orientation of the magnetic nanowires can also be different.

Scanning tunneling microscopy on areas with different local miscut orientations [63] reveals that the domain walls do not show conventional behavior, *i*.e. they do not rotate together with wires but are always oriented along the $[1\bar{1}0]$ direction, regardless of the orientation of the nanowires [63] . Figure 3.2 shows the topography (a) and maps of differential tunneling conductance (b-d) of 1.7 ML Fe/W(110). While the $\mathrm{d}I/\mathrm{d}U$ map of Fig. 3.2(b) has been measured simultaneously with and at the same position as the topographic image, the $\mathrm{d}I/\mathrm{d}U$ maps of Fig. 3.2(c) and (d) show other areas of the same sample which exhibit different local miscut orientations. The maps of the differential tunneling conductance correlate with the local density of states directly under the tip and provide information about the magnetic polarization of the sample. The double layer nanowires shown in Fig. 3.2(a,b) extend approximately along [001], the ones in Fig. 3.2(c) along $[1\bar{1}0]$, while in Fig. 3.2(d) the wire direction is intermediate, roughly along $[1\bar{1}1]$. Due to unequal diffusion energies the Fe stripes grow smoothest along [001] and least smooth along $[1\bar{1}0]$. After initial pseudomorphic growth the high tensile strain starts to relax by insertion of dislocation lines in the Fe double layer which run along the [001] direction. These are imaged as narrow black lines in the $\mathrm{d}I/\mathrm{d}U$ maps. The double layer nanowire has a periodic magnetic structure with out-of-plane domains alternatingly magnetized up and down. These domains are separated by 180° in-plane domain walls, which are imaged as white lines in this experiment. The typical distance between adjacent walls is 23 ± 2 nm [61]. Regardless of the direction of the nanowires the domain walls run along the $[1\bar{1}0]$ direction, i.e., perpendicular to the dislocation lines. As a consequence, the domain walls within the nanowires are infinitely long in the case of Fig. 3.2(c) (disregarding interruptions due to structural imperfections), and very short in case of Fig. 3.2(b) where they run perpendicular to the axis of the nanowire. More than that, the predominant $[1\bar{1}0]$ direction is not even a principal direction of an ideal bcc-lattice as it does not coincide with the primitive vectors of the bcc-structure. This anisotropic behavior can be found as in the regime of the high wall density as for the low density of domain walls.

Another experimental system with perpendicular magnetization for which an anisotropy in the domain wall orientation was observed in the ultrathin limit is Co(0001) films grown on a Mo(110) buffer [41]. The preferred domain wall direction has been found to be parallel to the [001] direction of the Mo buffer which corresponds to the $[11\bar{2}0]$ axis of the hcp-Co. In many other ultrathin systems, *e*.g. Co/Au(111) a completely isotropic distribution of domain wall orientations has been reported [37].

Thus, the orientation of domain walls in ultrathin nanomagnets is at variance to their mesoscopic and bulk counterparts and at first glance seems to be rather perplexing. While in ultrathin Fe/W(110) and Co(0001)/Mo(110) magnetic structures the walls are anisotropic, they are fully isotropic in Co/Au(111) films in the same thick-

ness range. In addition, the anisotropy in the wall orientation cannot be explained by the minimization of the shape anisotropy as the orientation of walls is independent of the orientation of a nanomagnet. In the following a systematical analysis of orientational wall dependency in nanomagnets on different lattice structures will be presented.

3.3 Theoretical Analysis: Isotropic Exchange Integral

To gain understanding of the unusual adherence of magnetic walls to certain crystallographic directions in Co/Mo(110) and Fe/W(110), and of the complete disregard of the crystallographic symmetry by these walls in Co/Au(111), Monte Carlo simulations and phenomenological analysis have been performed of the orientation of domain walls in ultrathin films with different atomic symmetries and perpendicular magnetic anisotropy [63, 64]. In the first set of calculations the exchange constants between all pairs of nearest neighbors are supposed to be identical.

3.3.1 Monte-Carlo Simulations

The Monte Carlo (MC) description of the magnetic ordering is fully stochastic. It is based on minimization of a system Hamiltonian by performing statistical sampling experiments on a computer. In the popular Metropolis algorithm during one MC step every magnetic moment tries to make a rotation into a new, randomly determined orientation. This new orientation is accepted or rejected on the base of the Boltzmann probability [65]. A properly equilibrated MC system satisfies the fluctuation-dissipation theorem. Hence, the temperature effects are naturally included in the calculations. Modern MC computational schemes are able to describe large systems consisting of many tens thousands of atoms [3, 4, 23, 58, 60, 66, 67]. The long-range magnetostatic interactions and all kinds of anisotropy can be incorporated into the model Hamiltonian with reasonable efforts. A large advantage of the MC approach is that a discrete lattice structure of a specific material can be introduced into the calculations. Introduction of lattice symmetry provides a unique opportunity to account for the effects arising from the discrete nature of matter [23–25]. Due to these advantages MC simulations have been successfully applied for many structural phenomena such as magnetization reversal, domain or vortex formation, and spin reorientation transitions [23–25]. Since magnetic ordering is a complicated many-body problem, driven by minimization of the total energy, this method is extremely powerful for the description of magnetic domain structures.

The system Hamiltonian reads:

$$\begin{aligned} H &= -\sum_{<i,j>} J_{[hkl]}\, \mathbf{S_i} \cdot \mathbf{S_j} \\ &+ D \sum_{i,j} \left(\frac{\mathbf{S_i} \cdot \mathbf{S_j}}{r_{ij}^3} - 3 \frac{(\mathbf{S_i} \cdot \mathbf{r_{ij}})\,(\mathbf{S_j} \cdot \mathbf{r_{ij}})}{r_{ij}^5} \right) \\ &+ k_1 \sum_i \sin^2\theta + k_2 \sum_i \sin^4\theta \\ &- k_p \sum_i \sin^2\theta \cos^2(\varphi - \beta) \ , \end{aligned} \tag{3.1}$$

where $J_{[hkl]}$ denotes the effective nearest neighbor exchange coupling constant along different bonds, D is the dipolar coupling parameter, θ and φ are the spherical angles and $\mathbf{r_{ij}}$ the vector between sites i and j. The coefficients k_1 and k_2 are the first- and second-order anisotropies per atom, respectively. k_p is an in-plane anisotropy per atom. The in-plane anisotropy can have any angle β with respect to the x-axis. For the MC computations one or two layers of classical, three-dimensional magnetic moments $\mathbf{S}$ on different surfaces of *sc*, *fcc* and *bcc* lattices of about 20000 effective magnetic sites have been considered. The MC procedure is described elsewhere [23]. A realistic ratio of the exchange and the dipolar constants $D/J = 10^{-3}$ has been used. First the case will be discussed where exchange constants between all pairs of nearest neighbors are identical. The anisotropy constants have been widely varied in the regime of vertical and in-plane magnetization. The best agreement with the experimental results [63] (domain width of 20–25 nm and wall width of 6–9 nm) give constants corresponding to an anisotropy energy density $K_1 = (1.6\text{–}2.0) \cdot K_d$, $K_2 = (0\text{–}0.7) \cdot K_d$, $K_p = (0\text{–}0.6) \cdot K_d$ with $K_d = 2\pi M_s^2$ the shape anisotropy. The value of the out-of-plane anisotropy is $K_1 = (2\text{–}2.1) \cdot K_d$.

Fig. 3.3 shows typical MC low-temperature domain configurations found for thin films with *sc*(110), *bcc*(110), *fcc*(110) and *fcc*(100) surfaces, while Fig. 3.4 gives the structure of the corresponding unit cells. The domain walls in *sc*(110) films are mainly oriented along [001], while the walls in *bcc*(110) films are oriented along the $[1\bar{1}0]$ direction (Fig. 3.3 a,b and Fig. 3.4 b,c). The domain walls of *fcc*(110) films (Fig. 3.3c and Fig. 3.4d) are more disordered and can run along $[1\bar{1}0]$, $[1\bar{1}2]$ or intermediate crystallographic directions. However, one never finds a [001] orientation. The domain pattern of an *fcc*(100) film, shown in Fig. 3.3d, is completely disordered. All possible orientations of domain walls can be found in the magnetization configuration. Similar results have been obtained for all other surfaces of cubic crystals. Thus, for isotropic exchange interactions the orientation of domain walls of (110) surfaces of cubic crystals is highly anisotropic, whilst this is not the case for the (100) and (111) surface orientations. Those results are consistent with experiments where anisotropic wall patterns have been found for bcc(110) surfaces [41, 63] while a disordered configuration has been revealed for an fcc(111) film surface [37]. Why it happens? To answer this question all energy contributions should be analyzed separately.

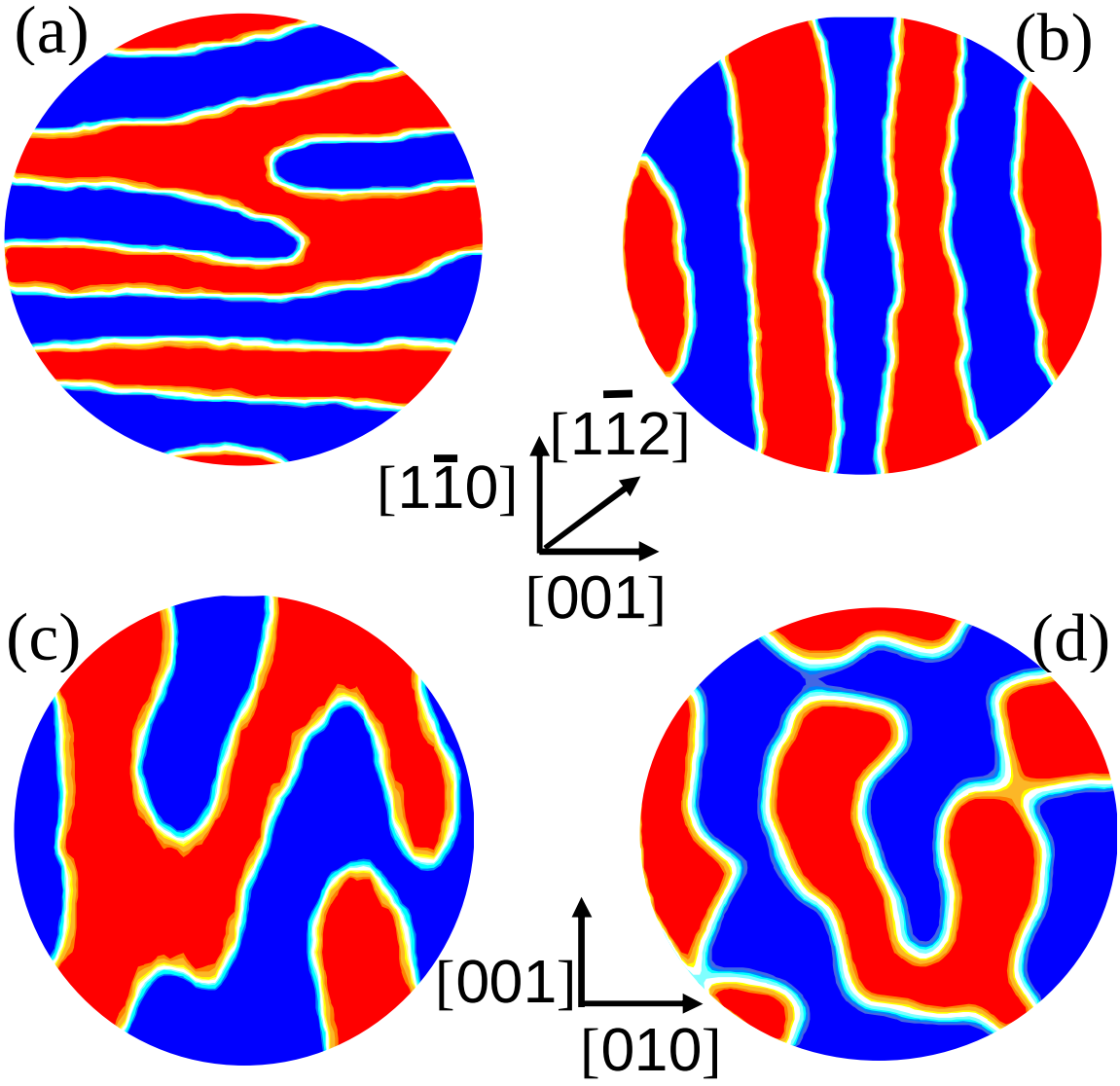

Figure 3.3: Top-view of MC domain configurations in 600 nm large and 2 ML thick samples with: $sc(110)$ **(a)**, $bcc(110)$ **(b)**, $fcc(110)$ **(c)** and $fcc(100)$ **(d)** surfaces. Opposite domains are imaged as dark and light areas. Exchange interactions are isotropic, $kT = 0.05J$, $K_1 = 9 \cdot 10^{-3}J$. Upper directions correspond to (110)**(a-c)** while bottom to (100) **(d)** surface.

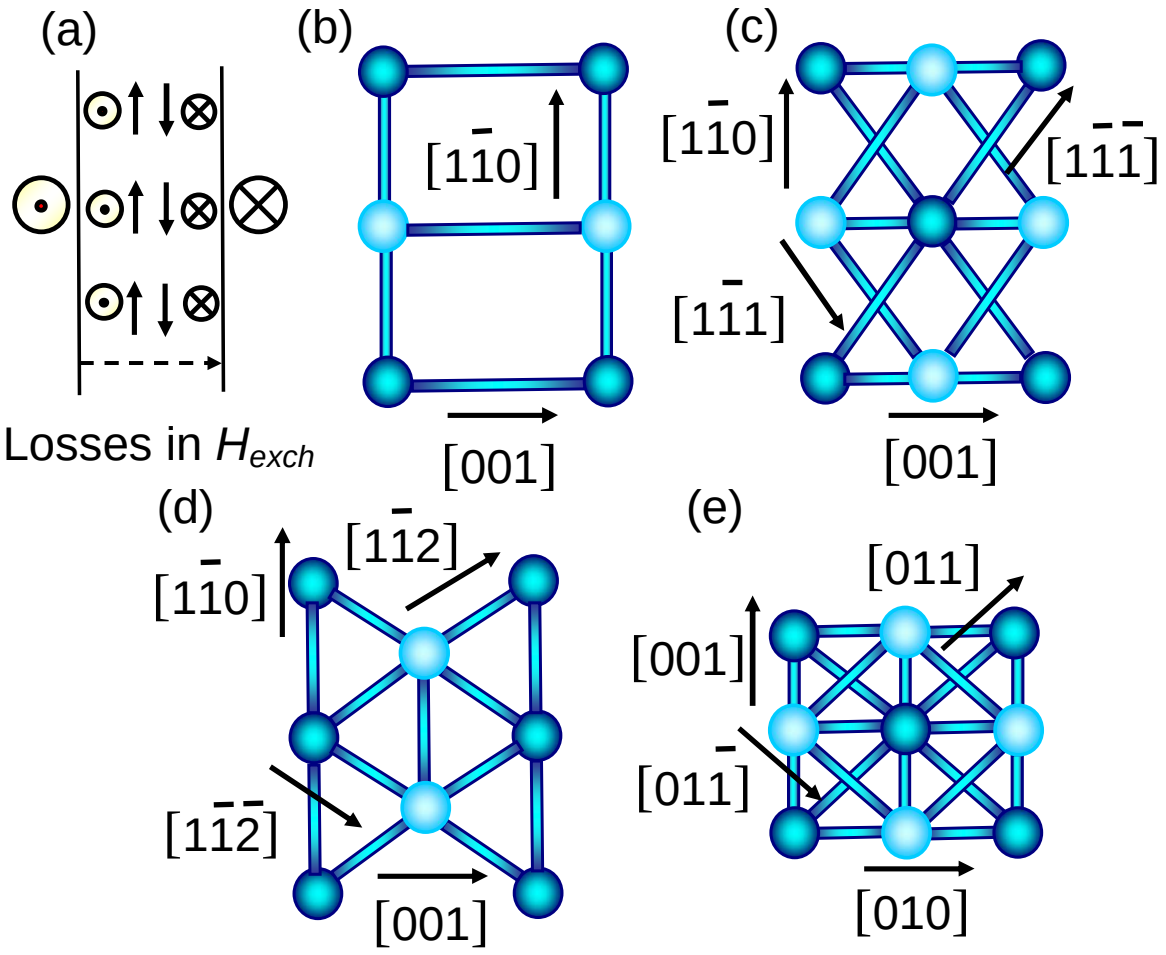

Figure 3.4: Schematic top view of a Bloch wall, the magnetization is represented by arrows **(a)**. Top view of the unit cell of 2 ML thick $sc(110)$ **(b)**, $bcc(110)$**(c)**, $fcc(110)$**(d)** and $fcc(100)$**(e)** films. Dark and light balls denote the atoms belonging to the first and the second layer correspondingly. Nearest neighbor bonds are shown as connections between the atoms.

3.3.2 Magnetocrystalline and Shape Anisotropy

To check whether the shape and the magnetocrystalline anisotropy can influence the orientation of magnetic domain walls several parameters have been widely varied in the simulations. First, the uniaxial anisotropy constants k_1 and k_2 have been changed in the regime of vertical magnetization. The thickness of domain walls decreases with increasing absolute value of k_1 and/or k_2. However, the orientation of domain walls is not influenced by the perpendicular anisotropy. The reason for such behavior is a strong reduction of the shape anisotropy in monolayer thick nanomagnets with (110) surface symmetry as has been demonstrated recently [49, 50]. As a result the gain in the shape anisotropy due to reorientation of domain walls at thicknesses $t \leq 4$ ML is negligibly small, *i*.e., in contrast to thicker magnets described in the Fig. 3.1 the shape and the uniaxial vertical anisotropy cannot govern the wall orientation.

Next, an additional in-plane anisotropy k_p has been strongly varied in the regime of vertical magnetization for different sample shapes [63]. Fig. 3.5 shows a portion of an elongated nanowire of rectangular shape with a low wall density. Increase of the in-plane anisotropy only leads to an alignment of the magnetization within the wall with no consequences for the wall direction. This happens for a similar reason as in the case of a uniaxial perpendicular anisotropy. The wall cross sections are so thin, that their charging due to the strong in-plane anisotropy leads to only a very weak stray field, which is insufficient for the reorientation of walls. This shows that the mechanism of wall orientation described here is distinct from the one observed in bulk and mesoscopic magnets, which is often governed by the magnetic anisotropy and the dipolar energy.

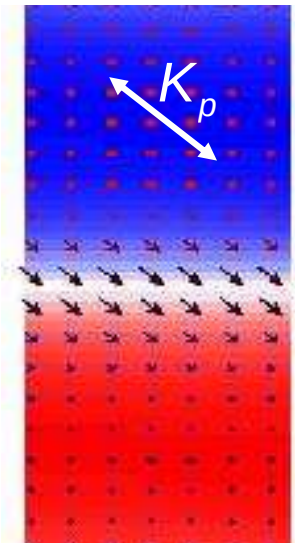

Figure 3.5: Top-view of a simulated nanowire sections of 20 nm width with a small density of domain walls. Black (red) and dark-grey (blue) areas denote up- and down-magnetized domains correspondingly. The magnetization is represented by arrows. White contrast gives the orientation of domain walls.

3.3.3 Exchange Energy

While in the atomistic approximation the exchange energy is often described by the Heisenberg Hamiltonian (see Eq. 3.2) with exchange integral J_{hkl} as an interaction parameter, in a continuum theory a so-called exchange stiffness tensor A is used instead. The exchange stiffness relates the exchange integral with the symmetry of a lattice: $A = \frac{2J_{hkl}S^2}{a} \cdot c$, where $c = 1$ for the primitive cubic lattice, $c = 2$ for the bcc lattice and $c = 4$ for the fcc lattice [68].

Orthorhombic-like Symmetry

For lattices with cubic symmetry A is isotropic. For orthorhombic lattices with a translation vector $\mathbf{T} = h\mathbf{a_1} + k\mathbf{a_2} + l\mathbf{a_3}$ where $h \neq k \neq l$ are generally non-equal integers and $\mathbf{a_1}$, $\mathbf{a_2}$, $\mathbf{a_3}$ is a set of three linearly independent vectors, A may be anisotropic in spite of the isotropy of J_{hkl} constants. The reason is the proportionality of the components of the exchange tensor A_{hkl} to the absolute values of $a_1 = h\mathbf{a_1}$, $a_2 = k\mathbf{a_2}$ and $a_3 = l\mathbf{a_3}$ [68]

$$A_h = \frac{2J_hS^2}{a_2a_3}a_1 \quad \neq \quad A_k = \frac{2J_kS^2}{a_1a_3}a_2 \quad \neq \quad A_l = \frac{2J_lS^2}{a_1a_2}a_3 \quad . \tag{3.2}$$

It has recently been demonstrated [69] that an anisotropy of the exchange stiffness tensor can lead to the anisotropic orientation of the domain walls in bulk orthorhombic materials. At first sight this theory is not applicable to the case of double layers with lattices of perfect cubic symmetry.

However, let us look more closely the unit cells of different surfaces described in the Section 3.3.1. What is the main difference between the (110) surface of a 2 ML thick film and all others? While the basis of all non-(110) surfaces is a square, the basis of (110) surfaces is a rectangle (see Fig. 3.4). This happens because the (110) surface is a diagonal plane of a cube. If a film is only two monolayers thick such a symmetry can be regarded as a part of an orthorhombic Bravais cell with a translation vector $\mathbf{T} = h\mathbf{a_1} + k\mathbf{a_2} + l\mathbf{a_3}$ with $h \neq k \neq l$, where h and k are the sides of the rectangular base. Therefore, the exchange stiffness parameter of (110) surfaces is anisotropic, whereas all other surfaces have an isotropic A. In thicker films the cubic symmetry of the lattice structure with *fcc*, *sc* or *bcc* stacking is restored. All three unit vectors become equal and the anisotropy in the orientation of magnetic domain walls induced by the orthorhombic-like symmetry of ultrathin films disappears.

Thus, the orthorhombic-like symmetry explains qualitatively an anisotropic distribution of domain walls in ultrathin films with (110) surface. Quantitative predictions of preferential wall orientations can be made on the basis of a phenomenological model developed in [64], which will be described below. Both methods give identical results which are consistent as with the Monte Carlo simulations as with experiments [37, 63].

Phenomenological Model

Fig. 3.4 shows a top-view of a conventional Bloch wall (a) and unit cells of a double-layer with an $sc(110)$ (b), a $bcc(110)$ (c), a $fcc(110)$ (d) and a $fcc(100)$ (e) crystalline lattice. Atoms are sketched as balls where dark ones belong to the surface and light balls to the subsurface layer. Connections between atoms indicate nearest neighbor bonds. From Fig. 3.4(a) it is clearly visible that the magnetization rotates along an axis perpendicular to the plane of the wall while magnetic moments belonging to planes which are parallel to the plane of the wall are parallel. Since in a ferromagnet neighboring spins hold the lowest energy when they are parallel, the loss in the exchange energy due to the wall formation results from the bonds which have non-zero projection on the direction perpendicular to the course of the wall. For example, if the wall is oriented along the [010] direction of the $fcc(100)$ surface (Fig. 3.4e) the magnetic moments connected by [010] bonds will be parallel while moments connected by [001] bonds will have a maximal possible mutual angle and, consequently, a maximal increase in the exchange energy $\triangle {E_J}^{[001]}$. The moments connected by [011] and $[01\bar{1}]$ bonds will have intermediate mutual angles as they are neither parallel nor perpendicular to the direction of energy loss. It means, that the local increase in the exchange energy due to the magnetization rotation in a domain wall will be proportional to the projection of an atomic bond on the axis perpendicular to the wall orientation.

To obtain losses in the exchange energy due to formation of a domain wall in this model, in a first step projections of all bonds to the axis perpendicular to the plane of the wall ($P_{\perp to[hkl]}$) were calculated for single and double layers of (100), (111) and (110) surfaces of bcc, fcc and sc crystals. The nearest neighbor bonds have been assumed to be of unit length. The length and the number of projections $P_{\perp to[hkl]}$ for double layers with (110) surface are brought together in Table 3.1. The loss in the exchange energy per unit cell for a wall along one of the $[hkl]$ directions has then been calculated by summing up the exchange coupling constants ($J_{[hkl]} = 1.0$) multiplied by $P_{\perp to[hkl]}$ for all bonds in the unit cell:

$$\triangle E_J^{[hkl]}[a.u./unit\ cell] = \sum_i J_{[hkl]} \cdot P_{\perp to[hkl]} \ .$$

For a wall along $[1\bar{1}2]$ of an $fcc(110)$ lattice, for example, this results in (see also Table 3.1):

$$\triangle E_J^{[1\bar{1}2]} = 3 \cdot \sqrt{\frac{2}{3}} + 4 \cdot \sqrt{\frac{2}{3}} + 4 \cdot \frac{1}{\sqrt{12}} = 5.74\ [a.u.] \ .$$

The exchange energy of a domain wall per unit cell is smallest for the $[1\bar{1}0]$ direction of the $bcc(110)$ and for the [001] direction of the $sc(110)$ surface. In case of an $fcc(110)$ crystal two orientations have similar energy. These are the $[1\bar{1}2]$ direction with $\triangle {E_J}^{1\bar{1}2} = 5.74$ and $[1\bar{1}0]$ with $\triangle {E_J}^{1\bar{1}0} = 5.65$. Hence, the exchange energy cost in the systems described above is orientation dependent. The preferential orientations of walls derived in the phenomenological model are $[1\bar{1}0]$ for $bcc(110)$ and [001] for

Table 3.1: $\triangle E_J^{[hkl]}$ and the projections of nearest-neighbor bonds onto the direction perpendicular to the plane of the domain wall for double layer films with (110) surface orientation.

Stacking	Wall orientation $[hkl]$	$\triangle E_J^{[hkl]}$/ unit cell [a.u.]	$P_{\perp to[hkl]}$[a] of bonds running along
			$[001](4)$ $[1\bar{1}0]$ (4) $[1\bar{1}1]$ (8)
bcc	[001]	8.52	0 $\frac{1}{\sqrt{2}}$ $\frac{1}{\sqrt{2}}$
(110)	$[1\bar{1}0]$	6.00	$\frac{1}{2}$ 0 $\frac{1}{2}$
	$[1\bar{1}1]$	6.76	$\frac{1}{\sqrt{6}}$ $\frac{\sqrt{3}}{2}$ $\frac{1}{\sqrt{6}}$
			$[1\bar{1}0](3)$ $[1\bar{1}2](4)$ $[1\bar{1}\bar{2}](4)$
fcc	[001]	7.00	1 $\frac{1}{2}$ $\frac{1}{2}$
(110)	$[1\bar{1}0]$	5.65	0 $\frac{1}{\sqrt{2}}$ $\frac{1}{\sqrt{2}}$
	$[1\bar{1}2]$	5.74	$\sqrt{\frac{2}{3}}$ $\sqrt{\frac{2}{3}}$ $\frac{1}{\sqrt{\bar{1}2}}$
sc			$[001](2)$ $[1\bar{1}0](2)$
(110)	[001]	1.41	0 $\frac{1}{\sqrt{2}}$
	$[1\bar{1}0]$	2.00	1 0

[a] Number of bonds per unit cell is given in brackets.

$sc(110)$ crystalline films. For $fcc(110)$ the wall orientation is defined by the competition between $[1\bar{1}0]$ and $[1\bar{1}2]$ directions. The cost in the exchange energy $\triangle {E_J}^{hkl}$ for other surfaces is constant and does not depend on the wall orientation. Hence, for [001] and [111] surfaces of a cubic crystal the domain walls are predicted to have no preferential orientation. The results described above give a quantitative measure of the orientation dependent exchange energy loss due to formation of a domain wall.

3.4 Theoretical Analysis: Anisotropic Exchange Integral

As has been shown in the previous Section magnetic domain walls are anisotropic in ultrathin films with (110) surface orientation. In case of ideal lattice structures this anisotropy comes from the orthorhombic-like symmetry of an incomplete cubic cell. Real materials grown on a substrate, however, almost never have an ideal structure because of the lattice mismatch. For the example of Fe/W(110) the first two Fe layers grow pseudomorphically and adopt the lateral lattice constant of tungsten, which is about 10% larger than that of bulk iron. As a consequence, the Fe–Fe interlayer distance relaxes below the Fe bulk value [70]. This leads to a change of the interatomic distances. Namely, the neighbor distance in the $[1\bar{1}0]$ direction, marked red in Fig. 3.6,

decreases to a value close to the nearest neighbor distance in bulk iron, and the spacings in $[1\bar{1}1]$ and $[1\bar{1}\bar{1}]$ direction (blue) are increased. Hence, instead of six nearest neighbors as in an ideal, 2 ML thick bcc(110) film, in Fe/W(110) all atoms have eight bonds of similar length. Following Ref. [70], the respective distances in units of the lattice constant of bulk Fe are $d_{001} = 0.95$, $d_{1\bar{1}1} = 1.10$, and $d_{1\bar{1}0} = 1.15$.

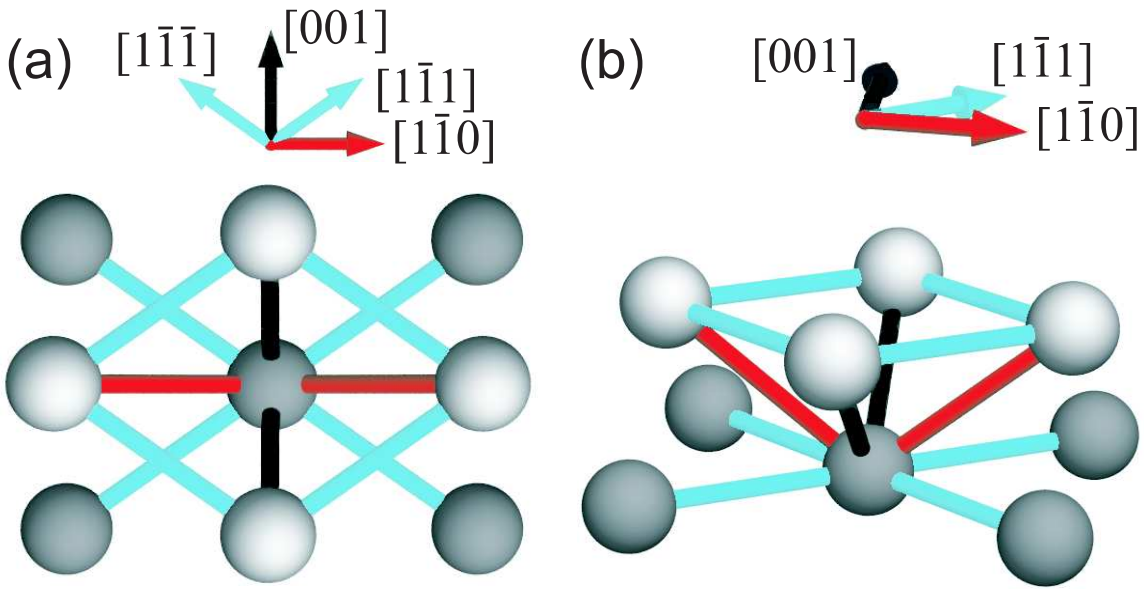

Figure 3.6: Unit cell of 2 ML Fe/W(110) in (a) top and (b) perspective view. Blue and black lines denote the nearest neighboring bonds in an undistorted, ideal crystal. Red lines denote additional nearest neighboring bonds due to relaxation.

As follows from the Eq. 3.2, the anisotropy of the exchange stiffness parameter A may come not only from the orthorhombic-like lattice symmetry but from the anisotropy of the exchange integral $J_{[hkl]}$ as well. The exchange integral is very sensitive to the nearest neighbor distance. Hence, the lattice mismatch in real materials may also lead to anisotropic effects. In the literature the calculation of $J_{[hkl]}$ as a function of relative position $\mathbf{r_{ij}}$ of the magnetic moments i and j has been performed for several ferromagnetic materials [71, 72]. These calculations show that the strength of the exchange coupling is a function of $\mathbf{r_{ij}}$. Especially interesting is the behavior of $J(\mathbf{r_{ij}})$ in Fe. For Fe a reduction in nearest neighbor spacing d_{NN} with respect to the bulk value drives the exchange towards antiferromagnetism. This effect has been made responsible for the fact that fcc-Fe is antiferromagnetic while bcc-Fe is a ferromagnetic material [73, 74]. This argument is also supported by the position of Fe on the Bethe-Slater curve, which is widely used in the physics of ferromagnetic alloys [74]. Thus, a decrease of the interatomic distance in [001] direction can lead—in contrast to other ferromagnets—to a reduction of the ferromagnetic exchange parameter.

For Fe nanowires on W(110) the situation is even more subtle due to hybridization and polarization effects at the Fe/W interface. All the more interesting is the advance,

described in very recent studies [75, 76], where the exchange stiffness of Fe films adsorbed on a W(110) surface has been calculated. The authors find that for a bcc lattice the exchange stiffness $A_{bcc} = 2JS^2/a$, depends on the direction along which the spin-wave is excited. For one monolayer Fe/W(110) the exchange stiffness in the $[1\bar{1}0]$ direction is 4 times larger than in the [001] direction [76]. For a 2 ML film the difference is found to be smaller but the tendency remains the same. The physical reason for this anisotropic behavior can lie in changes of interatomic spacing, as discussed above, or in additional indirect spin interactions through the W substrate [76]. In any case, the dependence of the exchange interaction on $\mathbf{r_{ij}}$ must be taken into account in the simulation of the magnetic ordering. This is especially important if other effects can influence the orientation of the domain walls.

An example of such a situation is provided by narrow Fe/W(110) nanowires having low wall density. In this case the wall orientation can be determined apart from the anisotropic exchange stiffness by the minimization of the wall length. If the shortest path does not coincide with the preferential direction for the exchange stiffness the two effects compete. This happens for $[1\bar{1}\bar{1}]$ oriented, 20 nm wide Fe nanowires. The shortest distance lies perpendicular to the sides of the wires, while exchange stiffness prefers the $[1\bar{1}0]$ orientation. For isotropic exchange constants a typical Monte-Carlo configuration in narrow nanowires consists of walls which are neither perpendicular to the sides of a wire as expected from the minimization of the wall length nor parallel to the easy $[1\bar{1}0]$ direction as expected from the orthorhombic-like lattice symmetry. The domain walls are mainly oriented along an intermediate $[1\bar{1}1]$ axis. In case of narrow [001] or $[1\bar{1}0]$ oriented wires the domain walls run perpendicular to the wire sides, *i*.e. the length minimization wins.

In the next set of calculations three different exchange constants J_{hkl} for the 3 nonequivalent pairs of neighboring magnetic moments have been introduced. Different ratios of $J_{1\bar{1}0} : J_{1\bar{1}1} : J_{001}$ (red, blue and black bonds in Fig. 3.6, respectively) have been explored. The best overall accordance with the experiment is found for $J_{1\bar{1}0} : J_{1\bar{1}1} : J_{001} = 4 : 2 : 1$ (Fig. 3.7(b) and (c)). For $[1\bar{1}1]$ nanowires (Fig. 3.7(b)) the majority of the walls follow the $[1\bar{1}0]$ axis. However, $[1\bar{1}1]$ walls can also be found. For $[1\bar{1}0]$ nanowires of 40 nm width (Fig. 3.7(c)) $[1\bar{1}0]$ oriented domain walls have also been obtained. The walls are not perfectly straight but show some irregularities. For example, the wall is forced out of the $[1\bar{1}0]$ direction at the rim of the nanowire. A similar behavior has also been found experimentally (see circle in Fig. 3.2(a)). Different orientations and strengths of the in-plane anisotropy K_p have been explored in [63]. As already mentioned above the only effect of a strong K_p is an alignment of the magnetic moments in the wall along the respective axis and broadening of the walls. The orientation of domain walls is not influenced by K_p, in accordance with the continuum model (Fig. 3.7(a)), showing that the mechanism of wall orientation described here is distinct from the one observed in bulk material, which is governed by magnetic anisotropy and dipolar energy.

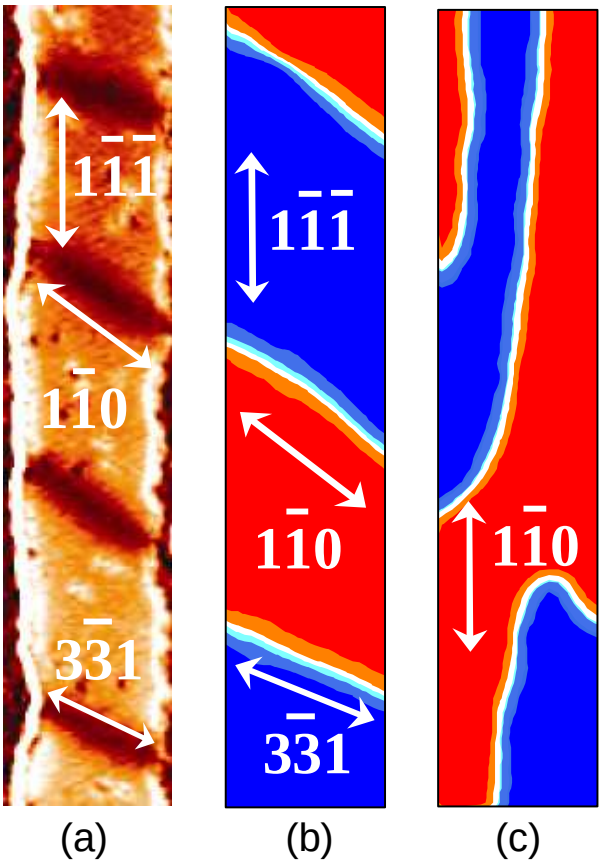

Figure 3.7: Top-view of experimental (a) and simulated (b),(c) Fe/W(110) nanowire sections of 20 nm (a),(b) and 40 nm (c) width. Majority of the walls run along $[1\bar{1}0]$ independent on the orientation of nanowires.

3.5 Summary

In conclusion, the orientation of magnetic domain walls in ultrathin films and nanomagnets is strongly influenced by the atomic lattice structure. The exchange stiffness tensor is anisotropic in mono-, double- and triple-layers with cubic structure and (110) orientation of the film surface due to the orthorhombic-like lattice symmetry of the incomplete cubic cells. The exchange stiffness for all other surface orientations of ideal cubic crystals is isotropic. Apart from the orthorhombic like symmetry the exchange stiffness can admit anisotropic character due to the anisotropy of the exchange integral resulting from the lattice relaxation. The anisotropy in the exchange stiffness leads to anisotropy in the orientation of magnetic domain walls. The magnetic anisotropy and the magnetostatic energy which govern wall orientations in bulk material, play a minor role in the ultrathin film limit.

Chapter 4

Self-Competition of the Long-Range Interactions in Nanomagnets

4.1 Introduction

Various problems in the theory of nanosystems lead to the consideration of the interactions amongst dipoles. Whereas in atomic magnetic materials the exchange interaction usually dominates over dipolar interactions, the opposite happens in many nanoscale particle or clustered magnetic systems, for which the interparticle interactions are mainly of magnetostatic origin. Long-range magnetostatic interactions are also at the heart of the explanation of many peculiar or anomalous phenomena observed in systems of fine particles embedded in a nonmagnetic matrix systems, molecular networks, colloids and rare-earth ions such as the 2D honeycomb magnets ErX_3. These demonstrate that magnetostatic interactions can be crucial in determining the magnetic order at low temperatures. On the other hand, the long range nature of magnetostatic interactions inevitably leads to frustration – a spin cannot simultaneously satisfy the conditions dictated by all the interactions. Depending on a system the magnetostatic interactions may contain mainly dipolar contribution, as so-called dipolar magnets, or additional higher-order multipolar terms as nanomagnetic arrays. In the following the details of the self-competition in the dipolar and multipolar systems will be given.

4.2 Dipolar Interactions

The dipole-dipole interaction is described by the Hamiltonian

$$E_{\text{dip}} = D \sum_{i,j} \left(\frac{\mathbf{S}_i \cdot \mathbf{S}_j}{r_{ij}^3} - 3 \frac{(\mathbf{S}_i \cdot \mathbf{r}_{ij})\,(\mathbf{S}_j \cdot \mathbf{r}_{ij})}{r_{ij}^5} \right) , \tag{4.1}$$

where $D = \frac{\mu_0 \mu_g^2}{4\pi d^3}$ is the dipolar coupling parameter with μ_0 - permeability of the vacuum, μ_g - magnetic moment of a particle, d - interparticle distance, $\mathbf{S}$ - the unit vector and the relevant sum is running over all spin pairs i and j defining the vector $\mathbf{r}_{ij}$.

4.2.1 Ising Moments on a periodic Lattice

In contrast to the isotropic exchange coupling the dipolar interaction has an anisotropic character. This means that even in a simple Ising case the ground state depends on the spatial orientation of the magnetic moments. If for example two Ising moments have only up- or down-orientations with respect to a plane, the right part of the Eq.4.1 becomes zero as the cosine of 90 degree is zero. Therefore, the ground state configuration is an antiparallel alignment of the moments Fig. 4.1a with energy per moment $E_{dip} = -1$ for $D = 1$ and $r_{ij} = 1$. For right- or left- orientations in the film plane, however, the ground state is head-to-tail configuration Fig. 4.1b with $E_{dip} = -3$ as the right part of the Eq. 4.1 is not zero any more.

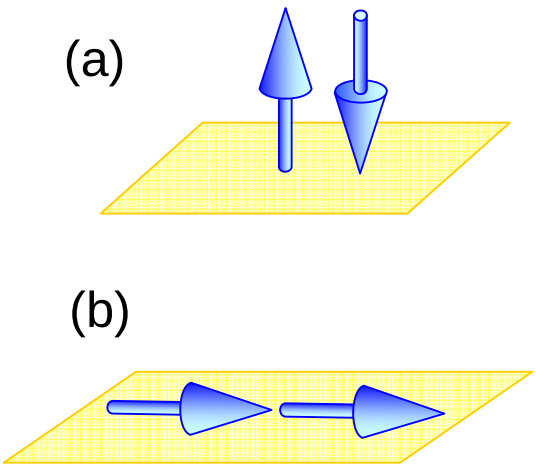

Figure 4.1: Ground dipolar states for two Ising moments which are oriented perpendicular (a) or parallel (b) to the film plane.

On a square lattice, the dipolar interaction between vertical spins corresponds to a long-range antiferromagnetic coupling and therefore leads to an unfrustrated checkerboard configuration. Fig. 4.2 shows Monte-Carlo structures for vertical Ising moments on a triangular lattice for two temperatures [20]. The configuration gives evidence of an effective in-plane anisotropy linked with the underlying discrete lattice. At a local size, an organization with parallel stripes of alternate spins occurs. At a larger scale stripes become organized with chevrons and labyrinthine patterns, as already observed in magnetic nanoarrays with uniaxial anisotropy [77] and magnetic liquids [78, 79]. With increasing temperature the zigzags and loops of complex labyrinthine structure roughen and shorten. An in-plane Ising dipolar system on a square lattice is frustrated. The ground states for this case are shown in Fig. 4.3. These are a single domain structure for a triangular and antiparallel stripes for a square lattice. The corresponding energies per spin on an infinite lattice for $D = 1$ are $E_{dip}^{square} = -2.5494$ for the configuration Fig. 4.3a and $E_{dip}^{triangle} = -2.7585$ for the configuration Fig. 4.3. The patterns of Figs. 4.1-4.2 appear because of the inability to form ideal configurations of Fig. 4.1 for all pairs of spins, i.e. because of frustration.

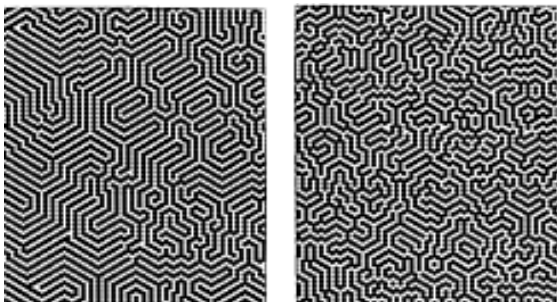

Figure 4.2: Pure dipolar coupling: portion of 200×200 vertical Ising spins on a triangular lattice with labyrinthine patterns of up (black) and down (white) spin domains. ¿From left to right: $kT/D = 0.05$ and 0.2.

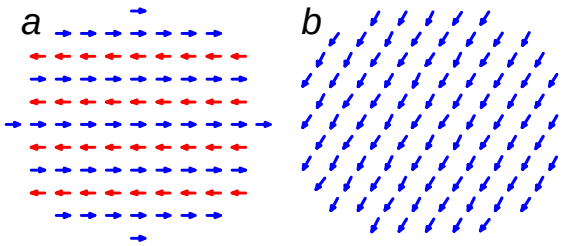

Figure 4.3: Zero temperature ground dipolar states for in-plane Ising moments on a square (a) and a triangular (b) lattice.

4.2.2 Vector Dipolar Moments on a Periodic Lattice

As it has been shown in the previous section in-plane configurations of magnetic/electric moments usually have lower dipolar energy than out-of-plane ordering. This becomes even more evident in systems consisting of vector moments which are free to choose any orientation in space. The pure dipolar systems on two-dimensional lattices often demonstrate in-plane alignment of moments due to an anisotropy arising from dipole-dipole interactions. In that case the XY and the Heisenberg models lead to very similar ground states.

Another striking feature of the dipolar interaction is that it decreases slowly as a function of the distance. As a consequence the dipolar field $\mathbf{H}_{dip}(i)$ experienced by a given moment $\mathbf{S}_i$depends significantly on the moments located at the boundary of the sample and this results in the so-called *shape anisotropy*. The shape anisotropy is usually calculated as a difference between the dipolar energy of a most unfavorable and that of a most favorable configuration.

It is well known that the ground state of a dipolar system on a square lattice is antiferromagnetic just as the in-plane Ising configuration. However, several studies of this ground state demonstrated that the situation is more subtle than one might initially suppose [80, 81]. The ground state of an infinite square lattice is highly degenerate and defines a continuous manifold of spin configurations at $T = 0$, although the dipolar coupling itself is not rotational invariant. The same is true for a dipolar system on a honeycomb lattice. For zero temperature the spins lie in the film plane but the ground state is continuously degenerate [82]. Examples of degenerated configurations are shown in Fig. 4.4. Configurations Fig. 4.4a,b have the same energy and are both ground states for a dipolar honeycomb lattice. The right configuration is obtained from the left one by the rotation of the sublattice A (red) by $\phi = +\pi/6$ and the sublattice B (blue) by $\phi = -\pi/6$, i.e. $\varphi(\mathbf{R}_A) \to \varphi(\mathbf{R}_A) + \phi$ and $\varphi(\mathbf{R}_B) \to \varphi(\mathbf{R}_B) - \phi$. The same transformation has been performed for a square lattice Fig. 4.4c,d.

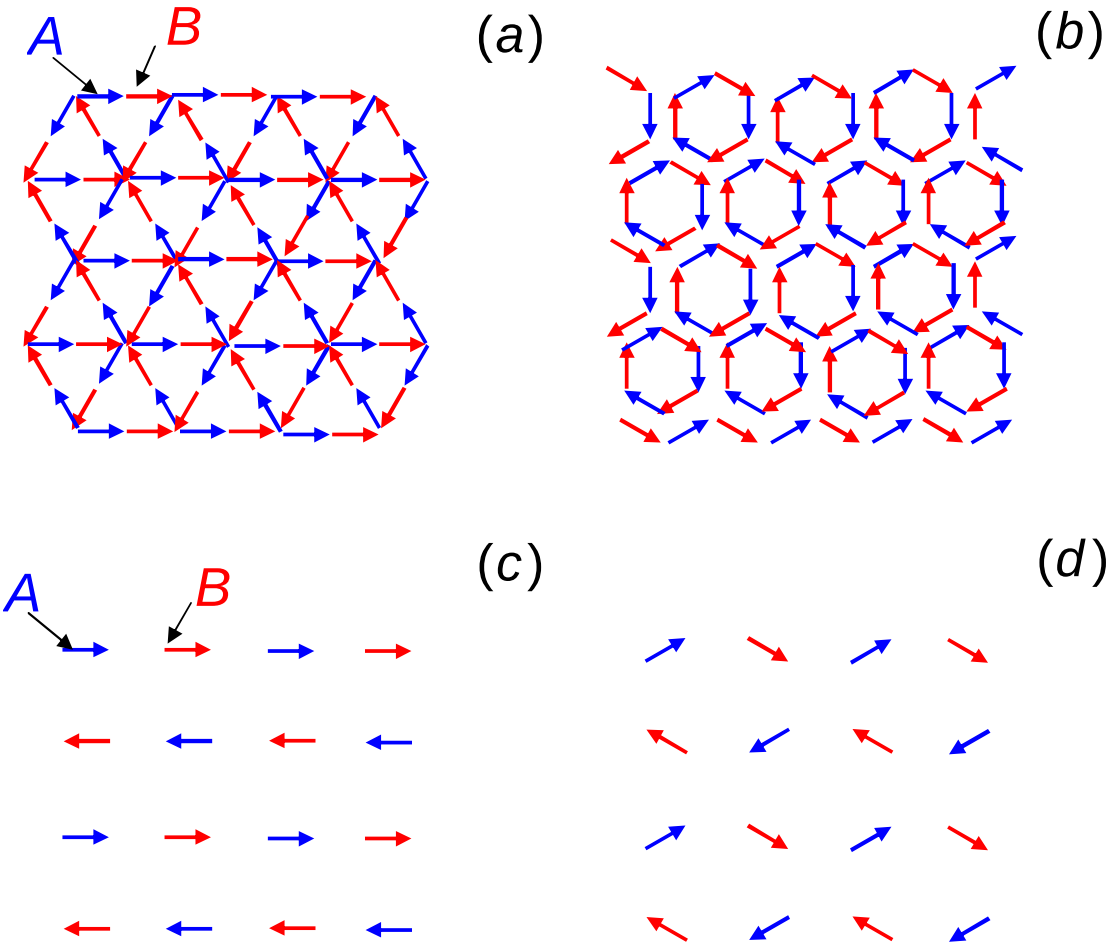

Figure 4.4: Two examples of the class of continuously degenerate ground states ($\phi = 0, \pi/6$) of a dipolar magnet on a honeycomb (a-b) and a square (c-d) lattice.

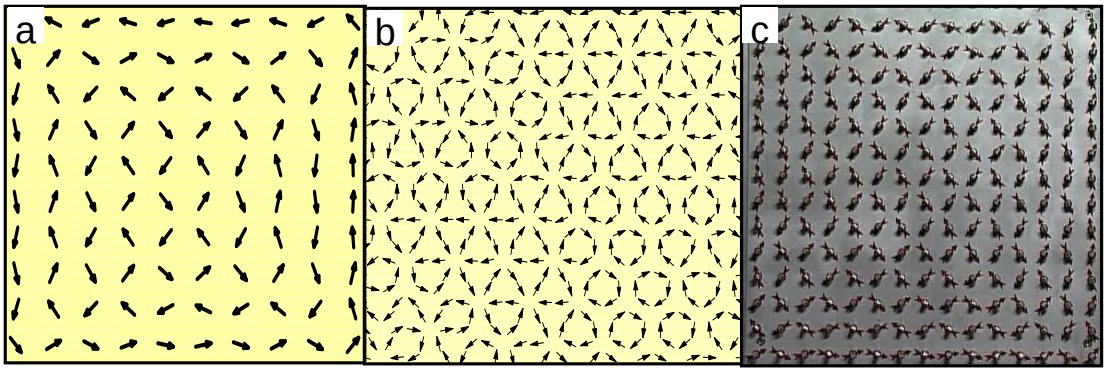

Figure 4.5: Pure dipolar coupling: top view of a portion of low-temperature ($kT = 0.05D$) Monte-Carlo configuration on (a) a square lattice, (b) a honeycomb lattice; (c) experimental dipolar model on a square lattice. The model belongs to the physical collection of J. Kirschner at the Max-Planck Institute for the microstructure physics in Halle, Germany

At finite temperatures the situation for the square and the honeycomb symmetry is different. As has been shown by Monte Carlo calculations and spin wave theory, a magnetic ordering and a critical temperature exists for dipole coupled spins on a square lattice [81, 83], since the magnetic and temperature excitations are not continuously degenerate. In this case a quartic shape anisotropy is present, the corresponding easy axes being the edges of the square lattice. In other words, the density of states and thus the entropy depends on the magnetic direction within the lattice. This phenomenon is an example of the *order-by-disorder* effect in frustrated magnets [83]. A typical configuration obtained by Monte-Carlo simulations for a finite square lattice at finite temperature is given in the Fig. 4.5a. Lines of dipoles are observed on the edges which are formed due to the pole avoidance principle. The microvortex $\phi = 45°$ configuration is formed in the center. Hence, the finite size and temperature remove the continuous degeneracy of the ground state. The Monte-Carlo data have been recently confirmed by an experimental model made of small magnets which are free to rotate in the XY-plane (see Fig. 4.5b). The density of states on a honeycomb lattice does not depend on a specific lattice direction and the ground state is degenerate with respect to continuous rotations of opposite sense on both sublattices [84]. Therefore, a low-temperature Monte-Carlo structure on honeycomb lattice shows different degenerate states in the same sample (see Fig. 4.5c).

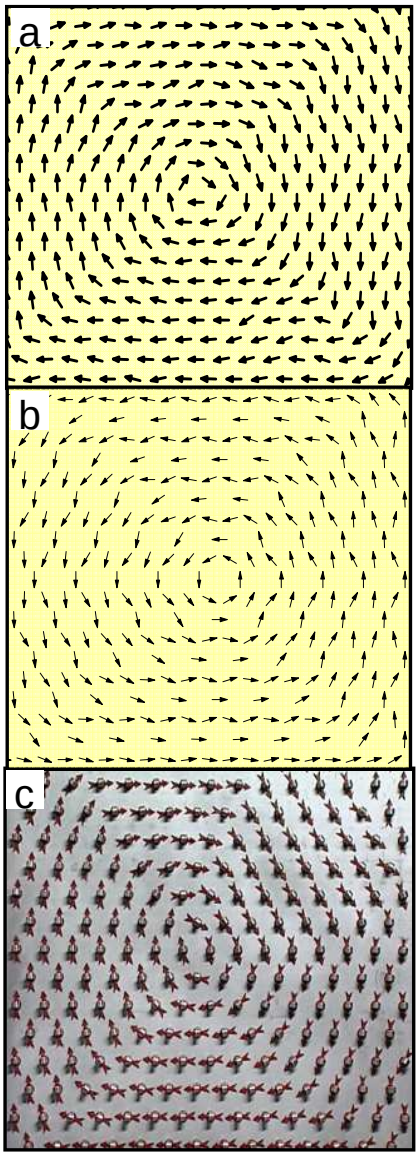

Figure 4.6: Pure dipolar coupling: top view of a portion of low-temperature ($kT = 0.05D$) Monte-Carlo configuration on (a) a triangular lattice, (b) a kagome lattice; (c) experimental dipolar model on a triangular lattice. The model belongs to the physical collection of J. Kirschner at the Max-Planck Institute for the microstructure physics in Halle, Germany

What happens with dipoles on a triangular and a kagome lattice? For open boundary conditions a planar vortex structure appears, which is formed to avoid free magnetic poles at the boundaries of the sample (see Fig. 4.6a,b). The ground state of an infinite sample is a ferromagnetic-like monodomain structure. In the Fig. 4.6c a picture of experimental verification of the dipolar system made of 364 small magnets on the triangular lattice is shown. The Monte-Carlo simulations and the experiment reveal identical structures. Thus, due to the geometric frustration of the lattice, which commonly leads to a disorder or a noncollinear-

ity, the perfectly ordered vortex is formed.

In conclusion, although the dipolar coupling has an antiferromagnetic nature the ground states of vector spins for pure antiferromagnetic and pure dipolar interactions are completely different. Square and honeycomb geometries which are unfrustrated in case of pure antiferromagnetic coupling lead to frustrated, non-collinear ground states in the pure dipolar case. Strongly frustrated, non-collinear for a pure antiferromagnetic interaction triangular and kagome lattices lead to ordered collinear low-temperature dipolar configurations.

4.3 Multipolar Interactions: Why can that be interesting?

Among the interactions in many-body atomic, molecular or nanoparticle systems those of electrostatic or magnetostatic nature are very important. Recently, arrays of nanoparticles or adsorbates have been proposed for a number of applications as storage [51], high speed non-volatile magnetic memory (MRAM) [52], and logic functions for computations [53]. Different applications require different properties of an array. While in storage applications every particle should be individually addressed; *i.e.* the nanoelements should not interact, for logic schemes strong interactions are necessary. In both cases the control of interactions between nanoparticles is very important. To derive the theory of these interactions one needs to know the charge distribution of a particle. One of the simplest and most effective ways to do this is to describe a distribution of charges as a series of multipole moments. There exist several different ways to explain what are the multipole moments. First a mathematical point of view will be addressed.

(ii) Multipole moments: Spherical Coordinates

Any two-dimensional periodic function can be expanded in terms of an infinite sum of sines and cosines with corresponding coefficients. This expansion is known as Fourier series

$$f(x) = \frac{1}{2}a_0 + \sum_{n=1}^{\infty} a_n \cos(nx) + \sum_{n=1}^{\infty} b_n \sin(nx) \ . \tag{4.2}$$

The coefficients $a_n$and b_n can be described as integrals of the periodic function Eq. 4.2 multiplied with $\cos(nx)$ or $\sin(nx)$

$$\begin{aligned} a_n &= \tfrac{1}{\pi} \int_{-\pi}^{\pi} f(x)\cos(nx)dx \ , \\ b_n &= \tfrac{1}{\pi} \int_{-\pi}^{\pi} f(x)\sin(nx)dx \ . \end{aligned} \tag{4.3}$$

Similarly, any scalar field on a sphere, which is periodic by definition, can be expressed in spherical coordinates $r = f(r, \theta, \varphi)$ (description of spherical coordinates is given in Fig. 4.7) as a series of *Spherical Harmonics* with corresponding coefficients,

$$H(\theta,\varphi) = \sum_{l=0}^{\infty}\sum_{m=-l}^{l} Q_{lm}R_{lm}(r) = \sum_{l=0}^{\infty}\sum_{m=-l}^{l} Q_{lm}Y_{lm}(\theta,\varphi)\frac{4\pi}{2l+1}r^l \ . \tag{4.4}$$

The coefficients Q_{lm} are the multipole moments, $R_{lm}(r) = \sqrt{\frac{4\pi}{2l+1}}r^l Y_{lm}(\theta,\varphi)$- normalized *Spherical Harmonics,* $Y_{lm}(\theta,\varphi)$- simple *Spherical Harmonics.* The spherical harmonic with $-l < m < l$ is a function of the two coordinates θ, φ on the surface of a sphere and can be modeled by special set of polynomials known as Legendre functions $P_{lm}(\cos\theta)$. Spherical harmonics are natural functions for the description of a system with spherical symmetry. For example, with spherical harmonics the 3D motion of an electron around a nucleus can be described. In that case a spherical harmonic can be though of as a 3D-path that a particle can travel without "destroying" itself energetically. This 3D-path is not fixed, and can take on many different shapes, even for one energy level. In this sense the spherical harmonics correspond to the angular part of the atomic orbitals. An example of typical representation of e.g. d_{z^2}orbital in physics is shown in the Fig. 4.8a.

The orbital corresponds to the spherical harmonic Y_{20} and is uniformly colored as it represents simply a volume of space within which an electron would have a certain

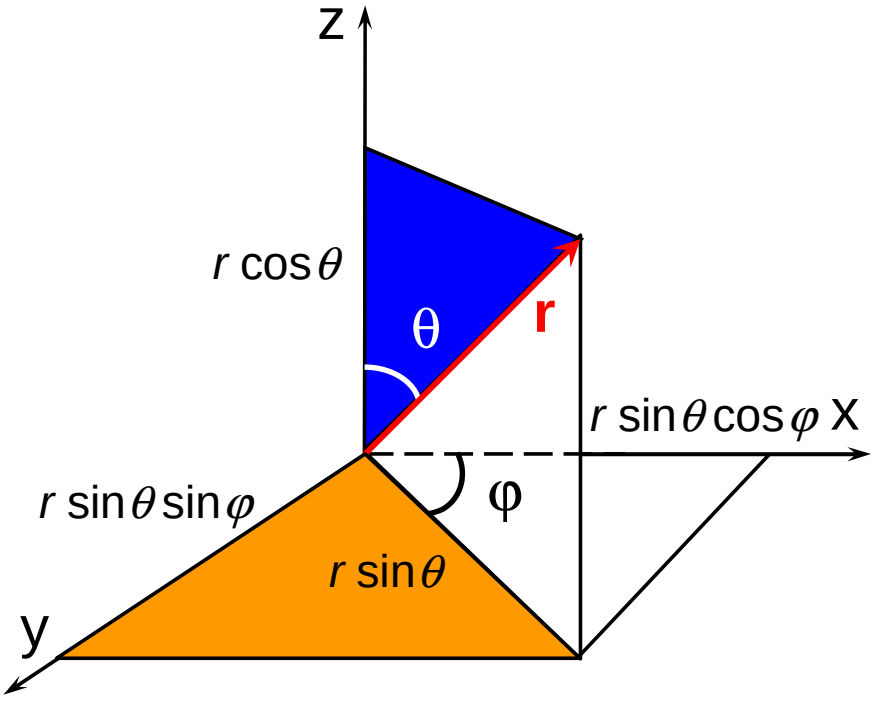

Figure 4.7: Definition of the spherical polar coordinates

probability of being (the wave-function of electron). On the other hand, with the spherical harmonics a spatial distribution of electric charges due to a molecule can be represented. In that case a charge distribution is usually two-colored as in the Fig. 4.8b. The colors correspond to positively and negatively charged parts of the distribution. This representation is typical for quantum chemistry or molecular biology. The multipole expansion plays an important role in the geosciences and the cosmology as well. With help of the multipoles gravity fields can be expanded and the linear polarization of the sky can be predicted. In geosciences and astronomy multipoles are defined with slightly different constants which lead to so-called zonal, tesseral and sectoral representations. A typical zonal image of $Y_{20}$is given in the Fig. 4.8c. There are many other applications of the multipole calculus throughout the physical sciences as nuclear physics, radio physics etc. The graphical representation, however, can be attributed to one of three examples of the Fig. 4.8.

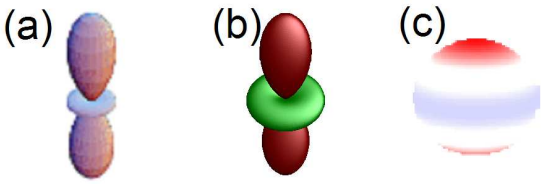

Figure 4.8: Representation of the spherical harmonic Y_{20} for the description of (a) atomic orbital, (b) distribution of charges, (c) sky polarization (zonal spherical harmonic)Representation of the spherical harmonic Y_{20} for the description of (a) atomic orbital, (b) distribution of charges, (c) sky polarization (zonal spherical harmonic)

Similarly to the Fourier coefficients of the Eq. 4.3, a multipole moment is nothing else as a volume integral of a charge distribution multiplied with the normalized spherical harmonic

$$Q_{lm} = \int_V \rho(r) R_{lm}(r) dV \ . \tag{4.5}$$

Hence, the multipoles themselves can be visualized as spherical harmonics. The Fig. 4.8 represents then Q_{20}.

(iii) Multipole moments: Cartesian Coordinates

For the calculation of the electrostatic potential φ of a charge density ρ at the distance $R >> r$ where r is the maximal size of the charge distribution ρ in Cartesian coordinates one can use so-called multipole expansion. An electrostatic potential as a function of R can be expanded in integral powers of a small parameter r/R; i.e., $\varphi(R)$ can be represented as a number series of a sum where higher terms include higher powers of r/R: $\varphi(R) = \varphi_0/R + \varphi_1/R^2 + \varphi_2/R^3 + ...$ and become less and less important at large distances. This is known as the multipole expansion with

0th order: Monopole potential (falls off like$1/R$, corresponds to Q_0)
1th order: Dipole potential (falls off like $1/R^2$, corresponds to Q_1)
2nd order: Quadrupole potential (falls off like $1/R^3$, corresponds to Q_2)

3rd order: Octopole potential (falls off like $1/R^3$, corresponds to Q_3)
etc....

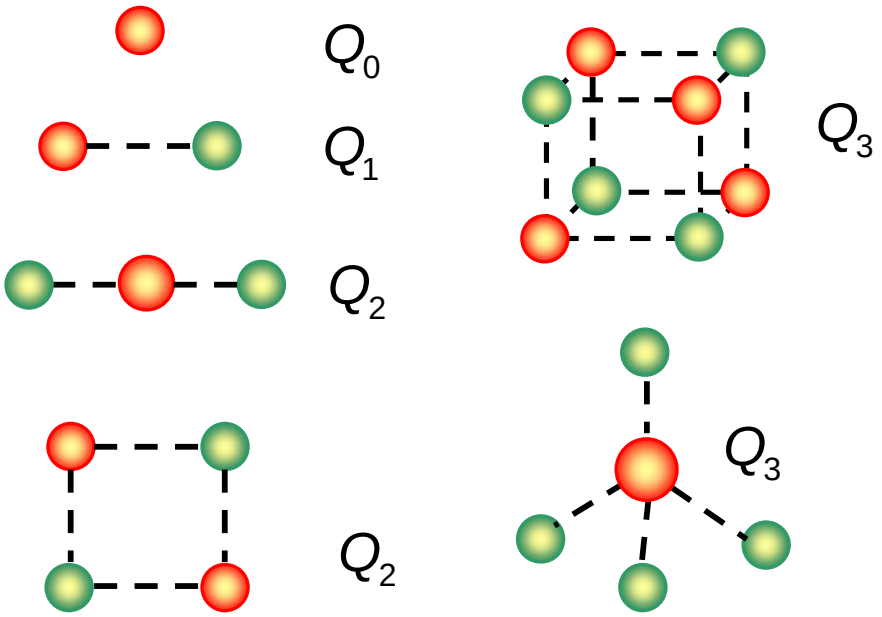

Figure 4.9: Possible shapes of multipoles composed of several electric charges. Q_0-monopole, Q_1-dipole, Q_2-quadrupole, Q_3-octopole

Shapes of multipoles to the third order in terms of electric charges are shown in the Fig. 4.9. The first term corresponds to a single charge and is called a "monopole moment"; it is a scalar. The dipole moment is a vector. In general, the order-n term in the sum is $1/|\mathbf{x}|^{n+1}$ times the contraction of a certain nth-rank tensor with n copies of; the tensor is the 2^n*-pole moment* of the configuration of charges.

4.3.1 Multipolar Moments of Molecular Systems and Bose-Einstein Condensate

Polar molecules with an asymmetric charge distribution; *i.e.* with one end of the molecule relatively negative with respect to the other possess a permanent dipole moment. Examples are HF, H_2O, FCl (where the F atom is negative with respect to the Cl atom), the polyatomic molecule $HCCl_3$ (where the H end of the molecule is positive with respect to the three Cl atoms), three isomers of 1,1-Dichloroethene; cis-1,2-Dichloroethene; trans-1,2-Dichloroethene and many others. As a dipole is a vector quantity a total molecular dipole can be obtained by summing up all individual bond-dipoles as shown in the Fig. 4.10.

Although linear molecules as CO_2 or acetylene (H-C≡C-H) and the planar molecule benzene (C_6H_6) do not have molecular dipole moments (Fig. 4.10), they have non-zero quadrupole moments [85]. Another example of organic quadrupoles give 3,4,9,10-perylenetetra-carbo-xylicdianhydride, better known as PTCDA molecules, which can

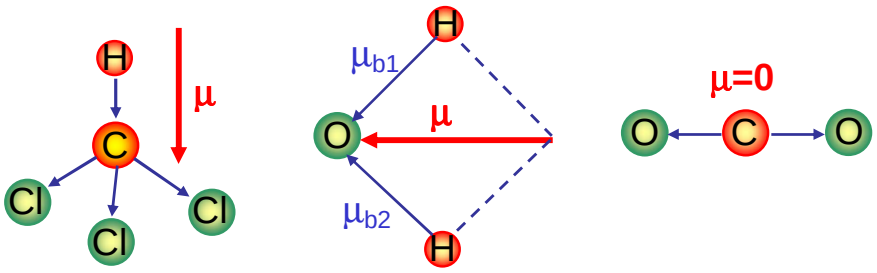

Figure 4.10: Molecular dipole moments μ of polyatomic molecules

be adsorbed on various substrates [86, 87]; H_2, N_2, CO on salts or metal surfaces; ortho-para hydrogen molecules adsorbed on hexagonal boron nitride; solid hydrogen; N_2Ar mixtures and many others [88–90]. There exist more complicated cases. For example, the total quadrupole moment of the water molecule is zero. However, Q_2^{xx},Q_2^{yy},Q_2^{xy},Q_2^{xz},Q_2^{yz} tensor components of the quadrupole moments in Cartesian coordinates have non-zero values. For more symmetrical molecules, the first non-zero multipole moments have higher order. Examples are the methane molecule (CH_4) and giant Keplerate molecule Fe_{30} which have no dipole or quadrupole moment, but has a non-zero octopole moment [91, 92].

More complicated molecular charge distributions have different multipolar contributions. For example an "American football" which is polarized along it's long axis has non-zero even multipolar contributions $Q_{football} = Q_0^{football} + Q_2^{football} + Q_4^{football} + Q_6^{football} + Q_8^{football} + ...$ The same is true for a discus or any other polarized object, which is rotationally symmetric and at the same time symmetric around it's equatorial axis. Rotationally symmetric but not equatorially symmetric objects as, *e.g.*, bowling pin possess as even as odd multipolar moments $Q_{b.pin} = Q_0^{b.pin} + Q_1^{b.pin} + Q_2^{b.pin} + Q_3^{b.pin} + Q_4^{b.pin} + ...$

A Bose-Einstein condensate is a phase of matter formed by bosons cooled to temperatures very near to absolute zero. At low temperatures, bosons can behave very differently than fermions because an unlimited number of them can collect into the same energy state, a phenomenon called "condensation". For the first experimental verification of this phase predicted by A. Einstein and S. Bose the Nobel Prize in Physics for 2001 has been awarded to Eric A. Cornell, Wolfgang Ketterle and Carl E. Wieman. They succeeded by cooling 2,000 rubidium atoms to a temperature less than 100 billionths of a degree above absolute zero to force the atoms to lose for 10 seconds their individual identities and behave as though they were a single "superatom". Nowadays magneto-optical traps for gas condensation became much more sophisticated and the drops of condensate can be arranged in a cubic structure in the potential minima of an optical lattice. Recent experimental and theoretical studies have established that ^{87}Rb spinor condensate may be ferromagnetic at zero temperature. It means, the expectation value of total spin of a condensate drop $\mathbf{F}$ is finite $\langle \mathbf{F} \rangle \neq 0$ [93, 94]. As a result, an ensemble of condensates acts much like large spins or dipoles on a crystalline lattice. The very new investigations [95] show that un-

der certain circumstances Bose-Einstein condensate columns may have quadrupolar moments.

4.3.2 Multipolar Moments of Nanomagnetic Particles

Particles with lateral size smaller than the characteristic exchange length $d < \chi_{ex}$ have a single domain magnetization configuration with a macroscopic magnetic moment. In case of an ideal single domain all elementary dipoles inside of a particle are compensated and only at the boundary appear uncompensated positive and negative magnetic poles (see Fig. 4.11).

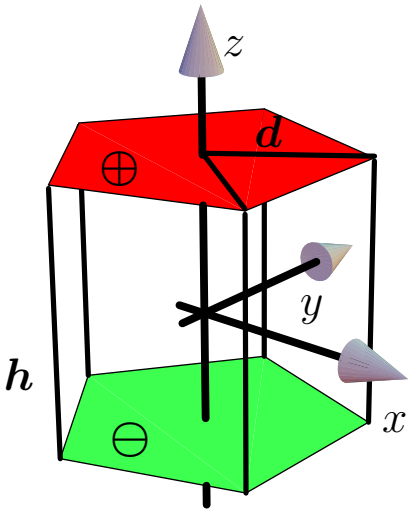

Figure 4.11: Scheme of a nanoparticle with n-fold symmetry. Every surface can be divided into n equivalent isosceles triangles with edge length d. The particle is magnetized in $z-$ direction

Isolated magnetic poles have never been observed in nature. They occur always in pairs as in the example described. However, it is often convenient to use instead of magnetic poles and the vector field quantity $\mathbf{H}$ the notion of magnetic charges and a scalar potential φ. The quantity φ is defined so that it's negative gradient is the magnetic field $\mathbf{H} = -\nabla\varphi$ where the operator ∇ is $\nabla = \mathbf{i}\frac{\partial}{\partial x} + \mathbf{j}\frac{\partial}{\partial y} + \mathbf{k}\frac{\partial}{\partial z}$. Here $\mathbf{i}, \mathbf{j}, \mathbf{k}$ are the unit vectors of a Cartesian coordinate system, and (x, y, z) are the coordinates at the point where the field or potential is under consideration. In the framework of this approximation the macroscopic moment of a polarized or magnetized particle can be obtained by means of the multipole expansion of a continuous magnetization distribution within a dot described in the Section 4.3 ((ii) or (iii). As can be seen from the Eq. 4.5 the strength of a multipole moment depends solely on a charge distribution; *i.e.* on a shape of an object and on a magnetization/polarization configuration. Hence, for typical magnetization distributions corresponding multipolar moments can be calculated on the basis of Eq. 4.5.

Let us assume a nanoparticle with n-fold symmetry ($n > 1$) within the $x - y$ plane, which is magnetized in z-direction (Fig. 4.11). The symmetry-axis is parallel to the polarization. The upper surface of the particle is positively charged with the surface charge density $\sigma = \mu_0 \mathbf{n} \cdot \mathbf{M}(\mathbf{r})$ due to uncompensated dipoles, with the unit vector $\mathbf{n}$ perpendicular to the surface and the magnetization vector field $\mathbf{M}(\mathbf{r})$. With this definition the unit for the magnetic charge is *Volt-second* and the magnetic dipole moment is measured in *Volt-second-meter*. The bottom charge is the mirror image of the positive charge distribution at the top of the particle. To find the integral Eq. 4.5 explicitly the charged surface can be into n identical triangles (Fig. 4.11). Then Q_{lm} are calculated by the sum over the triangles ($0 \leq j \leq n-1$) of the top and the bottom

surfaces. As the charged surfaces are planar the volume charge density ρ and the volume integration in the Eq. 4.5 can be substituted by the surface charge density σ and integration over the surface element dS

$$Q_{lm} = \sum_{j=0}^{n-1} \left(\int\limits_{j_{th} top-triangle} dS|\sigma(\mathbf{r})|R_{lm}(\mathbf{r}) - \int\limits_{j_{th} bottom-triangle} dS|\sigma(\mathbf{r})|R_{lm}(\mathbf{r}) \right) . \quad (4.6)$$

After several simplification steps this integral can be evaluated analytically. The details of the calculation can be found in [96]. Similar procedure can be applied to the in-plane magnetized discs shown in the Fig. 4.12.

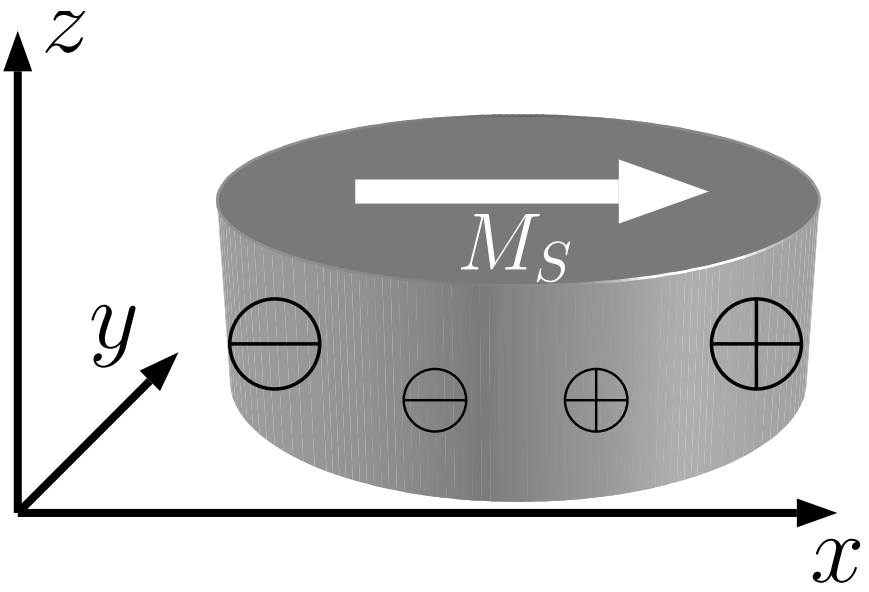

Figure 4.12: Scheme of a disk within the $x-y$-plane (magnetized in x-direction). Due to the magnetization a magnetic surface positive and negative charges emerge. In case of a uniform magnetization the charge is cosine distributed

Due to the natural symmetry of a disc it is trivially proportional to $\cos\varphi$ in cylindrical coordinates. Furthermore, the cosine charge distribution can be easily generalized for non-uniform onion states as the charge distribution can be expanded like $\rho(\mathbf{r}) \propto \sum_p c_p \cos^p \varphi$ with expansion coefficients c_p. Due to the symmetry of the onion configuration (Fig. 4.12) only odd integer p appear. The non-uniformity of the magnetization increases with increasing p. Expressing the volume element and normalized spherical harmonics of the Eq. 4.5 in cylindrical coordinates one obtains the following

integral

$$Q_{lm}^{p} = \mu_0 M_S \int_{-h/2}^{h/2} dz \int_{0}^{2\pi} r_0 d\varphi \left(\cos^p \varphi \cdot R_{lm}(\sqrt{r_0^2 + z^2}, \frac{\pi}{2} - \arctan \frac{z}{r_0}, \varphi) \right) . \qquad (4.7)$$

The integral in Eq. 4.7 has polynomial solutions for all integer p including $p = 1$ for uniform magnetization [97]. The low order moments of a particle Fig. 4.11 (Eq. 4.6) with four-fold and cylinder symmetry as a function of a surface area and a height are brought together in the Tab. 4.1.

Table 4.1: The multipole moments Q_{lm} in units of the surface charge density up to the order $(l, m) = (7, 0)$ of isotropically magnetized in z-direction particles with four-fold and cylindrical symmetry

l	m=0 (Four-fold Symmetry)	M=0 (Cylindrical Symmetry)
1	$2hd^2$	πhd^2
3	$hd^2(\frac{h^2}{2} - d^2)$	$\frac{\pi}{4}hd^2(h^2 - 3d^2)$
5	$\frac{h^5d^2}{8} - \frac{5h^3d^4}{6} + \frac{7hd^6}{12}$	$\frac{\pi}{16}hd^2(h^4 - 10h^2d^2 + 10d^4)$
7	$\frac{h^7d^2}{32} - \frac{7h^5d^4}{16} + \frac{49h^3d^6}{48} - \frac{3hd^8}{8}$	$\frac{\pi}{64}hd^2(h^6 - 21h^4d^2 + 70h^2d^4 - 35d^6)$

The dependency of the strength of multipole moments on the effective aspect ratio h/a of a particle with out-of-plane magnetization (Fig. 4.11) is shown in Fig. 4.13a while for an in-plane magnetized disc (Fig. 4.12) in Fig. 4.13b.

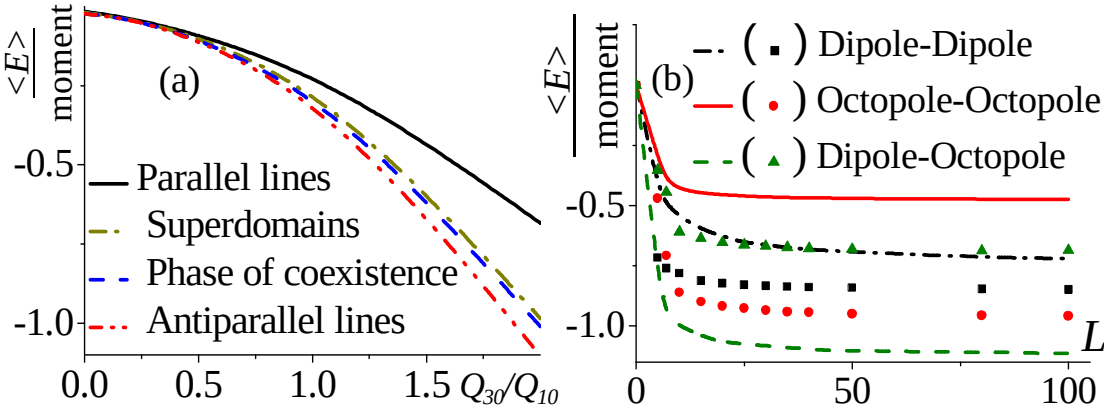

Figure 4.13: a) The low order multipole moments Q_{lm} (normalized to dipolar moment Q_{10}) of particles with fourfold symmetry with height h and edge length a. For $h \to 0$ $Q_{30} \approx -0.25Q_{10}$. (b) The multipole moments in units of the dipolar moment of the in-plane magnetized discs with height h and radius a. Magnetization configuration is a non-uniform onion state

The most important conclusions are following. First, all homogeneously out-of-plane magnetized prismatic particles with even rotational symmetry (Fig. 4.11) and all in-plane magnetized discs (Fig. 4.12) do not possess multipolar moments with even l; i.e., the quadrupoles (Q_{20}), the hexadecapoles (Q_{40}) etc. are not allowed (see Fig. 4.11). The lowest moment with l even is $(l, m) = (4, 3)$ for an odd, three-fold prism. The first possible multipole moment with even l for a five-fold symmetry is $(l, m) = (6, 5)$. The functions $Q_{lm}(h, a)$ may cross zero. This happens for example for the octopole moments of a cube (see Fig. 4.13a). For vertically magnetized particles the octopole moment reaches 25% of the dipole moment in the limit of small thicknesses. This geometry corresponds to sizes of particles often used in experimental studies [98–101]. For vertically elongated particles, such as arrays of magnetic nanocolumns [77, 99] or liquid colloidal crystals with rod-like components [102] the magnitude of the octopole moments exceeds that of the dipolar one. Similar results have been obtained for in-plane magnetized dots. For $h \approx a$ the multipolar moments are smaller than the dipolar one. However, in the limit of small thickness ($h << r_0$) the octopole moment Q^p_{31} reaches -61% of the dipole moment Q^p_{11} for all odd p and even the dotriacontapole (Q^p_{51}) is of the order of $0.5Q^p_{11}$ (see Fig. 4.13b). Hence, the multipole moments of ultrathin, in-plane magnetized discs may also be comparable with their dipolar counterparts. The described geometry is typical for on-going experimental studies on magnetic arrays.

4.3.3 Multipole-Multipole Interactions

Knowing the multipole moments of two particles the multipole-multipole interaction energy can be calculated. The most general formulation for two non-intersecting charge distributions is given by [103]

$$E_{AB} = \frac{1}{4\pi\mu_0} \sum_{l_A l_B m_A m_B} T_{l_A l_B m_A m_B}(R_{AB}) Q^A_{l_A m_A} Q^B_{l_B m_B} \tag{4.8}$$

with the geometric interaction tensor $T_{l_A l_B m_A m_B}$ [85, 104]

$$T_{l_A l_B m_A m_B}(\mathbf{R}_{AB}) = (-1)^{-l_B} I^*_{l_A+l_B m_A+m_B}(\mathbf{R}_{AB}) \sqrt{\frac{(l_A + l_B - m_A - m_B)!(l_A + l_B + m_A + m_B)!}{(l_A - m_A)!(l_B - m_B)!(l_A + m_A)!(l_B + m_B)!}} \; . \tag{4.9}$$

The multipole-multipole interaction is a long-ranged one. Therefore, for an ensemble of particles having higher order multipolar contributions the interaction energy between every pair of constituents has to be calculated. For large systems it is impossible. On the other hand the strength of the interaction between higher order multipoles decreases rather quickly with distance. The dependence on distance is given by the complex conjugate of the irregular normalized spherical harmonic function $I^*_{l_A+l_B m_A+m_B}(\mathbf{R}_{AB}) = \sqrt{\frac{4\pi}{2l+1}} \frac{Y_{lm}(\theta,\varphi)}{r^{l+1}}$. Hence, it follows from Eq. 4.9 that the interaction

energy between moments $Q^A_{l_A}$ and $Q^B_{l_B}$ of order l_A and l_B respectively decreases with increasing distance as $R^{l_A+l_B+1}_{AB}$. Consequently, higher order multipole moments are important mainly for $R \geq d$. Therefore, for multipoles of order $l \geq 3$ a so called cut-off procedure is appropriate; i.e. calculations of interaction energy may be restricted to several nearest neighbors only. To calculate ground states of multipolar systems one need either to guess a configuration, calculate it's energy and compare with another guesses or introduce the Hamiltonian Eq. 4.9 into the Monte-Carlo scheme [105].

4.3.4 Ground States for Multipoles of even Symmetry: Quadrupolar and Hexadecapolar Patterns

Fig. 4.14 shows low-temperature Monte-Carlo configurations of a pure quadrupolar system on a triangular and a square lattice for three-dimensional and XY planar moments [106]. The consideration is restricted to rotationally symmetric Q_{20} quadrupoles observed in nature [86, 88, 107, 108]. For three-dimensional moments on a triangular lattice a long-range, three-dimensional configuration consisting of seven-atomic rotors or "pinwheels" with the central atom oriented vertically and the others lying in the film plane has a minimal energy (Fig. 4.14a). The vertical moments form a triangular $2a$ superstructure. That structure corresponds to the so-called "4-phase" of hydrogen molecules on a triangular lattice found in mean-field and molecular-dynamics approximations [89, 90]. Every vertical quadrupole occupies the centre of a hexagonal pinwheel. For an ideal configuration every pinwheel element belongs simultaneously to two adjacent pinwheels, i.e. the unit cell has three in-plane and one vertical moment. Therefore, the perfectly ordered pinwheel phase has an average vertical projection per moment $\langle Q_{20z} \rangle = 0.25$.

The three-dimensional pinwheel structures have been observed experimentally, by means of nuclear magnetic resonance spectroscopy studies in ortho-hydrogen adsorbates[109] and $Ar_{1-x}(N_2)_x$ quantum crystals [88, 89, 109]. Hence, the symmetry of ground state confirms the pure quadrupolar nature of the pinwheel phase in those systems. The phase is double degenerate as the rotors can have clockwise or counter clockwise sense of rotation. In contrast to previous studies [89, 90] a 3D quadrupolar system on a triangular lattice easily admits domains (Fig. 4.14a) with different sense of rotation. Between the domains a domain wall consisting of moments with T-like mutual orientation is formed (Fig. 4.14a). The T-orientation is the energetically most favourable one for two quadrupoles. Therefore, the total energy of the domain structure is almost identical with that of a monodomain, while the entropy of the domain structure is higher. According to the principle of maximal entropy the domain structure represents the state of lowest free energy at finite temperatures. The crossing of the domain walls is, however, not allowed as this will lead to an increase of the internal energy due to the deviation of the moments from their equilibrium orientation in the neighbourhood of the crossing point. Two parallel domain walls cannot come closer than two primitive cells of the pinwheel structure ($4a$) without increase of the

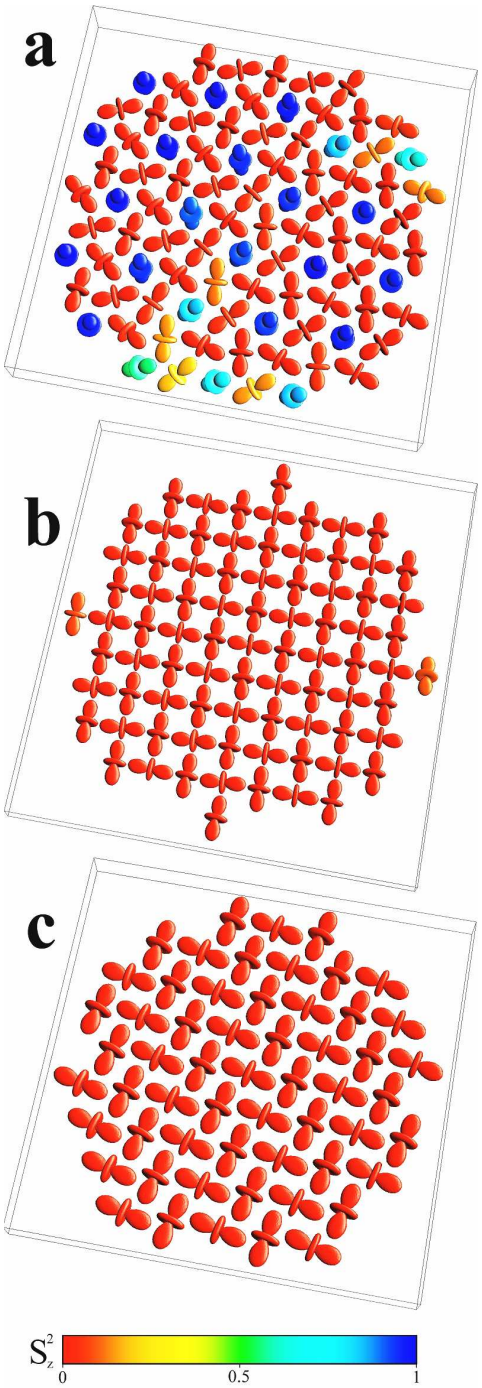

Figure 4.14: The low-temperature pure quadrupolar Monte-Carlo configurations on a triangular (**a,c**) and a square (**b**) lattice. The quadrupoles are represented by the spherical harmonic Y_{20} corresponding to the equipotential surface of a charge distribution with Q_{20} quadrupole moments; the two clubs represent positive charge, while the belly is negatively charged. Perspective view of a portion of a configuration. The colour scheme denotes the squared vertical component of the projection of a moment. The quadrupoles are $3D$ moments in (a, b) and XY moments in (c)

internal energy of the system. Therefore the low-temperature configuration of a large Q_{20} quadrupolar system on a triangular lattice consists of an array of clock-wise and counter-clockwise "pinwheel" domains separated by parallel domain walls.

In contrast to the triangular lattice the ground state configuration of quadrupoles on a square lattice is completely planar (Fig. 4.14b). The twofold lattice symmetry permits the T-configuration for every pair of nearest neighbours, i.e. the configuration is non-frustrated and monodomain. As the moments have not been constrained to lie in the XY plane it can be concluded that the quadrupolar interaction induces very strong easy-plane anisotropy for a square lattice. As this is not the case for a triangular lattice a low-temperature configuration of a quadrupolar XY system with threefold symmetry has been additionally calculated. Experimentally, this situation corresponds e.g. to organic PTCDA molecules adsorbed on Ag(111) [86] having some freedom of the rotation only in the XY-plane. The calculated ground state configuration is given in Fig. 4.14c. Instead of the pinwheel phase we find a "herringbone" structure consisting of lines of quadrupoles with two possible orientations. The moments make an angle of 15° to the principal lattice axes and 45° to the direction joining the atomic sites. Within the accuracy of our calculations the angle between two adjacent rows of moments is exactly 90°. The "herringbone" pattern found in the simulations is very similar to that of the Ref. [86]. However, the molecules in the experiment are oriented parallel to the principal axes and, consequently, the mutual angle between the rows is 60°. The analytical calculation of the energies for all possible relative orientations of rows of the "bones" shows that the absolute minimum belongs to the Monte-Carlo solution with the angle of 90°. From this finding we conclude that the configuration of Ref. [86] cannot be explained only from the minimization of electrostatic interactions originating from the quadrupolar field of a molecule. One possible explanation is that the rotation of the molecules is not free, another one is that the molecules possess higher order multipolar contributions.

Hexadecapolar (Q_{40}) ground states on a triangular and a square lattice for three-dimensional moments are given in Fig. 4.15. The both configurations are planar. A "herringbone" structure consisting of lines of hexadecapoles with two possible orientations is formed on both lattices. For a triangular lattice moments make angles of 69° and 157° to the x axis, while for a square symmetry angles of 9.5° and 49.5° are favorable. Within the accuracy of calculations [106] the angle between two adjacent rows of moments are 88° and 40° correspondingly. Hence, a hexadecapolar contribution supports the herringbone structure of a planar pure quadrupolar state on a triangular lattice (Fig. 4.14c). However, the symmetry of the structure changes significantly. Thus, the higher-order Q_{40} contribution is another possible explanation for the herringbone pattern of PTCDA adsorbates found experimentally.

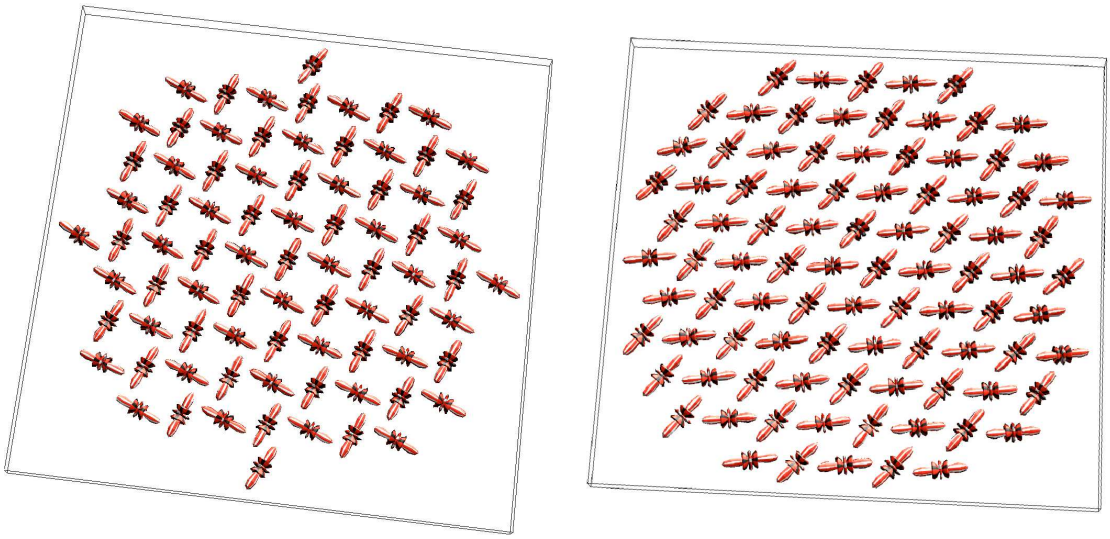

Figure 4.15: The low-temperature pure hexadecapolar Monte-Carlo configurations on a square (**a**) and a triangular (**b**) lattice. The hexadecapoles are represented by the spherical harmonic Y_{40} corresponding to the equipotential surface of a charge distribution with Q_{40} quadrupole moments; the two white-red clubs represent positive charge, while the bellies are alternately positively (white-red) or negatively (black-red) charged. Top perspective view of a portion of a configuration. The hexadecapoles are $3D$ moments

4.3.5 Ground States for Multipoles of odd Symmetry: Octopolar and Dotriacontapolar Patterns

The octopolar moments are unidirectional, i.e. they can be represented as vectors (see Fig. 4.16). The low-temperature configurations consist of moments oriented in principal directions of the underlying lattice. Hence, the octopolar interaction introduces not only an easy-plane but also a three- and twofold in-plane anisotropy respectively. On the square lattice octopoles form lines being aligned antiparallel (such as in Fig. 4.3a) while on the triangular lattice the domains show parallel alignment of the moments (Fig. 4.3b). The dotriacontapolar interactions break the isotropic behavior of dipoles on square and triangular lattices in the same way. Anti-parallel alignment is one of the ground states of an *infinite* pure dipolar system on a square lattice [81] while on its triangular counterpart the ferromagnetic alignment has the minimal energy. Hence, the octopolar interaction selects some of the dipolar ground states. The principal difference, however, is that the dipolar energy, because of its long-range character, can be minimized avoiding free poles in *finite* samples, i.e. a vortex on a triangular and a microvortex state on a square lattices are formed (see Section 4.2.2). In contrast to finite dipolar systems a finite octopolar system is not sensitive to the formation of free poles in most geometries as octopoles do not interact with a field but with the field curvature. Therefore, the gain in the internal energy

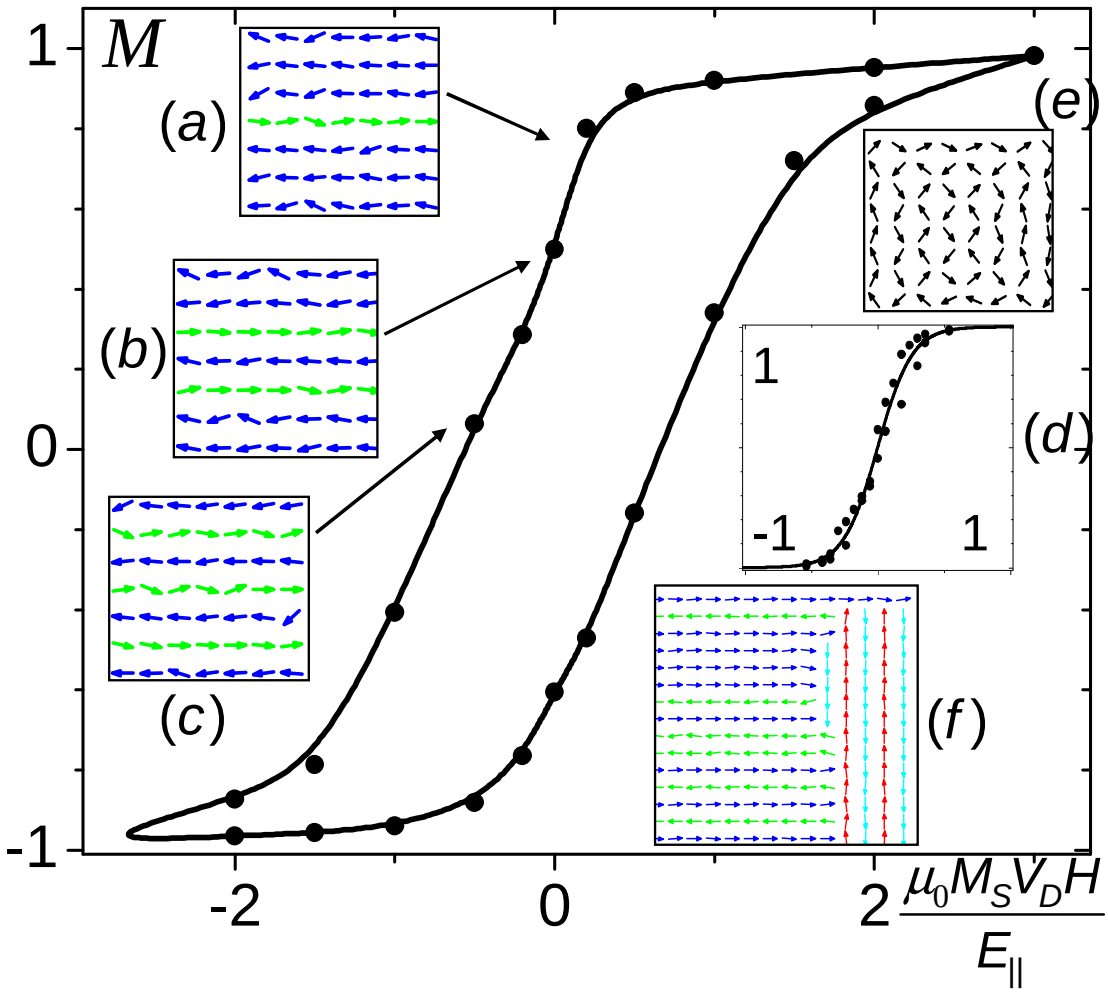

Figure 4.16: Hysteresis loops for a 20×20 square nanoarray with $Q_{30} = 0.5Q_{10}$ and a pure dipolar system (inset (d)). The magnetic field is applied in x-direction. Insets (a-c) give the central part of intermediate magnetic configurations; (f) and (e) show stable zero-field configurations for combined multipoles and the pure dipolar case respectively. Thermal energy is $kT = 0.6E_{||}$. The field is expressed in $\mu_0 M_S V_d / E_{||}$ with μ_0 - the permeability of free space and V_d - the volume of a dot

due the compensation of free magnetic poles at the sample boundary is not so strong as for pure dipolar systems and low-temperature configurations in finite samples are still parallel lines for a triangular and antiparallel lines for a square lattice.

4.3.6 Combined Multipoles in Nanomagnetic Arrays

As has been shown in the Section 4.3.2 the in-plane magnetized nanodiscs with height-to-diameter ratio $h/a \leq 0.5$ common for contemporary experimental studies possess dipolar and octopolar moments with $Q_3/Q_1 \geq 0.5$. Hence, for a real nano-

magnetic array neither pure dipolar, nor pure octopolar configurations are of relevance. Instead, ground states of an ensemble of combined multipoles should be calculated. Recently, those calculations have been carried out by means of Monte-Carlo simulations for case of rotationally symmetric multipoles [105]. Arrays of combined multipoles show maxima of specific heat and susceptibility at the same temperature confirming the existence of a phase transition. Whereas the zero-temperature ground state on a square lattice consists of antiparallel lines as in a pure octopolar system, at finite temperatures alternating regions of uniaxial parallel and antiparallel lines such as in Fig. 4.17b have been found. The width of regions with parallel lines is usually 2-3 lattice parameters. In $\approx 10\%$ of calculations despite a very long relaxation procedure superdomains (Fig. 4.16f) appear. On an infinite triangular lattice the ground state is a ferromagnetic single domain as in pure dipolar system. However, in finite systems the vortex configuration is never formed for $Q_3/Q_1 \geq 0.5$. Instead, large collinear domains appear. Hence, the interaction of dipoles with demagnetizing field is still too weak comparable to the anisotropy induced due to the octopole-octopole coupling.

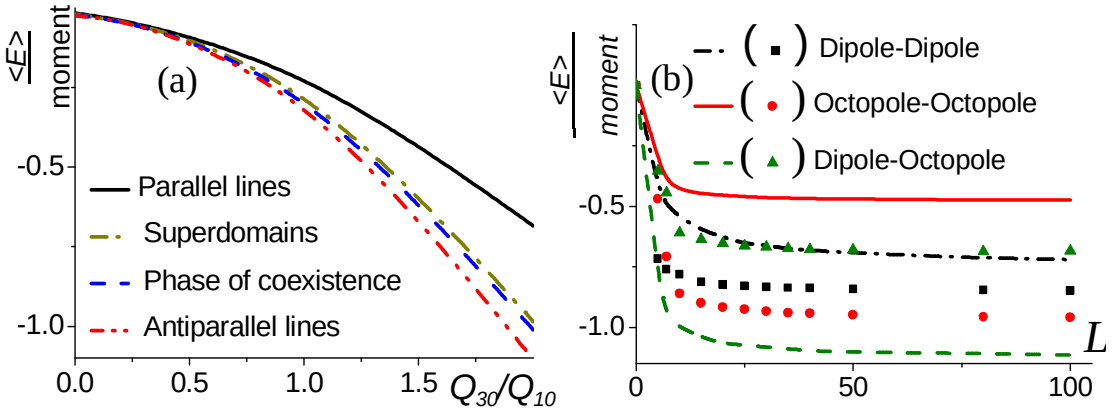

Figure 4.17: (a) Internal energy of ideal parallel, antiparallel, coexisting and superdomain configurations for $L = 20$ as a function of Q_{30}/Q_{10} on a square lattice; (b) Size dependence of different contributions of the magnetostatic energy for parallel (solid lines) and antiparallel lines (scatter graph) for $Q_{30}/Q_{10} = 0.5$

In order to understand why the state of coexisting parallel and antiparallel lines has the lowest internal energy, different energetic contributions (dipole-dipole, dipole-octopole and octopole-octopole) and the entropy have to be analyzed. The energy of ideal and MC configurations on a square lattice as a function of Q_{30}/Q_{10} is plotted in Fig. 4.17a. All energies are expressed in the pair interaction energy $E_{||}$ between two dots magnetized mutually parallel but perpendicular to the bond $E_{||} \propto 1/R_{AB}^{l_A+l_B+1}$. Fig. 4.17b gives size dependence of all energy contributions for parallel lines. It has been found that the dipole-octopole energy contribution E_{d-o} is minimal for the parallel while maximal for the antiparallel lines. The dipole-dipole (E_{d-d}) and octopole-octopole (E_{o-o}) interactions, in contrast, prefer antiparallel lines. Therefore for sample sizes $L < 9$ and $Q_{30}/Q_{10} < 0.8$ the state of coexisting parallel and antiparallel lines

has the lowest total internal energy. For $L > 9$ the antiparallel lines are preferable for all Q_{30}/Q_{10} as the long-range dipolar contribution increases. The energy difference between antiparallel lines and coexisting phases or superdomains δE grows with increasing Q_{30}/Q_{10} (Fig. 4.17a). However, for $Q_{30}/Q_{10} < 0.6$ δE is very small $\approx 2\%$, while the configurational entropy in a system of parallel or antiparallel lines drastically increases with the system size $S = k \cdot \ln(2 \times 2^L)$. As the entropy increases boundless with L, in contrast to the slow convergence of the dipolar sum, the free energy of the coexistence is lower for non zero temperatures. Formation of superdomains gives an additional contribution to the entropy. This contribution depends on size of superdomains. The size of superdomains in finite dipolar systems is driven by the pole avoidance principle. While the energy cost due to the wall formation increases only linearly with the domain size, the gain in the long range dipolar interaction increases with the square of the domain size and only a rare formation of superdomains is observed at low temperatures. The additional entropy for large superdomains is small. Approaching critical temperature the domain size decreases, the corresponding entropy increases and the superdomains appear more frequently. This finding is in accordance with the experiment [110] giving evidence for formation of the large in-plane collinear domains extending across several dots.

Thus, unlike the non-collinear ground states of pure dipolar systems their odd multipolar counterparts select collinear configurations from the dipolar manifold. The reason for this selection is two-fold. First, the octopolar/dotriacontapolar interaction on a triangular and a square lattice introduces an easy-plane and a tri- and a biaxial in-plane anisotropy respectively. Second, the pole avoiding principle does not hold for the octopole-octopole interaction energy contribution. Therefore, systems with strong octopolar contribution are not as sensitive to the formation of uncompensated magnetic poles at the sample boundary as systems with dominating dipolar interactions. Despite the collinearity the lattice structure plays an important role. While the ground state for $Q_{30}/Q_{10} \approx 0.5$ multipoles on a square lattice consists of antiparallel lines of magnetic moments, the triangular symmetry leads to the parallel ferromagnetic configuration.

4.3.7 Magnetization Reversal in Nanomagnetic Arrays

Experimental investigations show that in comparison with an infinite film the interparticle interactions usually lead to a decrease of the switching field in patterned media with out-of-plane magnetization [77, 98, 99] and to an increase of the coercivity for in-plane magnetized particles [99, 111–113]. Although in some cases an agreement of switching behavior with theoretical predictions has been obtained, it is often found that measured switching fields deviate significantly (10-15%) from those expected from pure dipolar interactions. In the following the field dependence of magnetization in square and triangular array of dots with in-plane magnetization and $Q_{30}/Q_{10} \geq 0.5$ will be analyzed and compared with hysteretic properties of a pure dipolar system.

Fig. 4.16 shows the magnetization reversal of a square lattice with $Q_{30}/Q_{10} = 0.5$

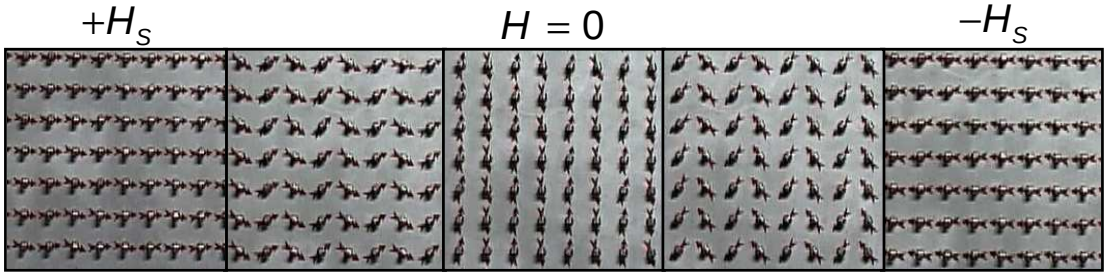

Figure 4.18: Snapshots of the central part of an experimental dipolar model on a square lattice during a magnetization reversal. The magnetic field is changed from $+x$ to $-x$ direction. The first and the last insets give the central part of saturated magnetic configurations for positive and negative field respectively. The central inset shows stable zero-field configuration while two other insets represent intermediate configurations

corresponding to an array of ultrathin particles with $h/2a \leq 0.5$ and for a pure dipolar system ($h/2a \approx 1$, Fig. 4.16d). A pure dipolar system does not show any easy-axis hysteresis. The reason for that is clear from the Fig. 4.18 where several snapshots of a hysteresis on a pure dipolar square lattice are shown where the whole magnetization reversal in an experimental dipolar model is registered. In a pure dipolar case all magnetic moments rotate coherently. Therefore, the total magnetization decreases continuously from unity at saturation field H_S to zero for $H = 0$. In a multipolar array, on the contrary, the hysteresis loop is quite open. The squareness s depends on the composition, the strength of multipoles and on the temperature. The field is scaled with $E_{||}$ described in the previous section. Therefore, contributions from moments of different order in combined multipoles scale differently with R_{AB}. All values are given for $Q_{30} = 1$, $Q_{10} = 2$ and $R_{AB} = 1$. This gives $s \approx 0.5$ and $H_c\mu_0 M_S V_d \approx 0.7E_{||}$. By calculating $E_{||}$ this result can be scaled to a square array of any material with any interdot distance. For example, for an array of permalloy particles at room temperature $M_S = 8 \cdot 10^5$A/m, and vanishing anisotropy $K_1 < 1000$J/m^3 with $h =$ 20nm, $d = 2a = 70$nm and $R = 100$nm we find $H_c \approx 20$mT.

Magnetic moments do not rotate continuously as in a pure dipolar system (see Fig. 4.16d, Fig. 4.18 and animation Hysteresis(Dipolar).avi) but are reoriented line-by-line (Fig. 4.16a-c and animation Hysteresis(Multipolar).avi) as noncollinear configurations are energetically unfavorable. From our calculations follows that the competition between the E_{d-o} and $E_{d-d}+E_{o-o}$ interaction energy plays an important role for the magnetization reversal. As has been already demonstrated in Fig. 4.17a the total energy of the configuration Fig. 4.16b is close or even lower than that of Fig. 4.16c, where all chains are antiparallel. Hence, to go from configuration Fig. 4.16b to the configuration Fig. 4.16c an external magnetic field has to be applied and the hysteresis then appears. H_c increases with decreasing temperature. This effect is similar to the superparamagnetic temperature assisted switching. Thus, the hysteretic behavior is predefined by the competition between the octopole-dipole contribution of the magne-

tostatic energy and its dipole-dipole and octopole-octopole counterparts. Pure dipolar systems do not show any significant hysteresis.

On a triangular lattice H_c increases by $\approx 10\%$ compared to the pure dipolar system in good accordance with experiments [112]. However, the magnetization reversal is different from that on a square lattice. Hence, the ground sates and the magnetization reversal in dense packed nanomagnetic arrays is strongly influenced as by order of magnetostatic interactions as by underlaying lattice symmetry.

4.4 Summary

In conclusion, systematic investigation of multipolar and dipolar low-temperature stable configurations on a triangular and a square lattice have been carried out theoretically. In contrast to previous results we demonstrate that the multipole-multipole interactions change considerably stable low temperature dipolar states. The dipole-octopole interaction is an important component that might also explain the superferromagnetic behavior in dense grain magnetic materials and magnetic arrays. Tuning the multipole moments by changing the geometry of nanoparticles offers a new route to the control of the coupling behavior and therefore the hysteretic properties of magnetic nanoparticle arrays.

Chapter 5

Magnetic Ordering In Quasicrystals

5.1 Introduction

The last few years have shown a major growth in investigations on the spin order in frustrated magnets, motivated by the dramatic changes in the magnetic properties of such systems. The phenomenon of geometric frustration is simple and fundamental. It can be applied to different interactions and is present in a variety of physical systems like magnets, liquid crystals, protein structures or Josephson junction arrays [114]. A very simple example of local geometrical frustration is the arrangement of three identical units on an equilateral triangle (Fig. 5.1a). The units are constrained to have one of two opposite properties (black/white, up/down, on/off etc.) and the energy of the interaction between any two units is minimized if the two nearest neighbors on the triangle have different states. The all three elements, however, can by no means all have different states. Two out of three units will necessarily have the same property. Hence, the energy of the system cannot be entirely minimized. In case of magnetic or electric Ising moments, for example, there exist six possible configurations of equal energy with two units up and one down or vice versa. At equilibrium the system is hesitating between those six collinear configurations. Vector spins can manage the frustration better than Ising moments by adopting a noncollinear structure with the spins making an angle of 120 from each other. The noncollinear solution for a triangular lattice is known as Néel structure (Fig. 5.1b).

The overwhelming majority of the investigations on frustrated magnets concerns periodic crystals. One of the first works on the complex order in frustrated antiferromagnets on quasilattices is Ref. [115]. In that paper a renormalization scheme on the Penrose tiling for a Heisenberg exchange model with competing antiferromagnetic interactions has been introduced. A phase diagram consisting of a variety of ordered phases has been obtained. Subsequent study [116] has demonstrated that frustration leads to a central gap in the density of states for the Penrose lattice. In studies on quasiperiodic geometries emphasis has been put on collinear configurations of magnetic moments coupled by the short-range exchange interaction only [117–126].

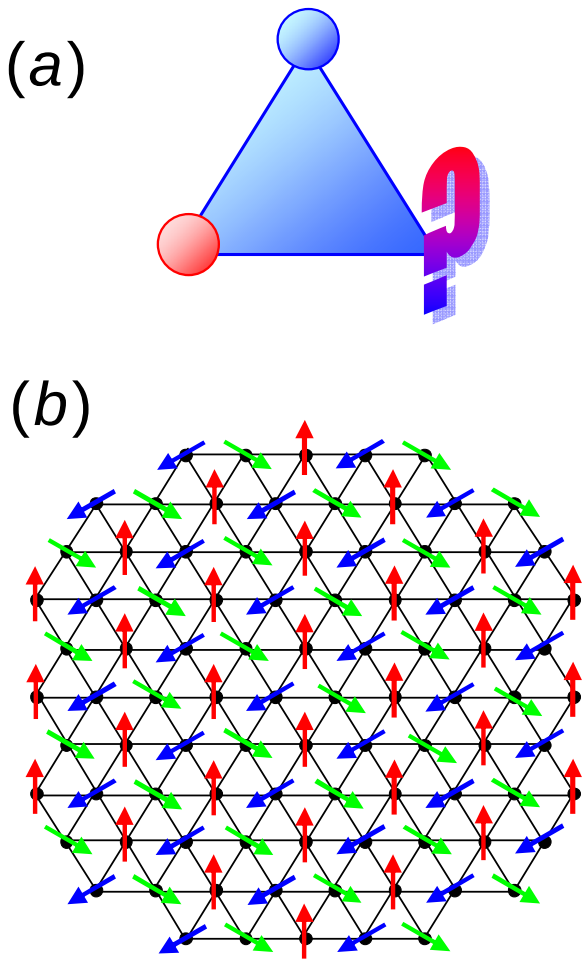

Figure 5.1: (a) Triangle building block of a two-dimensional crystal. Red and blue balls represent atoms or magnetic moments of different sort coupled by antiferromagnetic-like short-range interactions. The antiparallel alignment of all neighboring units is not possible; (b) Top view of a noncollinear Néel structure on a triangular lattice. Different colors represent three sublattices of the Néel configuration.

A complete list of literature on aperiodic lattice models can be found in Refs. [127, 128]. Noncollinear structures and long-range dipolar forces were traditionally not considered. The situation has changed at the end of the last century. In the early nineties rare-earth-based (RE) quasicrystals have been discovered [129–131]. The RE-containing icosahedral alloys of the RE-MgZn and RE-MgCd families are quite unique among known quasicrystals as magnetic moments of 4f electrons of the RE elements are sizable and well localized (a good collection of the literature can be found in Refs. [132, 133]). The hope that the RE-quasicrystals may become magnetically ordered at low temperatures evoked a considerable number of experimental and theoretical investigations of magnetic behavior on non-periodic lattices.

A first experimental finding of long-range antiferromagnetic order in rare-earth icosahedral quasicrystals [134] turned out to be an artefact [135, 136]. However, it gave a power stimulus to further theoretical and experimental investigations of magnetic ordering in aperiodic structures. Although the atomic and electronic structure of rare earth quasicrystals is not completely understood, it has been postulated [137] that the low-temperature microstructure of such a magnet resembles geometrically frustrated but site-ordered magnetic systems and consists of weakly interacting magnetically ordered clusters. Another interesting approach is based on recent elastic neutron scattering experiments on a Zn-Mg-Ho icosahedral quasicrystal [138]. This reveals a very peculiar diffuse scattering pattern with icosahedral symmetry at temperatures below 6K. In contrast to the Ref. [137], the authors interpret the diffraction pattern as that of several interpenetrating quasiperiodic sublattices, where all spins point in the same direction [139]. There are very helpful for the understanding of real-space

magnetic configurations leading to those long wave vector correlations coming from a noncollinear spin arrangement suggested by Lifshitz from pure geometrical considerations [140]. Recent interesting results for quantum spins on the octagonal tiling [141–143] and systematic calculations of the noncollinear magnetic ordering on eight- and ten-fold quasiperiodic tilings are seen in [139, 144, 145]. Distinct from the theoretical spin models including only short-range interactions is a calculation of the ground state of a long-range dipolar quasiperiodic magnet [146]. The calculation of the dipole-dipole interactions in quasiperiodic structures is important as for the RE-based quasicrystals, as is the case for magnetostatically coupled nanoarrays. In the following, the influence of the structural quasiperiodicity on the antiferromagnetic and dipolar magnetic ordering will be reviewed.

5.2 Quasiperiodic Tilings

Starting from the famous pattern of Roger Penrose many different ways have been discovered to tile a plane non-periodically with a similar set of regular polygons [147, 148]. Later many of these purely mathematical constructions have found their realisations in real materials. The work on quasicrystals has opened up the way to the very wide field of quasicrystals approximants [149]. Nevertheless two most popular among quasiperiodic tilings remain the ten-fold Penrose [150] and the eight-fold Ammann-Beenker [151] structures.

The Penrose pattern consists of two rhombuses with edges of length a, one with angles of 36° and 144° and the other with angles 72° and 108° (Fig. 5.2). The rhombic tiles are arranged without gaps or overlaps according to matching rules [150]. Alternatively, the planar Penrose tiling can be generated using a single kind of tile, a decagon [152–156]. Every decagon consists of Penrose rhombuses. In contrast to periodic lattices a decagonal atomic cluster can share atoms with its neighbors. The overlapping rules have been mathematically proven [153]. Only two types of the overlap (A and B) are allowed [152]. Location of "A" and "B" in a Penrose lattice are marked in Fig. 5.2. The octagonal tiling is made out of two other motifs: a square and a rhombus of equal edge lengths (Fig. 5.3a) with the angles of $\pi/4$ and $3\pi/4$ for the rhombic tile.

5.3 Peculiarities of Magnetic Coupling in Quasiperiodic Structures

The quasicrystals can be structurally ranked in-between the periodic lattices and completely disordered media. In contrast to periodic crystals, in quasicrystals the number of nearest neighbors varies widely from one point to another like in disordered matter. The Penrose tiling [150], for example, has atoms with coordination number changing from 3 to 7. Hence, the energy per magnetic moment also varies. Unlike the disordered media, however, this variation exhibits a long-range orientational order,

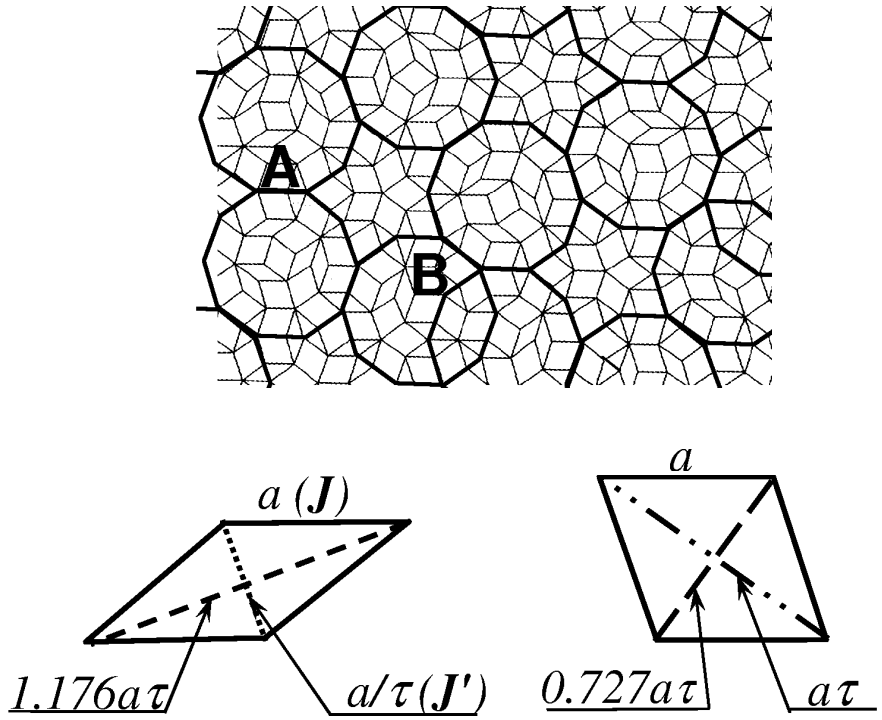

Figure 5.2: (a) A section of the Penrose tiling. The original Penrose rhombic tiles and the decagonal tiles are indicated. Two allowed overlapping of decagonal clusters are shown as A and B. (b) The original Penrose rhombic tiles. Five nearest neighbor distances (the sides and the diagonals of the rhombuses) and their lengths are given. τ is the golden mean. The two strongest exchange bonds according to two shortest nearest neighbor distances are denoted as J and J'.

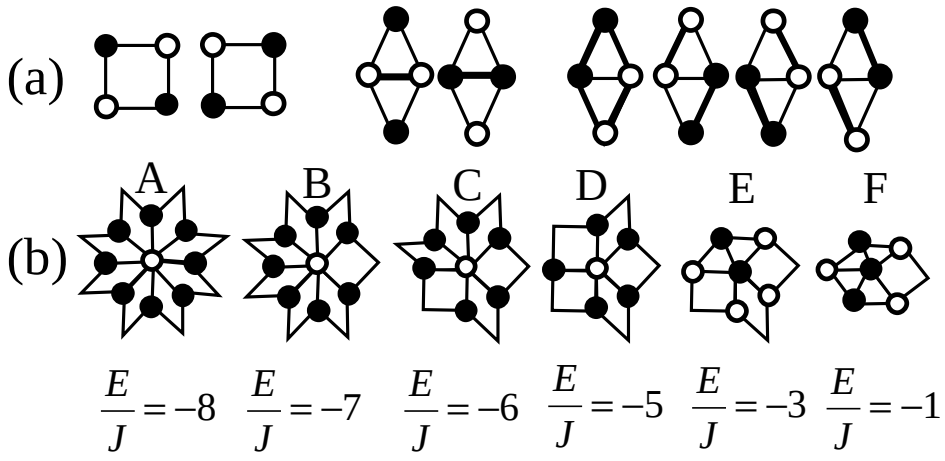

Figure 5.3: Configurations for a frustrated Ising antiferromagnet on (a) elementary tiles and (b) six local environments of the Ammann-Beenker tiling. Bold lines denote the frustrated bonds. The open and filled circles represent different spins.

i.e. any finite section of a quasicrystal is reproduced within a certain distance. In particular, fivefold symmetry, forbidden in conventional crystallography, can be observed in the diffraction patterns. Thus, the magnetic ordering in quasicrystals should be different from the collinear magnetism of periodic crystals and from spin-glass-like behavior of the disordered media.

The antiferromagnetic system on a quasicrystalline tiling can be geometrically frustrated as every rhombic tile consists of two triangles. The frustration in quasicrystals is different from that of periodic systems and that of disordered media. In highly ordered magnets the frustration is uniform, i.e. equal for all lattice points. In disordered materials the frustration is random. In quasicrystals the change in coordination number leads to spatial alternation of the exchange or the dipolar energy and, thus, the degree of frustration. However, the non-uniform magnetic frustration is not random. The non-uniform geometrical frustration is the second important ingredient for the definition of the magnetic microstructure in quasicrystals.

The exchange coupling in quasicrystals is also different from that of their periodic counterparts. Atoms on quasi-periodic lattices have not only varying number of neighbors but also several different nearest-neighbor distances (Fig. 5.2, 5.3). Accordingly, there are several different values of the exchange force which can even change sign. The existence of several exchange constants J can also exert a significant influence on the microstructure of the quasiperiodic magnets.

In summary, it is obvious that the varying number of nearest neighbors, non-isotropic magnetic frustration and varying J-constants are important for the magnetic ordering in quasiperiodic ultra-thin films. In the following a general spatial resolved description of the magnetic ordering on two-dimensional quasiperiodic tilings will be discussed.

5.4 Computational Details and an Experimental Model

Since a magnetic structure on a quasicrystalline tiling is not periodic, an analytical description of the micromagnetic structure is hardly feasible. Therefore Monte-Carlo simulations are often utilized to find equilibrium spin configurations at a given temperature. Usually in the Monte-Carlo simulations only local exchange interactions have been considered [115, 117–126]. Here a more universal calculations with the local ferromagnetic or antiferromagnetic exchange interaction and the long-range dipolar coupling will be discussed [139, 144–146]. In most rare earth intermetallic compounds an oscillatory (RKKY - like) exchange interaction has been observed [157]. A theoretical treatment of RKKY systems is still lacking. This review is concentrated on studies of exponentially decreasing exchange coupling corresponding to a rapid-decaying limit

of an oscillatory interaction. We discuss the Hamiltonian given by

$$H = J_{ij} \sum_{\langle i,j \rangle} \mathbf{S}_i \cdot \mathbf{S}_j + D \sum_{ij} \left(\frac{\mathbf{S}_i \cdot \mathbf{S}_j}{r_{ij}^3} - 3 \frac{(\mathbf{S}_i \cdot \mathbf{r}_{ij})(\mathbf{S}_j \cdot \mathbf{r}_{ij})}{r_{ij}^5} \right) - K_1 \sum_i (\mathbf{S}_i^z)^2 \quad , \qquad (5.1)$$

where $\mathbf{S}_i$ is a three- or two-dimensional unit vector in the case of classical vector or xy-spins, and $\mathbf{S}_i^z$ is equal to ± 1 in the case of Ising spins (so $\mathbf{S}_i^x = \mathbf{S}_i^y = 0$); $\langle i, j \rangle$ denotes the nearest neighbor pairs. For an antiferromagnetic system, the exchange parameter J_{ij} is positive, and neighboring antiparallel spins contribute a lower energy than parallel neighbors. For a ferromagnetic system J_{ij} is negative and the parallel orientation of neighboring moments is favorable. The coefficient K_1 is the first-order anisotropy constant. The Monte-Carlo simulations have been carried out on finite Ammann-Beenker [151], Penrose, Anti-Penrose [150], Tübinger Triangular [158] and Tie-Navette [159] tilings with free boundary conditions. The procedure is a simulated annealing method with at least 15 successive temperature steps [139, 146]. At each temperature, the convergence of the relaxation process towards equilibrium has been observed for any initial configuration after a few thousand Monte Carlo steps per spin. Hence, the single-spin-update algorithm is efficient in this case. At the end of the cooling down process, the total energy is just fluctuating around its mean equilibrium value. To reduce boundary effects only the core of a tiling has been analyzed. The samples, which will be addressed in what follows, are circular, containing of order of 53000 magnetic moments. The dipolar interaction of each magnetic moment with all the other moments has been considered.

In order to calculate the exchange energy the set of nearest neighbors that are coupled via the short-range interaction has to be defined. In periodic crystals the exchange coupling between next nearest neighbors is usually enough to ensure the magnetic order. In quasicrystals the situation is different. The pattern consists of two motifs with edges of equal length a (Figs. 5.2, 5.3). The diagonal bonds are often neglected in the calculations. With such a treatment of bonds the lattice deviates from the original tiling. This disregard is physically questionable as the exchange coupling increases exponentially with decreasing interatomic distance. In investigations reviewed here, the short diagonal of the rhombus and the sides of the motifs for all tilings have been considered as nearest neighbors.

The simulation results will be compared with an original experimental dipolar system made of 309 small magnets on the Penrose lattice. The experimental system represents a pure dipolar model which corresponds to the numerical simulations for zero exchange interaction. It concerns a 480mm x 480mm Penrose lattice of magnets of 4 mm length separated by 30 mm. The large distance between the magnets is chosen on purpose to minimize multipolar terms that can trap the system into metastable states. The magnets are put onto nonmagnetic vertical axes and can rotate in the x, y plane.

5.5 Magnetic Ordering in Two-Dimensional Quasicrystals

5.5.1 Dominating Ferromagnetic Interactions

It seems that the ferromagnetic interaction cannot bring new interesting physics as its ground state should be a relatively simple ferromagnetic single domain. Recently, however, it has been demonstrated [146] that in quasicrystals the situation may be more involved than is usually expected. In this study Ref. [146] five different values of the exchange constant, i.e. for the sides and all diagonals of the rhombuses, have been considered. J has been taken to be unity. The exchange interaction decreases exponentially with the distance between magnetic moments. The strength of the exchange interaction has been defined as $J_{ij} = J\exp(1-\rho_{ij})$, where $\rho_{ij} = r_{ij}/a$ is the distance between two neighboring moments normalized to the length of the side of the rhombuses a. ρ_{ij} takes the lengths of the diagonals of the Penrose tiles. The shortest diagonal has a length of $\rho_{ij} = \tau^{-1} < 1$ with τ - the golden mean. Therefore $J' = J\exp(1-\tau^{-1})$, i.e. J' is larger than J. Further interactions become weaker than J with increasing distance as in that case $\rho_{ij} > 1$.

According to the Mermin-Wagner theorem [160], no long-range order exists in two-dimensions with continuous symmetry, because thermal fluctuations result in a mean-square deviation of the spins from their equilibrium positions which increases logarithmically with the size of the system. The addition of a very weak anisotropy stemming e.g. from the dipolar interactions does not change the distribution of the exchange energy, but permits the anchoring the absolute spatial orientation of the magnetization. Magnetic ordering depends on the ratio of exchange to dipolar constant $R = J/D$ and on the radius of the cut-off in the exchange coupling (ρ). In the quasiperiodic Penrose lattice with high R, i.e. with the strong exchange interaction, a single domain for all cut-off radii $\rho \geq a$ is found. It means that the exchange coupling acting along the two shortest bonds (J and J') is enough to ensure the ferromagnetic order. However, the

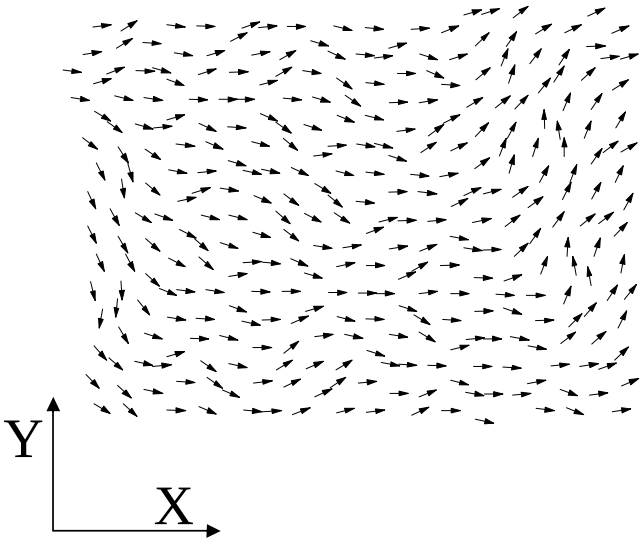

Figure 5.4: Top-view of the portion of the quasi-ferromagnetic spin configuration in a sample of finite size for $\rho = 1.176a\tau$ and $R = J/D = 5$. The magnetic moments are nearly coplanar to the sides of the decagons. The X-component of the average magnetization is $M_X = 0.85$.

degree of magnetic order increases remarkably with increasing ρ. While the average magnetization per moment at low temperature ($J/kT = 100$) and high ratio $R = 10^3$ is almost unity for the exchange cut-off radius $\rho = 1.176a\tau$ it is only $\bar{M}_1 = 0.975$ for $\rho = a$.

Hence, in contrast to periodic lattices the ferromagnetic order in quasicrystals depends strongly on the cut-off radius in the exchange interaction. In case of small ρ high magnetic frustration of the quasiperiodic structure leads to significant deviation of the average magnetization from unity even for very high R - ratios. An example of a ferromagnetic configuration on a Penrose tiling is shown in Fig. 5.4.

5.5.2 Dominating Antiferromagnetic Interactions

In the recent theoretical study [139, 145] we have derived stable low-temperature magnetization configurations on different quasiperiodic tilings. The results obtained provide an explanation for the origin of the antiferromagnetic modulations observed experimentally in Ref. [138]. While the spin order in antiferromagnets is usually characterized by a periodic modulation described by wave vectors on the order of inverse atomic distances, the spin order in antiferromagnetic quasicrystals admits three-dimensional noncollinear structures consisting of several interpenetrating subtilings with longer wave vectors. First the details of the low-temperature antiferromagnetic ordering on the octagonal tiling will be given. Then the results will be generalized for other tilings as well.

The short diagonal of the rhombus and the sides of the octagonal motifs have been considered as nearest neighbors. We distinguish the two cases $J_d > 2J$ and $J_d < 2J$, where J_d denotes the interaction along the short diagonal and the interaction strength along the sides J is unity. The first case corresponds to a rapid growth of the exchange coupling with decreasing interatomic distance. The two nearest-neighbor bonds form six local environments with coordination numbers varying from 5 to 8 as shown in Fig. 5.3(b). They occur with relative frequencies $\nu_A = 17 - 12\sqrt{2} \approx 2.9\%$, $\nu_B = -41 + 29\sqrt{2} \approx 1.2\%$, $\nu_C = 34 - 24\sqrt{2} \approx 5.9\%$, $\nu_D = -14 + 10\sqrt{2} \approx 14.2\%$, $\nu_E = 6 - 4\sqrt{2} \approx 34.3\%$, and $\nu_F = -1 + \sqrt{2} \approx 41.4\%$. Taking into account the short diagonals of the rhombic tiles increases the average coordination number of the tiling from 4 (the value without diagonals) to $8\nu_A + 7\nu_B + 6\nu_C + 5(\nu_D + \nu_E + \nu_F) = 8 - 2\sqrt{2} \approx 5.17$.

Ising spins

The square tile of the octagonal structure is non-frustrated as every pair of the moments can be chosen to be antiparallel (Fig. 5.3a). If we had not taken the short diagonals of the rhombic tiles into account, the same would be true for the entire tiling, and there would be no frustration, because the rhombic tiling is bipartite. Now, we consider spins on short diagonals as nearest neighbors, the rhombic tiles are always frustrated. If the energy of one nearest neighbor pair is minimized by

having antiparallel spins, the third and forth spins cannot be chosen to minimize the energy of both of its neighbors (Fig. 5.3a). The magnetic moment will necessarily be parallel to one of the neighbors. For $J_d < 2J$ two out of six possible configurations have smaller energy as they possess only one pair of parallel nearest neighbors per rhombus instead of two (Fig. 5.3a). In this case spins can have one of six possible energy values corresponding to different local environments (Fig. 5.3b). For $J_d > 2J$ the four configurations with two parallel bonds have lowest energy as their weight is smaller than that of the strong diagonal coupling. The second case comprises much more different possibilities of energy distribution. To give a quantitative description of the local frustration we introduce a local parameter $f = \frac{|E_{id}|-|E_i|}{|E_{id}|}$, where E_i is an actual energy of a spin i and E_{id} is a ground state energy of a relevant unfrustrated vertex. With this nomenclature, only the central spins of the vertices F and E are magnetically frustrated $f_F = 0.4$ and $f_E = 0.8$ for $J_d = J < 2J$. The Monte-Carlo simulations confirm our reasoning based on the analysis of frustration. Fig. 5.5a gives the frequency distribution of the exchange energy per atom E for two cases and a top-view of a portion of Ising configuration with $J_d > 2J$.

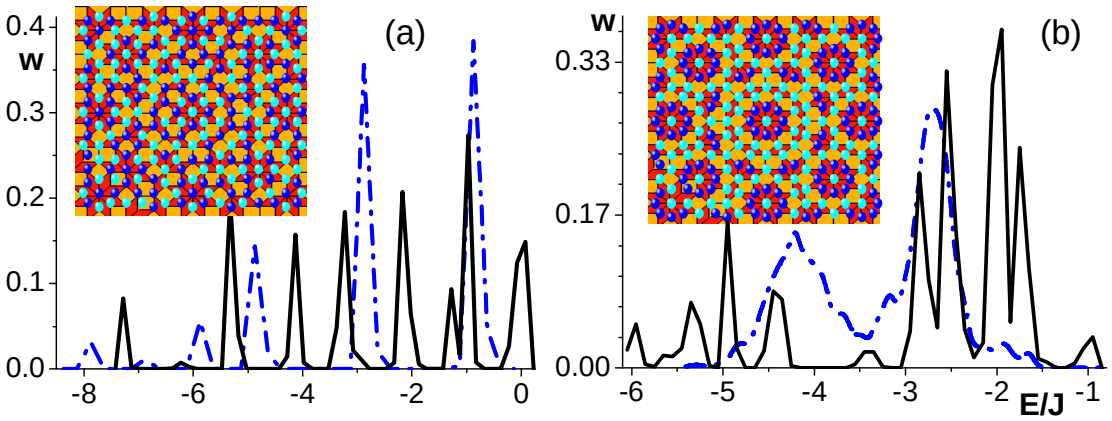

Figure 5.5: The frequency distribution of the energy per spin on the octagonal tiling for (a) Ising and (b) vector spins. Solid lines correspond to the case $J_d < 2J$, dashed lines to $J_d > 2J$. Purely antiferromagnetic interaction at $kT = 0.01J$ is considered. Top-views of portions of Monte-Carlo configurations with underlying tilings are shown as insets. The light and dark circles represent different spins in (a) and different energies in (b), respectively.

The energy distribution for $J_d < 2J$ simply reproduces the frequency of 6 vertex configurations. The "up" and "down" configurations are perfectly ordered and coincide with the black-and-white model of Niizeki [161]. For large J_d we find 8 possible energy values. The "up" and "down" subtilings, however, are spatially disordered (see inset Fig. 5.3a).

We have calculated the magnetic structure factor

$$S^{zz}(\mathbf{k}) = \frac{1}{N} \sum_{\mathbf{r},\mathbf{r}'} e^{i\mathbf{k}\cdot(\mathbf{r}-\mathbf{r}')} \langle S^z_{\mathbf{r}} S^z_{\mathbf{r}'} \rangle \tag{5.2}$$

using the Monte-Carlo data for different samples. Here $\mathbf{k}$ is the wave vector and $S^z_{\mathbf{r}}$ is a vertical component of a magnetic moment at the position $\mathbf{r}$. The diffraction pattern of the Niizeki configuration coincides with that of quantum Monte-Carlo calculations (Fig. 5c,d of Ref. [141]) and theoretical prediction [162], while the intensity map of the configuration Fig. 5.5a is almost structureless. It means that Ising solution with $J_d < 2J$ reproduces in essence the antiferromagnetic superstructure, corresponding to a modulation vector $\mathbf{q} = (\frac{1}{2}, \frac{1}{2}, \frac{1}{2}, \frac{1}{2})_{a^*}$ [138] in the octagonal tiling, whereas stronger coupling leads to a spin-glass state.

Vector spins

An exciting question is if the further minimization of the total energy and frustration by means of the noncollinear alignment of magnetic moments is possible. At first glance the magnetic structure of the low-temperature pure antiferromagnetic configuration seems to be rather disordered. The analysis of the local energies, however, reveals several characteristic energetic maxima in the frequency distribution shown in Figs. 5.5b and 5.6. The simple existence of the peaks means that there exist different sorts of magnetic moments having well-defined relative orientation to their nearest neighbors. This orientation, however, is not associated with any absolute direction in space. Therefore, in accordance with the Mermin-Wagner theorem, no long-range order exists in two-dimensions with continuous symmetry, because thermal fluctuations result in a mean-square deviation of the spins from their equilibrium positions which increases logarithmically with the size of the system.

The addition of a very weak anisotropy, which often exists in real samples, does not change the distribution of the exchange energy, but permits to anchor the absolute spatial orientation of the magnetization. Nevertheless, the total structure still looks spin-glass like. In the following it will be shown that the antiferromagnetic structure on quasiperiodic tilings is ordered but the order is non-trivial and unusual for periodic crystals. We concentrate further description on 3D vector spins while similar results for xy-spins have been obtained.

To obtain an absolute symmetry axis, we apply a very weak out-of-plane anisotropy $K_1 \approx 10^{-3}J$ to the system. The squared vertical component of magnetization $(S^z)^2$ becomes finite. The positions of the energy peaks on the frequency diagram remain unchanged. All maxima are different from those of the Ising model. It means that the angles between the neighboring magnetic moments are not always equal to 180° or 0°, i.e., the magnetic structure is noncollinear. The different number of peaks — eight for $J_d < 2J$ and two for $J_d > 2J$ (Fig. 5.5b) — already tells us that, in contrast to the Ising case, the maxima do not coincide with the 6 vertices of the tiling. The

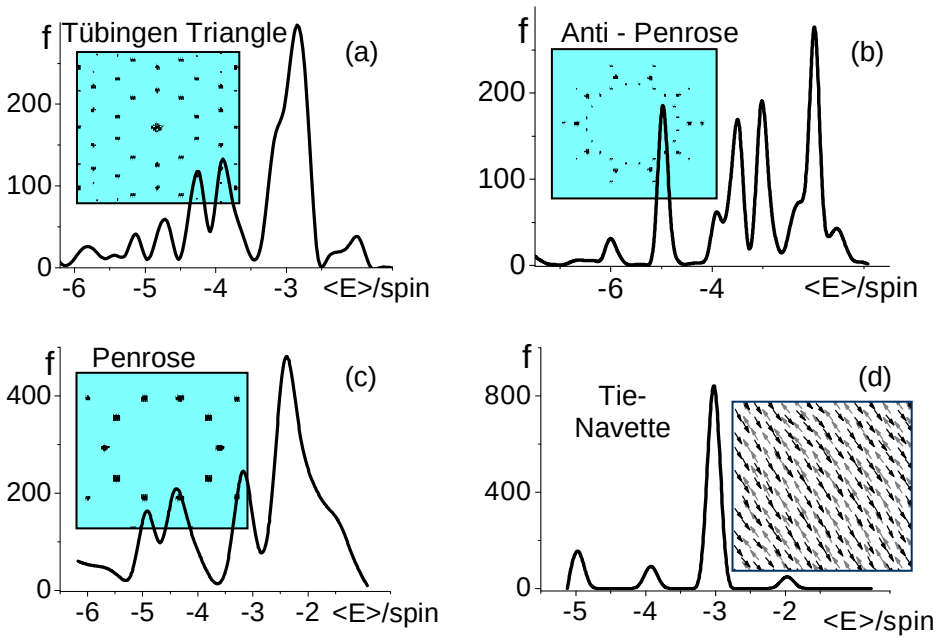

Figure 5.6: The frequency distribution of the energy per spin on the Tübingen triangle (a), Anti-Penrose (b), Penrose (c) and Tie-Navette (d) tilings for classical vector spins. A purely antiferromagnetic interaction J at a temperature $kT = 0.01J$ is considered. The insets (a-c) give calculated Bragg scattering of S^y component of magnetization for subtilings composed of magnetic moments belonging to peaks with $-6 < \frac{\langle E \rangle}{spin} < -4$. The scale goes from -6 to 6 $k^{S_y}_{x,y}/\pi$. The inset (d) gives a portion of the stable magnetic configuration on the Tie-Navette tiling as described in the text. Dark and light grey arrows denote antiparallel magnetic moments.

minimal possible local energy increases from $-8J$ to approximately $-6J$ for $J_d = J$ or $-5.44J$ for $J_d = 2.2J$. The average energy per spin, however, decreases by more than $0.3J$ and reaches the value of $E \approx -2.85J$ and $E \approx -3.30J$ respectively. Hence, the increase of the entropy permits to minimize the average frustration and the total energy of the system. Similar discrete energy spectrum has been found for other tilings as well (see Fig. 5.6). The number and positions of peaks variate for different tilings but the discrete character remains. Spatial arrangements of the magnetic moments as a function of the exchange energy for Penrose, Anti-Penrose, Tübinger Triangular and Tie-Navette tilings are given in Fig. 5.7. While spatial arrangements of different subtilings in the Fig. 5.7 are encoded in colors, for an octagonal tiling they are shown separately in Fig. 5.8.

Each configuration in Fig. 5.8 or each shade of grey in Fig. 5.7 represents a certain energy range corresponding to one of the peaks in the spectrum of Fig. 5.5b, 5.6. In Fig. 5.8 colors represent the x-projection of the magnetization. The magnetic moments form 8 subtilings of different energy $(E_1, \ldots, E_8)$ which generally do not coincide with a specific vertex type. The splitting of the energy and frustration levels is described in detail in Fig. 5.8. For example the vertices B and C (see Fig. 5.3) belong to

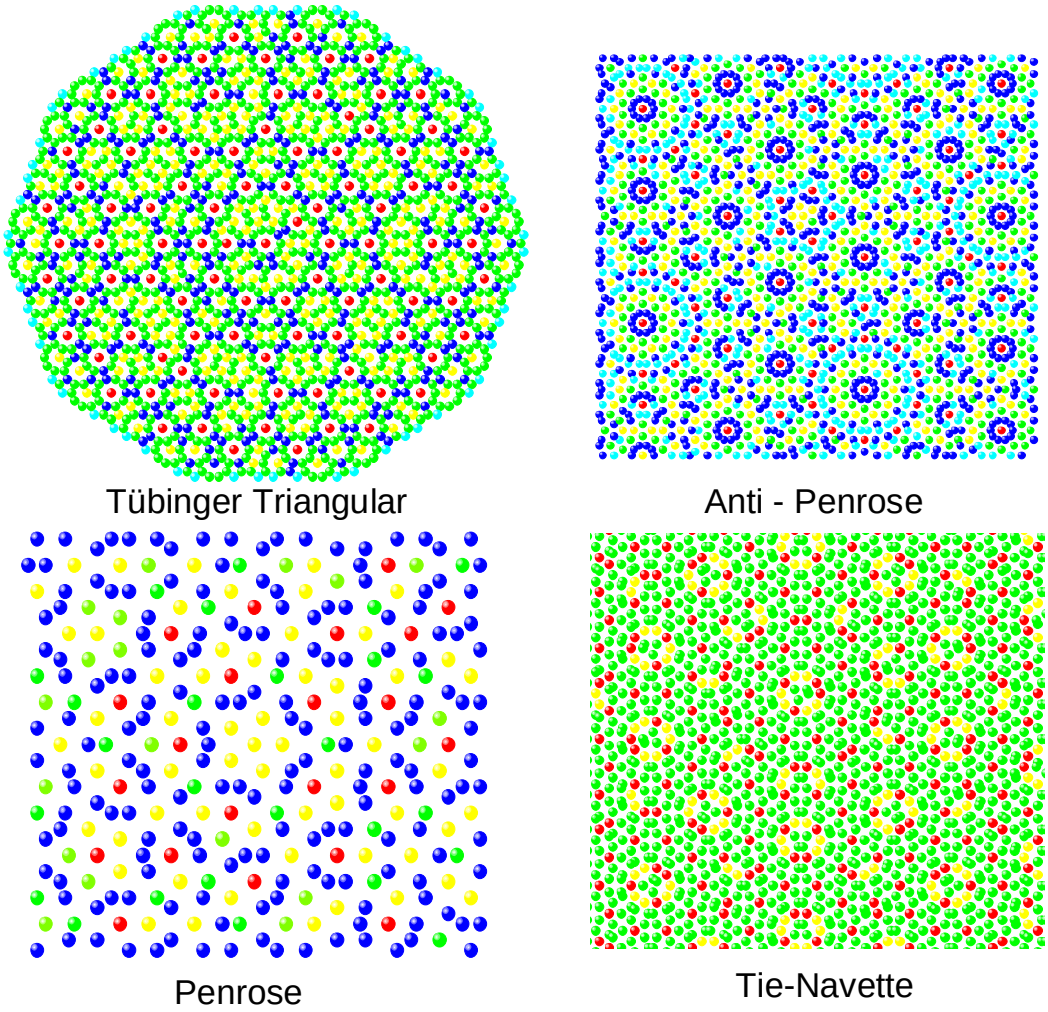

Figure 5.7: Energy maps for classical vector spins on Tübingen triangle (a), Anti-Penrose (b), Penrose (c) and Tie-Navette (d) tilings. The circles give positions of magnetic moments. Different shades of grey denote different energies corresponding to the peaks in figure 5.6. Purely antiferromagnetic interaction with $J = 1$ for all $r_{ij} \leq 1$ at $kT = 0.01J$ is considered.

the same energy maxima E_2 but have different local frustration $f_B = 0.24$, $f_C = 0.11$ (Fig. 5.8). At the same time the central spin of the vertex D can have either the energy E_3 or E_4 and, therefore, can have two different values of the frustration $f_{D1} = 0.01$ and $f_{D2} = 0.11$ depending on local surroundings. Thus, every configuration of the Figs. 5.8, 5.7 can enclose either a part of the atomic places belonging to one vertex type or two different vertex types together. Nevertheless all subtilings are spatially ordering. Each subtiling can be separated into the energetically degenerate 'right' and 'left' parts which also have a perfect quasiperiodic arrangement. Fig. 5.9 shows a perspective view of a portion of typical Monte-Carlo configuration for the Penrose and the octagonal tiling. The corresponding configurations represent the characteristic Pen-

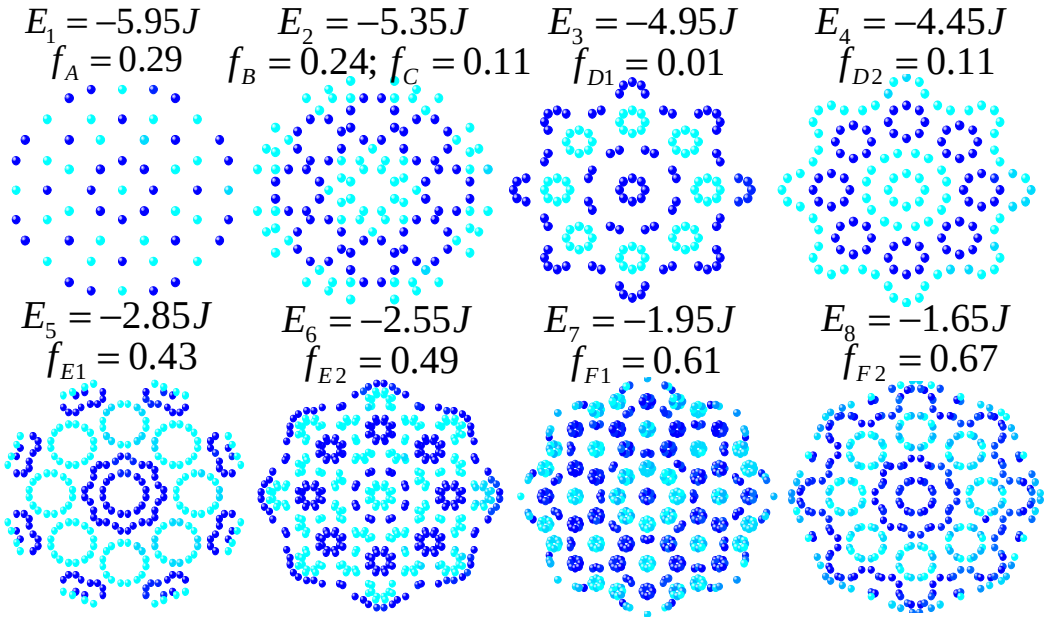

Figure 5.8: Spatial distribution of magnetic moments belonging to eight subtilings of a noncollinear configuration on an octagonal tiling consisting of 2193 spins. $J_d > 2J$. The light and dark circles represent positive and negative x-components of the magnetization. The in-plane components are not given for the sake of simplicity. Average values of the exchange energy E and the local frustration f per spin are indicated.

rose and Amman-Beenker 'stars', which are also shown in figure 5.9 for clarity. On the Penrose tiling, the 'star'-pattern can easily be recognised in the magnetic structure, because the moments belonging to the perimeter of enclosed 'stars' show perfectly antiparallel alignment. On the octagonal tiling, the situation is more complicated. The central magnetic moment is neither parallel nor antiparallel to the neighbouring magnetic moments. Its eight nearest neighbours have different sets of mutual angles. The moments forming the next ring have still another orientation with respect to their nearest neighbours. The noncollinear alignment of the neighbouring moments indicates that the system is geometrically frustrated, i.e. there is no possibility to align all neighbours in an antiparallel arrangement. Similar noncollinear antiferromagnetic configurations are formed in the Tübingen triangle and Anti-Penrose tilings. Within the examples of tilings considered here, the Tie-Navette tiling represents an exception. The magnetic structure observed for this geometry consists of two antiferromagnetically aligned quasiperiodic sublattices, as shown in figure 5.6d. This means that every pair of nearest neighbouring moments can be aligned antiparallell, i.e. the antiferromagnetic configuration is not frustrated.

The diffraction pattern of a quasiperiodic antiferromagnetic system is more complex than that of the Ising or the quantum-mechanical [141] model. As the spin structure is noncollinear, not only the structure factor S^{zz}, but also S^{xx} and S^{yy} can

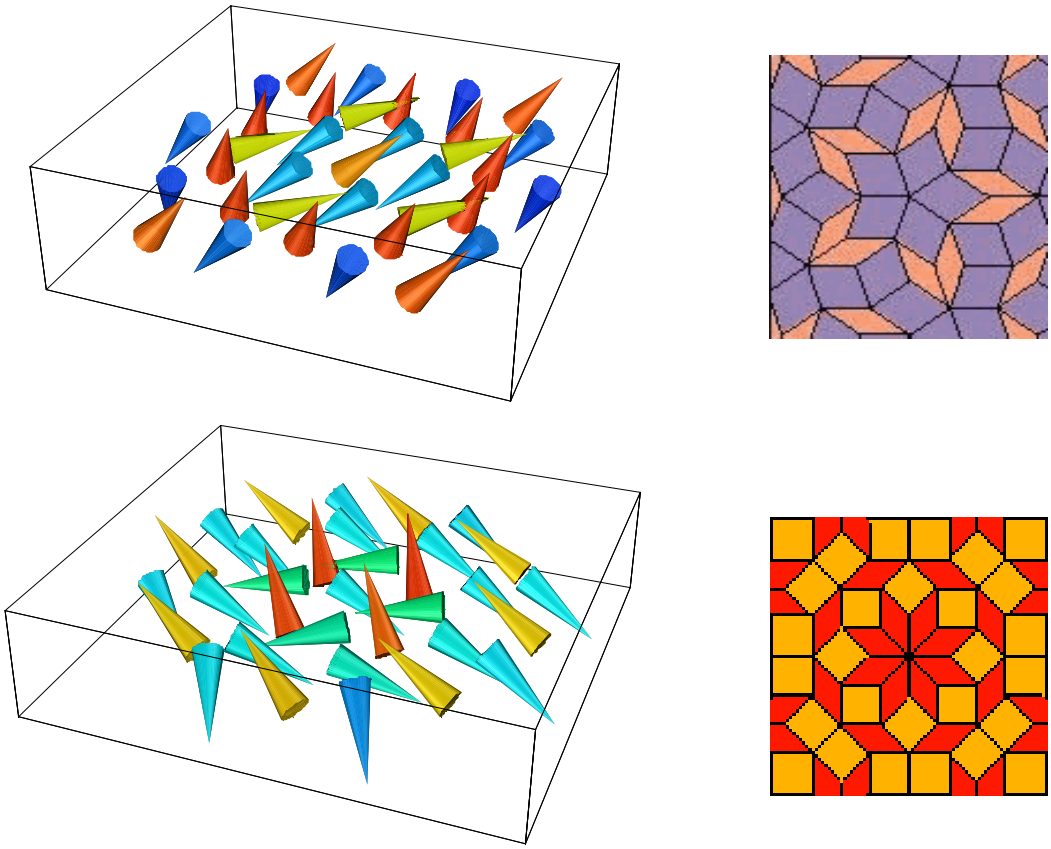

Figure 5.9: Perspective view of a portion of a Monte-Carlo configuration on the Penrose tiling (top) and the octagonal tiling (bottom). Top views of the corresponding patches are shown on the right. The magnetic moments are represented as cones.

be recognized. The calculated S^{yy} Bragg maps for different tilings are given in the insets to the Fig. 5.6 whereas diffraction patterns for all three magnetization components of an octagonal tiling are presented in Fig. 5.10. The eightfold S^{xx} and S^{zz} patterns contain additional long wave-vector peaks which could not be identified in the previous investigations [141]. In dependence on the anisotropy (or on the initial random configuration for $K_1 = 0$) new peaks also occur in S^{yy}. The Bragg reflexes found in study [139] select a subset of the wave vectors given in Ref. [140] where $n_1 + n_2 + n_3 + n_4$ is odd. Peaks with $n_1 + n_2 + n_3 + n_4$ even are extinct. According to the nomenclature of Ref. [162], the following wave vectors can be identified: $(1,0,0,0)$, $(1,-1,1,0)$, $(3,-2,1,1)$, $(3,-1,-1,2)$, $(1,1,-1,0)$, $(1,0,1,-1)$, $(0,2,-1,0)$, $(0,0,1,-2)$, $(-1,0,1,-3)$, $(0,2,-2,1)$, $(0,1,-2,2)$. Hence, the non-collinearity of the spin structure gives rise to selection rules different from those of collinear models [140, 141].

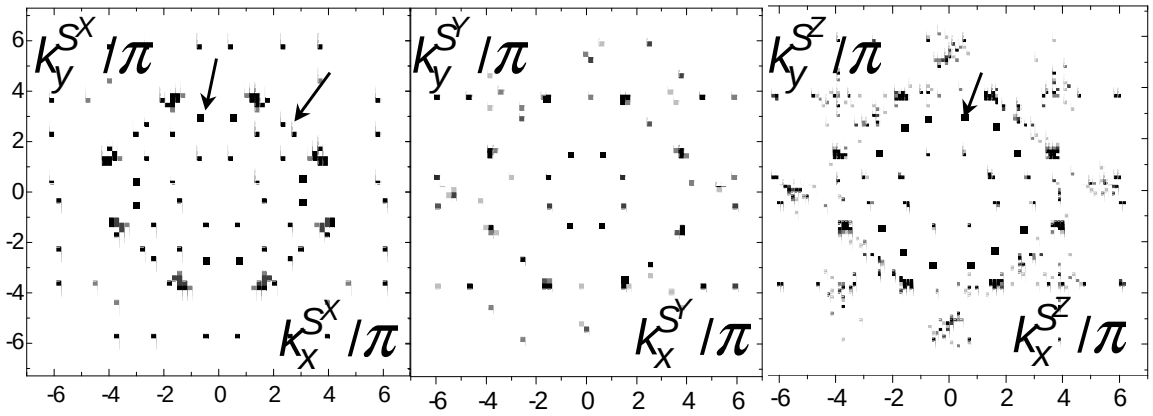

Figure 5.10: The calculated Bragg scattering of S^x, S^y and S^z component of magnetization for the antiferromagnetic superstructure. Reflexes indicated by arrows are new in comparison to previous studies.

5.5.3 Dominating Dipolar Interaction

Fig. 5.11 shows examples of relaxed magnetic configuration for pure dipolar interactions obtained in the numerical (Fig. 5.11a) and in the experimental (Fig. 5.11b) model. Both studies show that after different relaxation procedures a micromagnetic pattern can have different local arrangement of dipoles. The total energy, however, is always identical. Thus, the ground state in case of $J = 0$ is highly degenerate. All patterns, theoretical and experimental, have features in common. Magnetic moments are ordered in circular loops. The diameters of the loops are identical all over the sample. The loops overlap. This overlapping is not accidental but follows certain rules. Amazingly, these rules coincide with the recently proposed "decagonal model" of quasicrystals described in the section 5.2.

The decagons can be easily recognized in the magnetic microstructure of the numerical and the experimental model (Fig. 5.11a,b). In order to minimize the dipolar energy the magnetic moments located on the perimeter of a decagon form closed chains. The moments are coplanar to the sides of the decagons. The overlapping rings of magnetic moments can have the same or opposite sense of rotation. The orientation of the moments that do not belong to the perimeter of decagons is highly frustrated and varies from cluster to cluster. The overlapping magnetic decagon-chains form a quasiperiodic pattern. Thus, in case of pure dipolar interaction the magnetic pattern is formed on the scale of the lattice constant, i.e. a microscopic pattern is formed. In zero magnetic field this state is degenerate and represents a manifold of quasiperiodic spin configurations.

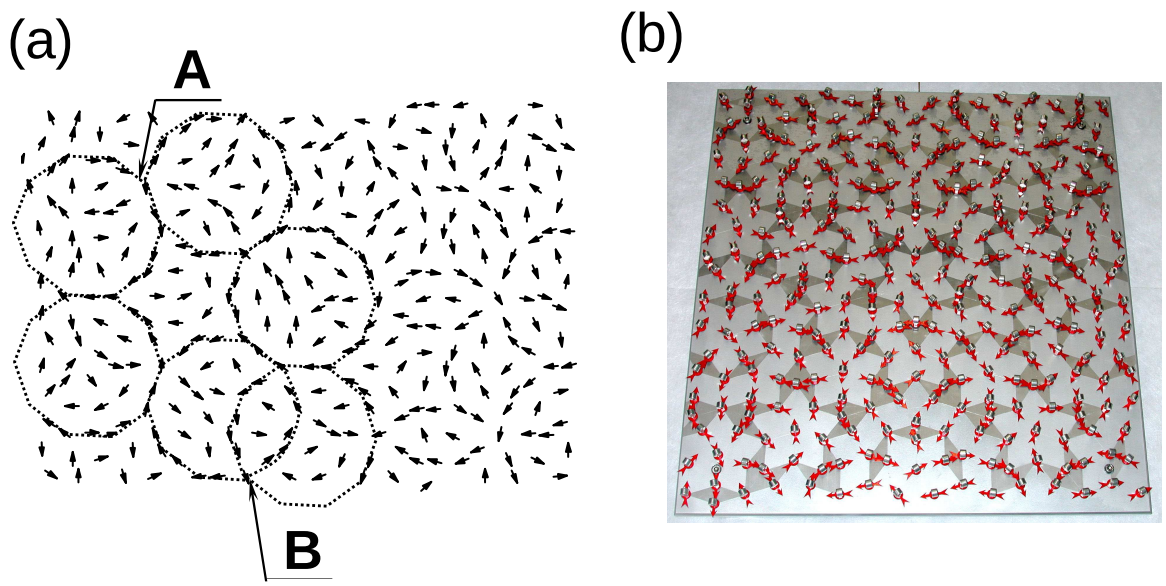

Figure 5.11: (a) Monte-Carlo simulations. Top-view of the portion of the magnetic structure in a sample of finite size for pure dipolar interaction, i.e. $R = J/D = 0$. The microstructure has been obtained for a square sample of about 10500 vector spins on the Penrose lattice for $D/k_B T = 100$. The spins belonging to the perimeter of decagons (marked) form closed chains. The chains overlap according to rules given in Fig. 5.2. **(b)** Experimental model. The perspective view of the magnetic microstructure. The red arrows represent the orientation of dipolar moments of magnets fixed onto the nodes of the Penrose tiling (rhombuses). The magnets can rotate in the horizontal plane.

5.5.4 Analysis of Stability

The most interesting features of the decagonal structure relate to its stability. To see the time-dependent changes in a magnetic structure in the simulations an extremely slow annealing procedure has been applied in the Monte-Carlo simulations Ref. [145]. The overlapping rings of magnetic moments have been found to be very stable. The decagons can have the same or opposite sense of rotation. However, once the sense of the rotation has been chosen it remains unchanged. The magnetic moments inside of the ring seem to be disordered. In zero magnetic field this state is degenerate and represents a manifold of spin configurations. Orientations of disordered dipoles are not static at temperatures $kT > 0.2D$. They change continuously during the Monte Carlo run while the decagon chains remain stable and the total energy oscillates around its minimal value. In the experimental model the temperature has been simulated by application of an alternating magnetic field. When a very weak field is applied the magnetic moments inside of the rings begin to oscillate. The moments on the perimeter of decagons, in contrast, remain stable to very high values of the field (of order of 1 T). In addition to the alternating magnetic field a constant external magnetic field can be

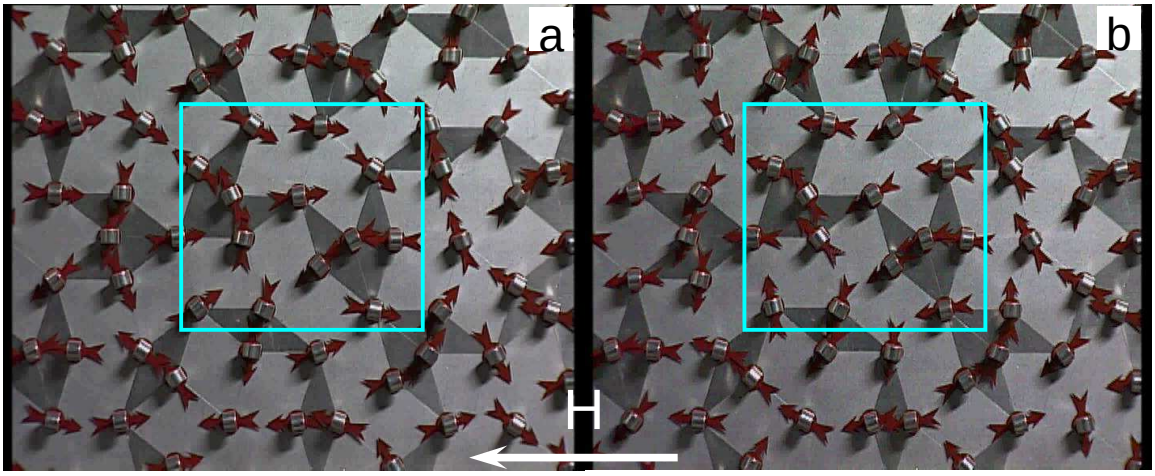

Figure 5.12: Two snapshots of a decagon from the experimental model Fig. 5.11 for different strength of the applied permanent in-plane magnetic field: (a) $H = 0$, (b) $H > 1\,T$. Frustrated moments (highlighted) change their orientation while the ring remain stable.

also applied to the structure (see the snapshots for different fields in Fig. 5.12). Even a strongest possible in-plane magnetic field was not enough to destroy the experimental decagonal pattern while the frustrated inner dipoles were immediately aligned (see Fig. 5.12b). In the simulations the field necessary for the alignment of the chains must be at least an order stronger than that needed for the alignment of the frustrated moments. Thus, in the quasiperiodic magnetic structure the stable decagonal pattern coexists with highly frustrated, glass-like phase.

Usually frustrated systems have either a continuously degenerated, periodic ground state (antiferromagnetic spins on a honeycomb, a kagome, a triangular, a pyrochlore lattice) or a completely disordered one (spin glasses). The superposition of both types of frustration has not been reported neither for periodic nor for disordered systems. Thus, a magnetic system on a Penrose tiling belongs to a new class of frustrated systems where the degenerated ground state is aperiodic and consists of two parts: ordered decagon rings and disordered spin-glass-like phase inside the decagons. The Penrose tiling is no exception. The coexistence of ordered and frustrated parts is characteristic for dipolar or antiferromagnetic ensembles on many of aperiodic tilings. Two examples are given in Fig. 5.13.

5.6 Summary

In conclusion, magnetic ordering on quasiperiodic tilings for dominating ferromagnetic, antiferromagnetic and dipolar interactions has been reviewed.

It has been shown that vector spin system with antiferromagnetic coupling on dif-

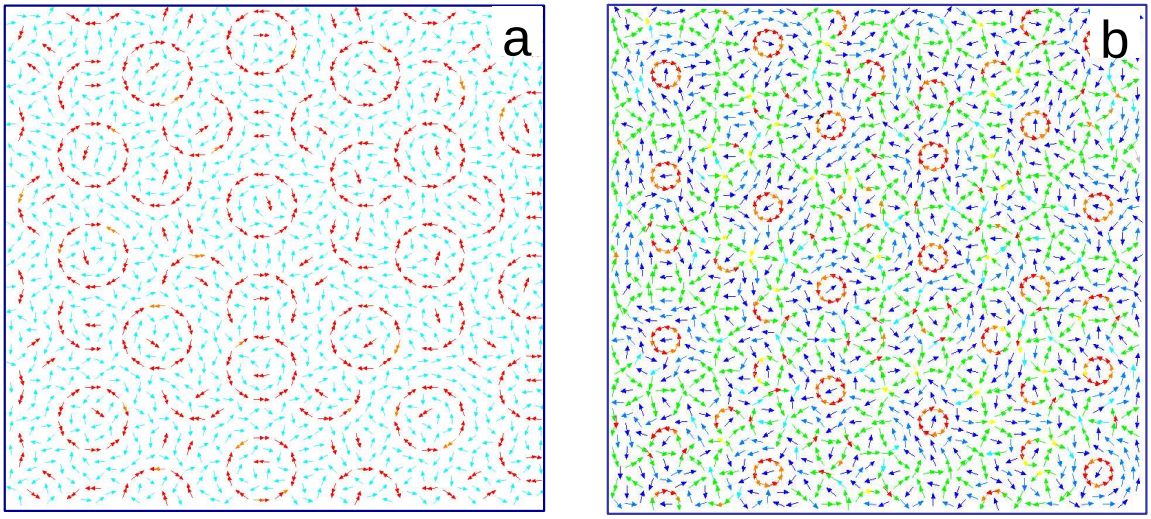

Figure 5.13: Portions of the low-temperature pure dipolar configurations for an Anti-Penrose (a) and a Tie-Navette (b) tilings. The color scheme defines an average energy per magnetic moment: from lowest energy (red) to the highest energy (dark blue). Red moments are stable while the blue ones frustrated.

ferent quasiperiodic tilings is locally frustrated. All spins can be divided into several quasiperiodic (in our two-dimensional physical space) or periodic (in the corresponding four-dimensional periodic hypercrystal) subtilings of different energy, which generally do not coincide with a specific vertex type. The vector spin system admits a three-dimensional noncollinear magnetic structure. The noncollinearity of the magnetic configuration permits to minimize the degree of frustration and the total energy of the system in comparison with the collinear case. The co-directional spins of every subtiling reveal quasiperiodic ordering with a wave vector which is specific for a given subtiling. The Tie-Navette tiling is not frustrated and admits collinear magnetic configurations. For the short-ranged exchange interaction, this arises as a consequence of the bipartiteness of the graph formed by connecting interacting pairs of spins; however, we observe that the antiferromagnetic order persists for the case of a long-range, exponentially decreasing exchange interaction.

A ferromagnetic ordering in quasicrystals depends on the range of the interaction. For the ferromagnetic exchange of a very short range the average magnetization deviates significantly from the unity.

For pure dipolar interaction the magnetic pattern is highly degenerate. That state represents a new class of frustrated systems where the structure is aperiodic and consists of ordered, stable parts and an unstable, spin-glass phases.

Bibliography

[1] D. Sander, J. Phys.: Condens. Matter **16**, R603 (2004).

[2] L. Udvardi, L. Szunyogh, A. Vernes, and P. Weinberger, Phil. Mag. B **81**, 613 (2001).

[3] A. Hucht, A. Moschel, and K. D. Usadel, J. Magn. Magn. Mater. **148**, 32 (1995).

[4] A. Hucht and K. D. Usadel, J. Magn. Magn. Mater. **156**, 423 (1996).

[5] A. B. Ryzhenko and E. V. Sinitsyn, Phys. of Metals and Metallography **85**, 130 (1998).

[6] A. B. MacIsaac, J. P. Whitehead, K. De'Bell, and P. H. Poole, Phys. Rev. Lett. **77**, 739 (1996).

[7] A. B. MacIsaac, K. De'Bell, and J. P. Whitehead, Phys. Rev. Lett. **80**, 616 (1998).

[8] S. T. Chui, Phys. Rev. B **50**, 12559 (1994).

[9] A. Berger and R. P. Erickson, J. Magn. Magn. Mater. **165**, 70 (1997).

[10] P. J. Jensen and K. H. Bennemann, Phys. Rev. B **52**, 16012 (1995).

[11] Y. Yafet and E. M. Gyorgy, Phys. Rev. B **38**, 9145 (1988).

[12] R. Czech and J. Villain, J. Phys.: Condens. Matter **1**, 619 (1989).

[13] D. Pescia and V. L. Pokrovsky, Phys. Rev. Lett. **65**, 2599 (1990).

[14] Z. Malek and V. Kambersky, Czech. J. Phys. **8**, 416 (1958).

[15] D. P. Pappas, K.-P. Kämper, and H. Hopster, Phys. Rev. Lett. **64**, 3179 (1990).

[16] R. Allenspach and A. Bischof, Phys. Rev. Lett. **69**, 3385 (1992).

[17] H. P. Oepen, Y. T. Millev, and J. Kirschner, J. Appl. Phys. **81**, 5044 (1997).

[18] M. Farle, W. Platow, A. N. Anisimov, B. Schulz, and K. Baberschke, J. Magn. Magn. Mater. **165**, 74 (1997).

[19] T. Duden and E. Bauer, in *MRS Symposium Proceedings* (1997), p. 475.

[20] E. Y. Vedmedenko, A. Ghazali, and J.-C. S. Lévy, Surf. Sci. **402-404**, 391 (1998).

[21] E. Y. Vedmedenko, A. Ghazali, and J.-C. S. Lévy, Phys. Rev. B **59**, 3329 (1999).

[22] J.-C. S. Lévy, A. Ghazali, and E. Y. Vedmedenko, Acta Phys. Polonica A **97**, 431 (2000).

[23] E. Y. Vedmedenko, A. Ghazali, J.-C. S. Lévy, H. P. Oepen, and J. Kirschner, Phys. Rev. Lett. **84**, 5884 (2000).

[24] E. Y. Vedmedenko, H. P. Oepen, and J. Kirschner, J. Appl. Phys. **89**, 7145 (2001).

[25] E. Y. Vedmedenko, H. P. Oepen, and J. Kirschner, Phys. Rev. B **66**, 214401 (2002).

[26] A. Wachowiak, J. Wiebe, M. Bode, O. Pietzsch, M. Morgenstern, and R. Wiesendanger, Science **298**, 577 (2002).

[27] H. B. G. Casimir, J. Smit, U. Enz, J. F. Fast, H. P. J. Wijn, E. W. Gorter, A. J. W. Duyvesteyn, J. D. Fast, and J. J. de Jong, Le Journal de Physique et le Radium **20**, 360 (1959).

[28] C. Chappert and P. Bruno, J. Appl. Phys. **64**, 5736 (1988).

[29] H. Fritzsche, J. Kohlhepp, and U. Gradmann, J. Magn. Magn. Mater. **148**, 154 (1995).

[30] S. Nieber and H. Kronmüller, Phys. Stat. Sol. B **165**, 503 (1991).

[31] Y. Millev and J. Kirschner, Phys. Rev. B **54**, 4137 (1996).

[32] K. Baberschke and M. Farle, J. Appl. Phys. **81**, 5038 (1997).

[33] J.-C. S. Lévy, Phys. Rev. B **63**, 104409 (2001).

[34] W. Kuch, J. Gilles, S. S. Kang, S. Imada, S. Suga, and J. Kirschner, Phys. Rev. B **62**, 3824 (2000).

[35] R. Zdyb and E. Bauer, Phys. Rev. B **67**, 134420 (2003).

[36] M. Farle, B. Mirwald-Schulz, A. N. Anisimov, W. Platow, and K. Baberschke, Phys. Rev. B **55**, 3708 (1997).

[37] M. Speckmann, H. P. Oepen, and H. Ibach, Phys. Rev. Lett. **75**, 2035 (1995).

[38] P. Castrucci, R. Gunnella, R. Bernardini, P. Falcioni, and M. De Crescenzi, Phys. Rev. B **65**, 235435 (2002).

[39] A. Kubetzka, O. Pietzsch, M. Bode, and R. Wiesendanger, Phys. Rev. B **63**, 140407R (2001).

[40] S. Pütter, H. F. Ding, Y. T. Millev, H. P. Oepen, and J. Kirschner, Phys. Rev. B **64**, 92409 (2001).

[41] M. Tekielak, Z. Kuranta, A. Maziewski, L. T. Baczewski, A. Maneikis, and A. Wawro, J. Magn. Magn. Mater. **290-291**, 783 (2005).

[42] K. Ha and R. C. O'Handley, J. Appl. Phys. **87**, 5944 (2000).

[43] G. Gubbiotti, G. Carlotti, M. G. Pini, P. Politi, A. Rettori, P. Vavassori, M. Ciria, and R. C. O'Handley, Phys. Rev. B **65**, 214420 (2002).

[44] H. P. Oepen and J. Kirschner, Solid State and Material Science **4**, 217 (1999).

[45] J. A. Osborn, Phys. Rev. **67**, 351 (1945).

[46] E. C. Stoner, Phil. Mag., ser. 7 **36**, 803 (1945).

[47] H. J. G. Draaisma and W. J. M. de Jonge, J. Appl. Phys. **64**, 3610 (1988).

[48] B. Heinrich, S. T. Purcell, J. R. Dutcher, K. B. Urquhart, J. F. Cochran, and A. A. S., Phys. Rev. B **38**, 12879 (1988).

[49] E. Y. Vedmedenko, H. P. Oepen, and J. Kirschner, J. Magn. Magn. Mater. **256**, 237 (2003).

[50] Y. Millev, E. Y. Vedmedenko, and H. P. Oepen, J. Phys. D: Appl. Phys. **36**, 2945 (2003).

[51] P. J. Jensen, Ann. Phys. (Leipzig) **6**, 317 (1997).

[52] E. Y. Vedmedenko, H. P. Oepen, and J. Kirschner, Phys. Rev. B **90**, 12409 (2003).

[53] M. Maret, A. Maier, F. Treubel, B. Riedlinger, M. Albrecht, E. Beaurepaire, and G. Schatz, J. Magn. Magn. Mater. **242-245**, 420 (2002).

[54] R. Lundin, Proc. IEEE **73**, 1428 (1985).

[55] J. Brooke, T. F. Rosenbaum, and G. Aeppli, Nature **413**, 6856 (2001).

[56] C. T. Black, C. B. Murray, R. L. Sandstrom, and S. Sand, Science **290**, 5494 (2000).

[57] O. Pietzsch, A. Kubetzka, M. Bode, and R. Wiesendanger, Science **292**, 5524 (2001).

[58] J. Fidler, T. Schrefl, W. Scholz, D. Suess, R. Dittrich, and M. Kirschner, J. Magn. Magn. Mater. **272**, 641 (2004).

[59] A. Hubert and R. Schäfer, *Magnetic Domains: the analysis of magnetic microstructures* (Springer, Berlin, 1998), p. 231.

[60] D. Ha, R. Hertel, and J. Kirschner, Europhys. Lett. **64**, 810 (2003).

[61] A. Kubetzka, M. Bode, O. Pietzsch, and R. Wiesendanger, Phys. Rev. Lett. **88**, 057201 (2002).

[62] M. Bode, S. Heinze, A. Kubetzka, O. Pietzsch, X. Nie, G. Bihlmayer, S. Blügel, and R. Wiesendanger, Phys. Rev. Lett. **89**, 237205 (2002).

[63] E. Y. Vedmedenko, A. Kubetzka, K. von Bergmann, O. Pietzsch, M. Bode, J. Kirschner, H. P. Oepen, and R. Wiesendanger, Phys. Rev. Lett. **92**, 077207 (2004).

[64] E. Y. Vedmedenko, K. von Bergmann, H. P. Oepen, and R. Wiesendanger, J. Magn. Magn. Mater. **290-291**, 746 (2005).

[65] M. E. J. Newman and G. T. Barkema, *Monte Carlo Methods in Statistical Physics* (Clarendon Press, Oxford, 1999).

[66] D. Hinzke and U. Nowak, Phys. Rev. B **61**, 6734 (2000).

[67] J. Sasaki and F. Matsubara, J. Phys. Soc. Jpn. **66**, 2138 (1996).

[68] H. Kronmüller and M. Fähnle, *Micromagnetism and the microstucture of ferromagnetic solids* (Cambridge University Press, Cambridge, 2003).

[69] K. D. Belashchenko, J. Magn. Magn. Mater. **270**, 413 (2004).

[70] I. Galanakis, M. Alouani, and H. Dreyssé, Phys. Rev. B **62**, 3923 (2000).

[71] A. Liechtenstein, M. Katsnelson, V. Antropov, and V. Gubanov, J. Magn. Magn. Mater. **67**, 65 (1987).

[72] S. Frota-Pessôa, R. Muniz, and J. Kudrnovsky, Phys. Rev. B **62**, 5293 (2000).

[73] M. Hatherly, K. Hirakawa, R. Lowde, J. Mallett, M. Stringfellow, and B. Torrie, Proc. Phys. Soc. **84**, 55 (1965).

[74] Q. Pankhurst, L. Barquin, J. Wicks, R. McGreevy, and M. Gibbs, J. Phys.: Condens. Matter **9**, L375 (1997).

[75] R. Muniz and D. Mills, Phys. Rev. B **66**, 174417 (2002).

[76] R. Muniz, A. Costa, and D. Mills, J. Phys.: Condens. Matter **15**, S495 (2003).

[77] K. Nielsch, R. B. Wehrspohn, R. Barthel, J. Kirschner, S. F. Fischer, H. Kronmüller, T. Schweinböck, D. Weiss, and U. Gösele, J. Magn. Magn. Mater. **249**, 234 (2002).

[78] R. E. Rosensweig, M. Zahn, and R. Shumovich, J. Magn. Magn. Mater. **39**, 127 (1983).

[79] J.-C. Bacri, R. Perzynski, and D. Salin, Recherche **18**, 1150 (1987).

[80] V. M. Ogenko, V. M. Rosenbaum, and A. A. Chuiko, *Theory of oscillations and reorientations in atomic groups at the surface. (in Russian)* (Naukova Dumka, Kiev, 1991).

[81] K. De'Bell, A. B. MacIsaac, I. N. Booth, and J. P. Whitehead, Phys. Rev. B **55**, 15108 (1997).

[82] G. O. Zimmerman, A. K. Ibrahim, and F. Y. Wu, Phys. Rev. B **37**, 2059 (1988).

[83] S. Prakash and C. L. Henley, Phys. Rev. B **42**, 6574 (1990).

[84] H. B. Braun and B. Roessli, unpublished.

[85] A. J. Stone, *The Theory of Intermolecular Forces* (Clarendon Press, Oxford, 1996).

[86] M. Eremtchenko, J. A. Schaefer, and F. S. Tautz, Nature **425**, 602 (2003).

[87] F. Würthner, Chem. Commun. **1**, 1564 (2004).

[88] K. Kim and N. S. Sullivan, J. Low Temp. Phys. **114**, 173 (1999).

[89] S. Raugei, G. Cardini, and V. Schettino, J. Chem. Phys. **106**, 8196 (1997).

[90] A. J. Berlinsky and A. B. Harris, Phys. Rev. Lett. **40**, 1579 (1978).

[91] S. F. O'Shea, J. Chem. Phys. **71**, 2399 (1979).

[92] A. S. Mishenko, A. S. Chernyshov, and A. K. Zvezdin, Europhys. Lett. **65**, 116 (2004).

[93] K. Gross, C. P. Search, H. Pu, W. Zhang, and P. Meystre, Phys. Rev. A **66**, 033603 (2002).

[94] V. Dunjko, V. Lorent, and M. Olshanii, Phys. Rev. Lett. **86**, 5413 (2001).

[95] K. Bongs, unpublished.

[96] N. Mikuszeit, E. Y. Vedmedenko, and H. P. Oepen, J. Phys.: Condens. Matter **16**, 9037 (2004).

[97] N. Mikuszeit, E. Y. Vedmedenko, H. P. Oepen, and R. Wiesendanger, J. Appl. Phys. **97**, 10J502 (2005).

[98] T. Aign, P. Meyer, S. Lemerle, J. P. Jamet, J. Ferré, V. Mathet, C. Chappert, J. Gierak, C. Vieu, F. Rousseaux, et al., Phys. Rev. Lett. **81**, 5656 (1998).

[99] C. A. Ross, M. Hwang, M. Shima, J. Y. Cheng, M. Farhoud, T. A. Savas, H. I. Smith, W. Schwarzacher, F. M. Ross, M. Redjdal, et al., Phys. Rev. B **65**, 144417 (2002).

[100] J.-P. Jamet, S. Lemerle, P. Meyer, J. Ferré, B. Bartenlian, N. Bardou, C. Chappert, P. Veillet, F. Rousseaux, D. Decanini, et al., Phys. Rev. B **57**, 14320 (1997).

[101] K. Koike, H. Matsuyama, Y. Hirayama, K. Tanahashi, T. Kanemura, O. Kitakami, and Y. Shimada, Appl. Phys. Lett. **78**, 784 (2001).

[102] J. S. van Duijneveldt, A. Gil-Villegas, G. Jackson, and M. P. Allen, J. Chem. Phys. **112**, 9092 (2000).

[103] P. Popelier and D. Kosov, J. Chem. Phys. **114**, 6539 (2001).

[104] D. A. Varsalovich, A. N. Moskalev, and V. K. Khersonskii, *Quantum Theory of Angular Momentum* (World Scientific, Singapure, 1988).

[105] E. Y. Vedmedenko, N. Mikuszeit, H. P. Oepen, and R. Wiesendanger, Phys. Rev. Lett. **95**, 207202 (2005).

[106] E. Y. Vedmedenko, submitted to Nanoletters.

[107] I. E. Dzyaloshinskii, E. I. Kats, and J. Lajzerowocz, JETP Letters **68**, 785 (1998).

[108] V. E. Klymenko, V. M. Rozenbaum, V. V. Kukhtin, and O. V. Schramko, Sol. State Comm. **88**, 373 (1993).

[109] J. A. Hamida, N. S. Sullivan, and M. D. Evans, Phys. Rev. Lett. **73**, 2720 (1994).

[110] Y. B. Xu, A. Hirohata, Gardiner, M. Tselepi, J. Rothman, M. Klaui, L. Lopez-Diaz, J. A. C. Bland, Y. Chen, E. Cambril, et al., IEEE Trans. Magn. **37**, 2055 (2001).

[111] R. P. Cowburn, J. Phys. D: Appl. Phys. **33**, R1 (2000).

[112] J. Y. Cheng, W. Jung, and C. A. Ross, Phys. Rev. B **70**, 064417 (2004).

[113] C. Miramond, C. Fermon, F. Rousseaux, D. Decanini, and F. Carcenac, J. Magn. Magn. Mater. **165**, 500 (1997).

[114] C. Lacroix, *Encyclopedia of Materials: Science and Technology Updates* (Elsevier, Oxford, 2005), chap. Magnetic Systems: Lattice Geometry originated Frustration.

[115] C. Godréche, J. M. Luck, and H. Orland, J. Stat. Phys. **45**, 777 (1986).

[116] G. G. Naumis, R. A. Barrio, and C. Wang, Phys. Rev. B **50**, 9834 (1994).

[117] E. S. Sorensen, M. V. Jaric, and M. Ronchetti, Phys. Rev. B **44**, 9271 (1991).

[118] H. Tsunetsugu and K. Ueda, Phys. Rev. B **36**, 5493 (1987).

[119] Y. Achiam, T. C. Lubensky, and E. W. Marshall, Phys. Rev. B **33**, 6460 (1986).

[120] H. Aoyama and T. Odagaki, J. Stat. Phys. **48**, 503 (1987).

[121] Y. Okabe and K. Niizeki, J. Phys. Soc. Jpn. **57**, 16 (1988).

[122] A. Doroba and K. Sokalski, Phys. Stat. Sol. B **152**, 275 (1989).

[123] D. Ledue, D. P. Landau, and J. Teillet, Phys. Rev. B **51**, 12523 (1995).

[124] D. Ledue and D. P. Landau, Phys. Rev. B **63**, 054425 (2001).

[125] R. W. Reid, S. K. Bose, and B. Mitrovic, J. Phys.: Condens. Matter **10**, 2303 (1998).

[126] G. Amarendra, G. Ananthakrishna, and G. Athithan, Europhys. Lett. **5**, 181 (1988).

[127] U. Grimm and M. Baake, *The Mathematics of Long-Range Aperiodic Order* (Kluwer, Dordrecht, 1997), p. 199.

[128] E. Y. Vedmedenko, *Encyclopedia of Materials: Science and Technology Updates* (Elsevier, Oxford, 2005), chap. Quasicrystals: Magnetism, p. 1.

[129] Z. Luo, S. Zhang, Y. Tang, and D. Zhao, Scr. Metall. Mater. **28**, 1513 (1993).

[130] A. Niikura, A. P. Tsai, A. Inoue, and T. Masumoto, Philos. Mag. Lett. **69**, 351 (1994).

[131] A. P. Tsai, A. Niikura, A. Inoue, T. Masumoto, Y. Nishida, K. Tsuda, and M. Tanaka, Philos. Mag. Lett. **70**, 169 (1994).

[132] J. Hafner and M. Krajči, Phys. Rev. B **57**, 2849 (1998).

[133] K. Fukamichi, *Physical Properties of Quasicrystals* (Springer-Verlag GmbH, Berlin and New York, 1999), p. 295.

[134] B. Charrier, B. Ouladdiaf, and D. Schmitt, Phys. Rev. Lett. **78**, 4637 (1997).

[135] T. J. Sato, H. Takakura, A. P. Tsai, and K. Shibata, Phys. Rev. Lett. **81**, 2364 (1998).

[136] M. Scheffer and J.-B. Suck, Mat. Sci. Eng. A **294**, 629 (2000).

[137] J. Dolinšek, Z. Jagličić, T. J. Sato, J. Q. Guo, and A. P. Tsa, J. Phys.: Condens. Matter **15**, 7981 (2003).

[138] T. J. Sato, H. Takakura, A. P. Tsai, K. Shibata, K. Ohoyama, and K. H. Andersen, Phys. Rev. B **61**, 476 (2000).

[139] E. Y. Vedmedenko, U. Grimm, and R. Wiesendanger, Phys. Rev. Lett. **93**, 076407 (2004), cond-mat/0406373.

[140] R. Lifshitz, in *Proceedings of the 5th International Conference on Quasicrystals*, edited by C. Janot and R. Mosseri (World Scientific, Singapore, 1995), pp. 43–46.

[141] S. Wessel, A. Jagannathan, and S. Haas, Phys. Rev. Lett. **90**, 177205 (2003).

[142] A. Jagannathan, Phys. Rev. Lett. **92**, 047202 (2004).

[143] A. Jagannathan, Phys. Rev. B **71**, 115101 (2005).

[144] E. Y. Vedmedenko, Ferroelectrics **305**, 129 (2004).

[145] E. Y. Vedmedenko, U. Grimm, and R. Wiesendanger, Phil. Mag. (2005), in print; cond-mat/0509461.

[146] E. Y. Vedmedenko, H. P. Oepen, and J. Kirschner, Phys. Rev. Lett. **90**, 137203 (2003).

[147] C. L. Henley, *Quasicrystals: The State of the Art* (World Scientific, Singapore, 1991), p. 429.

[148] D. P. DiVincenzo and P. J. Steinhardt, *Quasicrystals The State of the Art* (World Scientific, Singapore, 1991).

[149] F. Gähler, P. Kramer, H.-R. Trebin, and K. Urban, eds., *Proceedings of the 7th International Conference on Quasicrystals*, vol. 294-296 (Mat. Sci. Eng, 2000).

[150] R. Penrose, Bull. Inst. Math. Appl. **10**, 266 (1974).

[151] R. Ammann, B. Grünbaum, and G. Shephard, Discrete Comput. Geom. **8**, 1 (1992).

[152] S. E. Burkov, Phys. Rev. Lett. **67**, 614 (1991).

[153] P. Gummelt, Geometriae Dedicata **62**, 1 (1996).

[154] P. J. Steinhardt and H. C. Jeong, Nature **382**, 433 (1996).

[155] H. C. Jeong and P. J. Steinhardt, Phys. Rev. B **55**, 3520 (1997).

[156] K. W. Urban, Nature **396**, 14 (1998).

[157] P. Häussler and E. Kay, Zeitschrift für Phys. Chemie Neue Folge **157**, 377 (1988).

[158] M. Baake, P. Kramer, M. Schlottmann, and D. Zeidler, Int. J. Mod. Phys. B **4**, 2217 (1990).

[159] R. Lück and K. Lu, Alloys Compd. **209**, 139 (1994).

[160] N. D. Mermin and H. Wagner, Phys. Rev. Lett. **17**, 1133 (1966).

[161] K. Niizeki, J. Phys. A: Math. Gen. **23**, 5011 (1990).

[162] R. Lifshitz, Acta Cryst. A **60**, 167 (2004).

VOLUME 84, NUMBER 25 PHYSICAL REVIEW LETTERS 19 JUNE 2000

Magnetic Microstructure of the Spin Reorientation Transition: A Computer Experiment

E. Y. Vedmedenko,[1,*] H. P. Oepen,[1] A. Ghazali,[2] J.-C. S. Lévy,[3] and J. Kirschner[1]

[1]*Max-Planck-Institut für Mikrostrukturphysik, Weinberg 2, 06120 Halle, Germany*

[2]*Groupe de Physique des Solides, UMR 7588–CNRS, Universités Paris 7 et Paris 6, 75251 Paris 5, France*

[3]*Laboratoire de Physique Théorique de la Matière Condensée, Université Paris 7, case 7020, 75251 Paris 5, France*

(Received 25 August 1999)

The scenario of the spin reorientation in two-dimensional films within first-order anisotropy approximation is theoretically studied by means of Monte Carlo simulations. The magnetic microstructure is investigated as a function of the ratio of the perpendicular anisotropy energy to the dipolar one. If the anisotropy dominates, out-of-plane domains will be found while in-plane vortices appear for a vanishing anisotropy. In the range of comparable anisotropy and dipolar energies a complex domain pattern evolves yielding a continuous transition between the two structures. The structure with equally distributed magnetic moment orientations is stable at the point where anisotropy and dipolar energies cancel each other.

PACS numbers: 75.70.Ak, 75.40.Mg, 75.60.Ch, 75.70.Kw

Over the last decade the investigation of the spin reorientation in ultrathin films has been a vivid field in basic research. Experimentally, the studies reveal that the magnetic microstructure at the spin reorientation determines the details of the switching of the magnetization and thus the macroscopic behavior of the ferromagnet [1–5]. Theoretically, Monte Carlo simulations and analytical studies have been performed in first-order approximation of perpendicular magnetic anisotropy. In those investigations emphasis was put on the change of the magnetization orientation as a result of competing anisotropy and dipolar energies with temperature or thickness as a driving parameter [6–15]. Phase diagrams were put forward and noncontinuous magnetization changes postulated [6,9]. The evolution of the magnetic microstructures was not studied in these numerical investigations.

An early analytical model of the spin reorientation, however, was mainly based on the microstructure that can evolve when perpendicular anisotropy becomes weak [13]. Based on the assumption of a stripe domain pattern [16] domain walls of finite width were introduced in the one-dimensional model as the microstructure. It was found that the existence of domain walls is crucial around the point where anisotropy and dipolar energies cancel. At that point the walls have microscopic dimensions, touch each other, and create a wavelike magnetic microstructure.

In summary, it is obvious from the experiments that microstructures are important in spin reorientation transition but from a theoretical point of view no general approach has been made up to now. The aim of our investigation is to achieve a general spatially resolved description of the magnetization reorientation in the framework of competing dipolar and anisotropy energies for a given exchange coupling. For this purpose, Monte Carlo (MC) simulations have been performed to find the equilibrium spin configuration of a monoatomic layer at a given temperature. The approach is more general than the model Ref. [13] as neither a restriction to one dimension is made nor a particular domain structure and wall profile is assumed.

The Hamiltonian of the problem includes exchange, dipolar interactions, and perpendicular anisotropy

$$\mathcal{H} = -J\sum_{\langle ij\rangle}\mathbf{S}_i\cdot\mathbf{S}_j + D\sum_{ij}\left(\frac{\mathbf{S}_i\cdot\mathbf{S}_j}{r_{ij}^3} - 3\frac{(\mathbf{S}_i\cdot\mathbf{r}_{ij})(\mathbf{S}_j\cdot\mathbf{r}_{ij})}{r_{ij}^5}\right) - K_1\sum_i S_{i,z}^2, \quad (1)$$

where J is the exchange coupling constant which is nonzero only for nearest-neighbor spins, D the dipolar coupling parameter, and $\mathbf{r}_{ij}$ the vector between sites i and j. The coefficient K_1 is the first-order anisotropy constant and a is the lattice parameter. In the calculations the ratio $D/(Ja^3) = 0.1$ was used. Via simple scaling arguments the realistic effective values for the ratio of dipolar to exchange interactions can be achieved by considering spin blocks of appropriate size [17,18]. We have performed MC simulations for three typical values of the ratio $R = J(a^3)/D$, namely $R = 10$, $R = 1$, and $R = 0$ (pure dipolar interactions with K finite). In all simulations continuous transitions were found. We focus on the results for $R = 10$ as the scales for Co/Au(111) (5 nm mesh width and 500 nm sample size) are best adopted to the microstructures that appear in the spin reorientation transition.

For the extended MC computations we take a monolayer of classical magnetic moments on a regular, triangular lattice of about 10 000 effective magnetic sites. This corresponds to a surface orthogonal to the c axis of a hcp lattice or to the (111) surface of a fcc structure. Assuming the parameters of Co/Au(111) for the interatomic distance, the exchange constant, and dipolar interaction constant, the MC calculations present sample sizes of about 500 nm. The magnetic moment is described by a three-dimensional vector $\mathbf{S}$ of unit length. The calculations have been performed for free boundaries. The commonly used periodic boundary conditions are dismissed, since they might

 0031-9007/00/84(25)/5884(4)$15.00

VOLUME 84, NUMBER 25 PHYSICAL REVIEW LETTERS 19 JUNE 2000

induce artificial patterns commensurate with the size of the sample.

Because of the long-range character of the dipolar interaction, special attention was paid to the following problems: (i) As the demagnetizing field is depending on the shape of the sample we have to expect inhomogeneities at the sample edges. We have investigated the dependence of the microstructure on the sample geometry. The results for disc and square-shaped samples are identical for $f > 1.46$ (vertical regime). For the configurations with nearly in-plane moments the square-shaped samples have been avoided to obtain the "easy-axis" to "easy-plane" transition. (ii) Most of the computing time is spent on calculating the dipolar interaction between all magnetic moments. Computing time can be saved by calculating an effective dipolar field at one moment, which is created by moments in close vicinity. This is the main idea of the so-called cutoff in MC simulations. If the dipolar energy E_D is comparable to or larger than the anisotropy energy E_A any cutoff will affect strongly the MC spin configuration [17]. To prevent artificial effects due to the cutoff we have considered the dipolar interaction of each magnetic moment with all the other moments, i.e., we used no cutoff.

The MC simulations have been performed in the following way: (i) A random moment configuration is taken as the starting configuration representing the equilibrium at infinite temperature. (ii) The next step is to perform a MC relaxation at a finite temperature still above the Curie temperature. (iii) This high temperature MC equilibration is followed by a stepwise cooling until a low-temperature configuration is reached. At each temperature step a MC relaxation is performed and controlled by checking the total energy evolution. The relaxation is stopped when the energy does not show any remarkable drift over several hundred MC steps per magnetic moment.

We have investigated the magnetic microstructure for different ratios of the competing anisotropy and dipolar energies. In contradiction to previous studies [6,9] we find a continuous transition from vertical to in-plane orientation of magnetization. It is the magnetic microstructure we will discuss in the following that eliminates any discontinuity. Our MC study gives the complete transition from the vertical to the in-plane state of magnetization.

The results are presented as a low-temperature phase diagram in Fig. 1. We have plotted the averaged values of the vertical component S_z and the squared value S_z^2 of the magnetic moment versus f with $f = E_A/E_D$ as the ratio of perpendicular anisotropy energy E_A to the dipolar energy E_D. Usually the MC results are plotted as a function of K_1/D. As the behavior of the magnetic sample is governed by the total energy we find normalized energies more convenient. The magnetostatic energy is defined as the difference between the vertical single domain configuration and a stray field free vortex structure. This energy and the anisotropy energy is normalized with respect to the number of moments and used for calculating the f value

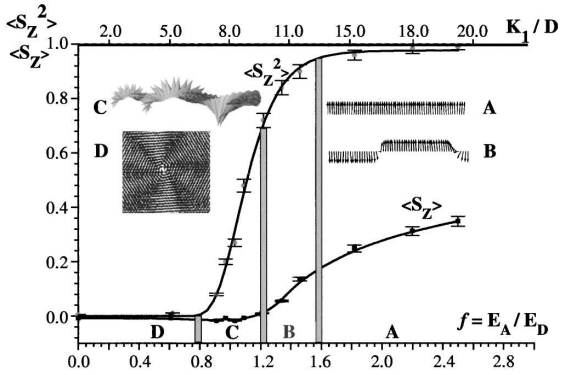

FIG. 1. Plot of $\langle S_z^2 \rangle$ and $\langle S_z \rangle$ versus f. $\langle S_z \rangle$ is the perpendicular component of magnetization and $f = E_A/E_D$ is the ratio of anisotropy energy to dipolar energy. The shaded areas separate the phases (A, B, C, D). The phases are characterized by the different microstructures, which are shown as insets in the diagram. The microstructures have been obtained for disk-shaped ($f \leq 1.46$) and rectangular samples ($f > 1.46$) of about 10 200 vector spins on a triangular lattice for $k_BT/J = 0.01$.

given in Fig. 1. By this we avoid major effects of shape and size on the graph and obtain a generalized behavior of the spin reorientation in thin films. $\langle S_z \rangle$ and $\langle S_z^2 \rangle$ have been obtained from the simulations. While $\langle S_z^2 \rangle$ is proportional to the total amount of the structure with out-of-plane magnetization orientation, $\langle S_z \rangle$ reveals information about the occupation of the two vertical states of magnetization.

As long as the perpendicular anisotropy E_A is dominant ($f > 1.5$), mesoscopic or even macroscopic domains with vertical magnetization appear. This phase corresponds to region A in Fig. 1 where $\langle S_z^2 \rangle$ is almost one and $\langle S_z \rangle$ is close to 0.4. Here the domain size is larger than the size of the sample (~500 nm). The anisotropy is very strong and within the mesh size the domain walls cannot be described accurately. The energy difference between the single domain state and the configuration with two domains is very small (<0.3%) as the wall energy is underestimated. The energy gain is so small that the sample will remain in a state with two domains if by chance two domains are created during cooling. For $\langle S_z \rangle = 0.4$ a large fraction (70%) of the domains is magnetized in one direction while only 30% are oppositely magnetized. In the interval $1.2 < f < 1.5$ more and more vertically magnetized domains show up and become smaller with decreasing f. For $f \sim 1.4$ a domain structure as shown in Fig. 2 is observed. The domain sizes in the range from 200 to 400 nm and the domain walls are small but broader than in region A. In Fig. 1 this region is denoted by B. Domains of that size have been experimentally observed close to the reorientation transition in annealed Co on Au (111) films [3]. When the domains get smaller the numbers of up and down domains become almost the same and $\langle S_z \rangle$ approaches zero. $\langle S_z^2 \rangle$ decreases to about 0.7 instead of

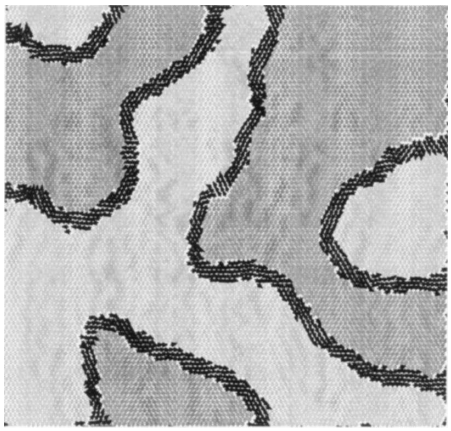

FIG. 2. Top view of the magnetic microstructure in a sample of finite size, i.e., ~500 nm for Co/Au(111) (for more details, see text). Dark and light-grey areas represent spin-up domains $S_z \geq 0.9|S|$ and spin-down domains $S_z \geq -0.9|S|$, respectively. The domains are separated by walls (black). The ratio of anisotropy energy to dipolar energy is $f = 1.4$; $T \sim 5$ K.

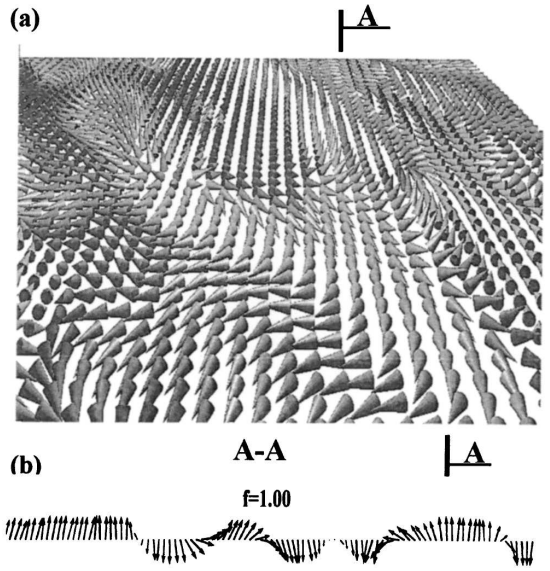

FIG. 3. Twisted spin structure for $f = E_A/E_D = 1$: (a) Perspective view of an enlarged part of the sample. For clarity, only one row out of two and one moment out of two in the row are drawn as cones. (b) Side view of the cross section *A*-*A*. $T \sim 5$ K. Same sample size as in Fig. 2.

being close to 1. The deviation is due to a slight tilting of the magnetization within the domains and a magnetization rotation within the domain walls. In the domains, however, the value of S_z is larger than $0.9|S|$. Further decreasing of f causes $\langle S_z^2 \rangle$ to approach zero continuously. For $\langle S_z^2 \rangle = 0$, all magnetic moments are lying in the film plane (*D* in Fig. 1). The region before that particular f ratio with $\langle S_z \rangle = 0$ and $\langle S_z^2 \rangle \neq 0$ is denoted by *C*. The walls get broader and broader and the wall width becomes comparable to the domain size. At $f = 1$, adjacent walls touch and no vertical domain persists any more. The microstructure consists of moments of spatially varying orientation. The arrangement of the magnetic moments is illustrated in Fig. 3(a) for $f = 1$. A side view is shown in Fig. 3(b). The magnetization rotates in a helicoidal form along all three principal axes. The structure formed is called the twisted phase. At this particular point the magnetic moments are evenly oriented in all directions, which is characteristic of the twisted configuration. This would yield $\langle S_z^2 \rangle = \langle S_y^2 \rangle = \langle S_x^2 \rangle = 1/3$ for a sample of infinite extension. In the simulation (see Fig. 1), however, the obtained value is smaller, which is due to the finite size of the sample. At the edges, the dipolar energy forces the moments into the film plane and parallel to the sample edges which gives a slightly lower occupation of the vertical component. The twisted phase corresponds to the two-dimensional wavelike profile of the Yafet and Gyorgy model [13]. The MC simulation, however, reveals a complete three-dimensional structure as no limitations to two dimensions were made. The twisted configuration is the starting point for the formation of vortices, as will be shown in the following.

Below $f = 0.8$ (region *D* in Fig. 1), both $\langle S_z^2 \rangle$ and $\langle S_z \rangle$ vanish revealing a complete in-plane orientation of the magnetic moments. Minimization of the magnetostatic energy causes vortex structures to form (Fig. 4). Details of this kind of configuration have been discussed in detail [17,19]. Between $f = 1$ and $f = 0.8$, the three-dimensional twisted configuration transforms continuously into the planar vortex structure.

Now we want to focus on some features of the magnetic microstructure within the reorientation transition. The first point is the stability of the twisted configuration. For $f = 1$ we have compared the energies for the twisted structure with several in-plane (vortex, single domain) and out-of-plane (with different periods of up and down domains) configurations. At that particular point of the phase diagram the twisted configuration remains the one with the lowest energy among all considered microstructures. The increase of the total energy per moment with respect to the twisted configuration is $2.5 \times 10^{-2} J$ for the ideal in-plane vortex, $3.5 \times 10^{-2} J$ for the in-plane single domain ferromagnetic state. The excess value varies between $2.58 \times 10^{-1} J$ and $1.7J$ for spin-up and spin-down striped domain configurations with periods from 1/2 to 1/10 of the sample size. These differences are comparable to the dipolar or anisotropy energies of that state. For the twisted phase the spin-spin correlation does not vanish on a large scale, which confirms the low-temperature long-range order of this structure [20].

VOLUME 84, NUMBER 25 PHYSICAL REVIEW LETTERS 19 JUNE 2000

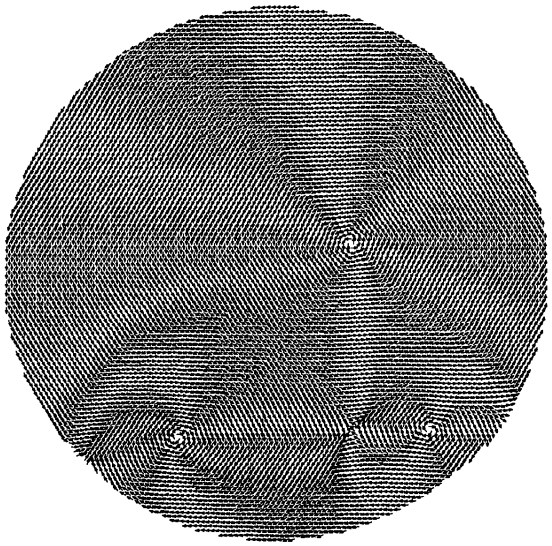

FIG. 4. Planar vortex spin configuration for the ratio $f = E_A/E_D = 0$; $T \sim 5$ K. Same sample size as in Fig. 2.

In conclusion, we have demonstrated that in first-order anisotropy approximation a continuous reorientation transition occurs from an out-of-plane magnetization to a vortex structure. A new phase, the twisted configuration, is found as an intermediate structure between these two states. At the point where the dipolar energy is equal to the perpendicular anisotropy energy the twisted configuration represents the minimum of the free energy.

*Corresponding author.
Email address: vedmeden@physnet.uni-hamburg.de

[1] D.P. Pappas, K.-P. Kämper, and H. Hopster, Phys. Rev. Lett. **64**, 3179 (1990).
[2] R. Allenspach and A. Bischof, Phys. Rev. Lett. **69**, 3385 (1992).
[3] H.P. Oepen, Y.T. Millev, and J. Kirschner, J. Appl. Phys. **81**, 5044 (1997); M. Speckmann, H.P. Oepen, and H. Ibach, Phys. Rev. Lett. **75**, 2035 (1995).
[4] M. Farle, W. Platow, A.N. Anisimov, B. Schulz, and K. Baberschke, J. Magn. Magn. Mater. **165**, 74 (1997).
[5] T. Duden and E. Bauer, MRS Symposia Proceedings No. 475 (Materials Research Society, Pittsburgh, 1997), p. 283.
[6] A. Hucht, A. Moschel, and K.D. Usadel, J. Magn. Magn. Mater. **148**, 32 (1995); A. Hucht and K.D. Usadel, J. Magn. Magn. Mater. **156**, 423 (1996).
[7] A.B. Ryzhenko and E.V. Sinitsyn, Phys. Met. Metallogr. **85**, 130 (1998).
[8] A.B. MacIsaac, J.P. Whitehead, K. De'Bell, and P.H. Poole, Phys. Rev. Lett. **77**, 739 (1996).
[9] A.B. MacIsaac, K. De'Bell, and J.P. Whitehead, Phys. Rev. Lett. **80**, 616 (1998).
[10] S.T. Chui, Phys. Rev. B **50**, 12559 (1994); S.T. Chui, Phys. Rev. Lett. **74**, 3896 (1995); S.T. Chui, J. Magn. Magn. Mater. **140–144**, 2007 (1995).
[11] A. Berger and R.P. Erickson, J. Magn. Magn. Mater. **165**, 70 (1997).
[12] P.J. Jensen and K.H. Bennemann, Phys. Rev. B **52**, 16012 (1995).
[13] Y. Yafet and E.M. Gyorgy, Phys. Rev. B **38**, 9145 (1988).
[14] R. Czech and J. Villain, J. Phys. Condens. Matter **1**, 619 (1989).
[15] D. Pescia and V.L. Pokrovsky, Phys. Rev. Lett. **65**, 2599 (1990); **70**, 1185 (1993); A. Kashuba and V.L. Pokrovsky, Phys. Rev. Lett. **70**, 3155 (1993); J. Castro, Phys. Lett. A **214**, 307 (1996).
[16] Z. Malek and V. Kambersky, Czech. J. Phys. **8**, 416 (1958); J. Kaczer and R. Gemperle, *ibid.* **10**, 505 (1960).
[17] E.Y. Vedmedenko, A. Ghazali, and J.-C.S. Lévy, Phys. Rev. B **59**, 3329 (1999).
[18] E.Y. Vedmedenko, A. Ghazali, and J.-C.S. Lévy, Surf. Sci. **402–404**, 391 (1998).
[19] J. Sasaki and F. Matsubara, J. Phys. Soc. Jpn. **66**, 2138 (1996).
[20] E.Y. Vedmedenko *et al.* (to be published).

JOURNAL OF APPLIED PHYSICS VOLUME 89, NUMBER 11 1 JUNE 2001

Magnetic microstructure of the spin reorientation transition

E. Y. Vedmedenko[a] and H. P. Oepen
Institut für Angewandte Physik, Universität Hamburg, Jungiusstr. 11, D-20355 Hamburg, Germany

J. Kirschner
Max-Planck Institut für Mikrostrukturphysik, Weinberg 2, D-06120 Halle, Germany

The scenario of the magnetization reorientation in second-order perpendicular anisotropy approximation is theoretically studied by means of Monte–Carlo simulations. The microstructure is investigated as a function of the difference between first-order anisotropy and demagnetizing energy $K_{\mathrm{eff}}=K_1-E_D$ and the second-order anisotropy K_2. An influence of the second-order perpendicular anisotropy on the spin reorientation transition is found when K_{eff} vanishes. The broadening and coalescing of domain walls found earlier for $K_2=0$ is prevented by positive K_2. The domain wall width and energy are determined by K_2. For $K_2>0$ the transition via a canted vortex-like structure is found which yields the smooth, continuous connection between the vertical domain structure and the vortex structure with in-plane magnetization. © *2001 American Institute of Physics.*
[DOI: 10.1063/1.1357154]

Experiments on spin reorientation transition in ultrathin films have revealed that the magnetic microstructure determines to a large extent the magnetic behavior of the system.[1–5] Theoretically, the microstructure of the spin reorientation transition (SRT) has been investigated in first-order approximation of perpendicular magnetic anisotropy.[6–8] In recent years, the importance of higher-order anisotropy contributions for SRT in ultrathin magnets has been pointed out.[9–13] Phase diagrams were put forward.[11,12,13] In continuum approximation,[11] the reorientation either through the canted phase or through the phase with coexistence of in-plane and vertical magnetization has been postulated. The evolution of the magnetic microstructure caused by higher-order perpendicular anisotropies, however, was not studied.

In this article, we present a spatially resolved description of the magnetization reorientation in the framework of competing dipolar, first- and second-order perpendicular anisotropy energies for a given exchange coupling. For this purpose, Monte–Carlo (MC) simulations have been performed to find the equilibrium spin configuration at a given temperature. The approach is more general than the models[6,12] as neither a restriction to one dimension is made nor a particular domain structure and wall profile is assumed. The Hamiltonian of the problem includes exchange, dipolar interactions, and perpendicular anisotropy of the first and the second order

$$H=-J\sum_{\langle i,j\rangle}\mathbf{S}_i\cdot\mathbf{S}_j+D\sum_{i,j}\left(\frac{\mathbf{S}_i\cdot\mathbf{S}_j}{r_{ij}^3}-3\frac{(\mathbf{S}_i\cdot\mathbf{r}_{ij})(\mathbf{S}_j\cdot\mathbf{r}_{ij})}{r_{ij}^5}\right)$$
$$+K_1\sum_i \sin^2\theta\pm K_2\sum_i \sin^4\theta, \qquad (1)$$

where J is the exchange coupling constant which is nonzero only for nearest-neighbor spins, D the dipolar coupling parameter and r_{ij} the vector between sites i and j. The coefficients K_1 and K_2 are correspondingly the first- and the second-order anisotropy constants. Via scaling arguments the realistic effective values for the ratio of dipolar to exchange interactions can be achieved by considering spin blocks of appropriate size.[14] For the extended MC computations, we take a monolayer of classical magnetic moments on a regular, triangular lattice of about 10 000 effective magnetic sites. This corresponds to a surface orthogonal to the c axis of a hexagonal-close-packed lattice or to the (111) surface of a face-centered-cubic structure. The magnetic moment is described by a three-dimensional vector S of unit length. The MC procedure is the same as in Ref. 8. To avoid artificial periodic patterns, we use open boundary conditions.

We have studied the magnetic microstructure in the anisotropy space of the system. The latter is represented by the difference between first-order anisotropy and demagnetizing energy $K_{\mathrm{eff}}=K_1-E_D$ and the second-order anisotropy K_2 (Fig. 1). Positive K_{eff} and K_2 favor vertical magnetization while the negative energies impose an in-plane state [see Eq.

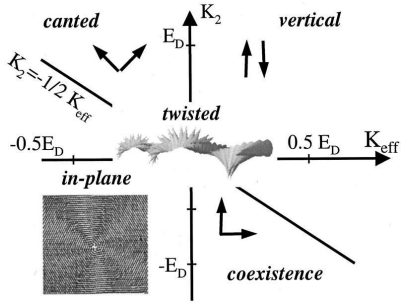

FIG. 1. Micromagnetic phases of a monolayer of classical magnetic moments as a function of the difference between first-order anisotropy and demagnetizing *energy* $K_{\mathrm{eff}}=K_1-E_D$ and the second-order anisotropy K_2. The lines $K_2=-1/2K_{\mathrm{eff}}$ and $K_{\mathrm{eff}}=0$ separate vertical, canted, in-plane, and coexistence phases (see the text). The reorientation transition is characterized by the evolution of magnetic microstructure between vertical and in-plane phases.

[a]Electronic mail: vedmedenko@physnet.uni-hamburg.de

7146 J. Appl. Phys., Vol. 89, No. 11, 1 June 2001 Vedmedenko, Oepen, and Kirschner

(1)]. In the region of ''vertical'' magnetization (Fig. 1), we find the following microstructure. Macroscopic domains with vertical magnetization appear for $K_2 > -1/2K_{\text{eff}}$. The results are the same as found before for $K_2 = 0$.[6,8] In the interval $0.2E_D < K_{\text{eff}} < 0.5E_D$ more and more vertically magnetized domains appear and become smaller with decreasing K_{eff}. The domain walls, on the other hand, become broader with decreasing K_{eff} (similar to Ref. 8). In the close vicinity of $K_{\text{eff}} = 0$ $(0 < K_{\text{eff}} < 0.2E_D)$ the width of the domain walls is determined mainly by K_2. This width is finite in contrast to the first-order anisotropy approximation. The stronger the second-order anisotropy the narrower are the walls. This means that K_2 substitutes K_1 in the definition of wall width and energy.[15] At $K_{\text{eff}} = 0$ and $K_2 = 0$, adjacent walls touch and no vertical domain persists anymore. The microstructure consists of moments of spatially varying orientation. The arrangement of the magnetic moments is illustrated in the central inset of Fig. 1. The magnetization rotates in a helicoidal form along all three principal axes. The structure formed is called the twisted phase. At this particular point, the magnetic moments are evenly oriented in all directions which is characteristic of the twisted configuration.[8]

For negative K_{eff} and $K_2 < -1/2K_{\text{eff}}$ (Fig. 1), the vertical magnetization vanishes revealing a complete in-plane orientation of the magnetic moments. Minimization of the magnetostatic energy causes vortex structures to form as the magnetic anisotropy in-plane is zero. With $K_2 = 0$ the three-dimensional twisted configuration transforms continuously into the planar vortex structure between $K_{\text{eff}} = 0$ and $K_{\text{eff}} = -0.2E_D$. A continuous reorientation transition occurs from an out-of-plane magnetization to a vortex structure via the origin of the anisotropy space.

In the region between $K_{\text{eff}} = 0$ and $K_2 = -1/2K_{\text{eff}}$ (Fig. 1) the negative K_{eff} competes with the positive K_2. The energy minimization causes the canted phase to appear.[11–13] The canting angle depends on the balance between K_{eff} and K_2. As we do not have any anisotropy in the film plane, the moments are canted with respect to the normal but are free to have any orientation in the film plane. On the other hand, the demagnetizing energy in finite-size samples supports the charge-free vortex structure. Due to the cooperation of these energies, a canted vortex structure forms (Fig. 2). The canted vortices transform continuously into their planar counterparts with decreasing K_2 and K_{eff}. A reorientation transition through continuous canting of the magnetization occurs.

In conclusion, an influence of the second-order perpendicular anisotropy on the spin reorientation transition is found when K_{eff} vanishes. The broadening of domain walls,

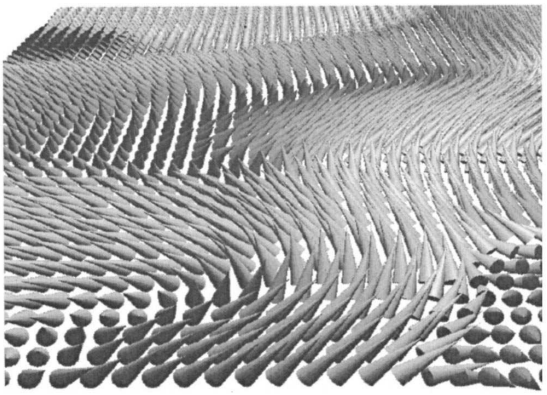

FIG. 2. Canted spin structure for $K_{\text{eff}} = -0.4E_D$, $K_2 = 0.75E_D$, and $k_BT/J = 0.05$. Perspective view of an enlarged part of the sample. For clarity, only one row out of two and one moment out of two in the row are drawn as cones.

found for $K_2 = 0$[6,8] is eliminated by positive K_2. The domain wall width and energy are determined by K_2. For $K_2 > 0$, the transition via a canted vortex-like structure is found which yields the smooth, continuous connection between the vertical domain structure and the vortex structure with in-plane magnetization. The investigation of the magnetic microstructure for negative K_2 is under progress.

[1] D. P. Pappas, K.-P. Kämper, and H. Hopster, Phys. Rev. Lett. **64**, 3179 (1990).
[2] R. Allenspach and A. Bischof, Phys. Rev. Lett. **69**, 3385 (1992).
[3] H. P. Oepen, Y. T. Millev, and J. Kirschner, J. Appl. Phys. **81**, 5044 (1997); M. Speckmann, H. P. Oepen, and H. Ibach, Phys. Rev. Lett. **75**, 2035 (1995).
[4] M. Farle, W. Platow, A. N. Anisimov, B. Schulz, and K. Baberschke, J. Magn. Magn. Mater. **165**, 74 (1997).
[5] T. Duden and E. Bauer, Mater. Res. Soc. Symp. Proc. **475**, 273 (1997).
[6] Y. Yafet and E. M. Gyorgy, Phys. Rev. B **38**, 9145 (1988).
[7] A. B. MacIsaac, K. De'Bell, and J. P. Whitehead, Phys. Rev. Lett. **80**, 616 (1998); K. De'Bell, A. B. Macisaac, I. N. Booth, and J. P. Whitehead, Phys. Rev. B **55**, 15108 (1997).
[8] E. Y. Vedmedenko, H. P. Oepen, A. Ghazali, J.-C. S. Lévy, and J. Kirschner, Phys. Rev. Lett. **84**, 5884 (2000).
[9] C. Chappert and P. Bruno, J. Appl. Phys. **64**, 5736 (1988).
[10] H. Fritsche, J. Kohlhepp, and U. Gradmann, J. Magn. Magn. Mater. **148**, 154 (1995).
[11] Y. Millev and J. Kirschner, Phys. Rev. B **54**, 4137 (1996).
[12] P. J. Jensen and K. H. Bennemann, Phys. Rev. B **52**, 16012 (1995).
[13] K. Baberschke and M. Farle, J. Appl. Phys. **81**, 5038 (1997).
[14] E. Y. Vedmedenko, A. Ghazali, and J.-C. S. Lévy, Phys. Rev. B **59**, 3329 (1999).
[15] H. Träuble, O. Boser, H. Kronmüller, and A. Seger, Phys. Status Solidi **10**, 283 (1965).

PHYSICAL REVIEW B **66,** 214401 (2002)

Microstructure of the spin reorientation transition in second-order approximation of magnetic anisotropy

E. Y. Vedmedenko,[1,2,*] H. P. Oepen,[1] and J. Kirschner[2]
[1]*Institut für Angewandte Physik, Jungiusstr. 11, 20355 Hamburg, Germany*
[2]*Max-Planck-Institut für Mikrostrukturphysik, Weinberg 2, 06120 Halle, Germany*
(Received 13 September 2001; revised manuscript received 16 September 2002; published 4 December 2002)

The microstructure of the magnetization reorientation in second-order perpendicular anisotropy approximation is theoretically studied by means of Monte Carlo simulations. The magnetic structure is investigated as a function of $K_1^{eff}=K_1-E_D$—the difference between first-order anisotropy and demagnetizing energy density—and the second-order anisotropy energy density K_2. For $K_2>0$ the transition from a vertical to in-plane orientation of the magnetization proceeds via the canting of magnetization. The canted phase consists of domains. The domain microstructure establishes the smooth, continuous connection between the vertical domain structure and the vortex structure for in-plane magnetization. For $K_2<0$ a continuous reorientation via a state of coexisting domains with vertical and in-plane magnetization is found. Within this state the size of the vertical and the in-plane domains depends on the ratio of K_1^{eff} and K_2 and changes continuously while the transition proceeds. Both, K_1^{eff} and K_2 determine the width and energy of the domain walls. The broadening and coalescing of domain walls found in first-order anisotropy approximation is prevented by the nonvanishing second-order contribution.

DOI: 10.1103/PhysRevB.66.214401 PACS number(s): 75.70.Kw, 75.70.Ak, 75.60.Ch, 75.40.Mg

Experiments on spin reorientation transition in ultrathin films have revealed that the magnetic microstructure determines to a large extent the magnetic behavior of the system.[1–7] Theoretically, the microstructure of the spin reorientation transition (SRT) has been investigated in first-order approximation of the perpendicular magnetic anisotropy.[8–10] The importance of higher-order anisotropy contributions in the spin reorientation transition has been pointed out,[11–13] and a phenomenological magnetic phase diagram in second-order anisotropy approximation was introduced in 1959.[11] In this approximation only two different kinds of reorientation have been postulated. The reorientation can proceed either through a canting of the magnetization or through a state of coexisting local minima for the in-plane and vertical magnetizations.

The first option is usually quoted as a second-order transition or a continuous reorientation. It is commonly believed that the canted magnetic moments in that, so-called, "cone state" are evenly distributed on the perimeter of the base of a cone with no preferred direction of the in-plane components. A possible microstructure of that phase has not yet been considered.

The second kind of transition proceeds via states of "coexisting phases." The reorientation through this path is often classified as a discontinuous or first-order SRT. The classification is due to the assumptions or the models that are made to explain the flip of the moment. In the state of coexisting phases both orientations of the magnetization have local minima. Hence there is a possibility for the magnetization to be oriented along one direction or the other. Two models of occupation are commonly accepted leading to a discontinuous flip, i.e., the "perfect delay" and the "Maxwell" convention.[14] Initially in both models the magnetization occupies the state of the lowest minimum. In the first model the magnetization is believed to stay in that state until the corresponding minimum of the free energy is completely erased. The second model assumes that the orientation of the magnetization is always determined by the lowest lying energy minimum. A sudden flop appears at the point where both minima have equal depth. Both models have been discussed in the literature for zero temperature. In the common discussion of the discontinuous transition neither the finite temperature nor any microstructure has been taken seriously into account.

This paper focuses on the magnetic microstructure within the spin reorientation, considering anisotropies in the second-order approximation. This is performed by means of computer simulations by a spatially resolved analysis of the magnetization reorientation in the framework of competing dipolar, first- and second-order contributions of the perpendicular anisotropy for a given exchange coupling. For this purpose Monte Carlo (MC) simulations have been performed to find the equilibrium spin configuration at a given temperature. The approach is more general than any previous attempt[8,15] as neither a restriction to one dimension is made nor is a particular domain structure and wall profile assumed. The films are described by an averaged anisotropy. An effect of the layer dependence of the anisotropy on the magnetization orientation is disregarded. The Hamiltonian of the problem includes the exchange, dipolar interactions, and perpendicular anisotropy of the first and second order,

$$\mathcal{H}=-J\sum_{\langle ij\rangle}\mathbf{S}_i\cdot\mathbf{S}_j+\mathbf{D}\sum_{ij}\left(\frac{\mathbf{S}_i\cdot\mathbf{S}_j}{\mathbf{r}_{ij}^3}-3\frac{(\mathbf{S}_i\cdot\mathbf{r}_{ij})(\mathbf{S}_j\cdot\mathbf{r}_{ij})}{\mathbf{r}_{ij}^5}\right)+\mathbf{K}_1\sum_i\sin^2\theta+\mathbf{K}_2\sum_i\sin^4\theta, \quad (1)$$

where J is the exchange coupling constant which is nonzero only for nearest-neighbor spins, D is the dipolar coupling parameter, and $\mathbf{r}_{ij}$ is the vector between sites i and j, θ denotes the angle to the surface normal. The coefficients K_1

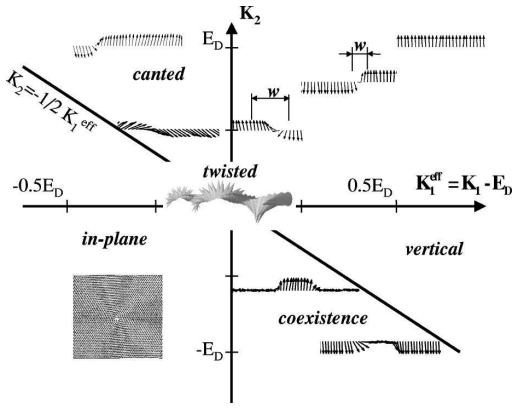

FIG. 1. Micromagnetic phases of a monolayer of classical magnetic moments in the anisotropy space (second-order uniaxial anisotropy approximation) after Ref. 11 and 15. K_1^{eff} is the difference between first-order anisotropy and demagnetizing energy density $K_1^{eff}=K_1-E_D$, and K_2 is the second-order anisotropy density. The lines $K_2=-\frac{1}{2}K_1^{eff}$ and $K_1^{eff}=0$ separate vertical, canted, in-plane, and coexistence phases (see the text). The reorientation transition is characterized by the evolution of magnetic microstructure between vertical and in-plane phases. Please note the different scale on the two axes.

and K_2 are correspondingly the first- and the second-order anisotropy constants. Via scaling the realistic effective values for the ratio of dipolar to exchange interactions can be achieved by considering spin blocks of appropriate size.[16] For the extended MC computations we take a monolayer of classical magnetic moments on a regular, triangular lattice of about 10 000 effective magnetic sites. This corresponds to a surface of an hcp(0001) structure or an fcc(111) structure. The magnetic moment is described by a three-dimensional vector S of unit length. The Monte Carlo procedure is the same as described in previous publications.[10,16] To avoid artificial periodic patterns we use open boundary conditions.

We would like to discuss the results in the appropriate anisotropy space. For the sake of simplicity the diagram is given by K_1^{eff}—the difference between the first-order anisotropy K_1 and the demagnetizing energy density E_D—and the second-order anisotropy energy density K_2 (Fig. 1). Thus K_1^{eff} takes the magnetostatic energy contribution into account. E_D is taken as the magnetostatic energy of an infinite film, i.e., $2\pi M_S^2$. We want, however, to strengthen that in the simulations the magnetostatic energies are calculated exactly while the phase diagram helps to make the presentation of the findings clearer. For positive K_1^{eff} and K_2 a vertical magnetization is favored, while negative values cause an in-plane state [see Eq. (1)].

In the region of "vertical" magnetization (Fig. 1), for positive K_1^{eff} and $K_2>-\frac{1}{2}K_1^{eff}$, we find the following microstructure. For large K_1^{eff} the vertically magnetized domains are very large. With K_1^{eff} decreasing more and more vertically magnetized domains appear, i.e., the domain size shrinks. Simultaneously the domain walls become broader. This result is similar to the findings in first-order anisotropy approximation.[8,10] Domains of that size have been experimentally observed close to the reorientation transition in annealed Co/Au(111) films.[3–5] If K_2 is large the domain size and the domain wall width are mainly determined by K_2. The trend is that the stronger the second-order anisotropy the narrower are domain walls and the larger the domains. In the close vicinity of $K_1^{eff}=0$ with nonvanishing K_2 the wall width is finite in contrast to the infinite sinuslike profile of the magnetization in the first-order anisotropy approximation. This means that K_2 substitutes for K_1 in the definitions of the wall width and energy which were already put forward in a theoretical paper[17] some time ago. For $K_1^{eff}=0$ and $K_2=0$ the microstructure consists of moments of spatially varying orientation. The arrangement of the magnetic moments is illustrated in the central inset of the Fig. 1. The magnetization rotates in a helicoidal form along all three principal axes. The structure that forms is called the twisted phase. At this particular point the magnetic moments are evenly oriented in all directions which is characteristic of the twisted configuration.[10]

For negative K_1^{eff} and $K_2<-\frac{1}{2}K_1^{eff}$ (the "*in-plane*" region in Fig. 1), the vertical magnetization vanishes and a complete in-plane orientation of the magnetic moments exists. To minimize the magnetostatic energy vortex structures form as the magnetic anisotropy in the film plane is set to zero. In the "in-plane" region K_2 has only a minor influence on the microstructure compared to the former situation with $K_1^{eff}>0$.

In the following we will discuss situations where the microstructure is strongly dominated by the interplay of K_1^{eff} and K_2. At first for $K_1^{eff}<0$ and $K_2>-\frac{1}{2}K_1^{eff}$ (inset *canted* in Fig. 1) the negative K_1^{eff} competes with the positive K_2. The energy minimization requires a canting of the magnetization to the film normal.[11–13,15,18] In fact we find a canting of magnetic moments in the simulation (Fig. 1). The vertical component of magnetization changes continuously from 1 at $K_1^{eff}=0$ to zero at $K_2\approx-\frac{1}{2}K_1^{eff}$. In the literature this phase is called the "cone state" as it is generally assumed that the canted magnetic moments are distributed uniformly on a perimeter of the base of a cone. We find, however, that the canted magnetic moments form domains with in-plane components oriented along the principal directions in the lattice plane although the in-plane anisotropy was set to zero. This is at variance with Ref. 19, where no preferred direction of the in-plane components was found. The principal axes of the triangular lattice become the in-plane easy axes of magnetization due to dipolar interaction.[20] We may conclude that in the canted phase the ferromagnetic system is already affected by negligibly small in-plane anisotropies. The in-plane anisotropy causes the appearance of domains with magnetization components along distinct in-plane directions. A top view of the domain structure in the canted regime is presented in Fig. 2. In Fig. 2(a) different shades of gray represent different orientations of the magnetic moments in the film plane. In Fig. 2(b) the different shades of gray give the up and down components of the magnetization. The frequency distribution of the in-plane component of magnetization in the down-canted domains is given in Fig. 2(c). This

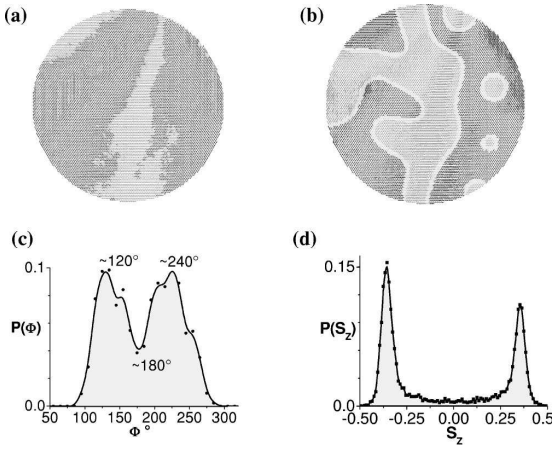

FIG. 2. Top view of the magnetic microstructure in the canted phase for $K_1^{eff}=-0.4E_D$, $K_2=0.65E_D$, and $k_BT/J=0.05$. (a) A top view of the microstructure. In this image the in-plane component of magnetization is coded in gray. Light-gray color gives the part of the sample with an in-plane component pointing mainly to left or right in the plane of drawing (azimuthal orientation of 0° or 180°). The dark-gray color indicates the regions having the in-plane components of magnetization at the angle of 60° or 240° to the horizontal within the plane of drawing. (b) Out-of-plane components of magnetization in the same sample. Dark and light-gray arrows represent canted-down and canted-up domains correspondingly. (c) The frequency distribution of the in-plane component of magnetization. The abscissa gives the angle of the magnetization to the horizontal within the plane of drawing. (d) The frequency distribution of the out-of-plane component of the magnetization. The abscissa gives the component of the magnetization along the normal.

demonstrates that two main in-plane orientations of the magnetization (around 240° and 120°) appear. For the vertical component the frequency histogram [Fig. 2(d)] reveals that the angle to the film normal is identical for all moments in the domains. The angle is equal to the value one obtains from the analytical treatment in case of

$$0 \leqslant -\frac{1}{2}\frac{K_1^{eff}}{K_2} \leqslant 1,$$

i.e.,

$$\theta_M \approx \arcsin\sqrt{-\frac{K_1^{eff}}{K_2}}.$$

The small amount of deviating orientations is found in the domain walls. A three-dimensional representation of the magnetic moments is given in Fig. 3.

We also find that in the canted state the domain size increases with increasing K_2 for a given K_1^{eff}. The width of the domain walls depends on both K_1^{eff} and K_2. The walls become broader with the ratio K_2/K_1^{eff} approaching $-1/2$. The broadening of domain walls causes a slower rotation of magnetization within the wall. As the canting angle is also

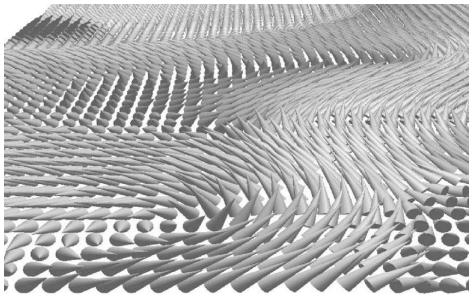

FIG. 3. Perspective view of the canted spin structure for $K_1^{eff}=-0.4E_D$, $K_2=0.65E_D$, and $k_BT/J=0.05$. For clarity only one row out of two and one moment out of two in the row are drawn as cones.

increasing with K_2/K_1^{eff} approaching $-1/2$ the walls fade away and domains and walls become indistinguishable. The latter process transforms the structure into a planar vortex which is the charge-free magnetization pattern. Hence a continuous reorientation transition through the phase of canted domains occurs. In this region K_2 has a strong influence on the microstructure of magnetization.

The third possible path for the reorientation of the magnetization proceeds via the forth quadrant of the anisotropy space ($K_1^{eff}>0, K_2<0$). In this region (inset *coexistence* in Fig. 1) we find that the average vertical component of magnetization goes gradually from almost unity above $K_2=-\frac{1}{2}K_1^{eff}$ to zero at $K_1^{eff}=0$. This continuous change of the magnetization component can lead to the erroneous conclusion that the reorientation proceeds via the canting of magnetization. The canting phase, however, does not exist in this part of the anisotropy space.[11,15] In the simulation we find a magnetic microstructure that consists of domains magnetized perpendicular and in plane, i.e., a coexistence of the two phases [histogram, Fig. 4(b)]. Hence the very existence of two local minima in the free energy[11] leads to the appearance of domains with vertical and in-plane orientations of the magnetization. The borderlines of the phase of coexisting domains in the calculations are in good agreement with the experimentally defined borders of the "gray" zone of SRT in Co/Au(111).[4] The first experimental manifestation of coexisting domains in Co/Au(111)/W(110) was published recently.[7]

In our simulation we find that the magnetic transition is continuous. Our results rule out the models discussed in literature for $T=0$ K, i.e., the "perfect delay" and the "Maxwell" convention.[14] A typical microstructure of a state of coexistence phases and the frequency distribution of the vertical component of magnetization for that state are presented in Fig. 4. The histogram [Fig. 4(b)] demonstrates that the majority of the magnetic moments build an angle of either 0 or $\pm\pi/2$ with the film normal, i.e., vertical and in-plane magnetized domains are formed. The domain walls cause a small amount of moments with deviating orientations. The depths of the local minima of the free energy depend on the values of K_1^{eff} and K_2.[11] In our simulations we find an increase/decrease of the in-plane/vertical domains size with

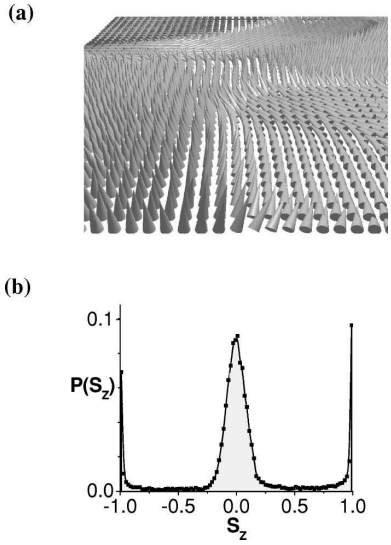

FIG. 4. Microstructure of the state of coexisting phases for $K_1^{eff}=E_D$, $K_2=-0.8E_D$, and $k_BT/J=0.05$. (a) Perspective view of an enlarged part of the sample. For clarity only one row out of two and one moment out of two in the row are drawn as cones. (b) Frequency distribution of the magnetization orientation. The population frequency is given as a function of the magnetization component along the normal. The plot is generated from the simulation shown in *a*.

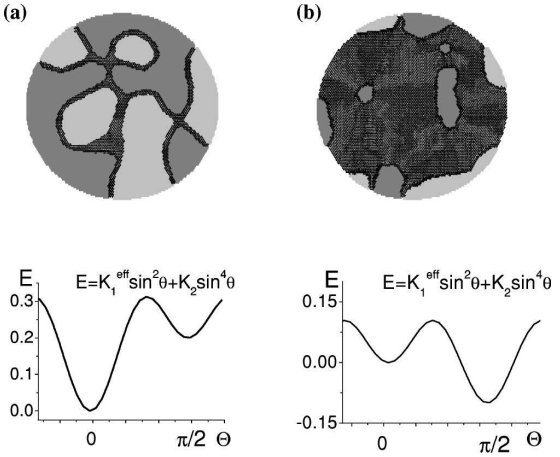

FIG. 5. Top view of the microstructure of the state of coexisting phases and corresponding energetic potential. Dark- and light-gray areas represent spin-up and -down domains correspondingly. Black arrows show the in-plane domains, $k_BT/J=0.05$. In (a) The situation of a deeper minimum for the vertical phase ($K_2=-0.8K_1^{eff}$) is shown. The region between the vertical domains are in-plane magnetized domains. (b) Exhibits the microstructure for the situation that the energy minimum for the in-plane phase is deeper ($K_2=-1.1K_1^{eff}$). Note that vertical domains remain at the edges and in the center of domains with "rotating" in-plane magnetization. They will shrink to the center of vortices found in the in-plane phase.

decreasing K_1^{eff}. This means that the frequencies of population of the two phases of the magnetization depend on the ratio K_1^{eff}/K_2.

A top view of the microstructures of the state of coexisting phases is presented in Fig. 5. Figure 5(a) represents the situation where the vertical magnetization is favored, which leads to the preponderance of vertically magnetized domains. On a first glance the in-plane domains could be misleadingly interpreted as walls. The magnetization profile, however, deviates completely from that of a domain wall. While in the wall a continuous tilting of the magnetization is expected, we find that all spins lie in the film plane except for a thin region, i.e., a wall, along the domain contours [Fig. 5(a)]. The walls are not exactly described in our simulations as the mesh size is too large. If the in-plane orientation is more favorable (deeper minimum) an in-plane vortex-like structure appears [Fig. 5(b)]. The vortex-structure is a consequence of the minimization of the magnetostatic energy as no in-plane anisotropy is assumed. The vertical domains remain in the core of the vortices and at the sample edges. Again a continuous transition between adjacent phases is achieved via the microstructure.

We have explored the population of the different states of the coexisting phases as a function of time and size of the sample. The relative population of the in-plane and vertical magnetizations persists for every relaxation process for a given geometry. The spatial arrangement of the vertical and in-plane domains, however, can change with time, i.e., the number of Monte Carlo steps. This means that snapshots of the equilibrium microstructure can differ during the same Monte Carlo procedure. Different spatial arrangements of domains also depend on the starting conditions for identical relaxation procedures.

The multidomain state of the coexisting phase transforms into a single domain state when the sample size is smaller than the typical domain size for a given K_1^{eff}/K_2. In that situation the ratio of K_1^{eff}/K_2 defines the probability to find the sample in a vertical or an in-plane magnetized single domain state. Domains with an in-plane magnetization do not show a vortex structure in small samples. The monodomain configuration is energetically preferred as the gain in the dipolar energy is lower than the loss in the exchange energy for small structures.[21]

In conclusion, a strong influence of the second-order perpendicular anisotropy on the microstructure of the spin reorientation transition is found. For $K_2>0$ a transition via a canted domain structure is established that yields a smooth, continuous connection between the vertical domain structure and the vortex structure with in-plane magnetization. For $K_2<0$ a continuous reorientation via a state of coexisting vertical and in-plane magnetized domains occurs. The sizes of the vertical and the in-plane domains depend on the ratio of K_1^{eff} and K_2. The spatial arrangement of the domains can change with time, while the frequency distribution of the in-plane and the vertical phases is invariable.

*Corresponding author. Email address: vedmedenko@physnet.uni-hamburg.de

[1]D. P. Pappas, K.-P. Kämper, and H. Hopster, Phys. Rev. Lett. **64**, 3179 (1990).

[2]R. Allenspach and A. Bischof, Phys. Rev. Lett. **69**, 3385 (1992).

[3]H. P. Oepen, Y. T. Millev, and J. Kirschner, J. Appl. Phys. **81**, 5044 (1997).

[4]H. P. Oepen, M. Speckmann, Y. T. Millev, and J. Kirschner, Phys. Rev. B **55**, 2752 (1977).

[5]M. Speckmann, H. P. Oepen, and H. Ibach, Phys. Rev. Lett. **75**, 2035 (1995).

[6]M. Farle, W. Platow, A. N. Anisimov, B. Schulz, and K. Baberschke, J. Magn. Magn. Mater. **165**, 74 (1997).

[7]T. Duden and E. Bauer, in *Magnetic Ultrathin Films, Multilayers and Surfaces*, edited by J. Tobin, D. Chambliss, D. Kubinski, K. Barmak, P. Dederichs, W. de Jonge, T. Katayama, and A. Schuhl, MRS Symposia Proceedings No. 475 (Materials Research Society, Pittsburgh, 1997), p. 273.

[8]Y. Yafet and E. M. Gyorgy, Phys. Rev. B **38**, 9145 (1988).

[9]A. B. MacIsaac, K. De'Bell, and J. P. Whitehead, Phys. Rev. Lett. **80**, 616 (1998); K. De'Bell, A. B. MacIsaac, I. N. Booth, and J. P. Whitehead, Phys. Rev. B **55**, 15 108 (1997).

[10]E. Y. Vedmedenko, H. P. Oepen, A. Ghazali, J.-C.S. Lévy, and J. Kirschner, Phys. Rev. Lett. **84**, 5884 (2000).

[11]H. B. G. Casimir, J. Smit, U. Enz, J. F. Fast, H. P. J. Wijn, E. W. Gorter, A. J. W. Duyvesteyn, J. D. Fast, and J. de Jong, J. Phys. Radium **20**, 360 (1959).

[12]C. Chappert and P. Bruno, J. Appl. Phys. **64**, 5736 (1988).

[13]H. Fritzsche, J. Kohlhepp, and U. Gradmann, J. Magn. Magn. Mater. **148**, 154 (1995).

[14]S. Nieber and H. Kronmüller, Phys. Status Solidi B **165**, 503 (1991).

[15]Y. Millev and J. Kirschner, Phys. Rev. B **54**, 4137 (1996).

[16]E. Y. Vedmedenko, A. Ghazali, and J-C. S. Lévy, Phys. Rev. B **59**, 3329 (1999).

[17]H. Träuble, O. Boser, H. Kronmüller, and A. Seger, Phys. Status Solidi **10**, 283 (1965).

[18]P. J. Jensen and K. H. Bennemann, Phys. Rev. B **52**, 16 012 (1995); K. Baberschke and M. Farle, J. Appl. Phys. **81**, 5038 (1997).

[19]R. Allenspach, J. Magn. Magn. Mater. **129**, 160 (1994).

[20]J.-C. S. Lévy, Phys. Rev. B **63**, 104409 (2001).

[21]W.F. Brown, in *Selected Topics in Solid State Physics*, edited by E. P. Wohlfarth (North-Holland, Amsterdam, 1962), Vol. I.

Available online at www.sciencedirect.com
SCIENCE DIRECT®
ELSEVIER
Journal of Magnetism and Magnetic Materials 256 (2003) 237–242
Journal of magnetism and magnetic materials
www.elsevier.com/locate/jmmm

Size-dependent magnetic properties in nanoplatelets

E.Y. Vedmedenko[a,b,*], H.P. Oepen[a], J. Kirschner[b]

[a] *Institut für Angewandte Physik, Jungiusstrasse 11 Uni-Hamburg, 20355 Hamburg, Germany*
[b] *Max-Planck-Institut für Mikrostrukturphysik, Weinberg 2, 06120 Halle, Germany*

Received 8 April 2002; received in revised form 15 July 2002

Abstract

We demonstrate that the discrete dipolar sums can be separated into two contributions: thickness- and geometry-dependent parts. The geometry-dependent part is analogous to the shape dependence of the continuum approach. The correct normalization of the dipolar energy eliminates the apparent discrepancies of the discrete summation with the experimental results and continuum Maxwell theory. The superposition of the two contributions explains a new phenomenon, i.e. the size-dependent spin reorientation transition and/or enhancement of the effective perpendicular anisotropy.

PACS: 75.70.Ak; 75.75.+a

Keywords: Magnetic nanostructures; Demagnetizing field; Dipole sums; Spin reorientation transition

1. Introduction

Magnetism at small length scales has lately attracted considerable scientific attention (see for review Ref. [1]). Interesting physical phenomena occur in magnets with all three dimensions on the nanometer scale. We call such structures ultra-low dimensional as they have small but finite dimensions. An array of such ultra-low-dimensional magnetic particles can potentially provide a huge gain in information storage density (see for review Ref. [1]). Hence, the understanding of the micromagnetic ordering in ultra-low-dimensional objects is of high significance for the fundamental physics of magnetic materials as well as for technological applications. The increased ratio of boundary to non-boundary atoms in such structures can lead to unusual physical phenomena.

The orientation of magnetization in a magnet is determined by the balance between the exchange energy, the magneto-crystalline anisotropy and the dipolar energy. The strong exchange interaction tends to line up the magnetic moments in the same direction but does not prefer any orientation in space. In ultra-thin platelets with lateral size L and thickness t, magnetization configurations are mainly determined by the competition between the anisotropy and the dipolar energy. In ultra-thin objects the surface(interface) contribution of the magneto-crystalline anisotropy is often responsible for perpendicular magnetization. The angle dependence of the free energy of such an uniaxial system can be written as $E_A =$

*Corresponding author. Institut für Angewandte Physik, Jungiusstrasse 11 Uni-Hamburg, 20355 Hamburg, Germany.
E-mail address: vedmedenko@physnet.uni-hamburg.de (E.Y. Vedmedenko).

0304-8853/03/$ - see front matter
PII: S0304-8853(02)00506-1

$K_1 \sum_i \sin^2\theta$, where K_1 is the first-order anisotropy constant and θ is the angle to the film normal [2].

The dipolar interaction is smallest when all magnetic moments compensate each other and the total magnetic charge is equal to zero. The dipolar energy E_D increases whenever magnetic poles are created in a material or at the boundaries. In magnets with $L \gg t$, E_D prefers an in-plane orientation of the moments. The contribution of E_D to the total anisotropy energy is called shape anisotropy. The shape anisotropy of a finite body (ΔE_D) is described by the demagnetizing tensor N: $\Delta E_D = N \cdot 2\pi M_S^2$, where M_S is the saturation magnetization and $2\pi M_S^2$ the shape anisotropy of the infinite continuous magnet. Neglecting the discrete nature of matter, N can be analytically calculated for uniformly magnetized bodies like ellipsoids.

2. Demagnetizing factors in continuum and discrete approach

Sufficiently large and thin, disk-shaped platelets ($L \gg t$) are usually considered to have the demagnetizing factors of an oblate spheroid (special case of ellipsoid).

The demagnetizing factors of such spheroids are well known [3,4]. For an oblate spheroid the shape anisotropy depends only on the ratio $k = L/t$ and can be represented by an universal curve $\Delta E_D = f(k)$ (Fig. 1). For the sake of simplicity, the shape anisotropy energy is normalized with respect to $2\pi M_S^2$ in Fig. 1. ΔE_D deviates from unity only for structures where L and t are comparable.

In literature [5–9], it is argued that in the limit of a few atomic layers the approximation of the film system by a magnetic continuum fails. The ultra-thin magnet must be regarded as an assembly of discrete magnetic dipoles on a crystalline lattice. For a laterally infinite discrete lattice of magnetic point-dipoles calculations of the dipolar interactions have shown that the dipolar (demagnetizing) field is not uniform as in the continuous ellipsoid approximation. The dipole field changes with depth and depends on the film thickness. The shape anisotropy of every atomic plane for different lattices has been calculated [7–11]. The

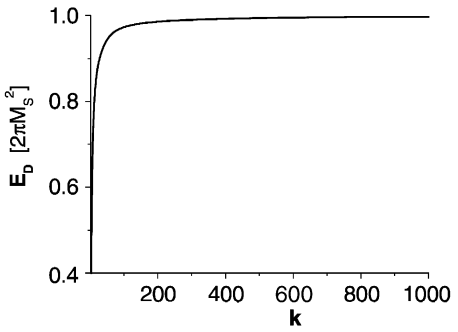

Fig. 1. Analytically calculated magneto-static energy density $\Delta E_D = (N_\perp - N_\parallel) \cdot 2\pi M_S^2$ as a function of the dimensional aspect ratio $k = L/t$ for the oblate spheroid in continuum approximation. The demagnetizing energy is normalized with respect to $2\pi M_S^2$.

average $\Delta\tilde{E}_D$ for a film containing N_{ML} atomic layers has been defined as $\Delta\tilde{E}_D = \sum_{i=1}^{N_{ML}} \Delta E_{D_i}/N_{ML} = c(N_{ML}) \cdot \Delta E_D$. Here $N_{ML} = t/d$ with d for the distance between two successive atomic layers. $\Delta\tilde{E}_D$ of an infinite film can deviate from ΔE_D of a continuum film by more than 10%. The deviation has been attributed to the change of the demagnetizing tensor $\tilde{N} = c(t) \cdot N$. The corrected demagnetizing factors for vertically magnetized infinite ultra-thin films $\tilde{N}_\perp = N_{ZZ}$ are listed in Refs. [7–9]. The in-plane demagnetizing factors are calculated as $\tilde{N}_\parallel = N_{XX} = N_{YY} = (1 - \tilde{N}_\perp)/2$ [8,9] as the sum rule for the demagnetizing field states that the diagonal sum of the demagnetizing tensor is unity inside the sample, i.e. $N_{XX} + N_{YY} + N_{ZZ} = 1$. From data given in Refs. [8,9] one can deduce that the in-plane demagnetizing field (and demagnetizing factors) of an infinite ultra-thin film is no longer zero, which is in disagreement with Maxwell's equations. In Ref. [7] this problem is avoided by assigning the change of the demagnetizing energy as an anisotropy contribution. Nevertheless, the authors claim that the $\tilde{N}$-tensor is thickness dependent. For the simple cubic lattice $\tilde{N}_\parallel$ is even negative as $\tilde{N}_\perp > 1$. All these statements are in contradiction with the continuum theory where the demagnetizing factor is introduced as a geometric parameter. The discrepancies of the continuum theory and the discrete calculations have lead to the opinion that the discrete summa-

tion of point-dipole fields can give questionable values of the demagnetization factors [9]. In this paper, we will show the connection between the classical continuous ellipsoid approach and the discrete dipolar model and solve the apparent controversy.

3. Results

We have investigated the size- and thickness dependence of the shape anisotropy in the ultra-thin platelets numerically. The platelets are disks of finite diameter L and thickness $t = N_{ML} \cdot d$ on a discrete lattice. We have considered the samples with dimensional ratio $k \geqslant 40$, i.e. with $L \gg t$. The shape anisotropy has been calculated as the difference between the dipolar energy of the vertical and the in-plane single domain state: $\Delta E_D = E_D(\perp) - E_D(\parallel)$. The dipolar energy of 1–6 monolayer (ML) thick disks has been calculated by direct lattice summation. Note that the discrete lattice sums are absolutely convergent due to the two-dimensional configuration of dipoles and finite sample dimensions.

The results of the calculations for a triangular lattice with HCP stacking are shown in Fig. 2 as a function of $k = L/t$ for 1–4 ML thick films. The

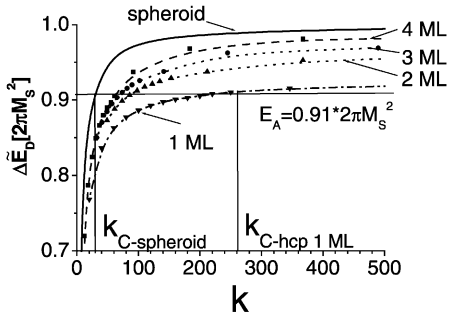

Fig. 2. Numerically calculated demagnetizing energy density $\Delta\tilde{E}_D$ as a function of the dimensional aspect ratio $k = L/d$ for 1–4 ML films on a triangular lattice with HCP stacking. $\Delta\tilde{E}_D$ is normalized with respect to the demagnetizing energy in the continuum limit $2\pi M_S^2$. The straight horizontal line corresponds to the perpendicular magneto-crystalline anisotropy E_A. The dashed vertical lines denote the critical size k_C of the reorientation.

calculated energies are normalized with respect to $2\pi M_S^2$. For other lattices similar results were obtained.

The exact calculation of the dipolar sums deviates strongly from the magneto-static energy obtained from the continuum ellipsoid-ansatz (Fig. 2). The energy depends on thickness and size ($\Delta\tilde{E}_D = f(L,t)$) and not solely on the ratio k. The demagnetizing energy of a platelet of 100×1, for example, is 1.2 times smaller than that of a platelet of 300×3 although $k = 100$ for both and the demagnetization factors should be the same (Fig. 2). $\Delta\tilde{E}_D$ is changing significantly up to high k-ratios ($k \approx 500$) while in the continuous ellipsoid model ΔE_D is almost constant and equal to $2\pi M_S^2$ for large k. With increasing thickness the differences between the individual $\Delta\tilde{E}_D(k,t)$ curves vanish. For $t > 5$ ML $\tilde{E}_D(k,t)$ merges into $\Delta E_D = f(k)$. The function $\Delta\tilde{E}_D = f(k)$ for $t > 5$ ML is close to that of the continuous spheroid. The interpolation of $\Delta\tilde{E}_D = f(L,t)$ to infinite L gives values which are in good agreement with the data given in Refs. [7,8] for infinite expansion. Thus, the rigorous calculation of the dipolar sums reveals that the shape anisotropy is size dependent. The size dependence of $\Delta\tilde{E}_D$ is in disagreement not only with the conventional shape effect $\Delta E_D = f(k)$ but also with the common assumption that the dimensions are only important for $L \approx t$. It has been never considered before that in the range $L \gg t$ the size of the sample can define the magnetic behavior. Next we want to solve the puzzle that emerges from the exact calculation.

4. Discussion

Generally, the total demagnetizing energy ΔE_D is normalized to $2\pi M_S^2 = \text{const}$. The deviation of the total demagnetizing energy from $2\pi M_S^2$ is then attributed to the demagnetizing tensor N: $\Delta E_D = N \cdot 2\pi M_S^2$. Following this assumption, however, means that one has to postulate that N depends not solely on geometry (i.e. ratio k) but also on t, as claimed in Ref. [7], and on L. This assumption is in contradiction to the concept of the demagnetizing factors based on Maxwell theory, as already mentioned.

On the other hand, the dipolar energy of the atoms in the top most layers of the film deviates from that of the bulk atoms. The ratio of boundary to non-boundary atoms in such structures is increased. Consequently, the average demagnetizing energy of an ultra-thin film can deviate from $2\pi M_S^2$ even if N is unchanged. Hence, we may conclude that the discrepancy between the continuous ellipsoid ΔE_D and the discrete $\Delta\tilde{E}_D$ approximation may have different reasons, i.e. $\tilde{N}$ (geometry effect), $(2\tilde{\pi}M_S^2)$ or the combination of both. In Refs. [7–9] it was not possible to distinguish between the three cases as those calculations are related to objects of the same shape, i.e. infinite ultra-thin films ($k=\infty$). In our calculations, the geometry of the sample can be varied from $k=1$ to ∞. Thus, we can analyze all possible situations explicitly.

Taking the assumption $\Delta\tilde{E}_D=\tilde{N}\cdot\Delta E_D$ as in Refs. [7–9] we find $N_{XX}+N_{YY}+N_{ZZ}\neq 1$ for $k<\infty$. This means that the sum rule for the demagnetizing field fails. Assuming $\Delta\tilde{E}_D=(2\tilde{\pi}M_S^2)=X\cdot\Delta E_D$ we find that $(2\tilde{\pi}M_S^2)$ should strongly decrease with decreasing size for a given sample thickness. This outcome makes no sense as for $t=\text{const}$ the dipolar sum differs only for magnetic moments at the sample edge [6] and X should be a constant as long as $L\gg t$. Besides, it is unreasonable to neglect completely the geometry effects. The only remaining explanation of the inequality $\Delta\tilde{E}_D\neq\Delta E_D$ is the superposition of the thickness dependence of the dipolar sums and the geometry effect $\Delta\tilde{E}_D=X\cdot\tilde{N}\cdot\Delta E_D$. In order to decide whether this statement is true or not it is necessary to separate both effects, to compare $\tilde{N},(2\tilde{\pi}M_S^2)$ with $N,2\pi M_S^2$, and to check the sum rule for $\tilde{N}$.

In the ellipsoid approximation $N_\perp=1$ and $N_\parallel=0$ for laterally infinite ultra-thin films of any thickness. Assuming $\tilde{N}_\perp(\infty)=N_\perp(\infty)=1$ the ratio $\Delta\tilde{E}_D(L=\infty)/\Delta E_D(L=\infty)$ is nothing else but the factor X. As discussed before, X is a constant for a constant thickness $t\ll L$. Hence, dividing $\Delta\tilde{E}_D$ by X for finite samples of different L but equal t, the pure geometry effect $\Delta\tilde{E}_D/X=\tilde{N}\cdot\Delta E_D$ can be separated.

The normalized curves $\Delta\tilde{E}_D/X=f(k)$ are given in Fig. 3. The functions are identical for all thickness and represent $\tilde{N}(k)$. Thus, an universal curve is found which one must expect from the classical continuum approximation as shape effect. More than that, the demagnetizing factors extracted from $\tilde{E}_D(\perp)/X=\tilde{N}_\perp\cdot 2\pi M_S^2$ and $\tilde{E}_D(\parallel)/X=\tilde{N}_\parallel\cdot 2\pi M_S^2$ give $\tilde{N}_\perp+2\cdot\tilde{N}_\parallel=1$ for all L and t, i.e. the sum rule for $\tilde{N}$ is confirmed. The demagnetizing factors are reasonable and close to those of the spheroid. The discrete model, however, gives a geometry dependence that saturates at higher k-values compared to the spheroid model. The reason for the minor difference between $\tilde{N}$ and N is the fact that the discrete model describes precisely the geometry which deviates from that of an ideal ellipsoid. Thus, the rigorous calculation of the dipolar sums for finite ultra-thin magnets are in accordance with the continuum approach.

The discrete summation, however, is more precise as it includes the thickness-dependent inhomogeneity of the dipolar energy while in the ellipsoid approximation $2\pi M_S^2$ is introduced as a constant. The values calculated in Refs. [7–9] are not the demagnetizing factors but the coefficients X as those calculations have been performed for infinite extended films with equal N. We have demonstrated that in contrast to the continuum ellipsoid approximation the demagnetizing energy in finite ultra-thin magnets is a two-variable function $\Delta\tilde{E}_D=f(L,t)$. The discrete dipolar sums can be separated into two contributions:

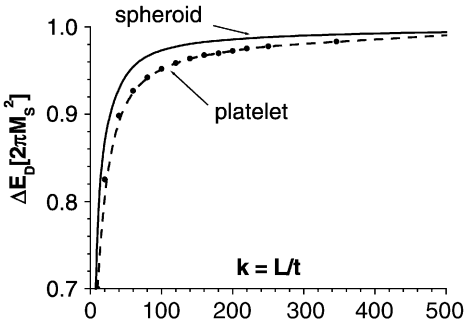

Fig. 3. Comparison of the shape effect of a continuous oblate spheroid and the geometry-dependence extracted from the numerically calculated $\Delta\tilde{E}_D$ of disks with thickness of 1–6 ML on a triangular lattice with the HCP stacking. The demagnetizing energy is normalized with respect to $2\pi M_S^2$.

thickness- and geometry-dependent parts. The geometry-dependent part is analogous to the shape dependence of the continuum approach.

We have checked the geometry effect and t-dependence of the demagnetizing energy for other lattice types. The results are presented in Tables 1 and 2. In Table 1, the demagnetizing factors of the platelets for $40 \leqslant k \leqslant 1000$ are listed. N depends only on the ratio k. The geometry effect does not depend on a lattice type. N is always lower than unity and identical for all lattices. The coefficients X found numerically for $N_{ML} \leqslant 6$ are given in the Table 2. They depend on the type of the lattice and on thickness. The calculated X-values are in good agreement with values of the "reduced anisotropy" given in Ref. [7]. In contrast to N, the coefficients X can be lower or larger than unity. Thus, neither N nor X are size dependent. However, the superposition of the geometry effect and the thickness dependence of $2\pi M_S^2$ leads to the new behavior, i.e. L and t-dependence of the demagnetizing energy. The L,t-dependence is different for different lattices.

Tables 1 and 2 are universal to find the L,t-dependence of the demagnetizing energy for disks with $40 \leqslant k \leqslant 1000$ and thickness $N_{ML} = t/d \leqslant 6$. As example, we find the demagnetizing energy of a platelet of diameter $L = 750a$ and thickness $N_{ML} = 3$ on FCC[1 0 0] lattice. The distance between two subsequent layers is $d = a/\sqrt{2}$ (see Table 2). Hence, $t = N_{ML} \cdot d = 3a/\sqrt{2}$ and $k = L/t \approx 350$. We find the coefficient $X = 0.922$ from Table 2 and $N_\perp - N_\parallel = 0.984$ from Table 1. Thus, the demagnetizing energy $\Delta\tilde{E}_D = (N_\perp - N_\parallel) \cdot X \cdot 2\pi M_S^2 \approx 0.9 \cdot 2\pi M_S^2$, i.e. 10% less than expected from the continuum theory. Coefficients X for platelets with $N_{ML} > 6$ can be derived from Ref. [7]. However, the values of X for thicker films have only minor deviations (<0.2%) from the values given for $N_{ML} = 6$. $X \approx 1$ for $N_{ML} > 6$. The demagnetizing factors for platelets with $k > 1000$ coincide with those of an oblate spheroid, i.e. are also close to unity [3,4]. Hence, the demagnetizing energy merges into $2\pi M_S^2$ for $N_{ML} > 6$ and $k \geqslant 1000$.

Table 1
The demagnetizing factors calculated numerically for ultra-thin disks

$k = L/t$	$N_\parallel$	$N_\perp$	$N_\perp - N_\parallel$
1000	0.001	0.998	0.997
600	0.003	0.995	0.992
350	0.005	0.989	0.984
250	0.007	0.985	0.978
220	0.008	0.983	0.975
200	0.009	0.982	0.973
180	0.010	0.981	0.971
160	0.011	0.979	0.968
140	0.012	0.976	0.964
120	0.014	0.973	0.959
100	0.016	0.968	0.952
80	0.019	0.961	0.942
60	0.024	0.951	0.927
40	0.034	0.932	0.898

5. Size-dependent spin reorientation transition

A manifestation of the above model is the size-dependent spin reorientation transition and the apparent enhancement of the perpendicular

Table 2
The thickness-dependent coefficients X calculated numerically for the ultra-thin platelets with thickness $N_{ML} \leqslant 6$ and the distances d between two successive layers. The apparent differences between the coefficients X for the structures having square lattice at 1 ML (SC(1 0 0), BCC(1 0 0), FCC(1 0 0)) are due to the different lattice constants a

Lattice	$N_{ML} = 1$	$N_{ML} = 2$	$N_{ML} = 3$	$N_{ML} = 4$	$N_{ML} = 5$	$N_{ML} = 6$	$d = \frac{t}{N_{ML}}$
SC[1 0 0]	1.079	1.039	1.026	1.020	1.016	1.013	a
BCC[1 1 0]	0.924	0.962	0.975	0.981	0.985	0.987	$a\sqrt{2/3}$
BCC[1 0 0]	0.564	0.783	0.856	0.892	0.914	0.929	$a/\sqrt{3}$
FCC[1 1 1]	0.931	0.966	0.977	0.983	0.986	0.988	$a/\sqrt{2/3}$
FCC[1 0 0]	0.765	0.883	0.922	0.941	0.953	0.961	$a/\sqrt{2}$
HCP[0 0 0 1]	0.932	0.966	0.976	0.982	0.986	0.988	$a\sqrt{2/3}$

anisotropy in ultra-low-dimensional objects as reported recently [12]. In ultra-thin objects, the surface/interface anisotropy E_A which often favors out-of-plane magnetization is competing with the dipolar energy E_D which prefers an in-plane orientation. The magnetic anisotropy is a local property and constant for a given thickness. Thus, it can be represented by a straight line in Fig. 2. The intersection of $\Delta\tilde{E}_D$ and E_A gives a critical length $L_C = k_C \cdot t$, where the magnetization orientation switches, i.e. reorientation appears. As the dipolar energy is size dependent the reorientation of the magnetization can take place far beyond the L_C range deduced from the ellipsoid approximation (see Fig. 2).This fact has been confirmed by means of Monte-Carlo simulations [12]. Thus, in contradiction to the analytical ellipsoid assumption the spin reorientation transition in finite ultra-thin platelets is size- and lattice dependent.

6. Conclusions

In conclusion, we demonstrate that the dipolar sum can be separated into two contributions: thickness- and geometry-dependent parts. The geometry-dependent demagnetizing factors found by means of the discrete summation are identical to those found in continuum ellipsoid approximation. The demagnetizing energy of the ultra-thin magnets is size- and lattice dependent. The size- and lattice dependence of $\Delta\tilde{E}_D$ is due to the superposition of the geometry effect and the thickness dependence of the demagnetizing energy. The combination of these two effects leads to a new phenomenon: size-dependent spin reorientation transition and/or an enhancement of the effective perpendicular anisotropy E_{eff} with shrinking size. Critical size L_C of the reorientation can be very large compared to the film thickness.

References

[1] H.P. Oepen, J. Kirschner, Curr. Opin. Solid State Mater Sci. 4 (1999) 217.
[2] S. Chickazumi, Physics of magnetism, Wiley, New York, 1964.
[3] J.A. Osborn, Phys. Rev. 67 (1945) 351.
[4] E.C. Stoner, Philos. Mag. 36 (1945) 803.
[5] M. Benson, D.L. Mills, Phys. Rev., 178. 839.
[6] P.H. Christensen, S. Morup, J. Magn. Magn. Mater. 35 (1983) 130.
[7] H.J.G. Draaisma, W.J.M. de Jonge, J. Appl. Phys. 64 (1988) 3610.
[8] B. Heinrich, S.T. Purcell, J.R. Dutcher, K.B. Urquhart, J.F. Cochran, A.S. Arrot, Phys. Rev. B 38 (1988) 12 879.
[9] M. Farle, A. Berghaus, K. Baberschke, Phys. Rev. B 39 (1989) 4838;
M. Farle, Rep. Prog. Phys. 61 (1998) 755,783.
[10] P.J. Jensen, Ann. Phys. (Leipzig) 6 (1997) 317.
[11] A. Hucht, Dissertation, Gerhard-Mercator-Universität-Duisburg, 1999.
[12] E.Y. Vedmedenko, H.P. Oepen, J. Kirschner, Phys. Rev. B, 2002, submitted for publication.

PHYSICAL REVIEW B **67,** 012409 (2003)

Size-dependent spin reorientation transition in nanoplatelets

E. Y. Vedmedenko,[1,2,*] H. P. Oepen,[1] and J. Kirschner[2]
[1]*Institut für Angewandte Physik, Jungiusstrasse 11, 20355 Hamburg, Germany*
[2]*Max-Planck-Institut für Mikrostrukturphysik, Weinberg 2, 06120 Halle, Germany*
(Received 27 March 2002; revised manuscript received 21 October 2002; published 31 January 2003)

We demonstrate that in nanometer-size magnets the superposition of the lattice dependence of the dipolar energy and the truncation of dipolar sums leads to size- and lattice-dependent effective perpendicular anisotropy. As a consequence, the spin reorientation transition in small platelets of identical shape on different lattices occurs at different sizes for identical anisotropy energy. In contrast to conventional results influences of size on the magnetic behavior can be found even at large aspect ratios of size to thickness.

DOI: 10.1103/PhysRevB.67.012409 PACS number(s): 75.70.Ak, 75.75.+a, 75.40.Mg, 75.70.Kw

The patterning of a continuous magnetic film into an array of small magnetic particles can potentially provide a huge gain in information storage density.[1] The increased ratio of boundary to nonboundary atoms in such nanostructures will lead to changes of physical properties. Hence, the understanding of the influence of the finite size on magnetic behavior in small magnets is of high significance for the fundamental physics of magnetic materials as well as for technological applications.

Theoretically, magnetic materials can be successfully treated as an ensemble of classical magnetic moments S, which are regularly arranged on a crystalline lattice.[2] The configuration of these moments, i.e., the magnetization configuration in the absence of an external magnetic field depends on the balance between the exchange energy, the dipolar energy, and the magnetocrystalline anisotropy.[2] The contribution of the dipolar interaction to the anisotropy energy is called demagnetizing energy or shape anisotropy. In thin films the demagnetizing energy is often responsible for in-plane magnetization. It is usually determined as the difference between the dipolar energy of the up- and the in-plane single-domain states $E_D=\xi_{\uparrow}-\xi_{\rightarrow}$. The infinite continuous magnet has $E_D=\text{const}=2\pi M_S^2$, where M_S is the saturation magnetization. M_S is defined as magnetic moment S per atomic volume V, $M_S=S/V$. We take $V=a^3$, with a the nearest-neighbor distance, for a square lattice that corresponds to the simple cubic stacking and $V=a^3/\sqrt{2}$ for a triangular lattice that corresponds to the hcp(0001) or fcc(111) stacking. The magnetocrystalline anisotropy energy (ξ_A) may be responsible for a perpendicular magnetization. ξ_A depends only on the orientation of the moment with respect to the film normal and does not depend on the neighboring moments. For a uniaxial system with a perpendicular easy axis the angle dependence of the free energy can be written as $\xi_A=K_1\Sigma_i \sin^2\theta$, where K_1 is the first-order anisotropy constant and θ is the angle to the film normal.[2] The total anisotropy energy is defined as $E_A=\xi_{A\uparrow}-\xi_{A\rightarrow}$.

The competition between the demagnetizing and the perpendicular magnetic anisotropy energy determines the magnetization direction. If the relative strength between these quantities is reversed a change of the magnetization orientation will occur. One such phenomenon called the spin reorientation transition (SRT) has been studied for infinite ultrathin films[3–6] and observed experimentally. In Co/Au(111) thin films, for example, a transition from vertical (low thickness) to in-plane magnetization (high thickness) was found around 5 monolayers (ML).[7]

Sufficiently large and thin disc-shaped platelets ($L \gg t$) are usually considered to have the demagnetizing energy of an oblate spheroid (a special case of ellipsoid). The shape anisotropy of such spheroids is well known.[8,9] For an oblate spheroid the shape anisotropy depends only on the ratio $k=L/t$ and can be represented by a universal curve $E_D=f(k)$ (Fig. 1). For the sake of simplicity the shape anisotropy energy is normalized with respect to $2\pi M_S^2$ in Fig. 1. E_D deviates from unity only for structures where L and t are comparable.

The magnetic anisotropy is a local property and is constant for a given thickness. Thus, it can be represented by a straight line in Fig. 1. The intersection of E_D and E_A gives a critical length $L_C=k_C\cdot t$ where the magnetization orientation switches, i.e., reorientation appears. Since the shape anisotropy in ellipsoid approximation deviates from unity only at small k the reorientation can happen only at $L\approx t$ (Fig. 1). Thus, it is commonly assumed that the orientation of mag-

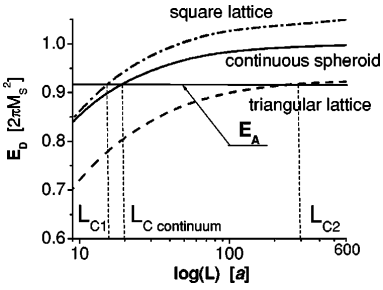

FIG. 1. Comparison of the analytically calculated magnetostatic energy density $E_D=\xi_{D\uparrow}-\xi_{D\rightarrow}$ of a continuum oblate spheroid and the numerically calculated shape anisotropy E_D of a disc on a triangular and a square lattice as a function of the diameter of a spheroid. The demagnetizing energy is normalized with respect to $2\pi M_S^2$. The straight horizontal line corresponds to the perpendicular magnetocrystalline anisotropy E_A. The vertical lines denote the critical sizes L_{C1}, L_{C2}, and $L_{Ccontin}$ of the reorientation for a triangular and square lattice, and an oblate spheroid.

netization in structures with $L \gg t$ depends only on the thickness and the temperature of the sample. If E_A is larger than the demagnetizing energy of the infinite film the reorientation of magnetization will not appear. However, the so-called effective anisotropy $E_{eff}=E_A-E_D$ will increase with shrinking size due to the truncation of the lattice sum.

On the other hand the demagnetizing energy of an infinite monolayer depends on the lattice structure.[3] The superposition of the lattice dependence and the shape dependence of the demagnetizing energy can lead to L_C different from that expected from continuum theory.

This study is devoted to analysis of the validity of the continuum ellipsoid approximation for ultrathin films on a discrete lattice. It turns out that the superposition of two effects—the lattice dependence of the demagnetizing energy and the truncation of dipolar sums—leads to a size- and a lattice-dependent change of the magnetization orientation and an apparent enhancement of the perpendicular magnetic anisotropy.

We have investigated discs of finite diameter L on a discrete lattice by means of Monte Carlo simulations. The Monte-Carlo procedure is the same as in Ref. 6. The Hamiltonian of the problem includes exchange, dipolar interactions, and perpendicular anisotropy: $H=\xi_{ex}+\xi_D+\xi_A$. The ratio of dipolar to exchange constant $D/J \approx 10^{-3}$ used in the calculations corresponds to real materials. Hence, we do not use any rescaling of the sample size. For the chosen D we expect to find a single-domain magnetization configuration in the samples. In that case the exchange energies of an in-plane and an out-of-plane configuration are identical for a collinear solution. First, we prove whether it is also true for the relaxed solution. Then we compare $E_D=f(L)$ and $E_A=f(L)$ for the relaxed and nonrelaxed solutions with the analytical ellipsoid approach.

For the computations we have taken a monolayer of three-dimensional classical magnetic moments S of a unit length on a triangular and a square lattice. We have investigated the low-temperature magnetic microstructure in samples of sizes $100a \leqslant L \leqslant 350a$ where a is the lattice parameter. Thus the lateral size of the platelets has been chosen to be much larger than the thickness t ($L>100t$).

For $D/J=10^{-3}$ and $L \leqslant 300a$ the exchange energy increase with increasing temperature T is size independent and proportional to $M(T)^2$, with $M(T)$ the magnetization. For given L the exchange energy of the relaxed solution $\xi_{ex}(relax)$ is identical for the up- and the in-plane configurations. This means that the deviation from the collinearity is merely due to temperature fluctuations and not to changes in the magnetic microstructure and ξ_{ex} does not influence the value of L_C. For $D/J>10^{-3}$ or for $D/J=10^{-3}$ and $L \gg 300a$ the microstructure, of the relaxed configuration (especially in plane) deviates from that of the thermally agitated monodomain. Different magnetization patterns can be obtained for different sets of D, K_1, and J. $\xi_{ex}(relax)$ is very sensitive to the type of microconfiguration (vortex, flower, leaf, etc.) and should be taken into account.[10,11] However, that investigation goes beyond the scope of the present paper.

We have explored a wide range of the total anisotropy energy. Here we report on the case in which E_A is slightly smaller than $2\pi M_S^2$, i.e., $E_A \approx 0.9 \cdot 2\pi M_S^2$. In the continuous ellipsoid approximation the selected sizes and anisotropy allow any shape effects to become effective at $L_C \approx 30t$. Hence, in all calculated structures with $L>100t$ an in-plane magnetization configuration should be expected. We have not considered different anisotropies for edge atoms since this goes beyond the scope of our paper.

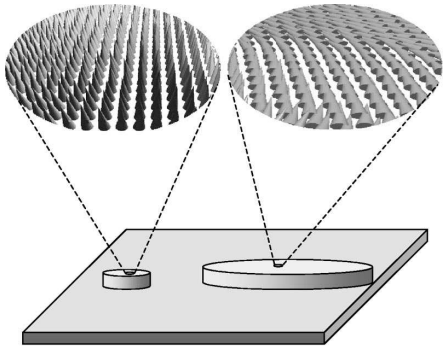

FIG. 2. The low-temperature magnetic microstructure of two discs on a triangular lattice with $L_1=100$ and $L_2=330$; $E_A=0.9(2\pi M_S^2)$. The exchange, the anisotropy, the dipolar energy constants, and the temperature are identical for both samples. For the sake of an appropriate representation a perspective view of an enlarged part of each sample is shown. For clarity, only one spin row out of two is drawn as cones. The smaller island has a vertical single-domain structure. The larger structure presents an in-plane single-domain magnetization configuration.

The results of the simulations for a triangular lattice are presented as magnetization configurations in Fig. 2. Above $L=300a$ the magnetization forms a single domain within the film plane in agreement with the ellipsoid approximation (Fig. 1). Surprisingly, we find a vertical monodomain below $L=230a$. For sizes between $L=230a$ and $L=300a$ intermediate-spin orientations are found. Thus, in contradiction to the analytical approximation the reorientation of the magnetization on a triangular lattice takes place far beyond the k range that is deduced from the ellipsoid approximation. Thus, the results of the Monte Carlo simulations demonstrate that the magnetization direction can change by shrinking the lateral size without changing parameters such as thickness or temperature.

For the square lattice the results are completely different. We find for all structures with $L>100t$ an in-plane single domain in accordance with the ellipsoid approximation. By comparison with the triangular lattice we see that the critical size of the reorientation L_C depends on the type of crystalline lattice.

To find an explanation we have calculated the anisotropy and the demagnetizing energy for a range of sizes L for collinear and relaxed magnetization orientations. In the collinear (nonrelaxed) case the anisotropy cannot be the reason for size-dependent transition since K_1 is a constant in the simulations. The functions $E_D(collinear)(L)$ are presented in Fig. 1. We obtain three different curves $E_D(L)$ for the spheroid and the platelets on the triangular or the square lattice.

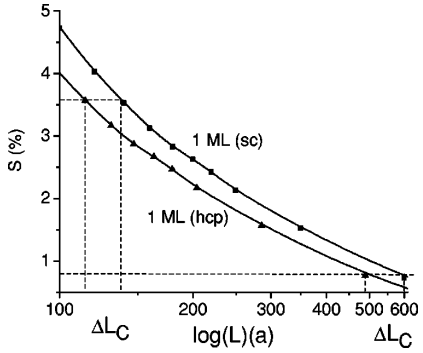

FIG. 3. The deviation of the demagnetizing energy from the saturation value $S=[E_D(L\to\infty)-E_D(L)]/[E_D(L\to\infty)]\cdot 100\%$ for a square and a triangular lattice as a function of size. Dashed vertical lines denote the hypothetical sizes at which S is identical in both lattices. ΔL_C denotes the shift of those sizes in different lattices.

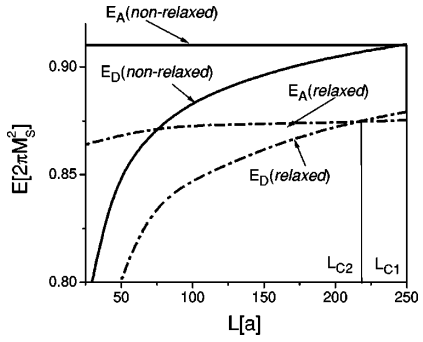

FIG. 4. Comparison of the demagnetizing E_D and the anisotropy E_A energy of a disc on a triangular lattice as a function of size for strictly collinear and relaxed solutions. All energetic parameters J, D, and K_1 are identical in both cases. The energy is normalized with respect to $2\pi M_S^2$, $kT/J=0.05$, and $D/J=10^{-3}$. The vertical lines denote the critical sizes L_{C1} and L_{C2} of the magnetization reorientation for collinear and noncollinear configurations.

For the triangular lattice $E_{D\Delta}(L)$ lies below $2\pi M_S^2$. For the square lattice $E_{D\square}(L)$ is larger than $2\pi M_S^2$ already for $L\approx 60a$. The critical size of the SRT can be derived from the data of Fig. 1 for a given value of E_A. For the case in which reorientation should happen, i.e., $E_A<2\pi M_S^2$ (horizontal line in Fig. 1) we might find one critical size $L_C=L_C(continuum)$ in all platelets. L_C of the triangular lattice, however, varies by more than a factor of 10 from that expected from the ellipsoid approximation and that for the square lattice ($L_{C\Delta}>10\cdot L_{C\square}$). For a different value of E_A one can get different values of critical size but $L_{C\Delta}$ will never equal $L_{C\square}$ as expected from the ellipsoid approximation. The slope of the $E_D(L)$ curves is different for square and triangular lattices. At large sizes the difference is less than 1% (see Fig. 3). However, even such small deviations lead to the remarkable shift of the critical size $\Delta L_C\approx 100a$ for large sizes while $\Delta L_C\approx 25a$ for smaller sizes despite the larger difference in curvature (Fig. 3).

E_D and E_A of the noncollinear solution due to thermal disorder are smaller than those of the collinear case. Figure 4 gives $E_D(L)$ and $E_A(L)$ of platelets on a triangular lattice for strictly collinear and noncollinear solutions. The dipolar and the anisotropy energies exhibit different temperature dependencies which is exactly the reason for the temperature-induced magnetic reorientation in a ferromagnetic monolayer. Interestingly, the anisotropy energy of the relaxed solution is no longer a constant but is size dependent. As a consequence L_C is shifted to smaller sizes comparably to the collinear case.

Thus the critical size of the reorientation is dependent on the lattice type and can be very large comparably to the thickness of the sample. This documents that the size dependence of the reorientation transition in discrete lattices is not due to the shape effect of the continuous model that depends on the ratio of the object dimensions. The effect found for the monolayer example is even more pronounced in thicker samples due to the thickness dependence of the demagnetizing energy of platelets on a discrete lattice.[13]

For $E_{D\Delta}(L\to\infty)<E_A<E_{D\square}(L\to\infty)$ the reorientation of magnetization will appear only in the platelet on a square lattice. The effective perpendicular anisotropy of a triangular lattice will increase due to the shape and the lattice dependence of E_D. This is sometimes erroneously interpreted as the increase of perpendicular magnetic anisotropy with shrinking size, since E_D is commonly assumed to be constant. Experimental findings pointing in this direction have been published recently.[14]

The size and lattice dependencies of the shape anisotropy arise from the inhomogeneity of the dipolar energy in ultrathin ferromagnets.[12] The dipole field in such magnets changes with depth and depends on the film thickness.[12] The dependence of the dipolar energy on the lateral position of an atom is just a consequence of the long-range character of the interaction. As the ratio of boundary to nonboundary atoms increases an influence of the inhomogeneous demagnetizing field on the shape effect appears.

In conclusion, we demonstrate that in laterally confined ultrathin magnetic structures the magnetic behavior depends on the type of the lattice and the sample size. As a consequence, the spin reorientation transition in small platelets of identical shape on different lattices occurs at different sizes for identical anisotropy energy. For $E_D<E_D(L\to\infty)$ the reorientation from an in-plane configuration for larger sizes to an out-of-plane configuration below a critical size L_C occurs. L_C can be very large compared to the film thickness. We have shown that an enhancement of the effective perpendicular anisotropy E_{eff} can occur with shrinking size.

*Corresponding author. Email address: vedmedenko@physnet.uni-hamburg.de

[1] For a review see H.P. Oepen and J. Kirschner, Curr. Opin. Solid State Mater. Sci. **4**, 217 (1999).
[2] S. Chickazumi, *Physics of Magnetism* (Wiley, New York, 1964).
[3] Y. Yafet and E.M. Gyorgy, Phys. Rev. B **38**, 9145 (1988).
[4] P.J. Jensen and K.H. Bennemann, Phys. Rev. B **52**, 16 012 (1995).
[5] A.B. MacIsaac, K. De'Bell, and J.P. Whitehead, Phys. Rev. Lett. **80**, 616 (1998).
[6] E.Y. Vedmedenko, H.P. Oepen, A. Ghazali, J.-C.S. Lévy, and J. Kirschner, Phys. Rev. Lett. **84**, 5884 (2000).
[7] C. Chappert, K.L. Dang, P. Beauvillain, H. Hurdequint, and D. Renard, Phys. Rev. B **34**, 3192 (1986); F.J.A. den Broeder, D. Kuiper, A.P. van de Mosselaar, and W. Howing, Phys. Rev. Lett. **60**, 2769 (1988); J. Pommier, P. Meyer, G. Pénissard, J. Ferré, P. Bruno, and D. Renard, *ibid.* **65**, 2054 (1990); R. Allenspach, M. Stampanoni, and A. Bischof, *ibid.* **65**, 3344 (1990); M. Speckmann, H.P. Oepen, and H. Ibach, *ibid.* **75**, 2035 (1995).
[8] J.A. Osborn, Phys. Rev. **67**, 351 (1945).
[9] E.C. Stoner, Philos. Mag. **36**, 803 (1945).
[10] R.P. Cowburn, D.K. Koltsov, A.O. Adeyeye, M.E. Welland, and D.M. Tricker, Phys. Rev. Lett. **83**, 1042 (1999).
[11] S.P. Li, D. Peyrade, M. Natali, A. Lebib, Y. Chen, U. Ebels, L.D. Buda, and K. Ounadjela, Phys. Rev. Lett. **86**, 1042 (2001).
[12] H.J.G. Draaisma and W.J.M. de Jonge, J. Appl. Phys. **64**, 3610 (1988); B. Heinrich, S.T. Purcell, J.R. Dutcher, K.B. Urquhart, J.F. Cochran, and A.S. Arrot, Phys. Rev. B **38**, 12 879 (1988).
[13] E.Y. Vedmedenko, H.P. Oepen, and J. Kirschner, J. Magn. Magn. Mater. **256**, 237 (2003).
[14] M. Maret, A. Maier, F. Treubel, B. Riedlinger, M. Albrecht, E. Beaurepaire, and G. Schatz, J. Magn. Magn. Mater. **242-245**, 420 (2002).

INSTITUTE OF PHYSICS PUBLISHING JOURNAL OF PHYSICS D: APPLIED PHYSICS
J. Phys. D: Appl. Phys. **36** (2003) 2945–2949 PII: S0022-3727(03)65911-5

Dipolar magnetic anisotropy energy of laterally confined ultrathin ferromagnets: multiplicative separation of discrete and continuum contributions

Y T Millev[1], E Vedmedenko[2] and H P Oepen[2]

[1] Science Division, Lander University, Greenwood, SC 29649, USA
[2] Institut für Angewandte Physik, Universität Hamburg, Jungiusstr. 11, D-20355 Hamburg, Germany

E-mail: ytm@aps.org

Received 8 July 2003
Published 19 November 2003
Online at stacks.iop.org/JPhysD/36/2945

Abstract
Very recent exact summation has indicated that the lateral confinement of ultrathin ferromagnetic islands brings about significant deviations from the usually assumed laterally infinite sample so far as the dipolar magnetic anisotropy is concerned. Here, it is demonstrated that the phenomenological rescaling of the structural detail leads to a fundamental micromagnetic (continuum theory) quantity, namely, the demagnetizing energy for the assumed shape of the mesoscopic island. The derivation of a compact analytical formula for the demagnetization factor of any right circular cylinder has been instrumental for this insight. The effects of discrete geometry (lattice and substrate orientation), thickness, and overall shape of the ultrathin structure are thus distilled into a form which exhibits a great deal of universality.

1. Introduction

The analysis of ferromagnetism in geometrically confined samples poses a number of fundamental questions, even if only ideal lattice arrangements and saturated magnetic configurations are considered. In many continuous theories of the solid state there is the concept, or anticipation, of some sort of dimensional crossover in such a way that the continuum theory goes through as one or more of the dimensions of the system under consideration become microscopic. In micromagnetism, though, dimensional crossover has not been analysed as an option beyond the formal taking of a limit for the demagnetization factors of ellipsoids; this limit in fact implies that the continuum approximation remains a valid one in the process.

Regular arrays of nanosized ferromagnetic particles have been examined more and more intensively from different aspects over the last few years (cf [1, 2] and references therein). Conditions are studied under which the particles are magnetically coupled either by dipolar interactions or by the itinerant electrons of the substrate. In fact, for the usually envisaged applications one needs to ensure that the individual islands would be well decoupled. Thus, the behaviour of a single island becomes of paramount importance. Needless to say, the simplest geometries for the individual islands are best reproducible and, hence, hold the best promise of reproducibility of structural and magnetic properties. Along these lines, one recognizes pretty soon that the magnetic object to be analysed is laterally mesoscopic, while vertically microscopic, when thicknesses of only a few monolayers are involved.

Naturally, two regular shapes come into question when the ultrathin regime is investigated, those of very flat right circular cylinders and of very flat right prisms. So far it has been invariably assumed that the samples can be considered as laterally infinite with microscopic vertical confinement. The breakdown of the validity of a naive continuum approximation has been actually shown by addressing the dipolar magnetic anisotropy energy (MAE) by taking into account the discreteness of the lattice [3–6]. This work held up

some fundamental principles of Maxwell's theory as applied to ferromagnetic bodies [7] and adapted them to account for the non-negligibility of discreteness as a result of the vertical confinement only. Deviations from the three-dimensional continuum approach were found and studied for different numbers of monolayers and for different lattice symmetries. In view of the size of the islands that are typical in nanoarrays, it appears, though, that no due account has been attempted for the finite lateral dimensions. Reference [3] is an exception. There, the dipolar MAE of a small ball has been studied. The results seemed to record the absence of any recognizable systematic behaviour, exhibiting a lot of sensitivity to the local-site detail.

2. Discrete mesoscopic structures

In a very recent study [8], saturated cylindrical islands of discrete dipoles were analysed. Their dipole MAE density was found as the energy density difference between the vertical and the in-plane saturated alignment of magnetic dipoles. Diameter-to-thickness ratios $\kappa = d/t$, ranging from 40 to 1000, with the thickness ranging from 1 to 6 monolayers as well as different crystal arrangements were considered. The limit of infinite lateral dimensions was studied and the results of previous studies [4–6] have been retrieved. A non-trivial step was to take the rather individual curves, corresponding to the different thicknesses at 'fixed' structure, and to normalize them against the value for the dipolar MAE of the laterally infinite sample. It was then established that all these individual curves collapsed to a single, and thus universal, curve whose precise appearance depended on the ratio κ of the cylindrical island only. This universal curve for the rescaled dipolar MAE was compared to the one for the dipolar MAE of an ellipsoid of revolution with the same aspect ratio in the continuum micromagnetic approximation (see, e.g. [9]).

In this paper, we identify precisely the universal curve, depending on $\kappa = d/t$ alone, as the dipolar MAE density for a ferromagnetically saturated right circular cylinder of geometric ratio κ. For the proper understanding of the advance, let us briefly summarize the salient features of [8] from the presently proposed perspective.

Let μ denote the magnitude of the individual microscopic magnetic moment and let μ_0 denote the magnetic permeability of the vacuum. One has to define the saturation magnetization as the density of magnetic moment $M_S = \mu/V_{dip}$, where V_{dip} is the volume per site, i.e. per magnetic moment. This is the definition used, e.g. by Draaisma and de Jonge [4]. The results of [8] boil down to the demonstration of the validity of the following relation for the dipolar MAE density:

$$\begin{aligned}\Delta E_{\text{dipolar}}(\text{discrete}) &\equiv E_{\text{dipolar}}(\perp) - E_{\text{dipolar}}(\parallel)\\ &\equiv E_{\text{axial}}(\text{discrete}) - E_{\text{diam}}(\text{discrete})\\ &= \tilde{N}\left(\frac{d}{t}\right)X(t) = \tilde{N}(\kappa)X(t). \qquad (1)\end{aligned}$$

Here and below, we suppress the dimension-carrying factor of $\frac{1}{2}\mu_0 M_S^2$. That is, the dipolar MAE density is given in natural units to avoid a repetitive occurrence of this factor. The numerical factor X encapsulates the entire lattice-specific contribution and additionally depends on the thickness. It has been tabulated for the most important planes of epitaxial growth and point-group symmetries [8]. At the same time, $\tilde{N}$ has been empirically seen to depend only on κ after the normalization (rescaling) described above: $\tilde{N} = \tilde{N}(\kappa)$. This universality was seen numerically at some 14 distinct points for different values of κ.

3. Magnetic continuum: the core contribution

One of the main points of this paper is to demonstrate that the empirical point-wise dependence $\tilde{N}(\kappa)$ is in fact derivable from exact results for the continuum demagnetizing tensor of a ferromagnetic cylinder with the same aperture as the mesoscopic platelet. Hence, the factor $\tilde{N}(\kappa)$ encompasses that part of the dipolar MAE density which is attributed to the cylindrical shape of the specimen, regardless of the fact that the platelet is by no means a continuous ferromagnet. This observation provides, in our opinion, the identification of universal features as far as they can possibly go in a system which is so distinctly discrete that it is not even micromagnetic in the strict 'continuum' sense of the word. It will also transpire from the following that the formulae for the continuum ferromagnetic cylinder are new in themselves, since they combine an early insight of Brown [7] with independent developments [10, 11], made in a non-micromagnetic context.

Brown has shown that, in continuum micromagnetics, magnetically saturated cylindrical bodies like platelets belong to the very few non-ellipsoidal cases where the demagnetization $\hat{N}$ tensor can be found exactly [7, 12]. Just like an ellipsoid of revolution, the right circular cylinder possesses axial symmetry about its geometrical symmetry axis. Consequently, the in-plane eigenvalues of the tensor $\hat{N}$ are equal. Thus, $N_{\text{axial}} + 2N_{\text{diam}} = 1$. Trivially, $N_{\text{diam}} = (1 - N_{\text{axial}})/2$ and, hence, for the difference of the two eigenvalues that will be needed below one gets in analogy with the case of an ellipsoid of revolution:

$$N_{\text{axial}} - N_{\text{diam}} = \frac{3N_{\text{axial}} - 1}{2}. \qquad (2)$$

In the thin-film context, one would usually denote the axial and diametral eigenvalues as vertical ($\perp$) and in-plane ($\parallel$), respectively, but there is always a certain amount of ambiguity, related also to the implied directions of the saturated magnetization. We want to avoid this ambiguity by appealing directly to the geometrical aspect of the platelets. Thus, we need to find N_{axial} and this is affected in two steps.

First, there is the relation [12] between N_{axial} and the self-inductance L of a finite single-layer circular solenoid ('current-sheet' circular coil) $N_{\text{axial}} = 1 - Y/(\kappa\pi^2)$ with κ defined as above and $Y = L/(N^2 d)$. In the last formula, N is the total number of turns in the coil; this should not be mistaken with the demagnetization factor or its eigenvalues as, in fact, the number of turns does not appear explicitly further in the paper. The existence of such a relation is suggested, generally, by the fact that both the demagnetization factor and the self-inductance coefficient derive from the self-energy of the two magnetization configurations, while, in particular, the geometries of the two distinct physical settings are identical and are finite right circular cylinders. The usefulness of the relation was seen by Brown in that available tables could be used for the quantity Y. A relatively large table of values can be conveniently found in [13], while Brown only provides a few

values for the case of the flat cylinder (cf [7] and the appendix in [12]).

Second, the self-inductance L of a single-layer circular coil has been long known in terms of a closed-form analytical expression, involving the complete elliptic integrals (see [13, 14] and the references cited therein). The elliptic-integral formulation, however, has several shortcomings which, being of more mathematical nature, will be discussed elsewhere. That is why we have found it advantageous to evoke an early result for the required inductance L by Butterworth [10] whose work has more recently been taken up as a starting point for astonishingly simple high-accuracy approximations [11] (see the appendix).

After some straightforward manipulations, one gets the following result:

$$N_{\text{axial}} = 1 + \frac{4}{3\pi}\kappa - \frac{{}_2F_1(5/2,\, 1/2;\, 2;\, \kappa^2/(1+\kappa^2))}{\sqrt{1+\kappa^2}}. \qquad (3)$$

There is no need to tabulate this function, because the hypergeometric Gauss function [15] ${}_2F_1(a, b; c; z)$ is built-in into widely spread computer-algebra packages. In the context of very flat cylinders, as is the case for the ultrathin-film cylindrical platelets, large values of $\kappa \gg 1$ are of interest. Although the relevant inductance results have been available for quite some time now, we believe that the formula provided under equation (3) is the first time that the demagnetization factors of the saturated zero-susceptibility [12, 16] cylinders are reported in terms of the hypergeometric function. It notably covers the whole range of possible values of κ $(0 < \kappa < \infty)$; in particular, one does not need to examine separately the thin (long) as opposed to the flat (short) cylinder.

With the help of the formula found for $N_{\text{axial}}(\kappa)$ above, one can now proceed to find the dipolar MAE density for the saturated continuous cylinder in units of $\frac{1}{2}\mu_0 M_S^2$:

$$\begin{aligned}\Delta E_{\text{dipolar}}^{\text{continuum}}(\kappa) &\equiv E_{\text{axial}}^{\text{continuum}}(\kappa) - E_{\text{diam}}^{\text{continuum}}(\kappa) \\ &= N_{\text{axial}}(\kappa) - N_{\text{diam}}(\kappa) = \frac{3N_{\text{axial}}(\kappa) - 1}{2},\end{aligned} \qquad (4)$$

where the N factors are those for the continuum cylinder. From equation (3), one easily finds that

$$\begin{aligned}\Delta E_{\text{dipolar}}^{\text{continuum}}(\kappa) \equiv S(\kappa) &= 1 + \frac{2}{\pi}k - \frac{3}{2}\frac{1}{\sqrt{1+\kappa^2}} \\ &\times {}_2F_1\left(\frac{5}{2}, \frac{1}{2}; 2; \frac{\kappa^2}{1+\kappa^2}\right).\end{aligned} \qquad (5)$$

The label chosen for the function $S(k)$ is to remind of the fact that it depends solely on the shape of the cylinder. We believe that this is the first time that the dipolar MAE density for the saturated cylinder has been cast in terms of the very flexible hypergeometric function of Gauss.

If the point $\kappa = \infty$ is to be examined more closely, the simple transformation $p = 1/\kappa$ produces immediately the result for both the dipolar energy and the axial demagnetization factor. The graphical representation of equation (5) is given in figure 1 for $k \gg 1$.

Let us now summarize what we have got. We have obtained new closed-form analytic expressions for the demagnetization factors $N_{\text{axial}}(\kappa)$ and $N_{\text{diam}}(\kappa) = [1 - N_{\text{axial}}(\kappa)]/2$

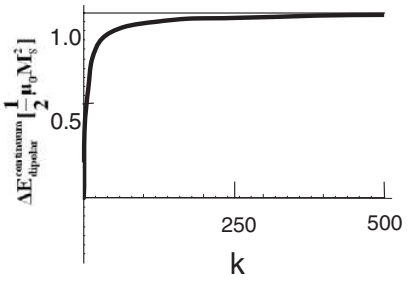

Figure 1. The MAE density $\Delta E_{\text{dipolar}}$ in units of $\frac{1}{2}\mu_0 M_S^2$. This is just the universal function $S(k) = [3N_{\text{axial}} - 1]/2$ with the newly found N_{axial}. In the ultrathin film context, κ is a large number ($\kappa \gg 1$).

for the right circular cylinder in the usual micromagnetic sense, i.e. in the continuum limit of micromagnetism. From this, we have obtained straightforwardly the continuum dipolar MAE density. All these quantities depend solely on the shape of the cylinder as specified by the geometric ratio $\kappa = d/t$. The expressions are superior to the usually quoted formulae in terms of the complete elliptic integrals. The latter are not immediately applicable to flat cylinders, and it is extremely flat cylinders that are of interest in the present context. Additionally, we provide in the appendix a very simple approximation for the demagnetization factors, based on inductance work by Lundin [11], which would allow their computation to an extremely high degree of accuracy on a simple calculator, bypassing altogether the implementation of either sophisticated software or numerical tables.

Now, the results above are valid for all values of the geometric ratio (aperture), i.e. for all shapes of the right cylinder, and not only for platelets. On the other hand, one has the result of [8], given in equation (1) and pertaining to the dipolar MAE density of the realistic discrete model of the platelet. While in both equations (1) and (5) for the discrete and continuum case, respectively, the MAE densities are measured in units of $(\frac{1}{2}\mu_0 M_S^2)$, the discrete MAE density is additionally modified (scaled) by the lattice- and thickness-specific factor X, discussed at the beginning. The very important finding in this paper is that

$$\frac{\Delta E_{\text{dipolar}}(\text{discrete})}{X} = \Delta E_{\text{dipolar}}(\text{continuum}) = S(\kappa) \qquad (6)$$

with $\tilde{N}(\kappa)$ from the numerical procedure of [8] being equal to the rigorous $S(\kappa)$ to within a very high accuracy.

In summary and with the original units restored, it has been established that the following form holds for the discrete mesoscopic system:

$$\Delta E_{\text{dipolar}}(\text{discrete}) = [X(\{\text{lattice}\}, t)][S(\kappa)]\left[\frac{\mu_0 M_S^2}{2}\right]. \qquad (7)$$

Thus, one can recognize immediately both the factorization of the dependences and the quantitative aspects involved, since X and $S(\kappa)$ are now known.

4. Discussion

Altogether, we believe to have shown and discussed in sufficient detail that the exact finite summation of the dipolar

sums for an essentially discrete dipole lattice, encountered in experimental situations in ultrathin ferromagnetic platelets, leads to a clear delineation of the validity of the micromagnetic continuum ansatz and the quantitative way in which the discreteness of the lattice bears on the final result for the MAE density. It should be obvious that the micromagnetic approach is alive and well in this limit of mesoscopic lateral dimensions and microscopic vertical dimensions. In particular, there is no place for ambiguous interpretation of experimental or theoretical findings in such ultrathin, laterally finite systems. Moreover, calculations of the type of those presented for laterally infinite films [4–6] find additional justification as they are reproduced by the present approach in the infinite lateral limit. Alternatively and not less importantly, the same 'factored' interpretation might well be used as a quantification of the extent of validity of the continuous approach. This should not be surprising as micromagnetism is nothing else but an advanced application of Maxwell's theory of continua. No matter from what side (discrete or continuum) one approaches the problem, one should be able to recognize the above results as an extremely useful starting point for further investigation into the electrodynamics of small systems.

As an important step-stone, we have derived a rather useful and compact formula for the demagnetization factors and the dipolar MAE density for a saturated (zero-susceptibility) continuum ferromagnet, possessing the shape of a right circular cylinder of any geometric ratio $\kappa = d/t$. Amazingly simple analytical approximations to the hypergeometric result are also provided in the appendix.

We would like to point out that non-saturated cylindrical ferromagnets have also been intensively considered. These are outside the scope of this study. A most recent and authoritative entrance to this subject is provided by [16] (see also [13] for an earlier discussion).

Acknowledgments

Financial support by SFB 508 is gratefully acknowledged. One of the authors (YM) acknowledges the hospitality of the Institute of Applied Physics (University of Hamburg) and a grant by the Lander Foundation. Warmest thanks are extended to Dan Lee (Jackson Library) for his unfailing expert support.

Appendix

To make this paper self-contained, we proceed to reproduce some important results, most of which are not well known or easily accessible.

In the first place, let us give some more detail from the work of Lundin [11]. An important older reference for work on self-inductance of finite coils is the book of Grover [14] (see also the papers cited in [13]). Below, we shall stick to the notations of Lundin, although in the bulk of the paper we have made the necessary adjustments of notation. Thus, only in the following, a stands for the radius of the finite circular coil whose self-inductance is evaluated, b stands for the axial length of the coil, N is the number of turns. The inductance L is then suitably represented in two equivalent scaled forms with the help of either of the functions $f(x)$ or $g(1/x)$:

$$L = \frac{\mu_0 \pi N^2 a^2}{b} f\left(\frac{2a}{b}\right) = \mu_0 N^2 a g\left(\frac{2b}{a}\right). \tag{A1}$$

The scaling function $f(x)$ is given by $f(x) = f_1(x^2) - 4x/(3\pi)$, while $f_1(y)$ is $f_1(y) = {}_2F_1(\frac{5}{2}, \frac{1}{2}; 2; y/(1+y))/\sqrt{1+y}$.

The function $g(x)$ has a somewhat more complicated appearance and, in fact, contains an infinite series; moreover, the latter series involves a two-position recursion relation for the evaluation of the successive terms.

Two approximate formulae, given by Lundin, may turn out to be useful, especially since they allow the calculations to be carried out with the help of a pocket calculator, if the conditions of their validity are met. Thus, a maximum relative error less than 0.3×10^{-5} is claimed to be guaranteed by the following approximate formulae, covering two different ranges. For $2a \leqslant b$, one has

$$L = \frac{\mu_0 \pi N^2 a^2}{b}\left[F_1\left(\frac{4a^2}{b^2}\right) - \frac{4}{3\pi}\frac{2a}{b}\right], \tag{A2}$$

while for $2a > b$, one gets

$$L = \mu_0 N^2 a\left[\ln\left(\frac{8a}{b} - \frac{1}{2}\right) F_1\left(\frac{b^2}{4a^2}\right) + F_2\left(\frac{b^2}{4a^2}\right)\right], \tag{A3}$$

where for $0 \leqslant x \leqslant 1$ the approximating functions F_1 and F_2 are given by

$$F_1(x) = \frac{1 + 0.383\,901x + 0.017\,108x^2}{1 + 0.258\,952x}, \tag{A4}$$

$$F_2(x) = 0.093\,842x + 0.002\,029x^2 - 0.000\,801x^3. \tag{A5}$$

To obtain the results for the axial demagnetizing factor of the ferromagnetically saturated cylinder as displayed in the bulk of the paper, one needs to follow the prescription of Brown.

For the sake of completeness, here follow the results of Stoner [17] and Osborn [18] for the oblate ellipsoid; N_z is the demagnetizing factor along the shortest axis of the ellipsoid; the aspect ratio $K = a/c$ with $a = b > c$ being the three semi-major axes:

$$N_z^{\text{oblate}}(K) = \frac{K^2}{K^2 - 1}\left[1 - \frac{\arcsin(\sqrt{K^2-1}/K)}{\sqrt{K^2-1}}\right]. \tag{A6}$$

Here, for the very flat oblate ellipsoid as in the platelets considered, there is the simple approximate formula $N_z = 1 - \pi/(2K) + 2/K^2 (K \gg 1)$.

A comparison between the factors for the oblate ellipsoid and the cylinder can be seen in figure 2. For very flat platelets the difference is significant, which is why one should use the now available analytical formulae for the cylinder. Note that this does not imply that the concept of the equivalent ellipsoid is wrong [7, 19]; rather, it implies that for the right circular cylindrical shape it is no longer needed as the exact result has been found in a closed analytical form. Very recently, the equivalent ellipsoid for a disc has actually been exhaustively determined by making use of the new hypergeometric result for the disc's demagnetization factor [20].

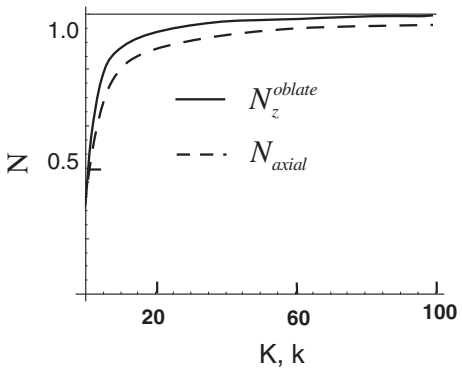

Figure 2. The upper curve is the universal curve for $N_z^{\text{oblate}}(K)$ where K is the aspect ratio: $K = a/c$ ($a = b \geqslant c$ are the semi-major axes of the ellipsoid). For comparison, we present also $N_{\text{axial}}(\kappa)$ for the cylinder, where κ is the diameter-to-thickness ratio.

Finally, we have compared the results we get by the hypergeometric formula with those published in the appendix 3 of [11] and those in table I of [12]. In the first case, the accuracy of Brown's table is better for the long cylinder as compared to the short cylinder (in this latter case, for the four values of κ that are only available there, the accuracy is better than 3.5×10^{-5}). In the second case, all of the digits given in table I there are exact and significant.

References

[1] Oepen H P and Kirschner J 1999 *Curr. Opin. Solid State Mater. Sci.* **4** 217
[2] Bland J A C, Lew W S, Li S P, Lopez-Diaz L, Vaz C A F, Natali M and Chen Y 2002 *J. Phys. D: Appl. Phys.* **35** 2384
[3] Christensen P H and Morup S 1983 *J. Magn. Magn. Mater.* **35** 130
[4] Draaisma H J G and de Jonge W J M 1988 *J. Appl. Phys.* **64** 3610
[5] Heinrich B, Purcell S T, Dutcher J R, Urquhart K B, Cochran J F and Arrott A S 1988 *Phys. Rev.* B **38** 12879
[6] Jensen P J 1997 *Ann. Phys.* (Leipzig) **6** 317
[7] Brown W F Jr 1960 *Am. J. Phys.* **28** 542
[8] Vedmedenko E, Oepen H P and Kirschner J 2002 *J. Magn. Magn. Mater.* **256** 237
[9] Aharoni A 1996 *Introduction to the Theory of Ferromagnetism* (Oxford: Oxford University Press)
[10] Butterworth S 1916 *Phil. Mag. J. Sci.* **31** 276
[11] Lundin R 1985 *Proc. IEEE* **73** 1428
[12] Brown W F Jr 1962 *Magnetostatic Principles in Ferromagnetism* (Amsterdam: North-Holland)
[13] Chen D-X, Brug J A and Goldfarb R B 1991 *IEEE Trans. Magn.* **27** 360
[14] Grover F W 1962 *Inductance Calculations* (New York: Dover) pp 142–7
[15] Oberhettinger F 1966 *Handbook of Mathematical Functions* ed M Abramowitz and I Stegun (New York: Dover) chapter 15
[16] Aharoni A 2002 *Phys. Stat. Sol.* b **229** 1413
[17] Stoner E C 1945 *Phil. Mag.* **36** 803
[18] Osborn J A 1945 *Phys. Rev.* **67** 351
[19] Brown W F Jr and Morrish A H 1957 *Phys. Rev.* **105** 1198
[20] Millev Y T 2002 *Bull. APS* **47** 21

ELSEVIER

Surface Science 402–404 (1998) 391–395

surface science

Magnetic structures of Ising and vector spins monolayers by Monte-Carlo simulations

E.Y. Vedmedenko [a,b], A. Ghazali [a,*], J.-C.S. Lévy [c]

[a] *GPS, UMR 7588 CNRS, Universités Paris 7 et Paris 6, 75251 Paris 5, France*
[b] *Biophysical Department, Medical University of Lugansk, Lugansk, Ukraine*
[c] *LPTMC, Université Paris 7, case 7020, 75251 Paris 5, France*

Received 4 August 1997; accepted for publication 18 September 1997

Abstract

We derive the optimal magnetic structures for monolayers of either square or triangular lattice symmetry with evidence for morphological di erences. The interplay between short-range exchange and long-range dipolar forces leads to quite di erent results for Ising spins and vector spins. For the Ising model, spin domains with parallel stripes, chevron patterns and labyrinths at di erent scales and with thermal disorder are deduced. For the vector model with a weak perpendicular anisotropy, the spins are planar and form a lattice of vortices of both signs. Such a structure remains stable even under a large perpendicular magnetic field, whereas a weak in-plane magnetic field is su cient to obtain a uniform magnetic domain. For a su ciently large perpendicular anisotropy, a mixed structure appears that includes spin vortex areas surrounding spin-up and spin-down areas.

Keywords: Ising spins; Magnetic monolayers; Monte-Carlo simulations; Vector spins

1. Introduction

It has been known for a long time both experimentally and theoretically that magnetism in thin films with a strong perpendicular magnetic anisotropy is associated with a very rich variety of magnetic domain structures with stripes, chevrons, labyrinths and even bubbles [1–4]. The recent experimental preparation of epitaxial magnetic monolayers [5] as well as the development of magnetic–non-magnetic multilayers for the purpose of giant magnetoresistance applications [6] brought a renewed interest in the magnetism of thin films, with evidence for new structures observed with spin-polarized low-energy electron microscopy [7]. This interest is still increasing since accurate methods of Foucault imaging of these domains [8–10] and magnetic force microscopy experiments [11] have now become available and bring more and more results on spin orientations at an almost atomic scale. Recent results suggest that spin reorientations, in the plane or perpendicular to it, occur within a quite small range of temperatures or of layer thicknesses [5].

Using rather large samples for Monte-Carlo

* Corresponding author. Fax: (+33) 1 43 54 28 78; e-mail: ghazali@gps.jussieu.fr

0039-6028/98/$19.00
PII: S0039-6028(97)01067-4

simulations, the present study is devoted to a comparison of magnetic structures of monolayers of Ising spins and vector spins, as well as to the comparison of spin morphologies due to the symmetry of the supporting lattice, together with the influence of external fields. Previous theoretical studies dealt with magnetic structures without any external field [12–16] using smaller samples. The Monte-Carlo (MC) method with the Metropolis algorithm is a good tool for dealing with ground-state and finite temperature spin structures of realistic models, especially in the case of frustration that occurs here at di erent levels because of long-range competing dipolar interactions.

Thus, the present work involves deriving stable structures at di erent temperatures by means of MC relaxations starting from a high-temperature random spin configuration. At a given temperature, several hundred MC steps per spin are achieved. The convergence of the relaxation process towards equilibrium is observed and followed by computing the total energy at each MC step. Several successive temperature steps are introduced in order to lower the temperature rather continuously. At the end of the cooling down process, the total energy is just fluctuating around its mean equilibrium value. Our samples are square and triangular lattices with a size ranging from 10 000 to 40 000 spins with free boundary conditions. Since the final spin configurations may depend on the sample shape, disks, squares and rectangles have been used. The Hamiltonian includes local ferromagnetic exchange, long range dipolar interactions, uniaxial anisotropy and external field.

2. Ising spins

With a monolayer lattice in the xy-plane of Ising spins $S_i = \pm 1$ in the z-direction, the total Hamiltonian reads

$$H = -\sum_{\langle ij \rangle} JS_i.S_j + D\sum_{ij} (S_i.S_j/r_{ij}^3) - \sum_i H_z.S_i \quad (1)$$

where J is the nearest neighbour ferromagnetic exchange parameter. D is the dipolar coupling parameter. The first sum is restricted to the nearest neighbours, whereas the second is running over all couples of spins i and j with distance r_{ij}. The external field H_z is perpendicular to the plane. This is useful to introduce the dimensionless parameter $K = D/(Ja^3)$ where a is the lattice parameter. Thus, it is possible to consider the cases with di erent ratios D/J as issued from the single case with a given K value but with di erent scaling parameters a. With these remarks in hand, the increase of the dipolar coupling D with a constant exchange must be considered as an increase in the e ective lattice parameter a. Thus, large values of D must be considered as being realized for large samples, and structural results become universal, but with size-dependent e ects. Fig. 1 shows the low-temperature MC relaxed structures of portions of

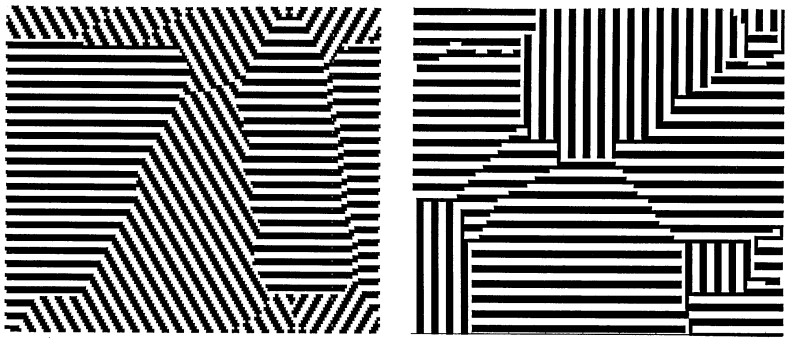

Fig. 1. Portions of 100×100 Ising spins at low temperature on square (right) and triangular (left) lattices. Black stripes, up spins; white stripes, down spins. $D/J = 0.75$ (right), $D/J = 1$ (left); $kT/J = 0.1$.

100×100 spin samples, for square and triangular lattices, without an external field. A comparison between the two spin configurations gives evidence of an e ective in-plane anisotropy linked with the underlying discrete lattice. At a local size, with a and thus D being small, an organization with parallel stripes of alternate spins occurs, whereas at larger sizes, with a and thus D being larger, stripes become organized with chevrons and later labyrinthine patterns, as already observed in materials with uniaxial anisotropy [1–4,17]. The universal character of these patterns at di erent scales is confirmed by these general observations. Fig. 2 gives the temperature e ect at a very large scale (200×200), in the case of a pure dipolar interaction: $J=0$. Note the complex labyrinthine structure at low temperature with zigzags, ramifications, loops and endpoints. As the temperature increases, the walls roughen and shorten. Fig. 3 summarizes the results obtained for structures with an external field, with evidence of hysteresis and the appearance of bubble domains. The progressive change from stripes to bubbles is initiated by stripe indentations that transform into closed bubbles when there are su cient numbers of them. This process of nucleation of independent indentations has not been observed experimentally and requires a large amount of local energy, whereas the process of bubble shrinkage and wall motion needs less energy as we have seen in the total energy analysis. This might explain why indentations have a short lifetime and are di cult to observe, whereas wall motions have a long lifetime and are easily observed.

3. Vector spins

With a monolayer lattice in the xy-plane of vector spins $\boldsymbol{S}_i$, the total Hamiltonian reads

$$H = -\sum_{\langle ij \rangle} J\boldsymbol{S}_{\mathrm{i}}.\boldsymbol{S}_{\mathrm{j}} + D\sum_{ij}\left(\frac{\boldsymbol{S}_{\mathrm{i}}.\boldsymbol{S}_{\mathrm{j}}}{r_{ij}^3} - 3\,\frac{(\boldsymbol{S}_{\mathrm{i}}.\boldsymbol{r}_{\mathrm{ij}})(\boldsymbol{S}_{\mathrm{j}}.\boldsymbol{r}_{\mathrm{ij}})}{r_{ij}^5}\right) - A\sum_i S_{iz}^2 - \sum_i \boldsymbol{H}.\boldsymbol{S}_{\mathrm{i}} \quad (2)$$

where J is the exchange parameter, which is non-zero only for the nearest neighbour pairs. D is the dipolar coupling parameter, and the relevant sum is running over all spin pairs i and j defining the vector $\boldsymbol{r}_{ij}$. The parameter A measures the uniaxial anisotropy along the z-axis, and the external field $\boldsymbol{H}$ can be in any direction. The previous reasoning about the universality of this system remains valid here with the new dimensionless parameter A/J for the reduced anisotropy. Thus a long-range dipolar e ect occurs when looking at a large scale, i.e. for a large value of the lattice parameter a. First, without an external field and without anisotropy, the results for the low-temperature structures obtained for di erent values of the dipolar parameter D, i.e. at di erent scales, show that all spins lie in the plane. This is in agreement with a known result from magnetostatics on the demagnetizing field in thin plates. These structures exhibit many vortices of both signs as seen in Figs. 4 and 4 where regions of strong vorticity are also highlighted and indicate both the vortex cores and the walls between uniform domains. These walls connect vortices of the same sign, just like von Kármán

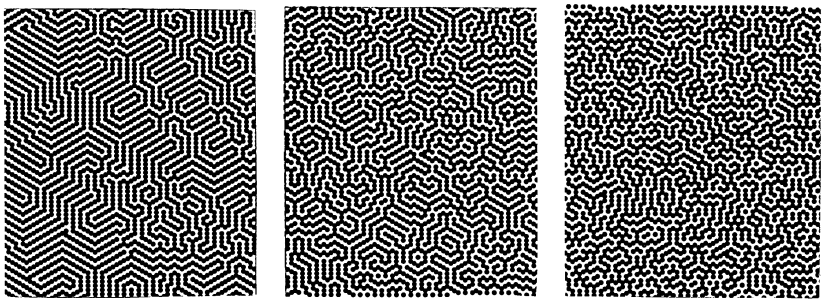

Fig. 2. Pure dipolar coupling: portion of 200×200 Ising spins on a triangular lattice with labyrinthine patterns of up (black) and down (white) spin domains. From left to right: $kT/D=0.05$, 0.2 and 0.4.

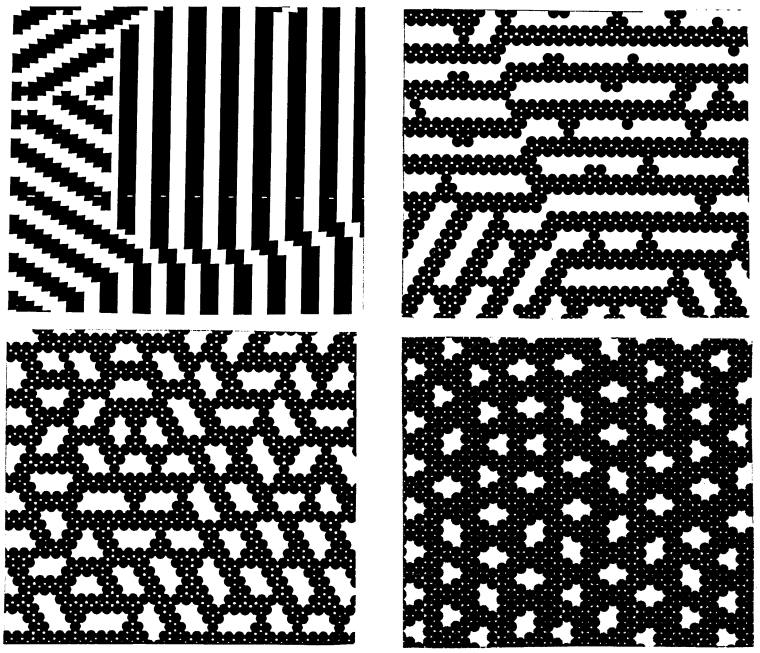

Fig. 3. Magnetic field e ects: portion of 100×100 Ising spins on a triangular lattice. $D/J=1$, $kT/J=0.05$. Clockwise: $H/J=0$, 1, 2.5 (after saturation) and 1.

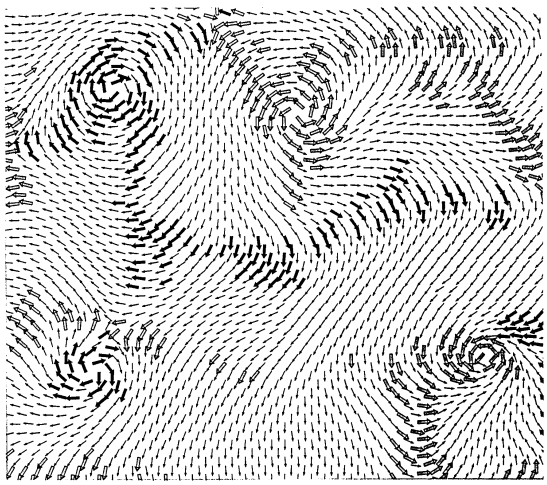

Fig. 4. Vector spins: portion of 10192 spins on a triangular lattice. $D/J=0.1$, $A=0$, $kT/J=0.01$. Sample = disk. Arrows are spins. Thick black (grey) arrows highlight the (counter) clockwise vortex cores with the relevant walls between spin domains.

vortex streets in turbulent flows (see, for example, Ref. [18]). The final structure with vortices, domains and walls can be compared to the classical cross-tie walls generally reported in thin films [19]. The application of a weak in-plane external field is enough to erase all vortices in the sample leading to a uniform domain up to boundary e ects, whereas a very high perpendicular field, about 30 times higher than the in-plane one, is required to make the sample magnetically uniform. Finally, for a su ciently large perpendicular anisotropy, a mixed structure appears that includes almost planar spin vortex areas surrounding nearly perpendicular spin-up and spin-down areas with a marked chirality. This is illustrated in Fig. 5. Let us stress that the spin orientation transition between quasi-planar spins and Ising-like spins occurs in a narrow region of anisotropy values at a su ciently low temperature when thermal excitations are weak.

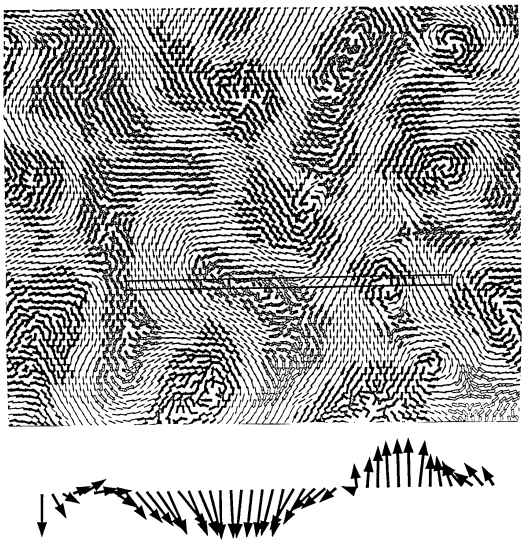

Fig. 5. Vector spins: spin orientation e ects. Portion of a disk of 10192 spins on a triangular lattice. $D/J=0.1$, $A/J=0.9$, $kT/J=0.01$. Thin arrows are quasi-planar spins. Thick black (grey) arrows highlight the spins standing out above (below) the plane. Bottom: spin profile in the vertical xz-plane along the path drawn in the figure.

Acknowledgements

Elena Y. Vedmenko acknowledges a postdoctoral grant from the French Ministry of Education (MENESR). Part of this work was done within the framework of contract CHRX-CT93-0320 of the European Economic Community.

References

[1] J. Kaczer, R. Gemperle, Czech. J. Phys. B 10 (1960) 614.
[2] C. Kooy, U. Enz, Philips Res. Rep. 15 (1960) 7.
[3] J.A. Cape, G.W. Lehman, J. Appl. Phys. 42 (1971) 5732.
[4] P. Molho, J. Gouzerh, J.L. Porteseil, J.C.S. Lévy, J. Appl. Phys. 61 (1987) 4188.
[5] R. Allenspach, J. Magn. Magn. Mat. 129 (1994) 160.
[6] P.M. Lévy, Solid State Phys. 47 (1994) 367.
[7] T. Duden, E. Bauer, Phys. Rev. Lett. 77 (1996) 2308.
[8] J.N. Chapman, J. Phys. D 17 (1984) 623.
[9] A.B. Johnston, J.N. Chapman, B. Khamsehpour, C.D.W. Wilkinson, J. Phys. D 29 (1996) 1419.
[10] A.C. Daykin, J.P. Jakubovics, J. Appl. Phys. 80 (1996) 3408.
[11] B. Raquet, M.D. Ortega, A. Sdaq, R. Mamy, M. Goiran, A.R. Fert, C. Armand, J.C. Ousset, J. Magn. Magn. Mat. 156 (1996) 197.
[12] S.T. Chui, Phys. Rev. B 50 (1994) 12559.
[13] S.T. Chui, Phys. Rev. Lett. 74 (1995) 3896.
[14] A.B. MacIsaac, J.P. Whitehead, K. De'Bell, P.H. Poole, Phys. Rev. Lett. 77 (1996) 739.
[15] A. Hucht, A. Moschel, K.D. Usadel, J. Magn. Magn. Mat. 148 (1995) 32.
[16] A. Hucht, K.D. Usadel, J. Magn. Magn. Mat. 156 (1996) 423.
[17] M. Seul, L.R. Molnar, L. O'Gorman, R. Wolfe, Science 254 (1991) 1616.
[18] Milton Van Dyke, An Album of Fluid Motion, The Parabolic Press, Stanford, CA, 1982.
[19] E.E. Huber, D.O. Smith, J.B. Goodenough, J. Appl. Phys. 29 (1958) 294.

Vol. **97** (2000) *ACTA PHYSICA POLONICA A* No. 1(2)

Proceedings of the European Conference "Physics of Magnetism 99", Poznań 1999

MAGNETIC STRUCTURES IN ULTRATHIN FILMS AND NANOSTRUCTURES : SIMULATION

J.-C.S. Lévy[a], A. Ghazali[b], E.Yu. Vedmedenko[c]

[a]LPTMC, case 7020, Université Paris 7, 75251 Paris 5, France
[b]GPS, UMR-7588 CNRS, Universités Paris 7 et Paris 6, 75251 Paris 5, France
[c]MPI für Mikrostrukturphysik, 06120 Halle, Germany
levy@ccr.jussieu.fr, ghazali@gps.jussieu.fr, vedmeden@mpi-halle.mpg.de

(Version date: April 30, 1999)

In magnetic ultrathin films and dots, competing exchange, anisotropy and dipolar couplings lead to a large variety of magnetic structures. These structures are obtained by means of Monte Carlo simulations. Three classes of magnetic structures are obtained according to anistropy-to-dipolar energy ratio: Ising striped structures, XY-spin structures with vortices and twisted spin phases at the spin reorientation transition. Domain wall nucleation and motion at the coercive field are also accessible.

PACS numbers: 75.70.Ak, 75.50.Tt, 75.60.Ch, 75.40.Mg

Ultrathin films of a single atomic monolayer or of a few monolayers deposited over non magnetic materials are now available for magnetic experiments [1]. Similarly nanostructures such as ultrafine magnetic particles have been obtained by different methods such as electrochemistry, or soft chemistry route such as the polyol process [2], or by nanolithography [3], or by aggregated atomic beams. These new materials are interesting both by their original properties and by the high density of independent objects they generate.

1. Magnetic interactions, model and simulation

The magnetic structures of these nanomaterials result from the competition between exchange interaction J with nearest spins, magnetocrystalline anisotropy, long-range dipolar coupling D between spins and Zeeman interaction with the external magnetic field $\mathbf{H}$. Here we assume a uniaxial first-order anisotropy K. The Hamiltonian with vector spins $\mathbf{S}_i$ reads:

$$H = -J \sum_{<ij>} \mathbf{S}_i \cdot \mathbf{S}_j - K \sum_i S_{i,z}^2 + D \sum_{ij} \left(\frac{\mathbf{S}_i \cdot \mathbf{S}_j}{r_{ij}^3} - 3 \frac{(\mathbf{S}_i \cdot \mathbf{r}_{ij})(\mathbf{S}_j \cdot \mathbf{r}_{ij})}{r_{ij}^5} \right) - \mathbf{H} \cdot \sum_i \mathbf{S}_i \quad (1)$$

These magnetic structures are expected to be complex due to the long-range dipolar interactions which yield antagonistic forces on the spins at all length scales.

In addition, the resulting magnetic patterns depend on the shape of the sample. Therefore, to account for such structures, all dipolar couplings between spins in the sample should be included.

The aim of this paper is to classify these magnetic structures in a wide range of parameter values by analyzing the various magnetic orders obtained from Monte Carlo (MC) simulations after annealing and slow cooling. Simple scaling arguments based on the values of the dimensionless ratio $R = D/Ja^3$ with the lattice parameter a, together with a consistent rescaling of the other Hamiltonian coupling parameters, allow to consider spin blocks of various sizes instead of single spins [4]. This is a very useful procedure since it permits to account for large sample patterns with a relatively limited number of effective spins.

Extensive Monte-Carlo simulations have been performed. Starting at a high enough temperature, different temperatures are explored in a slow cooling process in order to deduce the low temperature configurations. This is a very long process because of the intrinsic all range frustration due to dipolar couplings.

A useful criterion for selecting low temperature configurations is the energy comparison between relaxed MC configurations and hypothetic configurations suggested from symmetry or from simple considerations [4]. Such a control strongly helps in rationalizing the choice of optimal configurations, given the high degree of approximate degeneracy which makes the exact ground state very difficult to single out. Since the spin patterns are size- and shape-dependent, free boundary conditions are used. This also precludes any periodicity artificially induced by periodic boundary conditions [4].

Demagnetizing fields are due to dipolar interactions and are well known to be shape-dependent. Thus different sample shapes have been considered in order to settle this classification on a clear basis. For ultrathin films, square, rectangle or disk-shaped samples have been considered with two lattice types: the triangular lattice represents a (111)-oriented fcc lattice surface or a surface normal to the hcp-lattice c-axis and the square lattice represents a (001)-oriented fcc-lattice surface. For dots, hcp-lattice spheres of different sizes have been used. In our MC simulations, most samples contain about 10000 vector spins. The maximum size studied is about 50000 vector spins.

For all samples, three general classes of magnetic structures must be distinguished: i) With a very strong anisotropy, perpendicular to the film or along the dot c-axis, an Ising-like spin structure is formed in which the magnetization is parallel to this direction; ii) with a weak anisotropy energy as compared to dipolar energy, a planar (XY) vector spin structure appears at low temperaure in the film plane or in the plane normal to the c-axis of the dot; iii) in the intermediate case where the perpendicular anisotropy energy balances the dipolar energy, spins are evenly oriented in all directions. At this point, a spin reorientation transition occurs. In the following, we describe these different spin patterns in some detail.

2. Ultrathin films

For very thin films without external field, the low temperature structures are: i) With a strong perpendicular anisotropy (Ising-type spins), magnetic do-

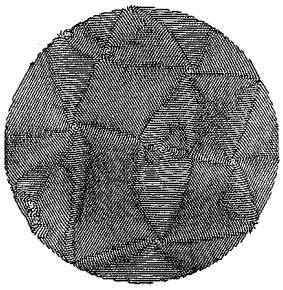

Fig. 1. Low-temperature in-plane spin pattern with vortices for a disk-shaped sample of 10 192 spins on a triangular lattice. $D/Ja^3 = 1$

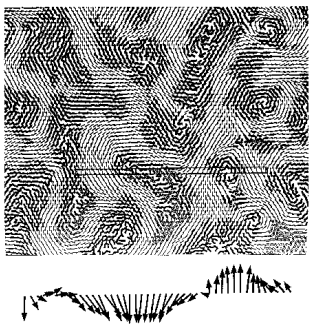

Fig. 2. Spin reorientation effects. Portion of a disk of 10 192 spins on a triangular lattice. Thin arrows are nearly in-plane spins. Thick arrows are out-of-plane spins, either above (black) or below (grey). Bottom: spin profile in the vertical plane along the indicated segment. $D/Ja^3 = 0.1$ and $K/J = 0.9$.

mains with up-spin and down-spin alternate stripes of equal width are arranged in chevry patterns. On a large scale, these domains define mazes [6]. Similar structures are already well known to occur for thicker samples [5]. ii) With a weak anisotropy, the low temperature configurations consist in planar (XY-type) spins with clockwise and anti-clockwise vortices [4]. These vortices are rather uniformly distributed over the sample as seen in Fig. 1. This new feature is not yet fully observed in ultrathin films, presumably because of the intrinsic difficulty to observe in-plane vector spin patterns at the nanometre scale. However, similar features were experimentally observed in magnetic-non magnetic multilayers by Lorentz microscopy [7]. iii) With an intermediate uniaxial anisotropy, i.e., around the reorientation transition, a modulated twisted spin configuration takes place and includes almost in-plane spin domains surrounding patches of out-of-plane spins. The latters are arranged as twisted spin bunches as seen in Fig. 2. Experimentally, the spin reorientation transition is now well known to occur as a function of various parameters, such as layer thickness, temperature, etc. [1], but the spin reorientation just starts to be observed at the nanometer scale [8] with results similar to those predicted here [6].

The magnetic structures described above are very sensitive to the action of

an external field. i) In the Ising case, stripes with spins parallel to the field start to widen out, with local indentations, at the expense of antiparallel spin stripes. As the external field is increased further, magnetic bubble domains appear until the magnetic saturation is reached. The bubbles remain in a metastable state after the field has been removed, just as in the case of thicker samples [5]. ii) With vector spins, when an in-plane external field is increased up to the coercive value, 360° walls nucleate at the sample edge and move through the sample as solitons which can be followed step by step during the MC calculations. This nucleation-propagation process is a quite general problem [9]. The study of the dynamics of this complex motion is in progress.

3. Magnetic dots

Let us now turn to the magnetic dots. Without external field, the low temperature structures are: i) For a large uniaxial anisotropy (Ising spins), the partition between up-spin and down-spin domains has a rather complex geometry. ii) For a small anisotropy, XY-spin structures develop in the densest planes with vortices. The core-vortex line is a skew line crossing the sample. iii) With a moderate anisotropy, complex three-dimensional magnetic structures appear that contains zones with spins parallel to the densest planes and other zones with spins normal to these planes. In between, the spins rotate on short distances.

The magnetic structure of dots in presence of a field is being processed now with preliminary results which are comparable to those obtained for ultrathin films, i.e., three-dimensional wall nucleation and wall motion with distorsion.

As a conclusion we emphasize the interest of the new magnetic structures described here. For instance, in ultrathin layers, magnetic vortices and twisted spin configurations are expected to occur, and preliminary observations of similar structures exist [8]. On the other hand, both stripe structures and vortex structures have been observed in magnetic dot arrays [3]. Another point of interest is the fast soliton dynamics which is shown to occur at the coercive field. This is crucial for recording applications and critical properties of this motion are now extensively studied experimentally and theoretically.

References

[1] R. Allenspach, *J. Magn. Magn. Mater.* **129**, 160, (1994).

[2] P. Toneguzzo, G. Viau, O. Acher, F. Fiévet-Vincent and F. Fiévet, *Adv. Mater.* **13**, 1032, (1998).

[3] M. Hehn, K. Ounadjela, J.-P. Bucher, F. Rousseaux, D. Decanini, B. Bartenlian, C. Chappert, *Science* **272**, 1782 (1996).

[4] E.Yu. Vedmedenko, A. Ghazali and J.-C.S. Lévy, *Phys. Rev. B* **59**, 3329, (1999).

[5] J.A. Cape and G.W. Lehman, *J. Appl. Phys.*, **42**, 5732 (1971).

[6] E.Yu. Vedmedenko, A. Ghazali and J.-C.S. Lévy, *Surf. Sci.* **402-404**, 391, (1998).

[7] A.C. Daykin and J.P. Jakubovics, *J. Appl. Phys.* **80**, 3408, (1996).

[8] T. Duden and E. Bauer, *Phys. Rev. Lett.* **77**, 2308, (1996).

[9] M.E. Gouvêa, G.M. Wysin, S.A. Leonel, A.S.T. Pires, T. Kamppeter and F.G. Mertens, *Phys. Rev. B* **59**, 6229, (1999).

VOLUME 92, NUMBER 7 PHYSICAL REVIEW LETTERS week ending 20 FEBRUARY 2004

Domain Wall Orientation in Magnetic Nanowires

E. Y. Vedmedenko,[1,2] A. Kubetzka,[2] K. von Bergmann,[2] O. Pietzsch,[2] M. Bode,[2] J. Kirschner,[1]
H. P. Oepen,[2] and R. Wiesendanger[2]

[1]*Max-Planck-Institut für Mikrostrukturphysik, Weinberg 2, D-06120 Halle, Germany*
[2]*Institute of Applied Physics, University of Hamburg, Jungiusstrasse 11, D-20355 Hamburg, Germany*

(Received 31 July 2003; published 20 February 2004)

Scanning tunneling microscopy reveals that domain walls in ultrathin Fe nanowires are oriented along a certain crystallographic direction, regardless of the orientation of the wires. Monte Carlo simulations on a discrete lattice are in accordance with the experiment if the film relaxation is taken into account. We demonstrate that the wall orientation is determined by the atomic lattice and the resulting strength of an effective exchange interaction. The magnetic anisotropy and the magnetostatic energy play a minor role for the wall orientation in that system.

DOI: 10.1103/PhysRevLett.92.077207 PACS numbers: 75.60.Ch, 07.79.–v, 75.70.Ak

Magnetism of systems with reduced dimensions poses a number of topical questions, one intriguing issue being the orientation of domain walls. It has been shown experimentally that the mesoscopic pathway of domain walls in ultrathin films can either be arbitrary, as in Co/Au(111) [1], or follow certain crystallographic directions, as in Fe/W(110) [2]. Although the knowledge of domain patterns and, in particular, the domain wall orientation on the nanoscale is of great importance for the fundamental physics of magnetism, as well as for technical applications, the orientation of domain walls on a local, microscopic scale has not yet been studied.

One experimentally accessible and, for future applications, very perspective geometrical shape is a so-called nanowire—a quasi-one-dimensional structure of infinite length and lateral dimensions on the nanometer scale. The nanowire geometry is particularly advantageous for the investigation of the domain wall orientation as the latter can be governed by a minimization of the total wall length. On the other hand, it has been demonstrated that in ultrathin nanostructures the discreteness of the crystalline lattice can also change the magnetization configuration [3]. The role of the lattice for the domain wall orientation has not been analyzed systematically.

For many experimental systems, e.g., Fe/Cu(100), the shortest wall path coincides with one of the crystallographic axes which makes it impossible to distinguish between the role of the lattice for the domain formation and other effects. Only if the shortest distance is different from any principal axes of a lattice the mechanism underlying the orientation of the domain walls can be revealed. A suitable and experimentally well-studied model system is the double layer (DL) Fe nanowires on stepped W(110) [2,4–8] being characterized by perpendicularly magnetized domains separated by domain walls. Experimental and *ab initio* electronic structure calculations [9] led to a comprehensive understanding of the electronic and the magnetic properties. The relationship between the orientation of domain walls and of the DL Fe stripes, however, has not yet been investigated.

This study is devoted to the analysis of the influence of the discrete nature of an atomic lattice on the orientation of domain walls in nanostructures. Scanning tunneling microscopy on areas with different local miscut orientations reveals that the domain walls are oriented along the $[1\bar{1}0]$ and less often along the $[3\bar{3}1]$ direction, regardless of the orientation of the nanowires. Employing Monte Carlo simulations (MCS) we demonstrate that the wall orientation is determined by the underlying crystalline lattice and the exchange interactions. The magnetic anisotropy and the magnetostatic energy, which can align walls along certain crystallographic directions in bulk material, play a minor role for the wall orientation. We regard these results to be valid for a large class of low symmetry ultrathin ferromagnetic films.

The experiments have been performed in a commercial variable temperature STM attached to a five-chamber UHV system. The instrument is equipped with an *x-y* sample positioning facility which allows one to access different areas on the same sample. We used etched tungsten tips for the measurements. Fe was deposited onto the W(110) substrate by molecular beam epitaxy at a pressure $p \leq 1 \times 10^{-10}$ mbar. To achieve step flow growth the crystal was held at $T = 500$ K during thin film deposition. Simultaneously to constant current images, maps of the differential conductance dI/dU were recorded by means of the lock-in technique.

Figure 1 shows the topography (a) and maps of differential conductance (b)–(d) of 1.7 ML (monolayer) Fe/W(110). While the dI/dU map of Fig. 1(b) has been measured simultaneously with and at the same position as the topographic image, the dI/dU maps of Figs. 1(c) and 1(d) show other areas of the same sample which exhibit different local miscut orientations. In any case the Fe DL nanowires can be distinguished from sample locations which are covered by a single Fe layer (SL) due to their different electronic properties resulting in a dI/dU signal that is lower for the SL than for the DL. The DL nanowires shown in Figs. 1(a) and 1(b) extend approximately along [001], the ones in Fig. 1(c) along $[1\bar{1}0]$, while in

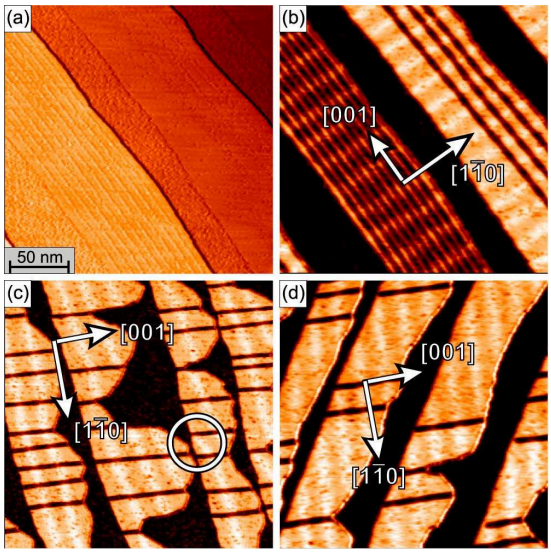

FIG. 1 (color online). (a) Topography and (b)–(d) dI/dU maps of 1.7 ML Fe/W(110) at different local miscut orientation. (a) and (b) were recorded simultaneously. The lateral scale is the same in all images. In all cases, domain walls (white lines) are oriented along [1$\bar{1}$0], regardless of the orientation of the nanowires. Parameters are $U = 5$ mV, $I = 0.5$ nA, $T =$ 75 K (b),(c), and 120 K (d).

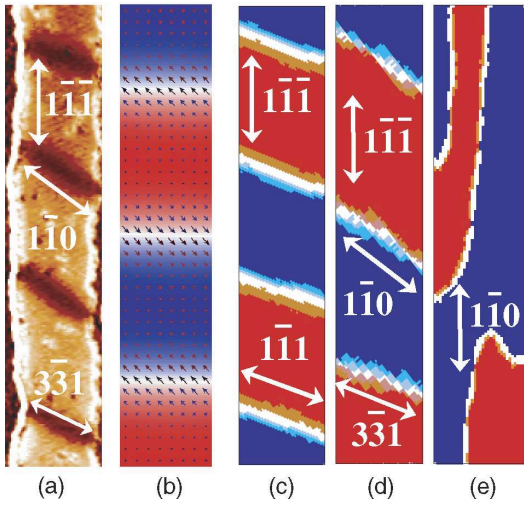

FIG. 2 (color online). Top view of experimental (a) and simulated nanowire sections of 20 nm (b)–(d) and 40 nm widths (e): (a) experiment, domain walls are imaged as dark lines; (b) continuum theory, isotropic exchange. MCS: (c) J_3:J_2:J_1 = 0:1:1 (identical exchange interaction along all nearest neighbor bonds); (d),(e) J_3:J_2:J_1 = 4:2:1.

Fig. 1(d) the wire direction is intermediate, roughly along [1$\bar{1}$1]. Because of unequal diffusion energies the Fe stripes grow smoothest along [001] and least smooth along [1$\bar{1}$0] [10]. After initial pseudomorphic growth the high tensile strain starts to relax by insertion of dislocation lines in the Fe DL which run along the [001] direction. These are imaged as narrow black lines in the dI/dU maps. The double layer nanowire has a periodic magnetic structure with out-of-plane domains alternatingly magnetized up and down. These domains are separated by 180° in-plane domain walls. The typical distance between adjacent walls is 23 ± 2 nm [8]. Because of spin-orbit coupling we can differentiate between areas with out-of-plane and in-plane magnetization even with nonmagnetic tips [4]. Since the bias voltage chosen for the measurements of Fig. 1 ($U = 5$ mV) is below the crossover of domain and domain wall spectra [see Fig. 1(e) in Ref. [4]] the domain walls are imaged as white lines in this experiment. Regardless of the direction of the nanowires the domain walls run mainly along the [1$\bar{1}$0] direction, i.e., perpendicular to the dislocation lines. As a consequence, the domain walls within the nanowires are infinitely long in the case of Fig. 1(c)(disregarding interruptions due to structural imperfections), and very short in case of Fig. 1(b) where they run perpendicular to the axis of the nanowire. Less often the domain walls run along [3$\bar{3}$1]. This effect can be seen in Fig. 2(a) where a DL, 20 nm wide nanowire is shown. As the bias voltage and the material of the STM tip were different from those of experiment Fig. 1 the domain walls are imaged as dark lines [2]. Both [1$\bar{1}$0] and [3$\bar{3}$1] directions are not principal directions of an ideal bcc lattice as they do not coincide with the primitive vectors of the bcc structure.

We have performed calculations following a widely used micromagnetic framework [11], where the nanowires consist of rectangular blocks of continuous material. For isotropic exchange stiffness A we obtain the wall direction that is determined by a minimization of the wall length, i.e., perpendicular to the nanowire direction [Fig. 2(b)]. This result is not consistent with the experimental observation of Fig. 1. It even cannot be corrected by an additional in-plane anisotropy [Fig. 2(b)]; this leads only to an alignment of the magnetization within the wall with no consequences for the wall direction. Varying A in the [1$\bar{1}$0] and in the [001] direction [12], we obtain a tilting of the domain wall [13]. Hence, in contrast to bulk materials where magnetic anisotropy may affect the wall direction, the exchange stiffness plays a more important role in the ultrathin limit. The anisotropy of the continuum parameter A can be governed either by noncubic symmetry of the lattice or by the varying exchange integral between nearest-neighboring atoms [12]. By fitting A to the experimental results we cannot distinguish between the two effects. Besides, we cannot explain the experimental observation of coexisting [1$\bar{1}$0] and [3$\bar{3}$1] walls. Thus, without consideration of the discrete atomic lattice the physics of the wall orientation in the ultrathin limit cannot be understood.

VOLUME 92, NUMBER 7 PHYSICAL REVIEW LETTERS week ending 20 FEBRUARY 2004

In order to explain the experimental results we performed MCS on a discrete lattice. In contrast to the case of localized spin systems, in itinerant-electron systems the exchange coupling between local moments does not explicitly enter into a Heisenberg-type Hamiltonian. However, within the framework of spin-density-functional theory expressions for the effective exchange pair interactions can be obtained [14,15]. With these effective constants the system Hamiltonian for the MC calculations reads

$$H = -\sum_{\langle i,j\rangle} J_k \boldsymbol{S}_i \cdot \boldsymbol{S}_j + D\sum_{i,j}\left(\frac{\boldsymbol{S}_i \cdot \boldsymbol{S}_j}{r_{ij}^3} - 3\frac{(\boldsymbol{S}_i \cdot \boldsymbol{r}_{ij})(\boldsymbol{S}_j \cdot \boldsymbol{r}_{ij})}{r_{ij}^5}\right) + k_1\sum_i \sin^2\theta + k_2\sum_i \sin^4\theta - k_p\sum_i \sin^2\theta\cos^2(\varphi - \beta),$$

where J_k denotes the effective nearest neighbor exchange coupling constant along different bonds (Fig. 3), D is the dipolar coupling parameter, θ and φ are the spherical angles, and $\boldsymbol{r}_{ij}$ is the vector between sites i and j. The coefficients k_1 and k_2 are the first- and second-order anisotropies per atom, respectively. k_p is an in-plane anisotropy per atom. The in-plane anisotropy can have any angle β with respect to the x axis. For the MC computations we consider two layers of classical, three-dimensional magnetic moments $\boldsymbol{S}$ on a bcc(110) lattice of about 20 000 effective magnetic sites. The Monte Carlo procedure is described elsewhere [16]. We use a realistic ratio of exchange and dipolar constants $D/J = 10^{-3}$. The anisotropy constants have been widely varied in the regime of the vertical magnetization. The best agreement with the experimental results (domain width of 20–25 nm and wall width of 6–9 nm) gives constants corresponding to an anisotropy energy density $K_1 = (1.6\text{–}2.0)K_d$, $K_2 = (0\text{–}0.7)K_d$, $K_p = (0\text{–}0.6)K_d$ with $K_d = 2\pi M_s^2$ the shape anisotropy. The value of the out-of-plane anisotropy is $K_1 = (2\text{–}2.1)K_d$. We have performed calculations for films, single wires, and arrays of three wires with periodic boundary conditions along the wires and open boundary conditions in the perpendicular direction.

In a first step we assume an idealized film with an "isotropic" nearest neighbor exchange, i.e., $J_1 = J_2$ and $J_3 = 0$ in the case of a bcc(110) lattice (cf. Fig. 3). In infinite sc(100) or an fcc(111) 1–2 ML films no preferred wall orientation is observed. In contrast, domain walls in a 2 ML bcc(110) film have mainly $[1\bar{1}0]$ orientation. This can be explained by the minimization of the density of nearest neighbor bonds per unit volume of a wall for this direction. As a consequence, the exchange energy cost due to the wall formation can be minimized. The same results have been obtained for wide wires (>40 nm). Those results are consistent with experiments and demonstrate that the crystal lattice can affect the wall orientation.

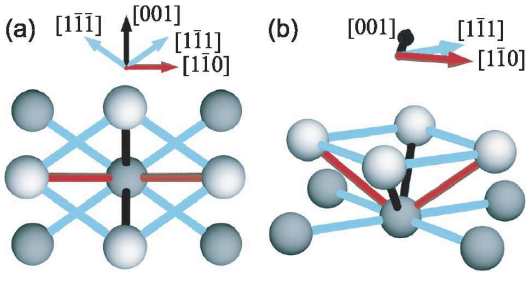

FIG. 3 (color online). Unit cell of 2 ML Fe/W(110) in (a) top and (b) perspective views. Black and light grey (blue) lines denote the nearest neighboring bonds J_1 and J_2 in an undistorted, ideal crystal. Dark grey (red) lines denote additional nearest neighboring bonds J_3 due to relaxation.

A typical result for the case of $[1\bar{1}\,\bar{1}]$ oriented, 20 nm wide nanowires is given in Fig. 2(c). In that case the walls deviate from the $[1\bar{1}0]$ direction. The orientation of walls is close to $[1\bar{1}1]$. Hence, the lattice symmetry alone is insufficient to orient the domain walls along $[1\bar{1}0]$. The calculations show that if the length of the walls can be minimized as, for example, in thin wires of Fig. 2(c) the wall orientation can deviate from $[1\bar{1}0]$. In the following we explain the discrepancy by taking into account the lattice relaxation.

Because of pseudomorphic growth the first two Fe layers adopt the lateral lattice constant of tungsten, which is about 10% larger than that of bulk iron. As a consequence, the Fe-Fe interlayer distance relaxes below the Fe bulk value [9]. This leads to a change of the interatomic distances. Namely, the neighbor distance in the [001] direction (black in Fig. 3) d_1 decreases, the spacings in the $[1\bar{1}1]$ and the $[1\bar{1}\,\bar{1}]$ direction d_2 (light grey) are increased, and the distance in the $[1\bar{1}0]$ d_3 direction (dark grey) decreases to a value close to the nearest neighbor distance in bulk iron. Hence, instead of six nearest neighbors as in an ideal, 2 ML thick bcc(110) film, in Fe/W(110) all atoms have eighth bonds of similar length. The respective distances in units of the nearest neighbor distance in bulk Fe are $d_1 = 0.82$, $d_2 = 0.96$, and $d_3 = 0.99$ [9].

The calculations [14,17–19] show that the strength of the exchange coupling is a function of relative position $\boldsymbol{r}_{ij}$ of the magnetic moments i and j. Especially interesting is the behavior of $J(\boldsymbol{r}_{ij})$ in Fe. For Fe a reduction in nearest neighbor (NN) spacing d_{NN} with respect to the bulk value drives the exchange towards antiferromagnetism. This effect has been made responsible for the fact that fcc-Fe is antiferromagnetic while bcc-Fe is a ferromagnetic material [20,21]. That argument is also supported by the position of Fe on the Bethe-Slater curve, which is widely used in the physics of ferromagnetic alloys [21,22]. Thus, a decrease of the interatomic distance in the [001] direction can lead — in contrast to other ferromagnets — to a reduction of the ferromagnetic exchange parameter.

For Fe nanowires on W(110) the situation is even more subtle due to hybridization and polarization effects at the Fe/W interface. All the more interesting is the advance, described in very recent studies [23,24], where the exchange stiffness of Fe films adsorbed on a W(110) surface has been calculated. The authors find that the exchange stiffness A, which is equal to $2JS^2/a$ for a bcc lattice [25], depends on the direction along which the spin wave is excited. For one monolayer Fe/W(110) the exchange stiffness in the $[1\bar{1}0]$ direction is 4 times larger than in the [001] direction [24]. For a 2 ML film the difference is found to be smaller, but the tendency remains the same. The physical reason for this anisotropic behavior can lie in changes of interatomic spacing, as discussed above, or in additional indirect spin interactions through the W substrate [24]. In any case, the dependence of the exchange interaction on $\boldsymbol{r}_{ij}$ must be taken into account in the simulation of the magnetic ordering.

According to this argument we introduce three different exchange constants J_i for the three nonequivalent pairs of neighboring magnetic moments. Hamiltonians of that type are widely used in models of frustrated magnetic systems [26]. We have explored different ratios of $J_3{:}J_2{:}J_1$ (dark grey, light grey, and black bonds in Fig. 3, respectively). Generally, the walls tend to be aligned along the axis of the strongest exchange coupling. The best overall accordance with the experiment is found for ratio $J_3{:}J_2{:}J_1 = 4{:}2{:}1$, which is in good agreement with Refs. [23,24] and the Bethe-Slater curve. For $[1\bar{1}1]$ nanowires [Fig. 2(d)] the majority of the walls follow the $[1\bar{1}0]$ axis. However, $[3\bar{3}1]$ walls are also found. For $[1\bar{1}0]$ nanowires of 40 nm width [Fig. 2(e)] we also get $[1\bar{1}0]$ oriented domain walls which cannot be expected from isotropic exchange interactions. The walls are not perfectly straight but show some irregularities. For example, the wall is forced out of the $[1\bar{1}0]$ direction at the rim of the nanowire. A similar behavior has also been found experimentally [see the circle in Fig. 1(c)]. We have also explored different orientations and strengths of the in-plane anisotropy K_p. As already mentioned above the only effect of a strong K_p is an alignment of the magnetic moments in the wall along the respective axis. The orientation of domain walls is not influenced by K_p showing that the mechanism of wall orientation described here is distinct from the one observed in bulk material, which is governed by magnetic anisotropy and dipolar energy.

In conclusion, we have demonstrated by means of an experimental study and extended Monte Carlo simulations that in contradiction to the isotropic continuum approximation the orientation of magnetic domain walls in ultrathin films is governed by the atomic lattice structure and the set of nearest neighbor moments. The magnetic anisotropy and the magnetostatic energy, which can govern wall orientations in bulk material, play a minor role in the ultrathin limit.

R.W. gratefully acknowledges financial support from the DFG (Grant No. Wi1277/19-1).

[1] M. Speckmann, H. Oepen, and H. Ibach, Phys. Rev. Lett. **75**, 2035 (1995).
[2] A. Kubetzka, M. Bode, O. Pietzsch, and R. Wiesendanger, Phys. Rev. Lett. **88**, 057201 (2002).
[3] E. Vedmedenko, H. Oepen, and J. Kirschner, J. Magn. Magn. Mater. **256**, 237 (2003).
[4] M. Bode, S. Heinze, A. Kubetzka, O. Pietzsch, X. Nie, G. Bihlmayer, S. Blügel, and R. Wiesendanger, Phys. Rev. Lett. **89**, 237205 (2002).
[5] M. Bode, A. Kubetzka, S. Heinze, O. Pietzsch, R. Wiesendanger, M. Heide, X. Nie, G. Bihlmayer, and S. Blügel, J. Phys. Condens. Matter **15**, S679 (2003).
[6] O. Pietzsch, A. Kubetzka, M. Bode, and R. Wiesendanger, Science **292**, 2053 (2001).
[7] O. Pietzsch, A. Kubetzka, M. Bode, and R. Wiesendanger, Phys. Rev. Lett. **84**, 5212 (2000).
[8] A. Kubetzka, O. Pietzsch, M. Bode, and R. Wiesendanger, Phys. Rev. B **67**, 020401 (2003).
[9] X. Qian and W. Hübner, Phys. Rev. B **60**, 16192 (1999).
[10] H. Elmers, J. Hauschild, and U. Gradmann, J. Magn. Magn. Mater. **221**, 219 (2000).
[11] The public domain OOMMF package is available at http://math.nist.gov/oommf/
[12] H. Kronmüller and M. Fähnle, *Micromagnetism and the Microstructure of Ferromagnetic Solids* (University Press, Cambridge, 2003), p. 17.
[13] A. Kubetzka, Ph.D., 2002.
[14] A. Liechtenstein, M. Katsnelson, and V. Gubanov, J. Phys. F **14**, L125 (1984).
[15] A. Liechtenstein, M. Katsnelson, V. Antropov, and V. Gubanov, J. Magn. Magn. Mater. **67**, 65 (1987).
[16] E. Vedmedenko, H. Oepen, A. Ghazali, J.-C. Lévy, and J. Kirschner, Phys. Rev. Lett. **84**, 5884 (2000).
[17] S. Frota-Pessôa, R. Muniz, and J. Kudrnovský, Phys. Rev. B **62**, 5293 (2000).
[18] M. Pajda, J. Kudrnovský, I. Turek, V. Drchal, and P. Bruno, Phys. Rev. Lett. **85**, 5424 (2000).
[19] O. Mryasov, A. Freeman, and A. Liechtenstein, J. Appl. Phys. **79**, 4805 (1996).
[20] M. Hatherly, K. Hirakawa, R. Lowde, J. Mallett, M. Stringfellow, and B. Torrie, Proc. Phys. Soc. London **84**, 55 (1965).
[21] Q. Pankhurst, L. Barquin, J. Wicks, R. McGreevy, and M. Gibbs, J. Phys. Condens. Matter **9**, L375 (1997).
[22] K. Gallagher, M. Willard, V. Zabenkin, D. Laughlin, and M. McHenry, J. Appl. Phys. **85**, 5130 (1999).
[23] R. Muniz and D. Mills, Phys. Rev. B **66**, 174417 (2002).
[24] R. Muniz, A. Costa, and D. Mills, J. Phys. Condens. Matter **15**, S495 (2003).
[25] S. Chikazumi, *Physics of Ferromagnetism* (Oxford University Press, Oxford, 1999).
[26] R. Feyerherm, A. Loose, and J. Manson, J. Phys. Condens. Matter **15**, 663 (2003).

ARTICLE IN PRESS

Available online at www.sciencedirect.com
SCIENCE DIRECT®

ELSEVIER

Journal of Magnetism and Magnetic Materials ▮ (▮▮▮▮) ▮▮▮–▮▮▮

Journal of magnetism and magnetic materials

www.elsevier.com/locate/jmmm

Lattice-dependent anisotropy in the orientation of magnetic domain walls

E.Y. Vedmedenko*,[1], K. von Bergmann, H.P. Oepen, R. Wiesendanger

Institute of Applied Physics, University of Hamburg, Jungiusstr. 11, D-20355 Hamburg, Germany

Abstract

We demonstrate theoretically that a large class of ultrathin ferromagnetic films shows anisotropy in the domain wall orientation in spite of the isotropy in the exchange interactions. The reason is an orientation-dependent density of nearest-neighbor atomic bonds due to the symmetry of an underlying atomic lattice.

PACS: 75.60.Ch; 75.70.Ak

Keywords: Domain wall; Atomic structure; Exchange coupling

1. Introduction

It has recently been shown that the magnetic anisotropy and the magnetostatic energy, which can align domain walls along certain crystallographic directions in bulk material, play a minor role for the wall orientation in ultrathin ferromagnetic films [1]. In case of low-symmetry objects the orientation of domain walls is mainly determined by the exchange interactions. Due to pseudomorphic growth the first few layers of a magnetic material can adopt the lattice constant of a substrate. This often leads to distortion of the atomic structure of a ferromagnet and consequently to an anisotropy in the exchange stiffness tensor [2,3]. Anisotropy of the exchange stiffness may significantly affect the micromagnetic configuration of domain walls and may lead to anchoring of the wall orientation to certain crystallographic directions [1].

If the exchange interaction is isotropic it cannot affect the global orientation of domain walls in bulk crystals of cubic symmetry as both the spin and the real space are isotropic. On the other hand, in films of a few monolayer thickness the density of nearest-neighbor atomic bonds per unit length may differ for different crystallographical directions because of reduced symmetry, i.e. the real space is not isotropic any more. This may lead to the orientational dependency of the exchange energy and, hence, to the preference of some crystallographical orientations. We study that possibility systematically by means of Monte-Carlo (MC) simulations and within a simple analytical approach.

2. Monte-Carlo simulations

First we discuss results of Monte-Carlo simulations on a discrete lattice. The system Hamiltonian reads

$$H = -\sum_{\langle i,j\rangle} J_{[xyz]}\mathbf{S_i}\cdot\mathbf{S_j} + \mathbf{k}_1\sum_i \sin^2\theta + D\sum_{i,j}\left(\frac{\mathbf{S_i}\cdot\mathbf{S_j}}{r_{ij}^3} - 3\frac{(\mathbf{S_i}\cdot\mathbf{r_{ij}})(\mathbf{S_j}\cdot\mathbf{r_{ij}})}{r_{ij}^5}\right),$$

*Corresponding author. Tel.: +49 40 428386230; fax: +49 40 428386368.

E-mail address: vedmedenko@physnet.uni-hamburg.de (E.Y. Vedmedenko).

[1]Financial support from the Interdisciplinary Nanoscience Center Hamburg is gratefully acknowledged.

0304-8853/$ - see front matter © 2004 Elsevier B.V. All rights reserved.
doi:10.1016/j.jmmm.2004.11.356

where $J_{[xyz]}$ denotes the effective nearest-neighbor exchange coupling constant, D is the dipolar coupling parameter, θ and φ are the spherical angles and $\mathbf{r_{ij}}$ the vector between sites i and j. The coefficient k_1 is the first-order anisotropy per atom. For the MC computations we consider one or two layers of classical, three-dimensional magnetic moments $\mathbf{S}$ on different surfaces of SC, FCC and BCC lattices of about 20000 effective magnetic sites. The MC procedure is described elsewhere [4]. We use a realistic ratio of the exchange and the dipolar constants $D/J = 10^{-3}$. The exchange constants between all pairs of nearest neighbors are identical. The anisotropy constants have been widely varied in the regime of vertical and in-plane magnetization. The thickness of domain walls decreases with increasing absolute value of k_1. However, the orientation of domain walls is not influenced by k_1 showing that the mechanism of wall orientation described here is distinct from the one observed in bulk material, which is governed by magnetic anisotropy and dipolar energy.

Fig. 1 shows typical MC low-temperature domain configurations found for SC(1 1 0) (a), BCC(1 1 0) (b), FCC(1 1 0) (c) and FCC(1 0 0) (d) surfaces while Fig. 2 gives the structure of the corresponding unit cells. The domain walls in SC(1 1 0) films are mainly oriented along [0 0 1], while the walls in BCC(1 1 0) films are oriented along the [1 $\bar{1}$ 0] direction (Figs. 1(a), (b) and Figs. 2(b), (c)). The domain walls of FCC(1 1 0) film (Figs. 1c and 2d) are more disordered and can run along [1 $\bar{1}$ 0], [1 $\bar{1}$ 2] or intermediate crystallographic directions. However, one never finds a [0 0 1] orientation. The domain pattern of an FCC(1 0 0) film, shown in Fig. 1d, is completely disordered. All possible orientations of domain walls can be found in the magnetization configuration. Similar results have been obtained for all other surfaces of cubic crystals. Thus, for isotropic exchange interactions the orientation of domain walls of (1 1 0) surfaces of cubic crystals is highly anisotropic while it is not the case for the (1 0 0) and (1 1 1) surface orientations. Those results are consistent with experiments where anisotropic wall patterns have been found for Fe/W(1 1 0) films[1] while a disordered configuration has been revealed for a Co/Au(1 1 1) [5]. Hence, the crystal lattice and the set of nearest neighbor moments can affect the wall orientation even for isotropic exchange interactions. The physical reason for that behavior is the different number of nearest-neighbor bonds per unit length along the one or the other direction. To make this statement and the results of MC simulations more quantitative, we introduce a simple phenomenological model to calculate the exchange energy loss for domain walls along different crystallographic directions.

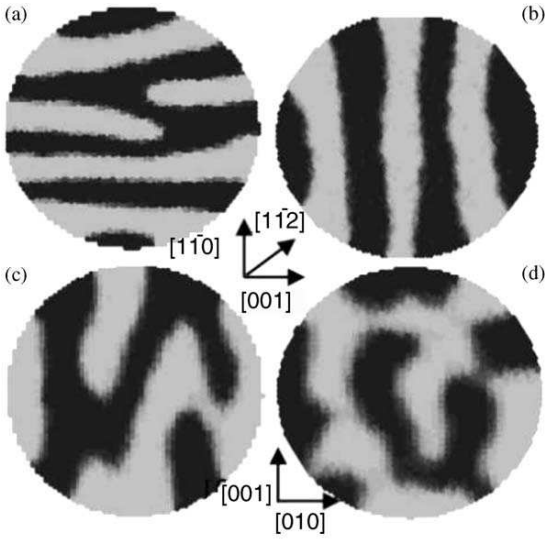

Fig. 1. Top-view of MC domain configurations in 600 nm large and 2 ML thick samples with: SC(1 1 0) (a), BCC(1 1 0) (b), FCC(1 1 0) (c) and FCC(1 0 0) (d) surfaces. Opposite domains are imaged as dark and light areas. Exchange interactions are isotropic, $kT = 0.05\,J$, $k_1 = 9 \times 10^{-3}$ J. Upper directions correspond to (1 1 0) (a–c) while bottom to (1 0 0) (d) surface.

3. Phenomenological model

Fig. 2 shows a top view of a conventional Bloch wall (a) and unit cells of a double layer with a SC(1 1 0) (b), a BCC(1 1 0) (c), a FCC(1 1 0) (d) and a FCC(1 0 0) (e) crystalline lattice. Atoms are sketched as balls where dark ones belong to the surface and light balls to subsurface layer. Connections between atoms indicate nearest-neighbor bonds. From Fig. 2(a) it is clearly visible that the magnetization rotates along an axis perpendicular to the plane of the wall while magnetic moments belonging to planes which are parallel to the plane of the wall are parallel. Since in a ferromagnet neighboring spins hold the lowest energy when they are parallel, the loss in the exchange energy due to the wall formation results from the bonds which have non-zero projection on the direction perpendicular to the course of the wall. For example, if the wall is oriented along the [010] direction of the FCC(1 0 0) surface (Fig. 2e) the magnetic moments connected by [010] bonds will be parallel while moments connected by [0 0 1] bonds will have a maximal possible mutual angle and, consequently, a maximal increase in the exchange energy $\Delta E_J^{[0\,0\,1]}$. The moments connected by [011] and [0 1 $\bar{1}$] bonds will have intermediate mutual angles as they are neither parallel nor perpendicular to the direction of energy loss. It means, that the local increase in the exchange energy due to the magnetization rotation in a

ARTICLE IN PRESS

E.Y. Vedmedenko et al. / Journal of Magnetism and Magnetic Materials ▮ (▮▮▮▮) ▮▮▮–▮▮▮ 3

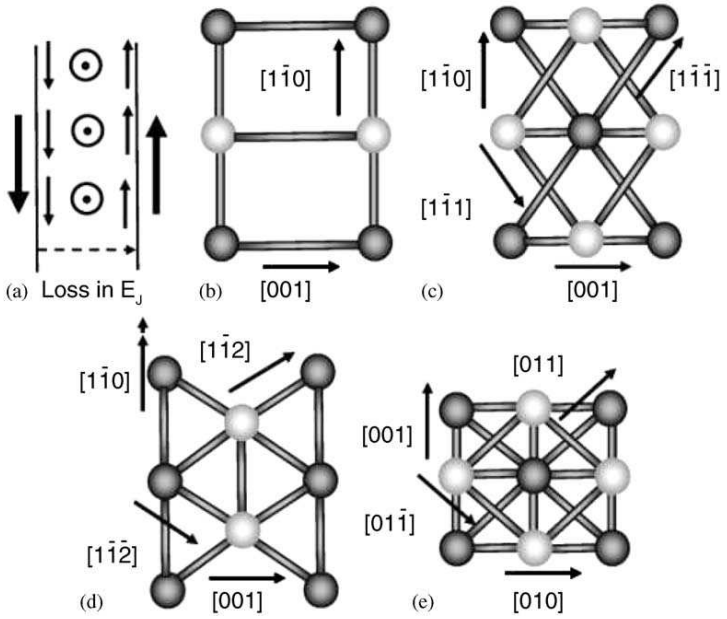

Fig. 2. Schematic top view of a Bloch wall, the magnetization is represented by arrows (a). Top view of unit cell of 2 ML thick SC(1 1 0) (b), BCC(1 1 0) (c), FCC(1 1 0) (d) and FCC(1 0 0) (e) films. Dark and light balls denote the atoms belonging to the first and the second layer correspondingly. Nearest-neighbor bonds are shown as connections between the atoms.

domain wall will be proportional to the projection of an atomic bond on the axis perpendicular to the wall orientation.

To obtain losses in the exchange energy due to formation of a domain wall in this model, in a first step projections of all bonds to the axis perpendicular to the plane of the wall ($P_{\perp to[xyz]}$) were calculated for single and double layers of (1 0 0), (1 1 1) and (1 1 0) surfaces of BCC, FCC and SC crystals. The nearest-neighbor bonds have been assumed to be of unit length. The length and the number of projections $P_{\perp to[xyz]}$ for double layers with (1 1 0) surface are brought together in Table 1. The loss in the exchange energy per unit cell for a wall along one of the [xyz] directions has then been calculated by summing up the exchange coupling constant ($J_{[xyz]} = 1.0$) multiplied by $P_{\perp to[xyz]}$ for all bonds in the unit cell

$$\Delta E_J^{[xyz]}[\text{a.u./unit cell}] = \sum_i J_{[xyz]} \cdot P_{\perp to[xyz]}.$$

For a wall along [1 $\bar{1}$ 2] of an FCC(1 1 0) lattice, for example, this results in (see also Table 1)

$$\Delta E_J^{[1\,\bar{1}\,2]} = 3 \cdot \sqrt{\square}\frac{2}{3} + 4 \cdot \sqrt{\square}\frac{2}{3} + 4 \cdot \frac{1}{\sqrt{\square}12} = 5.74\ (\text{a.u.}).$$

The exchange energy of a domain wall per unit cell is smallest for the [1 $\bar{1}$ 0] direction of the BCC(1 1 0) and for the [0 0 1] direction of the SC(1 1 0) surface. In case of an FCC(1 1 0) crystal two orientations have similar energy. These are the [1 $\bar{1}$ 2] direction with $\Delta E_J^{1\,\bar{1}\,2} = 5.74$ and [1 $\bar{1}$ 0] with $\Delta E_J^{1\,\bar{1}\,0} = 5.65$. Hence, the exchange energy cost in the systems described above is orientation dependent. The preferential orientations of walls derived in the phenomenological model are [1 $\bar{1}$ 0] for BCC(1 1 0) and [0 0 1] for SC(1 1 0) crystalline films. For FCC(1 1 0) the wall orientation is defined by the competition between [1 $\bar{1}$ 0] and [1 $\bar{1}$ 2] directions. The cost in the exchange energy ΔE_J^{xyz} for othersurfaces is constant and does not depend on the wall orientation. Hence, for [0 0 1] and [1 1 1] surfaces of a cubic crystal the domain walls are predicted to have no preferential orientation. The results described above are in agreement with those of MC simulations and experiments and give a quantitative measure of the orientation-dependent exchange energy loss due to formation of a domain wall.

4. Conclusion

In conclusion, we demonstrate that the orientation of magnetic domain walls in ultrathin single-crystalline films of cubic symmetry with (1 1 0) surface orientation is highly anisotropic while other surface orientations lead to isotropic wall configurations. The anisotropy is due to the orthorhombic-like symmetry of (1 1 0)

Table 1
$\Delta E_J^{[xyz]}$ and the projections of nearest-neighbor bonds onto the direction perpendicular to the plane of the domain wall for double layer films with (1 1 0) surface orientation

Stacking	Wall orientation (xyz)	$\Delta E_J^{[xyz]}$/unit cell (a.u.)	$P_{\perp to[xyz]}$[a] of bonds running along		
			[0 0 1] (4)	[1 $\bar{1}$ 0] (4)	[1 $\bar{1}$ 1] (8)
BCC	[0 0 1]	8.52	0	$\frac{1}{\sqrt{2}}$	$\frac{1}{\sqrt{2}}$
(1 1 0)	[1 $\bar{1}$ 0]	6.00	$\frac{1}{2}$	0	$\frac{1}{2}$
	[1 $\bar{1}$ 1]	6.76	$\frac{1}{\sqrt{6}}$	$\frac{\sqrt{3}}{2}$	$\frac{1}{\sqrt{6}}$
			[1 $\bar{1}$ 0](3)	[1 $\bar{1}$ 2] (4)	[1 $\bar{1}$ $\bar{2}$] (4)
FCC	[0 0 1]	7.00	1	$\frac{1}{2}$	$\frac{1}{2}$
(1 1 0)	[1 $\bar{1}$ 0]	5.65	0	$\frac{1}{\sqrt{2}}$	$\frac{1}{\sqrt{2}}$
	[1 $\bar{1}$ 2]	5.74	$\sqrt{\frac{2}{3}}$	$\sqrt{\frac{2}{3}}$	$\frac{1}{\sqrt{12}}$
SC			[0 0 1] (2)	[1 $\bar{1}$ 0] (2)	
(1 1 0)	[0 0 1]	1.41	0	$\frac{1}{\sqrt{2}}$	
	[1 $\bar{1}$ 0]	2.00	1	0	

[a]Number of bonds per unit cell is given in brackets.

surfaces of cubic crystals, which leads to an orientation-dependent density of the nearest-neighbor bonds.

References

[1] E.Y. Vedmedenko, A. Kubetzka, K. von Bergmann, O. Pietzsch, M. Bode, J. Kirschner, H.P. Oepen, R. Wiesendanger, Phys. Rev. Lett. 92 (2004) 077207.

[2] H. Kronmüller, M. Fähnle, Micromagnetism and the Microstructure of Ferromagnetic Solids, Cambridge University Press, Cambridge, 2003.

[3] R.B. Muniz, D.L. Mills, Phys. Rev. B 66 (2002) 174417.

[4] E.Y. Vedmedenko, H.P. Oepen, A. Ghazali, J.-C.S. Lévy, J. Kirschner, Phys. Rev. Lett. 84 (2000) 5884.

[5] M. Speckmann, H.P. Oepen, H. Ibach, Phys. Rev. Lett. 75 (1995) 2035.

ARTICLES

Atomic spin structure of antiferromagnetic domain walls

M. BODE*, E. Y. VEDMEDENKO, K. VON BERGMANN, A. KUBETZKA, P. FERRIANI, S. HEINZE AND R. WIESENDANGER

Institute of Applied Physics and Microstructure Research Center, University of Hamburg, Jungiusstrasse 11, 20355 Hamburg, Germany
***e-mail: mbode@physnet.uni-hamburg.de**

Published online: XX Month XXXX; doi:10.1038/nmatXXXX

The search for uncompensated magnetic moments on antiferromagnetic surfaces is of great technological importance as they are responsible for the exchange-bias effect that is widely used in state-of-the-art magnetic storage devices. We have studied the atomic spin structure of phase domain walls in the antiferromagnetic Fe monolayer on W(001) by means of spin-polarized scanning tunnelling microscopy and Monte Carlo simulations. The domain wall width only amounts to 6–8 atomic rows. Although walls oriented along ⟨100⟩ directions are found to be fully compensated, detailed analysis of ⟨110⟩-oriented walls reveals an uncompensated perpendicular magnetic moment. Our result represents a major advance in the field of antiferromagnetism, and may lead to a better understanding of the magnetic interaction between ferromagnetic and antiferromagnetic materials.

Antiferromagnetic surfaces play an important role in today's information technology as they are used to pin the magnetization direction of intrinsically bistable thin ferromagnetic films by the exchange-bias (EB) effect. This effect, discovered about 50 years ago[1,2], is based on the direct exchange interaction between an antiferromagnet and a ferromagnet it is in contact with, leading to a sign-dependent magnetic coercivity of the ferromagnet. Although the underlying physics of the EB effect was already correctly described in the original publication[2], the rather small size of the effect could only be explained recently. Namely, it was found that the vast majority of the antiferromagnet's surface spins are inactive, and only a few uncompensated spins contribute to the effect[3,4]. Up to now, spin–flop coupling[5,6], grain size[7,8], domains due to interface roughness[9] and non-magnetic defect sites[10,11] have been discussed as possible sources of uncompensated spins.

Owing to their essentially vanishing net magnetization, the experimental imaging of antiferromagnetic domains is particularly difficult. Only recently, domains[12–14] and domain walls[15] (DWs) have been observed by photoelectron emission microscopy with linearly polarized X-rays. The contrast mechanism of this technique relies on X-ray magnetic linear dichroism, which depends on the angle between the electrical field vector $\vec{E}$ and the sample's local magnetic axis $\vec{A}$. Consequently, it is only sensitive to orientational changes as schematically represented in the top panel of Fig. 1a. So-called phase domains (bottom panel of Fig. 1a), where the antiferromagnetic spin structure shifts laterally by one structural lattice constant can only be detected indirectly by the presence of DWs[14]. However, owing to spatial-resolution limitations, X-ray magnetic linear dichroism–photoelectron emission microscopy cannot detect details of the spin structure of DWs on the atomic scale. For this purpose, spin-polarized scanning tunnelling microscopy (SP-STM) is an ideal tool because its capability for atomic resolution has been demonstrated on ferromagnetic[16] and antiferromagnetic surfaces[17–19]. STM with non-magnetic tips is only sensitive to the spin-averaged local density of states $n(\mathbf{r}, E_F)$ at the Fermi level (low-voltage approximation) and tip position $\mathbf{r}$. The intrinsic spin-polarization of magnetic tips, $P_T \equiv (n^{\uparrow} - n^{\downarrow})/(n^{\uparrow} + n^{\downarrow})$, where $n^{\uparrow}$ and $n^{\downarrow}$ are

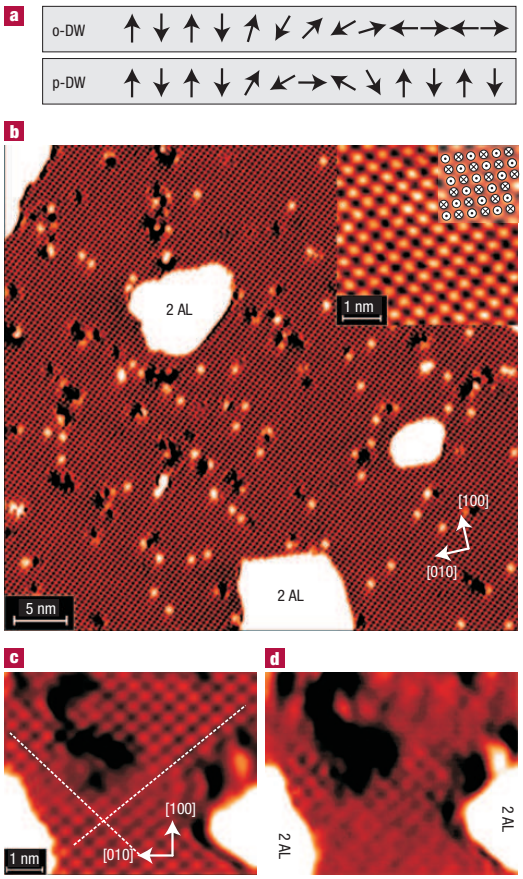

Figure 1 Schematic representation and experimental observation of DWs at antiferromagnetic surfaces. **a**, Scheme of an orientational domain wall (o-DW) and a phase domain wall (p-DW). **b**, SP-STM image of 1.1 AL Fe/W(001) measured with an Fe-coated probe tip at $\mu_0 H = 2$ T. The antiferromagnetic structure, which is shown at higher resolution in the inset, exhibits long-range periodicity without any DW visible in the field of view. Only at higher defect density do p-DWs appear, which can be imaged with **c**, out-of-plane ($\mu_0 H = 2$ T) and **d**, in-plane sensitive tips (no field). In the constriction between the two double-layer islands a p-DW, which runs along the [010] direction, can be seen. At the position of the p-DW, the magnetic structure shifts by one atomic site, that is, half the magnetic periodicity (see dashed lines).

the majority and minority density of states, introduces a spin-polarized contribution to the tunnelling current $I(\mathbf{r})$, which scales with the projection of the unit vector of tip magnetization $\mathbf{u}_T$ onto the local magnetization density of states at E_F, $\mathbf{m}(\mathbf{r}, E_F)$ (ref. 20):

$$I(\mathbf{r}) \propto n(\mathbf{r}, E_F) + P_T \mathbf{u}_T \cdot \mathbf{m}(\mathbf{r}, E_F). \qquad (1)$$

This leads to a magnetic contribution to constant-current mode images of periodic magnetic structures, which is superimposed on the conventional topographic image[18,19]. Here we demonstrate—on the model system of an antiferromagnetic Fe monolayer on W(001)[18]—that SP-STM can also be applied to non-periodic and non-collinear spin structures on the atomic scale. Our experimental results reveal that the phase DWs (p-DWs) in this model system are only 6–8 atomic rows wide, and that the wall centre is located between atomic rows. Together with Monte Carlo (MC) simulations we can infer the existence of uncompensated spins in p-DWs that are oriented along ⟨110⟩ crystallographic directions. Depending on the surface density of these p-DWs the resulting moment may lead to a significant contribution to EB.

The samples consist of iron films (nominal thickness of 1.1–1.4 pseudomorphic atomic layers (AL)) deposited onto a stepped W(001) single crystal held at slightly elevated temperature ($T = 400 \pm 50$ K). Figure 1b shows a constant-current image of 1.1 AL Fe/W(001) measured with an Fe-coated tip at $\mu_0 H = 2$ T. This field leaves the sample's antiferromagnetic structure unchanged as it is determined by the much stronger exchange coupling[18]. Although the topography seems flat if measured with a non-magnetic tip (not shown here), the use of an out-of-plane sensitive magnetic tip leads to the c(2 × 2) superstructure visible in Fig. 1b. The c(2 × 2) superstructure is caused by the above-mentioned spin-polarized contribution to the tunnelling current (equation (1)): because the spin has to be conserved during an elastic tunnelling process, the current (at equal distance) is higher (lower) if the magnetic moments of the tip and sample are parallel (antiparallel)[20,21]. In the constant-current mode, the feedback loop keeps $I(\mathbf{r})$ at a set-point value I_{set}, resulting in a magnetic-induced corrugation that amounts to 4 pm in Fig. 1b. The experimental results prove that the Fe monolayer on W(001) is indeed a perpendicular antiferromagnet with the magnetic moments of nearest-neighbour atoms pointing alternately up and down[18] (see inset). Although numerous defect sites, such as impurities and ad-atoms as well as ferromagnetic second-layer islands are visible, perfect long-range magnetic order without any DW is found on a scale of about 2 μm × 1 μm (see the Supplementary Information).

Only if the defect density was increased, for example, by increasing the Fe coverage to 1.3 AL, did we occasionally find short (1–2 nm) segments of p-DWs as shown in Fig. 1c. This particular DW is clamped between two double-layer islands, and extends along the [010] direction. By following the dashed lines in Fig. 1c along ⟨110⟩ directions, it becomes apparent that the phase of the magnetic lattice shifts at the position of the wall by one atomic site. Within the p-DW, which is only a few lattice sites wide, the magnetic signal seems rather blurred because here—regardless of whether the rotation takes place parallel (Bloch-like) or perpendicular (Néel-like) to the wall—the magnetic moments of the tip and sample are orthogonal. The in-plane c(2 × 2) superstructure within the same p-DW can be observed after releasing the external field (Fig. 1d), which makes the Fe tip sensitive to the in-plane component.

The internal spin structure of DWs was investigated theoretically by the MC method, which is capable of simulating complex spin structures of antiferromagnets[22]. It is based on the classical Heisenberg model, and includes long-range dipolar interactions

$$H = J_1^{ij} \sum_{\langle i,j \rangle} \mathbf{S}^i \cdot \mathbf{S}^j + J_2^{ij} \sum_{\langle\langle i,j \rangle\rangle} \mathbf{S}^i \cdot \mathbf{S}^j$$
$$+ D \sum_{ij} \left(\frac{\mathbf{S}^i \cdot \mathbf{S}^j}{(r^{ij})^3} - 3 \frac{(\mathbf{S}^i \cdot \mathbf{r}^{ij})(\mathbf{S}^j \cdot \mathbf{r}^{ij})}{(r^{ij})^5} \right) - K_1 \sum_i (S_z^i)^2,$$

where $\mathbf{S}^i$ is a three-dimensional unit vector-spin, which is separated by the distance r^{ij}. $\langle i,j \rangle$ and $\langle\langle i,j \rangle\rangle$ denote nearest-neighbour and next-nearest-neighbour pairs, respectively. All material parameters of Fe/W(001) were obtained from density functional theory calculations[23]. The nearest- and next-nearest-neighbour exchange

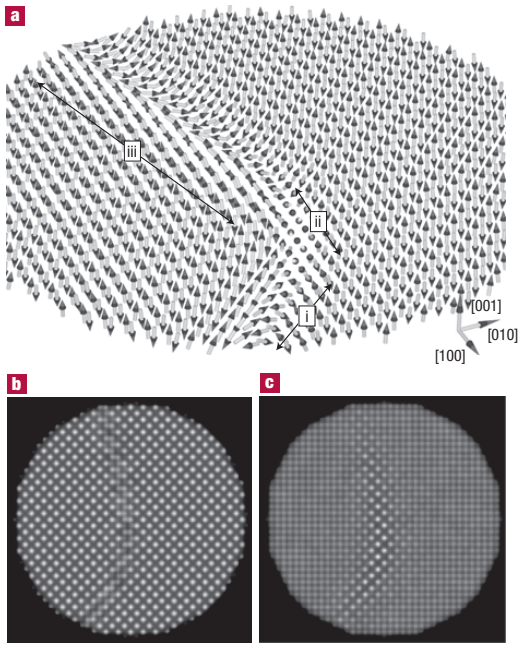

Figure 2 MC simulation of antiferromagnetic DWs. a, Rendered perspective image of the quenched spin structure of an antiferromagnetic material as obtained by MC simulation. A DW, which exhibits three different orientations: along the (i) [110], (ii) [100], and (iii) an intermediate direction, can be seen. Calculated STM images for **b**, out-of-plane and **c**, in-plane sensitive magnetic tips.

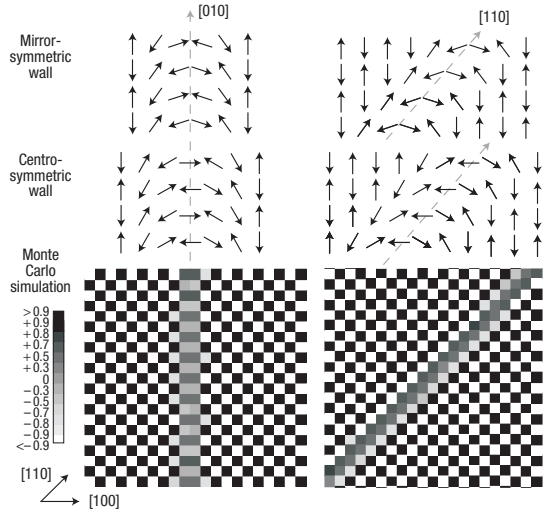

Figure 3 Spin configuration of [010]- and [110]-oriented DWs. Schematic representation of p-DWs that are centred between (top row) and on top of atomic rows (middle row). (bottom row) Part of a p-DW oriented along the [010] (left) and the [110] direction (right) from Monte Carlo simulations. The grey scale gives the calculated out-of-plane component of the magnetization.

parameters are $J_1^{ij} = 20.3$ meV and $J_2^{ij} = 2.4$ meV, respectively, and the anisotropy energy density is $K_1 = 2.4$ meV per atom (ref. 18). The magnetic dipole–dipole interaction is calculated by $D = (\mu_0 g^2 \mu_{Fe}^2)/(4\pi d^3)$, with μ_0 the permeability of the vacuum, $\mu_{Fe} = 2.67\ \mu_B$ the magnetic moment of antiferromagnetic iron and $d = 0.3165$ nm the interatomic Fe–Fe distance[18]. To avoid the sample eventually relaxing into a single-domain state it had to be quenched rapidly from a random start configuration to the measurement temperature, that is, $T \approx 13$ K. A typical result is shown in Fig. 2a. We find no preferred orientation of the DW but three segments oriented approximately along (i) the ⟨110⟩, (ii) the ⟨100⟩, and (iii) an intermediate direction.

To compare the theoretical spin structures with experimental STM data, we need to calculate SP-STM images of arbitrary non-collinear magnetic structures without having access to the full electronic structure of the sample. We extend the independent orbital approximation[24] to spin-polarized tunnelling by making the additional assumption that the electronic structure at every surface atom α is the same, except for a rotation of the local quantization axis by an angle ϑ_α with respect to the tip's magnetization direction $\mathbf{u}_T$. Here, we assume an effective spin-polarization of the tunnel junction $P_T \cdot P_S = 0.3$, with $P_{T,S}$ being the spin-polarization of the tip and the sample, respectively. We have checked that our model correctly reproduces the change from a non-magnetic STM image to an SP-STM image[17–20] of periodic collinear and non-collinear magnetic structures even at small effective spin-polarization.

The calculated STM images shown in Fig. 2b,c are in good qualitative agreement with the experiment (see Fig. 1c,d): the c(2 × 2) superstructure is clearly observed in the domains (DWs) with an out-of-plane (in-plane) sensitive tip. As also found experimentally, the apparent DW width is slightly larger for in-plane than for out-of-plane sensitive tips. This can be explained on the basis of equation (1): the magnetic corrugation at the DW scales cosine-like for an out-of-plane sensitive tip but sine-like for an in-plane sensitive tip, with the former having a rather steep zero-crossing at the DW position. The very weak topographical (non-magnetic) atomic contrast observed wherever $\mathbf{u}_T \perp \mathbf{m}(\mathbf{r})$ (see, for example, the domains in Fig. 2c) is below the experimental resolution limit[20,24].

To discuss whether p-DWs can cause uncompensated magnetic moments, we have schematically illustrated four principal types of p-DWs in Fig. 3. The p-DWs may be centred between (top row of Fig. 3) or on top of atomic rows (middle row), and either oriented along the [010] (left column of Fig. 3) or along the [110] direction (right column), respectively. For the ease of illustration, Fig. 3 shows a fully coplanar situation, but the following arguments are also valid for a system such as Fe/W(001), where the easy axis is perpendicular to the surface and to the wall direction. The schematic diagram reveals that—irrespective of their symmetry—⟨010⟩-oriented DWs are always compensated because adjacent spins within any row parallel to the wall point in opposite directions. The situation is different for p-DWs along ⟨110⟩ directions as their magnetic moments do not cancel. The direction of the uncompensated moment depends on the position of the p-DW centre: if the p-DW centre is on top of an atomic row it points along the spins that form the DW centre, in the case of a wall that is centred between two atomic rows it is along the quantization axis within the domains. The bottom row of Fig. 3 shows the perpendicular component of the magnetization as obtained from MC simulations for p-DWs, which almost perfectly run along the [010] (left column) and the [110] (right column) direction. In agreement with the arguments

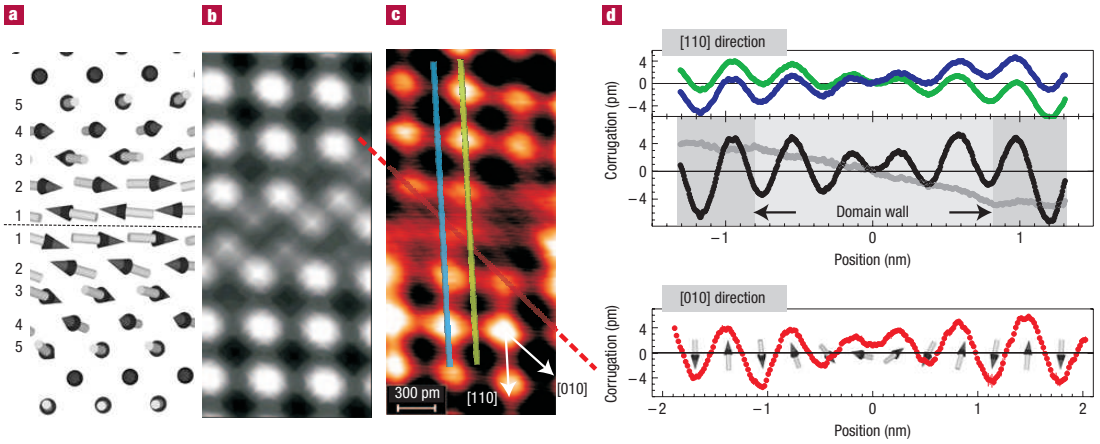

Figure 4 Detailed view of a ⟨110⟩-oriented p-DW. a, Theoretical spin structure, **b**, simulated, and **c**, experimental SP-STM image of a p-DW in the out-of-plane antiferromagnetic Fe monolayer on W(001). **d**, Height profiles drawn at the positions of the correspondingly coloured lines in **c** along the [110] (upper panel) and the [010] (lower panel) direction. Middle panel: sum (black) and difference (grey) of the line profiles shown in the upper panel. The wall is about 1.6-nm wide, and its out-of-plane component exhibits mirror symmetry.

mentioned above, the [010]-oriented wall is compensated (average total magnetization $\leq 10^{-4}$ μ_{Fe} per nm DW length). Although not perfectly mirror-symmetric, the DW centre of [110]-oriented p-DWs is always found between two atomic rows and—in agreement with the uncompensated moment in the simple sketch—a finite perpendicular moment of about 0.6 μ_{Fe} per nm DW length remains. We can only speculate about the cause of the deviation from perfect mirror-symmetry: possibly it is due to thermal fluctuations or an incommensurable DW width.

Now we want to focus on a wall approximately directed along the ⟨110⟩ direction. A closer view of the azimuthal orientation of spins within the wall of Fig. 2a (middle of segment (i)) is shown in Fig. 4a. As mentioned above, the MC simulations find the DW centre between two atomic rows. For clarity the atomic rows are numbered successively 1–5 with respect to their distance from the DW centre in Fig. 4a. The wall centre is formed by two rows 1 with a predominant in-plane orientation ($\Theta \geq 65°$). With increasing distance from the DW centre, the moments tilt more and more into the out-of-plane direction; the in-plane component of rows 4 and 5 is already very small. Apparently, the wall is 6–8 atomic rows wide and Bloch-like. Comparing equidistant atomic rows located on opposite sides of the DW centre it becomes clear that the in-plane component is reversed, whereas the out-of-plane component is equal. Thereby, the integrated in-plane component of magnetization is perfectly cancelled but, interestingly, a non-vanishing net magnetic moment remains for the out-of-plane component.

Figure 4b and c shows a calculated and experimental SP-STM image of such a wall, respectively. Although there are some differences regarding details of the contrast within the DW, the width and general appearance of the DW is well reproduced. To gain a better understanding of the experimentally observed structure we have plotted two experimental line sections taken on adjacent atomic rows along the [110] direction, that is, perpendicular to the wall (Fig. 4d (upper panel)). These two rows are approximately equally distant from the termination points of the DW. The middle panel shows the sum and the difference of these lines in black and grey, respectively. The difference (grey) shows an almost constant signal of opposite sign at the left and right rim of the line section, that is, far away from the DW centre. These regions (domains) are connected by a constant slope that extends over approximately 1.6 nm, which corresponds to the wall width of 6–8 atomic rows mentioned above. The sum (black) reveals that the average out-of-plane component of these atomic rows is mirror-symmetric. The mirror-symmetric appearance, which is also found in the line profile taken along the [010] direction (lower panel of Fig. 4d), indicates—in agreement with the above-mentioned MC calculations—that the DW centre is located between two atomic rows. This is also confirmed by an interpolation of the atomic periodicity from the two domains into the DW (arrows in lower panel of Fig. 4d). Possibly, the position of the DW centre moves out of a mirror-symmetric position between two atomic rows when approaching the termination points of the DW that are outside the field of view of Fig. 4c. Although we did not study the behaviour at the rim of the antiferromagnetic monolayer in detail, a similar effect appears in our MC simulations, best visible at the bottom-left edge of the spin disc in Fig. 2.

Owing to the fact that DWs in antiferromagnets cost exchange energy but cannot lower the dipolar energy, they are very rare and short on clean surfaces. However, we believe that they may be much more frequent in a typical EB situation. Here, the antiferromagnet is covered with a ferromagnetic film that typically has a higher magnetic ordering temperature than the antiferromagnet. Consequently, the antiferromagnet is in contact with a ferromagnet when it orders magnetically. In this case, we expect that the exchange coupling to the ferromagnet induces a relevant number of p-DWs. Whether the resulting uncompensated moment—in addition to moments that arise from known sources as grain size[4,7,8], step-edges[9], and non-magnetic defect sites[10,11]—significantly contributes to EB, is beyond the scope of our paper.

METHODS

The experiments were carried out in an ultrahigh-vacuum system (Omicron Multiprobe MX) specially designed for magnetic imaging[25]. Within a cryostat (on the basis of the model spectromag) from Oxford Instruments, it contains a

home-built low-temperature ($T = 13 \pm 1$ K) scanning tunnelling microscope[25], which is equipped with a tip-exchange mechanism allowing the *in vacuo* preparation of magnetic thin-film tips[21]. We used Fe-coated probe tips, which—in the absence of an external magnetic field—are magnetically in-plane sensitive with respect to the sample surface. Typical tunnelling parameters in this study were $U = 4$ mV (sample bias) and $I_{set} = 30$ nA (set-point of the tunnelling current). The tip magnetization can be reversibly forced into the direction along the tip axis by the field of a superconducting magnet (maximum field $\mu_0 H = 2.7$ T) leading to out-of-plane sensitivity.

Received 28 November 2005; accepted 23 March 2006; published XX Month XXXX.

References

1. Meiklejohn, W. H. & Bean, C. P. New magnetic anisotropy. *Phys. Rev.* **102,** 1413–1414 (1956).
2. Meiklejohn, W. H. & Bean, C. P. New magnetic anisotropy. *Phys. Rev.* **105,** 904–913 (1957).
3. Kiwi, M. Exchange bias theory. *J. Magn. Magn. Mater.* **234,** 584–595 (2001).
4. Ohldag, H. *et al.* Correlation between exchange bias and pinned interfacial spins. *Phys. Rev. Lett.* **91,** 017203 (2003).
5. Koon, N. C. Calculations of exchange bias in thin films with ferromagnetic/antiferromagnetic interfaces. *Phys. Rev. Lett.* **78,** 4865–4868 (1997).
6. Schulthess, T. C. & Butler, W. H. Consequences of spin-flop coupling in exchange biased films. *Phys. Rev. Lett.* **81,** 4516–4519 (1998).
7. Takano, K., Kodama, R. H., Berkowitz, A. E., Cao, W. & Thomas, G. Interfacial uncompensated antiferromagnetic spins: Role in unidirectional anisotropy in polycrystalline $Ni_{19}Fe_{19}$/CoO bilayers. *Phys. Rev. Lett.* **79,** 1130–1133 (1997).
8. Takano, K., Kodama, R. H., Berkowitz, A. E., Cao, W. & Thomas, G. Role of interfacial antiferromagnetic spins in unidirectional anisotropy in $Ni_{19}Fe_{19}$/CoO bilayers. *J. Appl. Phys.* **83,** 6888–6892 (1998).
9. Malozemoff, A. P. Random-field model of exchange anisotropy at rough ferromagnetic-antiferromagnetic interfaces. *Phys. Rev. B* **35,** 3679–3682 (1987).
10. Nowak, U. *et al.* Domain state model for exchange bias: I. Theory. *Phys. Rev. B* **66,** 014430 (2002).
11. Keller, J. *et al.* Domain state model for exchange bias: II. Experiment. *Phys. Rev. B* **66,** 014431 (2002).
12. Scholl, A. *et al.* Observation of antiferromagnetic domains in epitaxial thin films. *Science* **287,** 1014–1016 (2000).
13. Nolting, F. *et al.* Direct observation of the alignment of ferromagnetic spins by antiferromagnetic spins. *Nature* **405,** 767–769 (2000).
14. Hillebrecht, F. U. *et al.* Magnetic moments at the surface of antiferromagnetic NiO(100). *Phys. Rev. Lett.* **86,** 3419–3422 (2001).
15. Weber, N. B., Ohldag, H., Gomonaj, H. & Hillebrecht, F. U. Magnetostrictive domain walls in antiferromagnetic NiO. *Phys. Rev. Lett.* **91,** 237205 (2003).
16. Pratzer, M. *et al.* Atomic-scale magnetic domain walls in quasi-one-dimensional Fe nanostripes. *Phys. Rev. Lett.* **87,** 127201 (2001).
17. Heinze, S. *et al.* Real-space imaging of two-dimensional antiferromagnetism on the atomic scale. *Science* **288,** 1805–1808 (2000).
18. Kubetzka, A. *et al.* Revealing antiferromagnetic order of the Fe monolayer on W(001): Spin-polarized scanning tunneling microscopy and first-principles calculations. *Phys. Rev. Lett.* **94,** 087204 (2005).
19. Yang, H., Smith, A. R., Prikhodko, M. & Lambrecht, W. R. L. Atomic-scale spin-polarized scanning tunneling microscopy applied to Mn_3N_2(010). *Phys. Rev. Lett.* **89,** 226101 (2002).
20. Wortmann, D., Heinze, S., Kurz, P., Bihlmayer, G. & Blügel, S. Resolving complex atomic-scale spin structures by spin-polarized scanning tunneling microscopy. *Phys. Rev. Lett.* **86,** 4132–4135 (2001).
21. Bode, M. Spin-polarized scanning tunneling microscopy. *Rep. Progr. Phys.* **66,** 523–582 (2003).
22. Vedmedenko, E. Y., Grimm, U. & Wiesendanger, R. Noncollinear magnetic order in quasicrystals. *Phys. Rev. Lett.* **93,** 076407 (2004).
23. <http://www.flapw.de>.
24. Chen, C. J. *Introduction to Scanning Tunneling Microscopy* (Oxford Univ. Press, Cambridge, 1993).
25. Pietzsch, O., Kubetzka, A., Haude, D., Bode, M. & Wiesendanger, R. A low-temperature ultrahigh vacuum scanning tunneling microscope with a split-coil magnet and a rotary motion stepper motor for high spatial resolution studies of surface magnetisma. *Rev. Sci. Instrum.* **71,** 424–430 (2000).

Acknowledgements

We thank C. M. Schneider (FZ Jülich) and U. Nowak (University of York, UK) for helpful discussions. Financial support from the DFG (SFB 668 and Graduate School 'Design and characterization of functional materials'), from the EU project ASPRINT, from the Stifterverband für die Deutsche Wissenschaft, and from the Interdisciplinary Nanoscience Center Hamburg is gratefully acknowledged. Correspondence and requests for materials should be addressed to M.B.
Supplementary Information accompanies this paper on www.nature.com/naturematerials.

Competing financial interests

The authors declare that they have no competing financial interests.

PHYSICAL REVIEW B VOLUME 59, NUMBER 5 1 FEBRUARY 1999-I

Magnetic vortices in ultrathin films

E. Yu. Vedmedenko
Groupe de Physique des Solides, UMR 7588 - CNRS, Universités Paris 7 et Paris 6, 75251 Paris 5, France and Biophysical Department, Medical University of Lugansk, 348045 Lugansk, Ukraine

A. Ghazali*
Groupe de Physique des Solides, UMR 7588 - CNRS, Universités Paris 7 et Paris 6, 75251 Paris 5, France

J.-C. S. Lévy
Laboratoire de Physique Théorique de la Matière Condensée, Université Paris 7, case 7020, 75251 Paris 5, France
(Received 6 October 1998)

By means of Monte Carlo simulations, magnetic configurations with *vortices* are shown to appear in ultrathin magnetic films with exchange and dipolar interactions. The stability of these vortices is studied in detail. The presence of perpendicular anisotropy and external magnetic field is also investigated. A magnetic soliton is shown to appear during in-plane magnetization reversal. [S0163-1829(99)01005-X]

Recent experiments on epitaxial magnetic layers[1] have introduced a class of two-dimensional (2D) magnetic systems. Different complex domain structures with some evidence for defects have been observed in thin films and bilayer systems by means of Foucault imaging,[2,3] and in nanostructures, by magnetic force microscopy experiments.[4] Complex magnetic structures are inherent in such systems because of competitions between short-range and long-range interactions. Recent theoretical works on domain structures of vector spins in magnetic monolayers have been performed either by semianalytical calculations on conjectured configurations,[5] or by Monte Carlo simulations.[6,7] These theoretical studies provide evidence for the existence of several solutions for spin configurations. Major questions remain in such 2D complex systems: Are there uniform stable spin configurations or not, and if not, are there intrinsic topological defects and how are they organized? In order to answer these questions, numerical studies of the stability of realistic magnetic configurations with vector spins are needed. This is the aim of this paper. Spin configurations of much larger systems than those considered before[6,7] are obtained by means of extensive Monte Carlo (MC) treatments: Initial random configurations are submitted to a long annealing at a high enough temperature followed by a stepwise slow cooling down in order to obtain equilibrium spin configurations at very low temperature. Two particular configurations both with and without MC relaxation are also studied for energy comparison.

The general Hamiltonian of a monolayer lattice in the x-y plane with three-component vector spins $\mathbf{S}$ and $S=1$ includes local exchange, dipolar interactions, perpendicular anisotropy, and external field:

$$\mathcal{H}=-\sum_{\langle ij\rangle}\mathcal{J}\mathbf{S_i}\cdot\mathbf{S_j}+\mathrm{D}\sum_{\mathbf{ij}}\left(\frac{\mathbf{S_i}\cdot\mathbf{S_j}}{\mathbf{r_{ij}^3}}-3\frac{(\mathbf{S_i}\cdot\mathbf{r_{ij}})(\mathbf{S_j}\cdot\mathbf{r_{ij}})}{\mathbf{r_{ij}^5}}\right)$$
$$-\mathbf{A}\sum_{\mathbf{i}}\mathbf{S_{i,z}^2}-\sum_{\mathbf{i}}\mathbf{H}\cdot\mathbf{S_i}. \quad (1)$$

Here J is the exchange interaction which is assumed to be nonzero only for nearest-neighbor couplings. D is the dipolar coupling parameter and the running site subscripts i and j define the in-plane vector $\mathbf{r_{ij}}$. The parameter A measures the perpendicular single-site anisotropy energy. The external field $\mathbf{H}$ may have any direction.

Simple remarks can be deduced from a scaling approach. They enable us to consider very large samples which could not be introduced directly in the present numerical computation. Let us define the dimensionless parameter $K=D/(Ja^3)$ with the lattice parameter a. Without anisotropy and without external field, the scaling parameter a remains the only free variable: Different ratios D/J can be considered as issued from a single case with a given K value but with different effective lattice parameters a. As usual, this size scaling is valid as far as the discrete character of the lattice can be neglected. Thus increasing the dipolar coupling D while keeping the exchange coupling J constant amounts to a mere increase of the effective lattice parameter a. In the usual magnets, the ratio $D/(Ja_0^3)$ is of the order of 10^{-3}–10^{-4}, where a_0 is a typical atomic distance in metals. Thus, for $D/J=0.1$, $a\approx 5a_0$–$10a_0$ and for $D/J=1$, $a\approx 10a_0$–$20a_0$. So large values of D/J are relevant to large samples. In the present work, we used large values of D/J to consider scales much larger than a few tens of atomic distances.

In the present calculations, samples with free boundaries are considered. It is well known that dipolar contributions depend on the shape of the sample. This is the demagnetizing field effect. Without anisotropy and without external field, our final MC spin configurations at very low temperature are in-plane, in keeping with known results from magnetostatics. In addition, the boundary-layer spins are in general parallel to the sample boundary. This is in agreement with the van den Berg's geometrical approach to in-plane domain structures in 2D spin configurations.[8] We present results for disk-shaped and rectangle-shaped samples. Typical low-temperature spin morphologies obtained in this work are shown in Fig. 1 for disks of 10 192 spins on a triangular lattice with $D/J=0.1$, $D/J=1$, and $J=0$, respectively. The

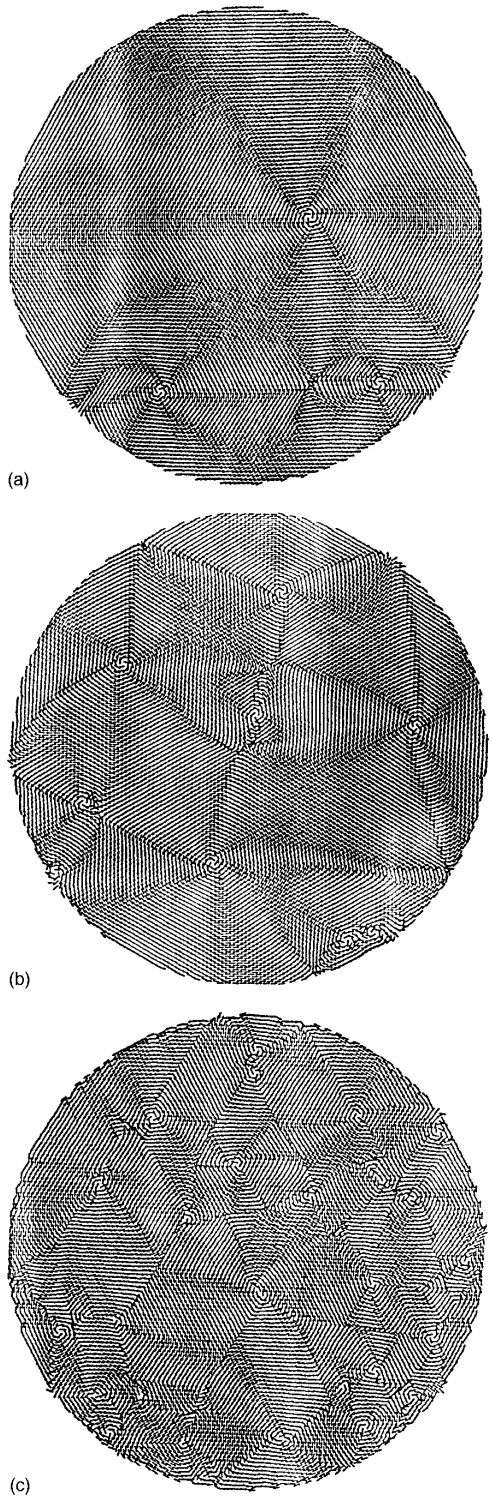

FIG. 1. Low-temperature spin configurations. Samples are disks of 10 192 vector spins on a triangular lattice: (a) $D/J=0.1$, (b) $D/J=1$, (c) pure dipolar coupling: $J=0$.

sample diameter covers about 106 effective spin sites. The MC calculations have been performed *without cutoff length* in the dipolar interactions. As will be discussed below, this is important because the screening of dipolar interactions due to in-plane configurations is very weak.

In the case $D/J=0.1$, i.e., at submicrometer size in a realistic material (disk diameter $\approx 500a_0-1000a_0$), the energies per spin obtained for the above-mentioned configurations are all quite close to each other. The ferromagnetic configuration has even a lower energy than the optimal MC configuration shown in Fig. 1 which contains only a few vortices. Thus for a sample of such a size, only one or two vortices are present in the ideal structure.

When $D/J=1$, i.e., at a larger size in a realistic material (disk diameter $\approx 1000a_0-2000a_0$), the ferromagnetic configuration has the highest energy among all the considered configurations. This is evidence for the stability of configurations with several vortices in the sample at such a mesoscopic size.

Finally, in the pure dipolar case, i.e., at a macroscopic scale in a realistic material, configurations obtained from MC simulations present many vortices with an energy per spin somewhat higher than the one obtained for just a single central vortex. In fact, a realistic spin configuration contains probably several vortices but less than what we found after several thousand MC steps per spin when starting from a random initial configuration. The reason for this limitation is that the single-spin MC procedure makes any vortex motion very difficult because vortices are correlated. However, expulsion of vortices is observed, generally by pairs, during a long time MC relaxation at a low temperature. Every pair expulsion is associated with a small stepwise energy drop. Thus the relaxation process is very long. This shows evidence of the strong frustration effects at all scales due to the long-range dipolar interactions.

All structures shown in Fig. 1 exhibit several *vortices*. The numbers of clockwise vortices and counterclockwise vortices are nearly equal. More precisely, one may define a local vorticity parameter as $q_i=(a/2)(\mathrm{curl}\ \mathbf{S_i})_\mathbf{z}$, with $|q_i| \leqslant 1$. This enables us to draw up the vorticity map of our samples. Figure 2 shows an example of the sign and strength of the spin field vorticity for the pure dipolar case. Spin sites with vorticity of strong absolute value define two interwoven networks of continuous lines which link the cores of vortices of the same chirality. It should be noticed that these strong vorticity lines are the domain walls. The local vorticity parameter q_i defined above provides an elegant way to find out all domain walls in a given sample. Let us mention that the strong vorticity lines are somewhat similar to von Kármán streets which link vortices of the same sign in 2D turbulent flows.[9] Such an analogy is probably connected with the strong spatial inhomogeneity of the dipolar field.

The vortex spatial distribution is analyzed by means of pair-distribution functions (PDF). When vortices of both signs are considered all together, they are distributed at random, as seen in the pictures of Fig. 1; their PDF has no significant structure. However, the PDF of vortices of a specific sign gives evidence for short-range repulsion. Thus the presence of vortices of both signs ensures a medium-range screening of the effective interaction between vortices. It must be noticed that the introduction of any cutoff length in

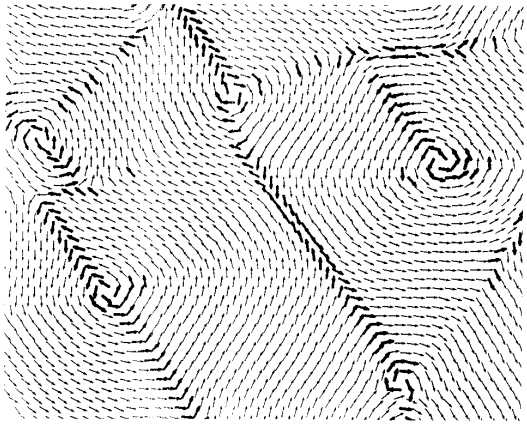

FIG. 2. Enlarged portion of Fig. 1 (c) showing domain walls defined by q_i (thick arrows). The walls connect vortices of the same sign. Here pure dipolar coupling; $k_BT/(D/a^3)=0.01$.

the dipolar interaction leads at the end of the MC thermalization process to a rather ordered vortex lattice. The lattice parameter of this lattice is approximately equal to the cutoff length. This has been checked for different cutoff lengths. It proves that the screening is very sensitive to the long-range part of the dipolar coupling. However the spin energy is only just altered by the cutoff. For instance, in a rectangle-shaped sample of 10 201 spins with pure dipolar couplings, and for cutoff lengths of 15 a and 20 a, energy differences compared to the full coupling case are found not to exceed 1%. In liquid crystals, similar ordered lattices of topological defects have been observed, as in cholesteric and smectic thin films under mechanical tension.[10] Here electric dipolar couplings play the same role as magnetic dipolar interactions in our case.[11] In liquid crystals, ion-induced screening yields a natural cutoff length and could be the reason for the appearance of such an order.

For disks of 10 192 spins on a triangular lattice, the low-temperature energies per spin for different D/J ratios are compared in Table I for (i) three MC relaxed magnetic structures derived from different initial configurations, and for (ii) two unrelaxed particular configurations. In all considered cases, the lowest energy is obtained for the configuration with a single central vortex. After a long relaxation process which ends at a very low temperature, the configuration with a single central vortex remains the one with the lowest energy among the considered configurations. This proves the stability of vortex configurations in all these cases.

TABLE I. Comparison of average energies per spin at very low temperature. Energy unit$=J$ ($=D$ for pure dipolar case).

	Energy per spin		
	$D/J=0.1$	$D/J=1$	$J=0$
MC relaxation	-3.220	-5.662	-2.701
Ideal ferro	-3.227	-5.595	-2.632
Ferro+MC	-3.223	-5.619	-2.616
1 central vortex	-3.234	-5.703	-2.743
1 vortex+MC	-3.231	-5.700	-2.740

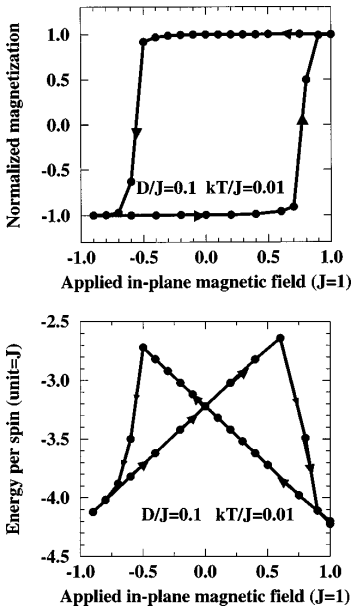

FIG. 3. In-plane field hysteresis loop: (top) magnetization, (bottom) spin energy vs applied field.

When introducing a large enough perpendicular anisotropy in the problem, all MC relaxed configurations contain many out-of-plane spins. The average value $\langle S_z^2 \rangle$ is a good measure of the transition from in-plane spins towards perpendicular spins. This spin reorientation transition occurs when the uniaxial anisotropy energy is of the order of magnitude of the dipolar interaction energy. It is characterized by the appearance of several domains of twisted bunches of nearly up spins or down spins. These domains are surrounded by domains with almost in-plane spins.[12] A detailed study of the reorientation transition will be given elsewhere.[13]

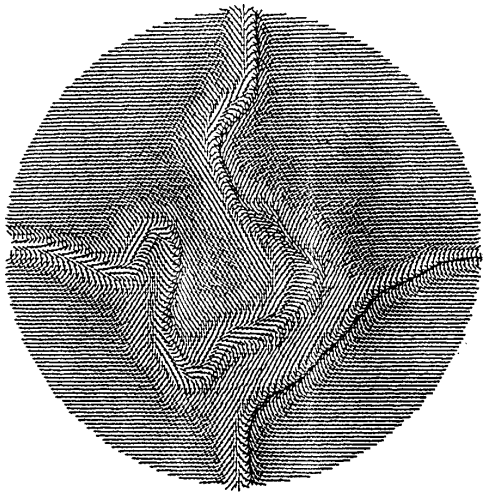

FIG. 4. Snapshot of a double-wall magnetic soliton at the in-plane coercive field. $D/J=0.1, H_x/J=-0.6, k_BT/J=0.01$.

The introduction of a high enough external field H_z normal to the surface leads also to the appearance of out-of-plane spins with a similar transition towards an Ising-type system. However, this transition occurs at a field value which is much larger than the dipolar field one.[12,13] On the contrary, the application of a moderate in-plane external field H_x is enough to saturate the in-plane magnetization. A typical rectangle-shaped magnetization *versus* applied field hysteresis loop and the respective energy *versus* field curve are reported in Fig. 3 for $D/J=0.1$. This gives evidence for a sharp quasistatic coercive field. Taking advantage of the slowness of the MC relaxation process at low temperature, we are able to show in Fig. 4 for $D/J=0.1$ a typical spin snapshot taken during magnetization reversal process. The latter occurs at a field just larger than the coercive field. The rapid propagation of the in-plane domain wall as a solitary wave, i.e., as a *soliton* with a double wall, is also evidence for strong nonlinear effects in this problem. Let us mention that some snapshots obtained in this work are very similar to those found experimentally for soft thin films; see Fig. 8 of Ref. 14.

In conclusion, let us mention that vortices were introduced as intrinsic defects in the general problem of 2D systems.[15] What we have shown here is that vortices are not only possible patterns in 2D magnetic systems with long-range dipolar interactions but that they do belong to the stable spin configurations in ultrathin films.

E.Yu.V. acknowledges financial support from the French Ministry of Education (MENESR). Part of this work was done within the framework of Contract No. CHRX-CT93-0320 of the European Economic Community.

*Author to whom correspondence should be addressed. Electronic address: ghazali@gps.jussieu.fr

[1] For a review, see R. Allenspach, J. Magn. Magn. Mater. **129**, 160 (1994).

[2] J. N. Chapman, J. Phys. D **17**, 623 (1984); A. B. Johnston, J. N. Chapman, B. Khamsehpour, and C. D. W. Wilkinson, *ibid.* **29**, 1419 (1996).

[3] A. C. Daykin and J. P. Jakubovics, J. Appl. Phys. **80**, 3408 (1996).

[4] M. Hehn, K. Ounadjela, J.-P. Bucher, F. Rousseaux, D. Decanini, B. Bartenlian, and C. Chappert, Science **272**, 1782 (1996).

[5] See, e.g., S. Prakash and C. L. Henley, Phys. Rev. B **42**, 6574 (1994).

[6] A. B. MacIsaac, K. De'Bell, and J. P. Whitehead, Phys. Rev. Lett. **80**, 616 (1998).

[7] A. Hucht and K. D. Usadel, J. Magn. Magn. Mater. **156**, 423 (1996).

[8] H. A. M. van den Berg, J. Appl. Phys. **60**, 1104 (1986).

[9] L. Prandtl and O. G. Tietjens, *Applied Hydro- and Aeromechanics* (Dover, New York, 1957), p. 130.

[10] F. Rondelez and H. Arnould, C. R. Seances Acad. Sci., Ser. B **273**, 549 (1971).

[11] For a review, see M. Seul and D. Andelman, Science **267**, 476 (1995).

[12] E. Y. Vedmedenko, A. Ghazali, and J.-C. S. Lévy, Surf. Sci. **402-404**, 391 (1998).

[13] E. Y. Vedmedenko, A. Ghazali, and J.-C. S. Lévy (unpublished).

[14] A. Hubert and M. Rührig, J. Appl. Phys. **69**, 6072 (1991).

[15] J. M. Kosterlitz and D. Thouless, J. Phys. C **6**, 1181 (1973); J. M. Kosterlitz, *ibid.* **7**, 1046 (1974).

INSTITUTE OF PHYSICS PUBLISHING JOURNAL OF PHYSICS: CONDENSED MATTER

J. Phys.: Condens. Matter **16** (2004) 9037–9045 PII: S0953-8984(04)83046-7

Multipole interaction of polarized single-domain particles

N Mikuszeit, E Y Vedmedenko and H P Oepen

Universität Hamburg, Institut für Angewandte Physik, Jungiusstrasse 11a, 20355 Hamburg, Germany

E-mail: Elena.Vedmedenko@physik.uni-hamburg.de

Received 28 June 2004, in final form 6 October 2004
Published 26 November 2004
Online at stacks.iop.org/JPhysCM/16/9037
doi:10.1088/0953-8984/16/49/019

Abstract

The multipole moments and multipole–multipole interactions of uniformly polarized particles have been calculated based on the fundamental theory of electrostatics. As the polarization of the particles is uniform, only surface charges are considered. The polarization may have its origin in magnetization or ferroelectricity or be an intrinsic property of molecules. It is demonstrated that, depending on the geometry of the particles, the higher order interactions can be comparable to or even stronger than the dipole–dipole interaction. The higher order moments give rise to an additional energy contribution in arrays of close packed polarized nanoparticles. The influence of particle aspect ratios as well as array periodicity is discussed.

1. Introduction

Miniaturization plays an important role in modern physics and chemistry as it gives access to new phenomena that can be used in technical applications. It is desirable to increase the density of clusters, dots and micelles, which is correlated with a decrease of their size. Often the particles are polarized or charged. In that case the particles interact. The strength of the interaction increases with decreasing interparticle distance and can be described by means of the multipole expansion. A general calculus for multipole moments can be found in textbooks [1]. However, higher order moments are only calculated to describe molecular orbitals in physical chemistry [2]. In all other cases (magnetic arrays, ferroelectric arrays, colloids etc) the calculations are restricted either to the pure dipole–dipole interaction between the dots [3] or to the first multipole correction to the dipolar coupling [6, 4, 5]. The higher order contributions have not been studied systematically as terms beyond the dipolar one are of minor importance for special cases of zero-thickness in-plane magnetized squares [4] /discs [5]. Only that kind of particles has been addressed in the literature. However, experimentally and industrially produced arrays consist of particles of variable geometry depending on material

and method of preparation. Thus, a general procedure for the calculus of multipole moments of polarized nanoparticles as a function of aspect ratio and symmetry is highly needed as the knowledge of the interaction energy of higher order multipole moments is crucial for further investigations on the magnetic order and magnetic phase transitions in stray field coupled systems.

The multipole expansion may be made either in Cartesian or in spherical coordinates. The advantage of the Cartesian expansion is that only real numbers are required. However, each term of the expansion is a tensor. The order L of the tensor is equivalent to the order of the expansion. The number of independent tensor components of a three-dimensional symmetric tensor increases with the square of L, thus it is a formidable task to treat terms with rank higher than two (quadrupole moments) [4, 6]. The spherical expansion needs complex numbers but its complexity does not change with the order of expansion as the number of independent components is proportional to L. So, it seems that almost any order can be calculated within reasonable effort. However, the treatment of a planar charge distribution in spherical coordinates leads to very complicated integrals. To avoid this difficulty we use the spherical harmonic formalism but express it in Cartesian coordinates. In this way we define a general procedure to calculate the multipole moments and the corresponding interaction energies of axially symmetric particles. This symmetry class has a wide range of application, e.g. in storage media [7–9]. We demonstrate that for prismatic particles with mirror symmetry only multipole moments of the same symmetry are different from zero. All other multipolar contributions are extinct. This permits us to decrease drastically the computational efforts for calculation of magnetostatic interactions in magnetic/electric arrays. For certain geometries the interaction due to higher order moments is of the same order of magnitude as the dipolar coupling. Hence, it must be considered in the description of order phenomena in close packed arrays or hysteresis and switching behaviour of magnetic or ferroelectric particles.

For the sake of simplicity we restrict the discussion to particles with n-fold rotational symmetry that are polarized parallel to the axis of symmetry or have charged base planes. Although we discuss in this paper only axial systems with point-symmetric charge distributions of negative parity the theory can be easily generalized to positive parity or other geometries, e.g. in-plane polarized discs.

2. Multipole moments of symmetric particles

The multipole moments of a charge distribution $\rho(\boldsymbol{r})$ in spherical coordinates $\boldsymbol{r} = (r, \theta, \varphi)$ are defined by [1]

$$Q_{l\,m} = \int_V \mathrm{d}V\ \rho(\boldsymbol{r}) R_{l\,m}(\boldsymbol{r}) \tag{1}$$

where the integration is performed over the volume V that encloses $\rho(\boldsymbol{r})$, weighted by the regular normalized spherical harmonic $R_{l\,m}(\boldsymbol{r})$ [1] (see also (4))

$$R_{l\,m}(\boldsymbol{r}) = \sqrt{\frac{4\pi}{2l+1}} r^l Y_{l\,m}(\theta, \varphi). \tag{2}$$

The spherical harmonics $Y_{l\,m}(\theta, \varphi)$ represent a complete set of orthogonal functions on the sphere [10]. They are numbered by two independent parameters l and m corresponding to the two degrees of freedom on a sphere θ and φ. The far-field potential is [1]

$$\Phi(\boldsymbol{r}) = \frac{1}{4\pi\mu_0} \sum_{l=0}^{\infty} \sum_{m=-l}^{l} I_{l\,m}(\boldsymbol{r}) Q^*_{l\,m} \tag{3}$$

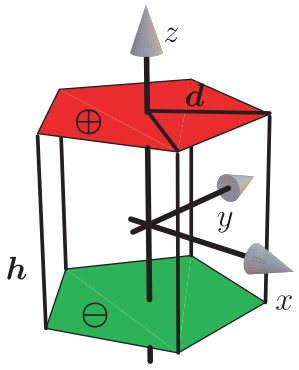

Figure 1. Scheme of a nanoparticle with fivefold (n-fold) symmetry. Every surface can be divided into five (n) equivalent isosceles triangles with edge length d. The particle is polarized in the z-direction.

(This figure is in colour only in the electronic version)

with the irregular normalized spherical harmonics

$$I_{l\,m}(\boldsymbol{r}) = \sqrt{\frac{4\pi}{2l+1}}\frac{Y_{l\,m}(\theta,\varphi)}{r^{l+1}} \tag{4}$$

and $Q^*_{l\,m}$ the complex conjugate of $Q_{l\,m}$. The field can be determined as the negative gradient of the potential $\boldsymbol{F} = -\nabla\Phi$. To ensure the uniqueness of the expansion, the origin of the coordinate system must coincide with the centre of charge

$$\boldsymbol{r}_\mathrm{s} = \frac{\int_V \mathrm{d}V\,\boldsymbol{r}\cdot|\rho(\boldsymbol{r})|}{\int_V \mathrm{d}V\,|\rho(\boldsymbol{r})|}, \tag{5}$$

i.e. $\boldsymbol{r}_\mathrm{s} = 0$; otherwise even the expansion of the potential of a point charge includes higher order moments. The remaining freedom of rotation is handled by tensor transformation rules for spherical harmonics given in [10].

2.1. The relationship between particle symmetry and multipole moments

Let us assume a nanoparticle with n-fold symmetry ($n > 1$) within the x–y-plane, which is polarized in the z-direction (figure 1). The symmetry axis is parallel to the polarization. The upper surface of the particle is positively charged with the surface charge density $\sigma(\boldsymbol{r}) = \mu_0\boldsymbol{n}\cdot\boldsymbol{M}(\boldsymbol{r})$ due to uncompensated dipoles, with the unit vector $\boldsymbol{n}$ perpendicular to the surface and the magnetization vectorfield $\boldsymbol{M}(\boldsymbol{r})$. Hence, with this definition the unit for the magnetic charge is V s and the magnetic dipole moment is measured in V s m. The bottom charge is the mirror image of the positive charge distribution at the top of the particle. To integrate (1) explicitly, we divide the surface into n identical triangles (figure 1). Then the $Q_{l\,m}$ are calculated by the sum over the triangles ($0 \leqslant j \leqslant n-1$) of the top and the bottom surfaces. As the charged surfaces are planar we replace the volume charge density $\rho(\boldsymbol{r})$ and the volume integration (1) by the surface charge density $\sigma(\boldsymbol{r})$ and an integration over the surface element $\mathrm{d}S$.

$$Q_{l\,m} = \sum_{j=0}^{n-1}\left(\int_{j\text{th top-triangle}}\mathrm{d}S\,|\sigma(\boldsymbol{r})|R_{l\,m}(\boldsymbol{r}) - \int_{j\text{th bottom-triangle}}\mathrm{d}S\,|\sigma(\boldsymbol{r})|R_{l\,m}(\boldsymbol{r})\right). \tag{6}$$

Due to the symmetry of spherical harmonics

$$Y_{l\,m}(\theta,\varphi) = (-1)^{l+m}Y_{l\,m}(\pi-\theta,\varphi) \tag{7}$$

Table 1. The multipole moments $Q_{l\,m}$ (in units of the surface charge density) up to the order $L = 7$ of a particle with fourfold symmetry. All $Q_{l\,m}$ with even l vanish.

l	$m = 0$	$m = 4$[a,b]
1	$2hd^2$	
3[c]	$hd^2\left(\frac{h^2}{2} - d^2\right)$	
5	$\frac{h^5d^2}{8} - \frac{5h^3d^4}{6} + \frac{7hd^6}{12}$	$-\sqrt{\frac{7}{10}}\frac{hd^6}{4}$
7	$\frac{h^7d^2}{32} - \frac{7h^5d^4}{16} + \frac{49h^3d^6}{48} - \frac{3hd^8}{8}$	$\sqrt{\frac{33}{14}}\frac{hd^8}{8} - \sqrt{\frac{77}{6}}\frac{h^3d^6}{16}$

[a] m must be zero or a multiple of 4.
[b] $Q_{l\,-m} = (-1)^m Q^*_{l\,m}$ due to the symmetry of spherical harmonics.
[c] Hence, $Q_{3\,0} = 0$ for $h = \sqrt{2}d$, i.e. a cube.

the sum over the bottom triangles is incorporated into the first sum by the term $(-1)^{l+m+1}$. The azimuthal symmetry $Y_{l\,m}(\theta, \varphi) \propto \exp(\mathrm{i}m\varphi)$ allows us to write

$$
\begin{aligned}
Q_{l\,m} &= \sum_{j=0}^{n-1} \int_{j\text{th top-triangle}} \mathrm{d}S\,(1 + (-1)^{l+m+1})|\sigma(\boldsymbol{r})|R_{l\,m}(\boldsymbol{r}) \\
Q_{l\,m} &= \int_{\text{one top-triangle}} \mathrm{d}S\,(1 + (-1)^{l+m+1})|\sigma(\boldsymbol{r})|R_{l\,m}(\boldsymbol{r}) \sum_{j=0}^{n-1} \exp\left(\mathrm{i}m\frac{2\pi}{n}j\right) \\
&= \int_{\text{one top-triangle}} \mathrm{d}S\,(1 + (-1)^{l+m+1})|\sigma(\boldsymbol{r})|R_{l\,m}(\boldsymbol{r}) n\delta_{0,\mathrm{mod}(m,n)} \qquad (8)
\end{aligned}
$$

where the Kronecker δ is unity for $n|m$ or $m = 0$ only.

The symmetry properties of (8) lead to several conclusions. Multipole moments with even l exist for $n \geqslant 3$ only and no quadrupole moment ($l = 2$) is allowed. If l is even m must be odd. Except for $m = 0$, the smallest m is $m = n$ as n must be a factor of m because of the Kronecker δ. Therefore, the lowest moment with l even is $(l, m) = (4, 3)$ for a threefold symmetry. The first possible multipole moment with even l for a fivefold symmetry is $(l, m) = (6, 5)$. Additionally, all particles with even rotational symmetry do not possess multipole moments with even l. This can be seen from the parity properties of $Y_{l\,m}(\theta, \varphi)$

$$\hat{P}Y_{l\,m}(\theta, \varphi) := Y_{l\,m}(\pi - \theta, \pi + \varphi) = (-1)^m Y_{l\,m}(\theta, \varphi). \qquad (9)$$

If the charge distribution has a negative parity ($\sigma(-\boldsymbol{r}) = -\sigma(\boldsymbol{r})$), which is the case for a particle with n even, the integration reduces to

$$Q_{l\,m} = \int_{\text{one top-triangle}} \mathrm{d}S\,(1 + (-1)^{l+1})|\sigma(\boldsymbol{r})|R_{l\,m}(\boldsymbol{r}) \cdot n \cdot \delta_{0,\mathrm{mod}(m,n)} \qquad (10)$$

and l must be odd.

Tables 1 and 2 give the low order moments of a particle with fourfold and cylindrical symmetry, respectively, as a function of the surface area ($\propto d^2$) and the height h of the particle. As expected the dipole moments are proportional to $d^2 \times h$. The dependence of the multipole moments on the effective aspect ratio $h/(\sqrt{2}d)$ of a particle with fourfold symmetry is shown in figure 2. The functions $Q_{l\,m}(h, d)$ may cross zero. This happens for example for the octopole moment of a cube [11] (see figure 2). In the limit of small thicknesses the octopole moment reaches -25% of the dipole moment. This geometry corresponds to sizes of particles often used in experimental studies [12–14]. For vertically elongated particles, such as arrays of magnetic nanocolumns [15, 16] or liquid colloidal crystals with rod-like components [17], the magnitude

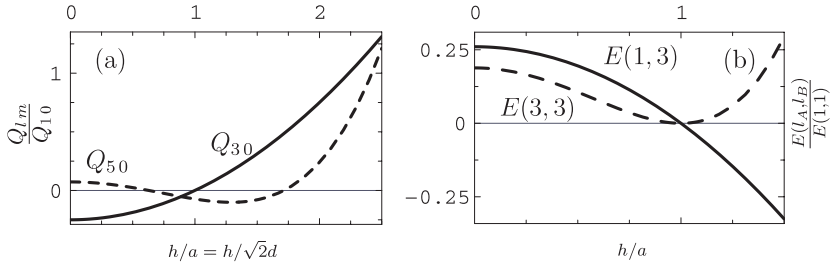

Figure 2. (a) The low order multipole moments $Q_{l\,m}$ (normalized to $Q_{1\,0}$) of particles with fourfold symmetry with height h and edge length a. For $h \to 0$ $Q_{3\,0}$ reaches -25% of $Q_{1\,0}$. (b) The low order multipole–multipole interaction energies $E(l_A, l_B)$ (normalized to the dipole–dipole interaction energy $E(1,\,1)$) of particles with fourfold symmetry with height h and edge length a. The parameters of $E(l_A, l_B)$ specify the multipole moments l_A and l_B that interact (including the sum over m_A and m_B).

Table 2. The multipole moments $Q_{l\,m}$ (in units of the surface charge density) up to the order $L = 7$ of a particle with cylindric symmetry. All $Q_{l\,m}$ with even l vanish.

l	$m = 0$[a]
1	$\pi h d^2$
3	$\frac{\pi}{4} h d^2 (h^2 - 3d^2)$
5	$\frac{\pi}{16} h d^2 (h^4 - 10h^2 d^2 + 10d^4)$
7	$\frac{\pi}{64} h d^2 (h^6 - 21h^4 d^2 + 70h^2 d^4 - 35d^6)$

[a] m must be zero for symmetry reasons.

of the octopole moment exceeds that of the dipole moment. Thus, many experimental systems require the consideration of higher order multipole moments while in the case of elongated polarized objects the consideration of octopole moments is indispensable.

3. The energy contribution of multipole moments with order $L \geqslant 1$

Exact analytical solutions include implicitly all expansion terms. However, one cannot distinguish between the contributions from different moments, i.e. it is impossible to assign the formation of superstructures in an ensemble of particles to particular features of their geometry. The calculation of the higher order multipole moments of a particle gives the possibility to predict the behaviour induced by multipole terms solely from the knowledge of the single particle and the array geometry. Thus, the use of higher order multipole moments is not meant to substitute analytical solutions, but reveals a new, rather simple treatment to distinguish symmetry effects due to single-particle properties on all length scales. The multipole moments give an additional contribution to the magneto-static interaction. The exact interaction energy, including all multipole terms, can be found in the literature, analytically solved for uniform magnetized bodies with fourfold symmetry [18]. However, the expression for the potential is very complicated and even more complex for the interaction energy.

Though the expansion of the potential of a charge distribution is straightforward, the expansion of the interaction of two charge distributions requires a more complex derivation, particularly in the case of intersecting charge distributions, which are included in the sophisticated treatment of that problem [19]. The formulae given in [19], however, demand a transformation of the coordinate system for each pair interaction. We focus on the most general formulation for non-intersecting charge distributions [2] to obtain results that are independent of the coordinate system.

Table 3. Multipole–multipole interaction energies (in units of $\sigma^2(4\pi\mu_0^{-1})$) of two particles with fourfold symmetry. The particles have an edge length $a = \sqrt{2}d$ and height h. The edges are parallel to the coordinate axes and the distance vector between the particles is $\boldsymbol{R}_{AB} = R \cdot \boldsymbol{e}_x$. Every entry of the table represents an interaction of the moment $Q^A_{l_A}$ with $Q^B_{l_B}$. The index m is omitted as the summation over m is carried out. As the table is symmetric, doubled entries are left blank for clarity.

	Q_1^A	Q_3^A	Q_5^A
Q_1^B	$\frac{4h^2d^4}{R^3}$	$-\frac{3h^2d^4(h^2-2d^2)}{2R^5}$	$\frac{h^2d^4(15h^4-100h^2d^2+28d^4)}{32R^7}$
Q_3^B		$\frac{25d^4(h^3-2hd^2)^2}{16R^7}$	$-\frac{7h^2d^4(105h^6-910h^4d^2+1692h^2d^4-584d^6)}{768R^9}$
Q_5^B			$\frac{7h^2d^4(567h^8-7560h^6d^2+28776h^4d^4-23840h^2d^6+9328d^8)}{4096R^{11}}$

If $\boldsymbol{R}_{AB}$ is the distance vector from charge distribution A with multipole moments Q^A to charge distribution B with multipole moments Q^B the interaction energy is

$$E_{AB} = \frac{1}{4\pi\mu_0} \sum_{l_A l_B m_A m_B} T_{l_A l_B m_A m_B}(\boldsymbol{R}_{AB})\, Q^A_{l_A m_A}\, Q^B_{l_B m_B} \tag{11}$$

with the geometric interaction tensor $T_{l_A l_B m_A m_B}(\boldsymbol{R}_{AB})$ [1]

$$T_{l_A l_B m_A m_B}(\boldsymbol{R}_{AB}) = (-1)^{-l_B} I^*_{l_A+l_B m_A+m_B}(\boldsymbol{R}_{AB}) \times \sqrt{\frac{(l_A+l_B-m_A-m_B)!}{(l_A-m_A)!(l_B-m_B)!}\frac{(l_A+l_B+m_A+m_B)!}{(l_A+m_A)!(l_B+m_B)!}}. \tag{12}$$

The dependence on the distance is given by $I^*_{l_A+l_B m_A+m_B}(\boldsymbol{R}_{AB})$. Hence, it follows from (12) that the energy contribution from the moments $Q^A_{l_A}$ and $Q^B_{l_B}$ of order l_A and l_b respectively decreases with increasing distance as $R_{AB}^{-\lambda}$ and $\lambda = l_A + l_B + 1$. Consequently, higher order multipole moments are important if $R \gtrsim d$. The infinite series converges to the exact solution.

The multipole–multipole interaction energies for two particles with square base of edge length a and height h (edges parallel to the coordinate axes) with distance vector $\boldsymbol{R}_{AB} = R \cdot \boldsymbol{e}_x$ have been calculated and are given in table 3. The multipole–multipole interaction energies as a function of the particle aspect ratio and $R = 1.2a$ are shown in figure 3. An interparticle distance of $R = 1.2a$ is in the range of experimental values (e.g. $R = 1.1a$ in [20] and $R = 1.4a$ in [21]). For small thickness h the dipole–octopole energy is about 26% and the octopole–octopole interaction is close to 19% of the dipole–dipole energy. As the octopole moment vanishes for a cube, the dipole–octopole interaction energy crosses zero at $h/a = 1$, while the octopole–octopole interaction energy has its minimum value, i.e. zero. For vertically elongated particles the multipole–multipole interactions are even stronger. The energy of multipole–multipole interactions between two particles with fourfold symmetry as a function of the interparticle distance R is presented in figure 3. One sees that for $h/a = 0.4$ and $R = 2a$ the pure dipolar approximation gives only 80% of the total energy. Obviously, for $R \leqslant 2a$ the octopole moment must be considered. For $R \leqslant 1.2a$ the 2^5-pole brings further important energy corrections. Hence, our quantitative results can be directly applied to analyse the magnetostatic interactions between square dots of the patterned $Co_{70}Cr_{18}Pt_{12}$ perpendicular media [21].

The interaction energies that correspond to the geometry and material of [21] are calculated in table 4. For $R = 100$ nm the interaction energy between two particles of size of $70 \times 70 \times 20$ nm^3 due to the octopole moments is 17% of the dipole–dipole energy. For

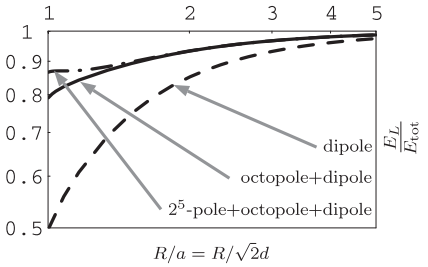

Figure 3. The sums of multipole–multipole energies up to order $L = 1, 3, 5$ normalized to the total energy $E_{\rm tot}$ as function of the interparticle distance R. The aspect ratio is $h/a = 0.4$.

Table 4. The temperature T of the multipole–multipole interaction energies $E = k_{\rm B}T$ of two particles with fourfold symmetry, where $k_{\rm B}$ is the Boltzmann constant. The particles have an edge length $a = 70$ nm and height $h = 20$ nm. The edges are parallel to the coordinate axes and the distance vector between the particles is $\boldsymbol{R}_{AB} = (100\ {\rm nm})\boldsymbol{e}_x$. Every entry in the table represents an interaction of the moment $Q^A_{l_A}$ with $Q^B_{l_B}$. The index m is omitted as the summation over m is carried out. For comparison the energy of $1/2\mu_0 M_S^2 V/k_{\rm B} = 9.44 \times 10^5$ K, where V is the particle volume and $M_S = 4.60 \times 10^5$ A m^{-1}. The numbers in brackets correspond to the values for an infinite square lattice. As the table is symmetric, doubled entries are left blank for clarity.

	Q^A_1	Q^A_3	Q^A_5
Q^B_1	14 719 K (1.33×10^5 K)	2484 K (0.13×10^5 K)	84 K (369 K)
Q^B_3		1165 K (5150 K)	164 K (685 K)
Q^B_5			140 K (572 K)

an infinite square lattice the octopolar energy per particle exceeds 13.5% of the dipolar one. The decrease of the octopolar contribution to the total magnetostatic energy density is due to the faster drop of its strength with the distance. Indeed, the dipolar lattice sum for a square lattice is $S(1, 0, 1; 3/2) = 4\beta(3/2)\zeta(3/2) \approx 9.034$,[1] i.e. in an infinite lattice the field on one lattice site is approximately nine times the field due to one nearest neighbour while for the dipole–octopole interaction the factor is $S(1, 0, 1; 5/2) \approx 5.01$; this equals 56% of the factor for the dipolar interaction. Nevertheless, even a 13.5% effect may significantly change critical properties of an array. For example, a critical temperature $T_{\rm c}$ at which an array becomes ordered due to dipolar plus octopolar interactions will increase by ≈13.5% comparably to a pure dipolar case. Hence, in order to allow for independent particle switching for the perpendicular memory applications one should increase R beyond 100 nm.

In the case of the system from [21] the dipolar interaction alone can induce a long-range order in the array for $R < 150$ nm as the strength of the dipole–dipole coupling $E(1, 1)$ exceeds room temperature (see table 4). A more interesting situation arises for the case of dots with smaller dimensions $30 \times 30 \times 4$ nm^3. In this case the dipole moments of dots decrease and a long-range dipolar ordering cannot be stabilized in an array even for very small interparticle distance of $R = 40$ nm ($E(1, 1) \leqslant 300$ K). The octopole–octopole and dipole–octopole contributions increase the total magnetostatic energy by ≈30% so that the total magnetostatic energy increases to almost 400 K. This is well above the room temperature. Hence, in a certain temperature range a long-range magnetic order in that case can be established. In contrast to the previous situation, however, it is only ensured via higher order magnetostatic contributions.

[1] Where $S(a, b, c; s) = \sum'_{ij}(ai^2 + bij + cj^2)^{-s}$ excluding $i = j = 0$ and $\beta(z)$ and $\zeta(z)$ are the Dirichlet beta function and the Riemann zeta function, respectively [22].

Table 5. The same as in table 4, but for particles with an edge length $a = 8$ nm and height $h = 2$ nm. The distance vector between the particles is $\boldsymbol{R}_{AB} = (9\text{ nm})\boldsymbol{e}_x$. In this case the self-energy is $1/2\mu_0 M_S^2 V/k_B = 1233$ K.

	Q_1^A	Q_3^A	Q_5^A
Q_1^B	34.4 K (311.2 K)	9.6 K (48.7 K)	0.7 K (2.9 K)
Q_3^B		7.4 K (32.7 K)	1.9 K (7.8 K)
Q_5^B			2.4 K (9.9 K)

The third interesting situation arises when the particles have dimensions within the superparamagnetic regime, e.g. $8 \times 8 \times 2$ nm^3 for a material with a weak magnetocrystalline anisotropy. Magnetic moments in those dots are strongly coupled by the exchange interaction and can still be described as magnetized objects. In contrast to the previous situation, however, the anisotropy energy per particle is also comparable with the room temperature and the dots are dynamically unstable. The dipolar energy is comparable with the room temperature (see table 5) as in the previous case. The octopole–octopole and dipole–octopole contributions increase the total magnetostatic energy in an infinite square lattice with period of $R = 9$ nm by $\approx$26%. Hence, the multipole–multipole interactions may bring the thermal stability into the system even in the superparamagnetic regime. This result is in accordance with a recent experimental study [23] on close-packed Co, NiFe and CoFe/Cu/NiFe magnetic particle arrays where a stabilization of magnetic configuration against superparamagnetism for small interparticle distances has been found.

Hence, higher order multipolar terms must be considered in systems of two particles as well as infinite lattices if the distance between the particles is of the same order of magnitude as their diameter ($R \gtrsim d$). Calculations of higher order magnetostatic contributions for many experimental situations can be easily made on the basis of table 3.

4. Summary

In conclusion we have developed a procedure to calculate the multipole moments up to any desired order as well as the correlated interaction energies of axially polarized prism-shaped particles including cylinders. The theory is scale invariant, but as we treat single-domain particles, it is of special interest in the nanoscale regime. We demonstrate that prismatic particles with mirror symmetry do not posses multipole moments of even symmetry (quadrupoles etc). Only the moments of odd symmetry (octopole etc) exist. Depending on the geometry and the interparticle distance, the higher order moments can exceed the dipole moment. Therefore, their contribution to the total energy of an array must be included in the case of close packed nanoparticles and the treatment solely by the dipole–dipole approximation is questionable. Higher order contributions may appear as additional anisotropies and cause anisotropy induced orientational order in colloids or liquid crystals. A shift of the superparamagnetic/super(anti)ferromagnetic transition might also be possible due to higher order multipole moments. This will be the subject of future investigations.

References

[1] Stone A J 1996 *The Theory of Intermolecular Forces* (Oxford: Clarendon)
[2] Popelier P L A and Kosov D S 2001 *J. Chem. Phys.* **114** 6539
[3] Bennett A J and Xu J M 2003 *Appl. Phys. Lett.* **82** 2503

[4] Jensen P J and Pastor G M 2003 *New J. Phys.* **5** 68.1
[5] Costa M D and Pogorelov Yu G 2001 *Phys. Status Solidi* a **189** 923
[6] Politi P and Pini G M 2002 *Phys. Rev.* B **66** 214414
[7] Howard J K 1986 *J. Vac. Sci. Technol.* A **4** 1
[8] Scott J F and Paz de Araujo C A 1989 *Science* **246** 1400
[9] Albrecht M, Rettner C T, Best M E and Terris B D 2003 *Appl. Phys. Lett.* **83** 4363
[10] Varsalovich D A, Moskalev A N and Khersonskii V K 1988 *Quantum Theory of Angular Momentum* (Singapore: World Scientific)
[11] Yan Y D and Della Torre E 1989 *IEEE Trans. Magn.* **25** 2919
[12] Jamet J P, Lemerle S, Meyer P, Ferré J, Bartenlian B, Bardou N, Chappert C, Veillet P, Rousseaux F, Decanini D and Launois H 1998 *Phys. Rev.* B **57** 14320
[13] Aign T, Meyer P, Lemerle S, Jamet J P, Ferré J, Mathet V, Chappert C, Gierak J, Vieu C, Rousseaux F, Launois H and Bernas H 1998 *Phys. Rev. Lett.* **81** 5656
[14] Koike K, Matsuyama H, Hirayama Y, Tanahashi K, Kanemura T, Kitakami O and Shimada Y 2001 *Appl. Phys. Lett.* **78** 784
[15] Fruchart O, Klaua M, Barthel J and Kirschner J 1999 *Phys. Rev. Lett.* **83** 2769
[16] Nielsch K, Wehrspohn R B, Barthel J, Kirschner J, Fischer S F, Kronmüller H, Schweinböck T, Weiss D and Gösele U 2002 *J. Magn. Magn. Mater.* **249** 234
[17] van Duijneveldt J S, Gil-Villegas A, Jackson G and Allen M P 2000 *J. Chem. Phys.* **112** 9092
[18] Rhodes P and Rowlands G 1954 *Proc. Leeds Phil. Lit. Soc.* **6** 191
[19] Buehler R J and Hirschfelder J O 1951 *Phys. Rev.* **83** 628
[20] Warin P, Hyndman R, Gierak J, Chapman J N, Ferré J, Jamet J P, Mathet V and Chappert C 2001 *J. Appl. Phys.* **90** 3850
[21] Rettner C T, Anders S, Thomson T, Albrecht M, Ikeda Y, Best M E and Terris B D 2002 *IEEE Trans. Magn.* **38** 1725
[22] Borwein J M and Borwein P B 1987 *Pi & the AGM: A Study in Analytic Number Theory and Computational Complexity* (New York: Wiley)
[23] Cheng J Y, Jung W and Ross C A 2004 *Phys. Rev.* B **70** 64417

JOURNAL OF APPLIED PHYSICS **97**, 10J502 (2005)

Multipole moments of in-plane magnetized disks

N. Mikuszeit, E. Y. Vedmedenko,[a] R. Wiesendanger, and H. P. Oepen
Universität Hamburg, Institut für Angewandte Physik, Jungiusstrasse 11a, 20355 Hamburg, Germany

(Presented on 11 November 2004; published online 12 May 2005)

The multipole moments of in-plane magnetized disks have been calculated based on the fundamental theory of magnetostatics. Analytical solutions for disks with uniform magnetization or an onion state are given explicitly. It is demonstrated that depending on the polarization configuration, higher-order multipole moments beyond the dipole moment appear. The strength of the multipole moments can be of the same order of magnitude as the dipolar moment. The higher-order moments give rise to an additional energy contribution in arrays of close-packed polarized disks. © *2005 American Institute of Physics*. [DOI: 10.1063/1.1847351]

I. INTRODUCTION

Physical properties of magnetic dot arrays are important from both fundamental and practical points of view as miniaturization gives access to new phenomena that can be used in technical applications. Because of the vanishing interdot exchange coupling magnetic properties of the arrays are governed by the magnetostatic interaction and the magnetocrystalline anisotropy. Magnetic memory applications require an increase in the density of dots per unit area, which is correlated with a decrease of dot sizes and interdot distances. With increasing density of packing higher-order magnetostatic terms due to the finite dot size may become increasingly important. The multipolar moments, however, have not been studied systematically. There are only few investigations on that subject.[1–3] In those studies a leading multipolar correction to the dipolar interaction has been calculated for uniformly magnetized[1,2,4] and double-domain dots,[3] while the strength and the order of further multipole moments have not been determined and noncollinear magnetic configurations have not been considered.

In the present investigation we derive a formalism that enables the calculation of multipole moments for magnetized disks of finite size. Uniformly magnetized particles and nonuniform onion magnetization configurations[5] with different degrees of inhomogeneity have been considered. We demonstrate that both the uniform and the onion in-plane magnetization configurations lead to strong multipole moments in ultrathin disks. The first nonvanishing multipolar terms are octopolar, while all even moments (including quadrupolar) are extinct. For both states the higher-order moments can be of the same order of magnitude as the dipolar one. Hence, they can influence the switching behavior of magnetic particle ensembles and must be considered in the description of ordering phenomena in close-packed arrays.

II. MULTIPOLE MOMENTS OF CHARGED OR POLARIZED PARTICLES

To derive the multipole moments of a magnetized disk we calculate the multipole expansion of a corresponding surface charge distribution. The multipole expansion can be made either in cartesian or in spherical coordinates. The cartesian expansion is more popular as only real numbers are required. However, each term of the expansion is a tensor. The order l of the tensor is equivalent to the order of the expansion. The number of independent tensor components of a three-dimensional symmetric tensor increases with the square of l; thus, it is a formidable task to treat terms with rank higher than two (quadrupole moments). The spherical expansion needs complex numbers but its complexity does not change with the order of expansion as the number of independent components is proportional to l. Therefore, we use spherical coordinates as almost any order can be calculated within reasonable effort and the symmetry is easily verified due to the well-known properties of spherical harmonics (see below).

The multipole moments of a charge distribution $\rho(\vec{\mathbf{r}})$ in spherical coordinates $\vec{\mathbf{r}}=(r,\theta,\varphi)$ is defined by[6]

$$Q_{lm}=\int_V \mathrm{d}V\rho(\vec{\mathbf{r}})R_{lm}(\vec{\mathbf{r}}), \tag{1}$$

where the integration is performed over the volume V that encloses $\rho(\vec{\mathbf{r}})$, weighted by a regular normalized spherical harmonic R_{lm},[6]

$$R_{lm}(\vec{\mathbf{r}})=\sqrt{\frac{4\pi}{2l+1}}r^l Y_{lm}(\theta,\varphi). \tag{2}$$

The spherical harmonics $Y_{lm}(\theta,\varphi)$ represent a complete set of orthogonal functions on the sphere.[7] They also have the properties of a tensor in spherical coordinates of order l with $2l+1$ independent components. To ensure the uniqueness of the expansion, the origin of the coordinate system must coincide with the center of charge

$$\vec{\mathbf{r}}_s=\frac{\int_V \mathrm{d}V\vec{\mathbf{r}}|\rho(\vec{\mathbf{r}})|}{\int_V \mathrm{d}V|\rho(\vec{\mathbf{r}})|}, \tag{3}$$

i.e., $\vec{\mathbf{r}}_s=0$.

[a]Electronic mail: vedmedenko@physnet.uni-hamburg.de

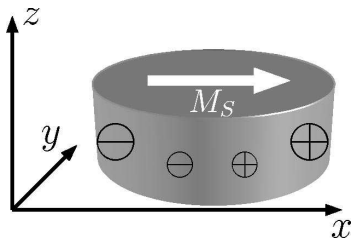

FIG. 1. Scheme of a disk within the *x*-*y* plane (magnetized in *x* direction). Due to the magnetization a magnetic surface charge emerges (positive charge ⊕ and negative charge ⊖). In case of a uniform magnetization the charge is cosine distributed.

TABLE I. The multipole moments Q^1_{lm} (in units of the surface charge density) up to the order $l=7$ of a disk with uniform in-plane magnetization. All Q_{lm} with even l vanish.

	$m=-1$[a,b]
$l=1$	$\frac{1}{\sqrt{2}}\pi h r_0^2$
$l=3$	$\frac{1}{4\sqrt{3}}\pi h r_0^2(h^2-3r_0^2)$
$l=5$	$\frac{\sqrt{3}}{16\sqrt{10}}\pi h r_0^2(h^3-10r_0^2h^2+10r_0^4)$
$l=7$	$\frac{1}{32\sqrt{14}}\pi h r_0^2(h^6-21h^4r_0^2+70h^2r_0^4-35r_0^6)$

[a]Only $|m|=1$ is allowed.
[b]$Q_{l1}=-Q^*_{l-1}$ due to the symmetry of spherical harmonics.

III. MULTIPOLE MOMENTS OF IN-PLANE MAGNETIZED DISKS

Let us assume a disk with a radius r_0, a height h, and a base coplanar to the *x*-*y* plane. The disk is magnetized in the *x* direction (Fig. 1). The center of mass and the center of charge are identical and coincide with the origin of the coordinate system. Thus, the *x*-*z* plane is a symmetry plane with positive parity while the *y*-*z* plane has negative parity, i.e., after a mirror operation with respect to this plane the charge must be multiplied by −1 to reproduce the initial state.

The surface charge is proportional to the saturation magnetization M_S and depends on the magnetic state of the sample. An expression for the charge distribution $\rho(\vec{\mathbf{r}})$ of a uniformly magnetized disk (Fig. 1) is very complicated in spherical coordinates, but due to the natural symmetry of a disk it is trivially proportional to $\cos\varphi$ in cylindrical coordinates. Furthermore, the cosine charge distribution can be easily generalized for nonuniform onion states as the charge distribution can be expanded like $\rho(\vec{\mathbf{r}}) \propto \Sigma_p c_p \cos^p\varphi$ with expansion coefficients c_p. Due to the symmetry of the onion configuration only an odd integer p appear. The nonuniformity of the magnetization increases with increasing p. Expressing the volume element and normalized spherical harmonics of Eq. (1) in the cylindrical coordinates, one obtains the following integral:

$$Q^p_{lm} = \mu_0 M_S \int_{-\frac{h}{2}}^{\frac{h}{2}} \mathrm{d}z \int_0^{2\pi} r_0 \mathrm{d}\varphi \times \left\{ \cos^p\varphi \left[R_{lm}\left(\sqrt{r_0^2+z^2}, \frac{\pi}{2} - \arctan\frac{z}{r_0}, \varphi \right) \right] \right\}. \quad (4)$$

The integral in Eq. (4) has polynomial solutions for all integer p including $p=1$ for uniform magnetization. For nonuniform magnetization additional volume charge appears. However, this volume charge distribution can be treated with the same mathematical procedure and is, therefore, not considered in the following.

As the charge distribution of an onion state fulfills $\rho(-\vec{\mathbf{r}})=-\rho(\vec{\mathbf{r}})$ and the *x*-*y* plane is a mirror plane with positive parity, Eq. (4) can be modified to

$$Q^p_{lm} = \mu_0 M_S \int_0^{\frac{h}{2}} \mathrm{d}z \int_{-\frac{\pi}{2}}^{\frac{\pi}{2}} r_0 \mathrm{d}\varphi \left\{ [1-(-1)^l][1-(-1)^m] \times \cos^p\varphi R_{lm}\left(\sqrt{r_0^2+z^2}, \frac{\pi}{2} - \arctan\frac{z}{r_0}, \varphi \right) \right\}. \quad (5)$$

The modification utilizes the parity properties of $Y_{lm}(\theta,\varphi)$

$$\hat{P}Y_{lm}(\theta,\varphi) := Y_{lm}(\pi-\theta,\pi+\varphi) = (-1)^m Y_{lm}(\theta,\varphi). \quad (6)$$

From Eq. (5) it directly follows that only odd integers are allowed for l and m. Due to the azimuthal symmetry of the spherical harmonics,

TABLE II. The multipole moments Q^5_{lm} (in units of the surface charge density) up to the order $l=7$ of a disk with an onion state. The surface charge disribution can be described by $\rho(\varphi)=\mu_0 M_S \cos^5\varphi$. All Q^5_{lm} with even l and even m vanish.

	$m=-1$[a]	$m=-3$	$m=-5$[b]
$l=1$	$\frac{5}{8}\frac{1}{\sqrt{2}}\pi h r_0^2$		
$l=3$	$\frac{5}{8}\frac{1}{4\sqrt{3}}\pi h r_0^2(h^2-3r_0^2)$	$\frac{5}{8}\frac{\sqrt{5}}{8}\pi h r_0^4$	
$l=5$	$\frac{5}{8}\frac{\sqrt{3}}{16\sqrt{10}}\pi h r_0^2(h^3-10r_0^2h^2+10r_0^4)$	$\frac{5}{8}\frac{\sqrt{35}}{96}\pi h r_0^4(3r_0^2-2h^2)$	$3\sqrt{7}/256\,\pi h r_0^6$
$l=7$	$\frac{5}{8}\frac{1}{32\sqrt{14}}\pi h r_0^2(h^6-21h^4r_0^2+70h^2r_0^4-35r_0^6)$	$\frac{5}{8}\frac{\sqrt{21}}{64\sqrt{2}}\pi h r_0^4(h^4-5h^2r_0^2+3r_0^4)$	$\frac{\sqrt{231}}{512\sqrt{2}}\pi h r_0^6(r_0^2-h^2)$

[a]$Q_{l-m}=(-1)^m Q^*_{lm}$ due to the symmetry of spherical harmonies.
[b]$|m|=5$ is the largest possible value.

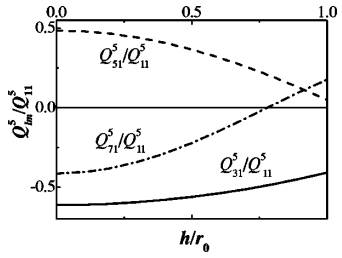

FIG. 2. The multipole moments in units of the dipolar moment of the in-plane magnetized disks with height h and radius r_0. Magnetization configuration is a nonuniform onion state.

$$Y_{lm}(\theta,\varphi) \propto e^{-im\varphi} = \cos m\varphi - i \sin m\varphi, \tag{7}$$

only $|m| \leqslant p$ are allowed, as the set of trigonometric functions is orthogonal.

Table I gives the low-order moments of a disk with a uniform magnetization as a function of the surface area ($\propto r_0^2$) and the height h. As expected, the dipole moment Q^1_{1-1} of a uniformly magnetized disk is proportional to the surface charge ($\propto r_0 \times h$) and to the distance between positive and negative charges (r_0). Higher-order multipole moments possess further polynomial factors depending on r_0 and h. The multipole moments for an onion configuration of the strength $p=5$ are listed in Table II. From the comparison of Tables I and II it can be seen that the dipole moment of an onion state is slightly lower than that of a uniformly magnetized monodomain. This is due to the decreasing amount of surface charge with increasing p. The strength of the higher-order moments as a function of the aspect ratio h/r_0 for $p=5$ is shown in Fig. 2. For $h \approx r_0$ the multipolar moments are smaller than the dipolar one. However, in the limit of small thickness ($h \ll r_0$) the octopole moment Q^p_{31} reaches -61% of the dipole moment Q^p_{11} for all odd p and even the dotriacontapole (Q^p_{51}) is of the order of $0.5Q^p_{11}$. Hence, the multipole moments of ultrathin, in-plane magnetized disks are comparable with their dipole moments.

The described geometry is typical for ongoing experimental studies on magnetic arrays.[8,9] In a recent study[9] it has been demonstrated that experimentally observed room-temperature ferromagnetism in arrays of magnetostatically coupled, in-plane magnetized dots with $h/2r_0 < 1$ and small interdot distance cannot be explained by dipolar interactions only. The authors suggested without proof that an indirect exchange interaction may be responsible for the long-range order. The multipole moments have not been considered at all in this study. However, as the influence of higher-order moments quickly increases with decreasing interparticle distance the common action of the dipolar and the multipolar interactions may overcome the thermal fluctuations and explain the experimentally found long-range superferromagnetic order in magnetic arrays. Hence, further investigation of the magnetic ordering in magnetostatically coupled arrays with multipole interactions is highly desirable.

IV. SUMMARY

In conclusion we have developed a formalism to calculate the multipole moments of in-plane polarized disks up to any desired order. The use of higher-order multipole moments is not meant to substitute analytical solutions, but reveals a new, rather simple treatment to distinguish symmetry effects due to single particle properties on all length scales. The theory is scale invariant, but as we treat uniform and nonuniform magnetization configurations, it is of special interest in the nanoscale regime. Depending on the aspect ratio and the micromagnetic state of the magnetized disk, the higher-order moments can be of order of the dipole moment. Therefore, their contribution to the total energy of an array must be considered for close-packed disks and the treatment solely by the dipole-dipole approximation is questionable. Due to the symmetry properties higher-order multipole moments can cause additional anisotropies and anisotropy-induced orientational order. As the interaction energy is influenced by corrections beyond the dipole approximation the results are important for the thermal stability close to the superparamagnetic limit.

ACKNOWLEDGMENT

Financial support from the Interdisciplinary Nanoscience Center Hamburg is gratefully acknowledged.

[1] P. J. Jensen and G. M. Pastor, New J. Phys. **5**, 68.1 (2003).
[2] P. Politi and G. M. Pini, Phys. Rev. B **66**, 214414 (2002).
[3] K. Y. Guslienko, Phys. Lett. A **278**, 293 (2001).
[4] M. D. Costa and Yu. G. Pogorelov, Phys. Status Solidi A **189**, 923 (2001).
[5] J. K. Ha and R. Hertel, Phys. Rev. B **67**, 224432 (2003).
[6] A. J. Stone, *The Theory of Intermolecular Forces* (Clarendon, Oxford, 1996).
[7] D. A. Varsalovich, A. N. Moskalev, and V. K. Khersonskii, *Quantum Theory of Angular Momentum* (World Scientific, Singapore, 1988).
[8] R. P. Cowburn, J. Phys. D **33**, R1 (2000).
[9] K. Scheinfein, K. Schmidt, K. Heim, and G. Hembree, Phys. Rev. Lett. **76**, 1541 (1996).

PRL 95, 207202 (2005) PHYSICAL REVIEW LETTERS week ending 11 NOVEMBER 2005

Multipolar Ordering and Magnetization Reversal in Two-Dimensional Nanomagnet Arrays

E. Y. Vedmedenko,[1] N. Mikuszeit,[2] H. P. Oepen,[1] and R. Wiesendanger[1]
[1]*Institut für Angewandte Physik, Universität Hamburg, Jungiusstrasse 11a, 20355 Hamburg, Germany*
[2]*Universidad Autónoma de Madrid, E-28049 Spain*
(Received 7 February 2005; published 7 November 2005)

The low-temperature stable states and the magnetization reversal of realistic two-dimensional nanoarrays with higher-order magnetostatic interactions are studied theoretically. For a general calculus of the multipole-multipole interaction energy we introduce a Hamiltonian in spherical coordinates into the Monte Carlo scheme. We demonstrate that higher-order interactions considerably change the dipolar ground states of in-plane magnetized arrays favoring collinear configurations. The multipolar interactions lead to enhancement or decrease of the coercivity in arrays with in-plane or out-of-plane magnetization.

DOI: 10.1103/PhysRevLett.95.207202 PACS numbers: 75.75.+a, 75.10.−b, 75.60.Jk

Magnetic properties of artificially structured and self-organized magnetic media belong to the central questions of nanomagnetism as they give access to new phenomena that can be used in technology [1–3]. Magnetic memory applications require the increase of the density of dots per unit area, which is correlated with a decrease of dot diameter d and interdot distances R. Particles with lateral size smaller than the characteristic exchange length $d < \chi_{ex}$ have a single domain magnetization configuration with a macroscopic magnetic moment. In densely packed systems these moments interact. The magnetostatic interaction is a crucial parameter as it determines the magnetization reversal. To identify the effects of the long-range interaction on magnetic behavior extensive experimental [2,4–9] and theoretical [10–12] studies of magnetic nanoarrays have been performed.

Experimental investigations show that in comparison with an infinite film, the interparticle interactions usually lead to a decrease of the switching field in patterned media with out-of-plane magnetization [2,5,7] and to an increase of the coercivity for in-plane magnetized particles [5,6,8,13]. Although in some cases an agreement of switching behavior with theoretical predictions has been obtained, it is often found that measured switching fields deviate significantly (10%–15%) from those expected from pure dipolar interactions ([5–7,9] and the references therein). The theory predicts a noncollinear antiferromagnetic ground state and weak coercivity for a square lattice, which comes close to the ideal situation of in-plane dipoles with zero in-plane self-coercivity [14,15], while experiments [6,13] reveal that patterning of a continuous film increases the coercivity considerably, e.g., $\mu_0 H_c$ goes from almost zero up to 22.8 mT for Co and 16 mT for NiFe arrays [6,13]. In addition, collinear magnetic superdomains in dense nanoarrays have been observed [16] instead of a noncollinear structure. In a triangular in-plane array a frustrated ferromagnetic state with closed loops and spirals has been predicted [11]. In the experiment, however, the vorticity was not observed and the coercivity exceeded that expected from the dipolar approximation [6,13]. A related nonsolved problem is the so-called superferromagnetism in two-dimensional nanoislands assemblies. Experimentally found superferromagnetic domains [9,17] lead to high coercivity, which is inconsistent with the strength of the dipolar coupling and the absence of the direct exchange interactions [9].

The quantitative disagreement between theory and experiment has been attributed to a variety of reasons as pinning of magnetization by structural inhomogeneities [6] or noncoherent rotation of magnetization [5,7]. Several investigations have been devoted to the question of how the dipolar interaction between the monodomain particles is modified by their finite size, i.e., the leading correction terms to the dipolar interaction have been determined [10,12]. The main conclusion is that the correction term reinforces the antiferromagnetic character of the ground state in a square and the ferromagnetic one in a triangular lattice. An increase in coercivity of the in-plane systems still cannot be quantitatively explained in the framework of those studies.

Recently, we have calculated explicitly the multipolar (MP) magnetic moments of uniformly and nonuniformly (e.g., onion state) magnetized objects of different symmetry [18,19]. It has been demonstrated that rotationally symmetric particles possess octopolar (Q_3) and dotriacontapolar (Q_5) moments, which can be comparable with the dipolar one (Q_1) for elongated (e.g., nanowires) or ultrathin (e.g., nanodiscs) geometry. The calculation of interaction energies between a pair of particles with multipole moments show, in agreement with [10,12], that the higher-order interactions reinforce the dipolar ones. However, in many-body systems the situation is much more complicated. As it is known from chemistry [20–22] the multipolar interactions may completely change the structure and physical properties of an ensemble. Hence, to make a reliable conclusion about the influence of multipolar interactions on switching behavior stable low-temperature multipolar states have to be calculated. So far, multipolar configurations in magnetic nanoarrays have not been considered despite the small interparticle distances and strong MP moments of the dots or grains.

PRL 95, 207202 (2005) PHYSICAL REVIEW LETTERS week ending 11 NOVEMBER 2005

Few existing calculations of stable MP configurations in physical systems (mainly gas adsorbates) have been usually made within the mean field or Monte Carlo (MC) approach in Cartesian coordinates [22,23]. We use spherical coordinates, as this allows a much easier treatment of higher-order moments and their interaction energies [see Eq. (1) below]. For example, the dotriacontapole has components Q_{5m} with $-5 \leq m \leq 5$ in spherical coordinates while it would be a tensor of the form D_{ijklm} with $(i, j, k, l, m) \in \{x, y, z\}$ in Cartesian coordinates. Even though the number of independent tensor components is the same, it is a formidable task to calculate all components of D_{ijklm} or even higher-order moments. Therefore, the technique, well established in chemical physics, of spherical coordinates is used to calculate the Coulomb interaction energy between two nonintersecting charge distributions [21,24]. A nanoarray is nothing but an ensemble of magnetic multipolar rotators on a lattice and can be described by the extension of this approach onto a many-body MP system.

In this study we introduce the Hamiltonian in spherical coordinates into the conventional MC scheme and derive the stable low-temperature configurations of magnetization as well as hysteretic properties of magnetic nanoarrays. It will be demonstrated that for in-plane systems multipolar interactions select collinear configurations from the dipolar manifold. In patterned media with combined dipolar and octopolar moments a competition between dipole-octopole and dipole-dipole plus octopole-octopole interactions leads to the increase of the coercivity. In out-of-plane systems the higher-order interactions do not change zero-field configurations. However, the multipolar contributions enlarge the interaction field by 10%–15% and, thus, decrease the switching field.

The Hamiltonian of the interaction reads

$$H = \frac{1}{4\pi\mu_0} \sum_{\substack{A \neq B \\ l_A l_B m_A m_B}} T_{l_A l_B m_A m_B}(\vec{R}_{AB}) Q^A_{l_A m_A} Q^B_{l_B m_B} + \sum_A \frac{1}{\sqrt{2}} H_x (Q^A_{11} - Q^A_{1-1}), \quad (1)$$

where $Q^A_{l_A m_A}$ and $Q^B_{l_B m_B}$ are the moments of multipoles A and B expressed in spherical harmonics [18] and $T_{l_A l_B m_A m_B}(\vec{R}_{AB})$ is the geometric interaction tensor depending on the interparticle distance vector $\vec{R}_{AB}$ [21] between multipoles on sites A and B:

$$T_{l_A l_B m_A m_B}(\vec{R}_{AB}) = (-1)^{l_B} I^*_{l_A + l_B m_A + m_B}(\vec{R}_{AB}) \sqrt{\frac{(l_A + l_B - m_A - m_B)!}{(l_A - m_A)!(l_B - m_B)!} \frac{(l_A + l_B + m_A + m_B)!}{(l_A + m_A)!(l_B + m_B)!}}, \quad (2)$$

where the dependency on the distance is given by the complex conjugate of the irregular normalized spherical harmonic function

$$I_{lm}(\vec{r}) = \sqrt{\frac{4\pi}{2l+1}} \frac{Y_{lm}(\theta, \varphi)}{r^{l+1}}. \quad (3)$$

H_x is the only nonvanishing component of an external uniform magnetic field of the form $\vec{H} = (H_x, 0, 0)$.

Two-dimensional films of multipoles or their combinations corresponding to particles of different geometry on a lattice have been considered. In this study we restrict ourselves to rotationally symmetric multipoles with dipolar and octopolar contributions (e.g., Q_{30} or $Q_{30} + Q_{10}$). Rotated moments have components with $m \neq 0$. In the following, the description Q_{l0} means that there exists a coordinate system in which the moments can be represented by Q_{l0}. The weak dotriacontapolar interaction is not presented here as octopolar and dotriacontapolar interactions break the isotropic behavior of dipoles on square and triangular lattices in the same way and the symmetry of the stable magnetic state remains unchanged. Our aim is to give a reasonable theoretical description of finite arrays. For that reason and in order to avoid symmetry adapted structures we use open boundary conditions. Lattice sizes up to 60×60 have been used. To prevent artificial effects we used no cutoff. A standard MC technique was used [3]. The rotational space was sampled uniformly and was not restricted, i.e., a moment can try any new angle. An extremely slow annealing procedure has been applied. To avoid metastable states we have performed two different simulations of the same system simultaneously starting them at different "seeds" for the random number generator to ensure that the samples take different path to the equilibrium. Only when both samples reached the same stable energy level it has been deduced that the system has reached equilibrium. The high in-plane coercivity is typically found in assemblies of single domain nanoparticles with a height-to-diameter ratio $h/d \leq 0.5$ [6,8,9,13]. Such particles possess dipole and octopole moments with $Q_{30}/Q_{10} \geq 0.5$ [19]. We have calculated stable configurations for pure octopoles and combined multipoles with $0 \leq Q_{30}/Q_{10} \leq 3.0$. The octopolar moments are unidirectional, i.e., they can be represented as vectors. We find that on the square lattice, octopoles form lines aligned antiparallel while on the triangular lattice the moments are ferromagnetically ordered. Hence, the octopolar interaction on a triangular and a square lattice introduces an easy-plane and a tri- and a biaxial in-plane anisotropy, respectively. In contrast to finite dipolar systems avoiding uncompensated poles by domain formation, a finite octopolar system is not sensitive to the formation of free poles in most geometries as octopoles do not interact with a field but with the field curvature. Therefore the low-temperature configurations in finite samples are still parallel lines for a triangular lattice and antiparallel lines for a square lattice.

With increasing dipolar interaction the pattern changes. A typical low-temperature configuration consists of alter-

nating regions of uniaxial parallel and antiparallel lines such as in Fig. 1(b). On a square lattice the width of regions with parallel lines is usually 2–3 lattice parameters. In ≈ 10% of calculations despite a very long relaxation superdomains [Fig. 1(f)] appear. The energy of ideal and MC configurations as a function of Q_{30}/Q_{10} is plotted in Fig. 2(a). Figure 2(b) gives the size dependence of all energy contributions for parallel lines. We find that the dipole-octopole energy contribution (E_{d-o}) is minimal for the parallel while maximal for the antiparallel lines. The dipole-dipole (E_{d-d}) and octopole-octopole (E_{o-o}) interactions, in contrast, prefer antiparallel lines. Therefore for sample sizes $L < 9$ and $0.25 < Q_{30}/Q_{10} < 0.8$ the state of coexisting parallel and antiparallel lines has the lowest total internal energy. For $L > 9$ the antiparallel lines are preferable for all Q_{30}/Q_{10} as the long-range dipolar contribution increases. The energy difference between antiparallel lines and coexisting phases or superdomains δE grows with increasing Q_{30}/Q_{10} [Fig. 2(a)]. However, for $0 < Q_{30}/Q_{10} < 0.6$ δE is very small (≈2%), while the configurational entropy in a system of parallel or antiparallel lines drastically increases with the system size $S_c = k \ln(2 \times 2^L)$. As the entropy increases boundless with L, in contrast to the slow convergence of the dipolar sum, the free energy of the coexistence is lower for nonzero temperatures.

Formation of superdomains gives an additional contribution to the entropy. The size of superdomains in finite dipolar systems is driven by the pole avoidance principle. While the energy cost due to the wall formation increases only linearly with the domain size, the gain in the long-range dipolar interaction increases with the square of the domain size and only a rare formation of superdomains is observed at low temperatures. The additional entropy for large superdomains is small. Approaching T_c the domain size decreases, the corresponding entropy increases and the superdomains appear more frequently. This finding is in accordance with the experiment [16] giving evidence for formation of the large in-plane collinear domains extending across several dots. At zero temperature the antiparallel lines are preferable.

We have calculated the specific heat $C_v(T, L)$, the order parameter q, and the susceptibility $\chi_q(T, L)$ for different L and Q_{30}/Q_{10}. Using $\beta = (kT)^{-1}$, $C_v(T, L)$ and $\chi_q(T, L)$ are deduced applying the fluctuation-dissipation theorem $C_v = k\beta^2(\langle E^2\rangle - \langle E\rangle^2)$ and $\chi_q = \beta E_{\|}(\langle q^2\rangle - \langle q\rangle^2)$. Figure 3 shows the thermodynamic characteristics in the case of a system with $Q_{30}/Q_{10} = 0.5$. We use $q = N^{-1}|n_x - n_y|$, where $N = n_x + n_y$ is the total number of moments and n_x, n_y number of moments aligned with X or Y directions [15]. All systems show maxima of specific heat and susceptibility at the same temperature confirming the existence of a phase transition. In the following it will be demonstrated that higher-order interactions significantly influence magnetization reversal in nanoarrays.

The field dependence of magnetization in square and triangular arrays of dots with in-plane magnetization and $0 \le Q_{30}/Q_{10} \le 1$ has been calculated. A pure dipolar system does not show any easy-axis hysteresis. In a multipolar array, on the contrary, the hysteresis loop is quite open. The squareness s depends on the composition, the strength of multipoles and on the temperature. Figure 1 shows the magnetization reversal of a square lattice with $Q_{30}/Q_{10} = 0.5$ corresponding to an array of ultrathin particles with $h/d \le 0.5$ [19] and for a pure dipolar system [$h/d \approx 1$, Fig. 1(d)]. The field is scaled with the pair interaction energy $E_{\|}$ between two dots magnetized mutually parallel but perpendicular to the bond $E_{\|} \propto 1/R_{AB}^{l_A+l_B+1}$, therefore, contributions from moments of different order in combined multipoles scale differently with R_{AB}. All

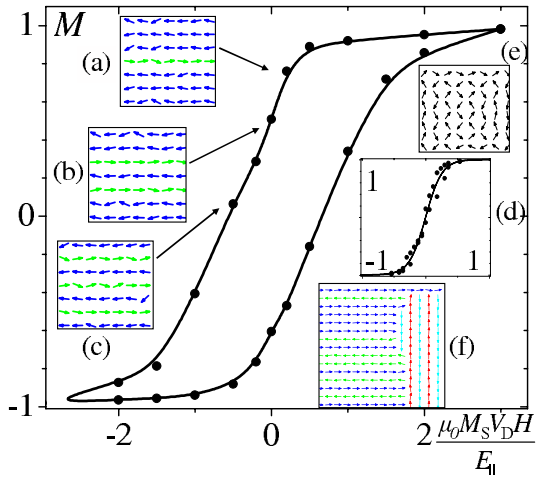

FIG. 1 (color online). Hysteresis loops for a 20×20 square nanoarray with $Q_{30} = 0.5Q_{10}$ and a pure dipolar system [inset (d)]. The magnetic field is applied in the x direction. Insets (a)–(c) give a part of the intermediate magnetic configurations; (f) and (e) show stable zero-field configurations for combined multipoles and the pure dipolar case, respectively. Thermal energy is $kT = 0.6E_{\|}$. The field is expressed in $\frac{\mu_0 M_S V_D}{E_{\|}}$ with μ_0—the permeability of free space and V_D—the volume of a dot.

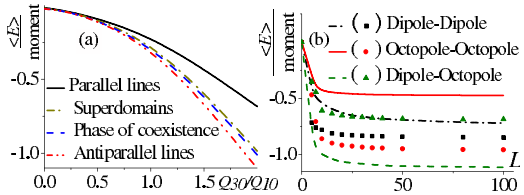

FIG. 2 (color online). (a) Internal energy of ideal parallel, antiparallel, coexisting, and superdomain configurations for $L = 20$ as a function of Q_{30}/Q_{10} on a square lattice; (b) Size dependence of different contributions of the magnetostatic energy for parallel and antiparallel lines (scatter) for $Q_{30}/Q_{10} = 0.5$.

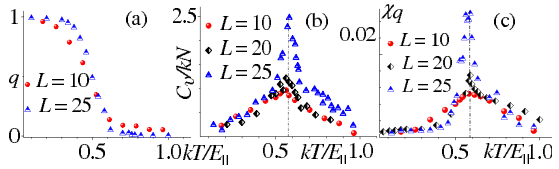

FIG. 3 (color online). MC results for the order parameter (a), specific heat (b), and susceptibility (c) of a system with $Q_{30}/Q_{10} = 0.5$ on a square lattice.

values are given for $Q_3 = 1$, $Q_1 = 2$ and $R_{AB} = 1$. This gives $s \approx 0.5$ and $H_c\mu_0 M_S V_D \approx 0.7E_{||}$. By calculating $E_{||}$ this result can be scaled to a square array of any material with any interdot distance. For example, for an array of permalloy particles at room temperature ($M_S = 8.0 \times 10^5$ A/m and vanishing anisotropy, $K_u < 1000$ J/m^3) with $h = 20$ nm, $d = 70$ nm, and $R = 100$ nm we find $\mu_0 H_c \approx 20$ mT. Magnetic moments do not rotate continuously as in a pure dipolar system but are reoriented line by line [Figs. 1(a)–1(c)] as noncollinear configurations are energetically unfavorable. From our calculations it follows that the competition between the E_{d-o} and $E_{d-d} + E_{o-o}$ interaction energy plays an important role for the magnetization reversal. As has been already demonstrated in Fig. 2(a) the total energy of the configuration Fig. 1(b) is close or even lower than that of Fig. 1(c), where all chains are antiparallel. Hence, to go from configuration Fig. 1(b) to the configuration Fig. 1(c), an external magnetic field has to be applied and the hysteresis appears. H_c increases with decreasing temperature. This effect is similar to the superparamagnetic temperature assisted switching. Thus, the hysteretic behavior is predefined by the competition between the octopole-dipole contribution of the magnetostatic energy and its dipole-dipole and octopole-octopole counterparts. Pure dipolar systems do not show any significant hysteresis.

On a triangular lattice H_c increases by ≈10% compared to the pure dipolar system in good accordance with experiments [6]. The increase is due to the support of the ferromagnetic single domain state by all interactions. For assemblies of single domain nanoparticles with out-of-plane magnetization [7] multipolar contributions do not change the ground states of a dipolar system (checkerboard pattern on a square and labyrinthine structure on a triangular lattice). They give, however, an additional energetic contribution promoting the magnetization reversal. Thus, one of the main reasons for increase (decrease) of coercivity in the in-plane (out-of-plane) magnetic nanoarrays are multipolar energetic contributions. In addition, the octopole-dipole interaction between magnetic grains of ultrathin geometry with in-plane magnetization might explain the origin and stability of superferromagnetic domains in magnetostatically coupled nanosystems [9,17].

In conclusion, systematic investigation of multipolar low-temperature stable configurations on a triangular and a square lattice have been carried out theoretically. In contrast to previous results we demonstrate that the MP-MP interactions change considerably stable low-temperature dipolar states. The dipole-octopole interaction is an important component that might also explain the superferromagnetic behavior in dense grain magnetic materials and magnetic arrays. Tuning the multipole moments by changing the geometry of nanoparticles offers a new route to the control of the coupling behavior and therefore the hysteretic properties of magnetic nanoparticle arrays.

Financial support from the Interdisciplinary Nanoscience Center Hamburg (INCH) is gratefully acknowledged.

[1] S.P. Li, W.S. Lew, J.A.C. Bland, L. Lopez-Diaz, M. Natali, C.A.F. Vaz, and Y. Chen, Nature (London) **415**, 600 (2002).
[2] T. Aign *et al.*, Phys. Rev. Lett. **81**, 5656 (1998).
[3] E.Y. Vedmedenko, A. Kubetzka, K. von Bergmann, O. Pietzsch, M. Bode, H.P. Oepen, and J. Kirschner, Phys. Rev. Lett. **92**, 077207 (2004).
[4] R.P. Cowburn and M.E. Welland, Science **287**, 1466 (2000).
[5] C.A. Ross *et al.*, Phys. Rev. B **65**, 144417 (2002).
[6] J.Y. Cheng, W. Jung, and C.A. Ross, Phys. Rev. B **70**, 064417 (2004).
[7] K. Nielsch *et al.*, J. Magn. Magn. Mater. **249**, 234 (2002).
[8] R.P. Cowburn, J. Phys. D **33**, R1 (2000).
[9] M.R. Scheinfein, K.E. Schmidt, K.R. Heim, and G. Hembree, Phys. Rev. Lett. **76**, 1541 (1996).
[10] P. Politi and M.G. Pini, Phys. Rev. B **66**, 214414 (2002).
[11] A.J. Bennett and J.M. Xu, Appl. Phys. Lett. **82**, 2503 (2003).
[12] P.J. Jensen and G.M. Pastor, New J. Phys. **5**, 68 (2003).
[13] C. Miramond, C. Fermon, F. Rousseaux, D. Decanini, and F. Carcenac, J. Magn. Magn. Mater. **165**, 500 (1997).
[14] K.Y. Guslienko, Appl. Phys. Lett. **75**, 394 (1999).
[15] E. Olive and P. Molho, Phys. Rev. B **58**, 9238 (1998).
[16] Y.B. Xu *et al.*, IEEE Trans. Magn. **37**, 2055 (2001).
[17] W. Kleemann, O. Petracic, C. Binek, G.N. Kakazei, Y.G. Pogorelov, J. Sousa, S. Cardoso, and P.P. Freitas, Phys. Rev. B **63**, 134423 (2001).
[18] N. Mikuszeit, E.Y. Vedmedenko, and H. Oepen, J. Phys. Condens. Matter **16**, 9037 (2004).
[19] N. Mikuszeit, E.Y. Vedmedenko, R. Wiesendanger, and H.P. Oepen, J. Appl. Phys. **97**, 10J502 (2005).
[20] M. Eremtchenko, J.A. Schaefer, and F.S. Tautz, Nature (London) **425**, 602 (2003).
[21] P. Popelier and D. Kosov, J. Chem. Phys. **114**, 6539 (2001).
[22] A.J. Berlinsky and A.B. Harris, Phys. Rev. Lett. **40**, 1579 (1978).
[23] V.E. Klymenko, V.M. Rozenbaum, V.V. Kukhtin, and O.V. Schramko, Solid State Commun. **88**, 373 (1993).
[24] S.F. O'Shea, J. Chem. Phys. **71**, 2399 (1979).

VOLUME 90, NUMBER 13 PHYSICAL REVIEW LETTERS week ending 4 APRIL 2003

Decagonal Quasiferromagnetic Microstructure on the Penrose Tiling

E. Y. Vedmedenko,[1] H. P. Oepen,[1] and J. Kirschner[2]
[1]*Institut für Angewandte Physik, Jungiusstrasse 11, 20355 Hamburg, Germany*
[2]*Max-Planck-Institut für Mikrostrukturphysik, Weinberg 2, 06120 Halle, Germany*
(Received 23 October 2002; published 4 April 2003)

The stable magnetization configurations of a ferromagnet on a quasiperiodic tiling have been derived theoretically. The magnetization configuration is investigated as a function of the ratio of the exchange to the dipolar energy. The exchange coupling is assumed to decrease exponentially with the distance between magnetic moments. It is demonstrated that for a weak exchange interaction the new structure, the quasiferromagnetic decagonal configuration, corresponds to the minimum of the free energy. The decagonal state represents a new class of frustrated systems where the degenerated ground state is aperiodic and consists of two parts: ordered decagon rings and disordered spin-glass-like phase inside the decagons.

DOI: 10.1103/PhysRevLett.90.137203 PACS numbers: 75.10.Hk, 75.70.Ak, 75.75.+a

There is currently a broad interest in the understanding of the magnetism of ultrathin magnetic structures due to the wide variety of industrial applications [1]. The discovery of the rare-earth-based quasicrystals [2] offers the unique opportunity to study the magnetic behavior of localized magnetic moments in magnets with nonperiodic structure. The combination of the structural quasiperiodicity with magnetic properties of ultrathin films can lead to new physical phenomena. Hence, the understanding of the micromagnetic ordering in such objects is of high significance for the fundamental physics of magnetic materials as well as for technological applications.

The critical behavior of localized magnetic moments on quasiperiodic tilings has been investigated theoretically [3]. In those studies emphasis has been put on critical exponents and transition temperatures of Ising, Potts, and *XY* models. In the investigations only the short-range exchange interaction has been taken into account. The long-range dipolar forces were not considered. On the other hand, due to the long-range character, a relatively weak dipolar interaction can compete with the strong but short-range exchange coupling [4]. The competition can lead to a variety of magnetic configurations in two-dimensional films [4]. In quasiperiodic magnets the magnetic pattern will be different from that of periodic crystals and disordered media.

The quasicrystals can be structurally ranked between the periodic lattices and completely disordered media. In contrast to periodic crystals, in quasicrystals the number of nearest neighbors varies widely from one point to another as in disordered matter. The Penrose tiling [5], for example, has atoms with coordination number changing from 3 to 7. Hence, the energy per magnetic moment also varies. Unlike the disordered media, however, this variation exhibits a long-range orientational order, i.e., any finite section of a quasicrystal is reproduced within a certain distance. In particular, fivefold symmetry, forbidden in conventional crystallography, can be observed in the diffraction patterns. Thus, the magnetic ordering in quasicrystals should be different from the collinear magnetism of periodic crystals and from spin-glass-like behavior of the disordered media.

The dipolar system on a Penrose tiling is geometrically frustrated; i.e., magnetic moments are unable to find an orientation satisfying the interactions with all neighbors. The frustration in quasicrystals is different from that of periodic systems and that of disordered media. In highly ordered magnets the frustration is uniform, i.e., equal for all lattice points. In disordered materials the frustration is random. In quasicrystals the change in coordination number leads to spatial alternation of the dipolar energy and, thus, the degree of frustration. However, the nonuniform magnetic frustration is not random. The nonuniform geometrical frustration is the second important ingredient for the definition of the magnetic microstructure in quasicrystals.

The exchange coupling in quasicrystals is also different from that of their periodic counterparts. Atoms on quasiperiodic tilings have not only a varying number of neighbors but also several different nearest neighbor distances (Fig. 1). Accordingly, there are several different values of the exchange force which can even change sign. The existence of several exchange constants J can also exert a significant influence on the microstructure of the quasiperiodic magnets.

In summary, it is obvious that the varying number of nearest neighbors, nonisotropic magnetic frustration, and varying J-constants are important for the micromagnetic ordering in quasiperiodic ultrathin films. From the theoretical point of view no general approach has been made up to now.

The aim of the present study is to achieve a general spatially resolved description of the magnetic ordering on the Penrose two-dimensional tiling. Since the Penrose tiling is aperiodic, an analytical description of the

VOLUME 90, NUMBER 13 PHYSICAL REVIEW LETTERS week ending 4 APRIL 2003

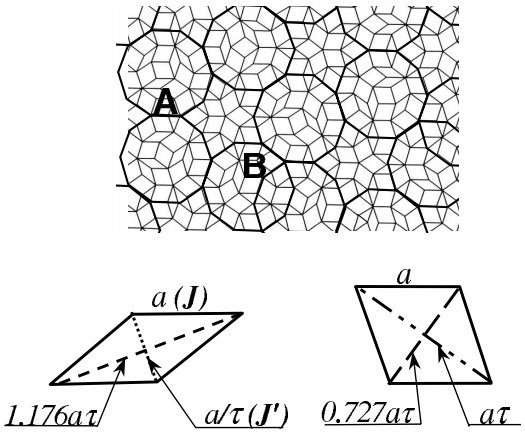

FIG. 1. (a) A section of the Penrose tiling. The original Penrose rhombic tiles and the decagonal tiles are indicated. Two allowed overlapping of decagonal clusters are shown as A and B. (b) The original Penrose rhombic tiles. Five nearest neighbor distances (the sides and the diagonals of the rhombuses) and their lengths are given. τ is the golden mean. The two strongest exchange bonds according to two shortest nearest neighbor distances are denoted as J and J'.

micromagnetic structure is hardly feasible. Therefore Monte Carlo simulations have been performed to find the equilibrium spin configurations at a given temperature. We present as well an original experimental dipolar system made of 309 small magnets on the Penrose tiling. In the Monte Carlo simulations the local ferromagnetic exchange interaction and the long-range dipolar coupling are considered. The experimental system represents a pure dipolar model which corresponds to the numerical simulations for zero exchange interaction. The effects of the indirect exchange coupling are neglected in this study. For a monolayer of three-dimensional vector spins $\mathbf{S}_i$ the Hamiltonian is given by

$$\mathcal{H} = -J\sum_{\langle ij\rangle}\mathbf{S}_i\cdot\mathbf{S}_j + D\sum_{ij}\left(\frac{\mathbf{S}_i\cdot\mathbf{S}_j}{\mathbf{r}_{ij}^3} - 3\frac{(\mathbf{S}_i\cdot\mathbf{r}_{ij})(\mathbf{S}_j\cdot\mathbf{r}_{ij})}{\mathbf{r}_{ij}^5}\right), \quad (1)$$

where J is the exchange coupling constant and $\langle i, j\rangle$ refers to the nearest neighbors, D the dipolar coupling parameter, and $\mathbf{r}_{ij}$ the vector between sites i and j.

The simulations have been carried out on finite Penrose tilings with free boundary conditions. The samples are squares or rectangles containing 400, 2500, and 10 500 magnetic moments. We have also used circular areas to cross-check our results. We have considered the dipolar interaction of each magnetic moment with all the other moments; i.e., we did not use a cutoff in calculating the dipolar coupling. The Monte Carlo procedure is the same as described in a previous publication [6]. The experimental model concerns a 480 mm $\times$ 480 mm Penrose tiling of magnets of 4 mm length separated by 30 mm. The large distance between the magnets is chosen on purpose to minimize multipolar terms that can trap the system into metastable states [7]. The magnets are put onto nonmagnetic vertical axes and can rotate in the x, y plane.

In order to calculate the exchange energy the set of nearest neighbors that are coupled via the short-range interaction has to be defined. In periodic crystals the exchange coupling between next nearest neighbors is usually enough to ensure the magnetic order. In quasicrystals the situation is different. The pattern consists of two rhombuses with edges of equal length a, one with angles of 36° and 144° and the other with angles 72° and 108° (Fig. 1). The rhombic tiles are arranged without gaps or overlaps according to matching rules [5]. The smallest distance between neighbor sites is the short diagonal of the tight rhombus (Fig. 1). The exchange interaction along this diagonal J' is nonpercolating; i.e., it can connect the spins into only very small clusters of a maximal size equal to three moments (see Fig. 1). Thus, it cannot ensure the magnetic alignment of the whole sample. To get a long-range magnetic order the exchange coupling along the sides of the rhombuses J must be included (Fig. 1). Usually, in theoretical studies of critical behavior of quasiperiodic systems only J or J and J' interactions are considered (longer bonds are neglected). With such a treatment of bonds the lattice deviates from the original Penrose tiling. In our study five different values of the exchange constant, i.e., for the sides and all diagonals of the rhombuses, have been considered. J has been taken to be unity. The exchange interaction decreases exponentially with the distance between magnetic moments. The strength of the exchange interaction is defined as $J_{ij} = J\exp(1-\rho_{ij})$, where $\rho_{ij} = r_{ij}/a$ is the distance between two neighboring moments normalized to the length of the side of the rhombuses a. ρ_{ij} takes the lengths of the diagonals of the Penrose rhombuses. The shortest diagonal has a length of $\rho_{ij} = \tau^{-1} < 1$ with τ as the golden mean. Therefore $J' = J\exp(1-\tau^{-1})$; i.e., J' is larger than J. Further interactions become weaker than J with increasing distance as in that case $\rho_{ij} > 1$.

Magnetic ordering depends on the ratio of exchange to dipolar constant $R = J/D$ and on the radius of the cutoff in the exchange coupling (ρ). We have performed calculations for R varying between 0 ($J = 0$, pure dipolar interactions) and 1000. The cutoff radius in the exchange interaction can take one of four values: $\rho = a$, which means that the exchange coupling is considered only along sides and the shortest diagonal of the Penrose rhombuses, $\rho = 0.727a\tau$, $\rho = a\tau$, or $\rho = 1.176a\tau$. The latter distances correspond to the exchange coupling along the longer diagonals (see Fig. 1).

Figure 2 shows examples of relaxed micromagnetic configurations for pure dipolar interactions obtained

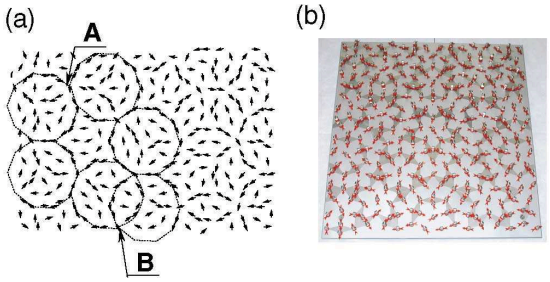

FIG. 2 (color). (a) Monte Carlo simulations. Top view of the portion of the magnetic microstructure in a sample of finite size for pure dipolar interaction, i.e., $R = J/D = 0$. The microstructure has been obtained for a square sample of about 10 500 vector spins on the Penrose tiling for $D/k_BT = 100$. The spins belonging to the perimeter of decagons (marked) form closed chains. The chains overlap according to rules given in Fig. 1. (b) Experimental model. The perspective view of the magnetic microstructure. The red arrows represent the orientation of dipolar moments of magnets fixed onto the nodes of the Penrose tiling (rhombuses). The magnets can rotate in the horizontal plane.

in the numerical [Fig. 2(a)] and in the experimental [Fig. 2(b)] models. Both studies show that after different relaxation procedures a micromagnetic pattern can have a different local arrangement of dipoles. The total energy, however, is always identical. Thus, the ground state in the case of $J = 0$ is highly degenerate. All patterns, theoretical and experimental, have features in common. Magnetic moments are ordered in circular loops. The diameters of the loops are identical all over the sample. The loops overlap. This overlapping is not accidental but follows certain rules. Amazingly, these rules coincide with the recently proposed "decagonal model" of quasicrystals [8–11].

In 1991 it was realized [8] that the planar Penrose tiling can be generated using a single kind of tile, a decagon. Every decagon consists of Penrose rhombuses. In contrast to the conventional tiling description the decagonal atomic clusters overlap, which means that they share atoms with their neighbors. The overlapping rules have been mathematically proven [9]. Only two types of the overlap (A and B) are allowed [8]. Location of "A" and "B" in a Penrose tiling are marked in Figs. 1 and 2(a).

The decagons can be easily recognized in the magnetic microstructure [Figs. 2(a) and 2(b)]. In order to minimize the dipolar energy the magnetic moments located on the perimeter of a decagon form closed chains. The moments are coplanar to the sides of the decagons. The overlapping rings of magnetic moments can have the same or opposite sense of rotation. The orientation of the moments that do not belong to the perimeter of decagons is highly frustrated and varies from cluster to cluster. The overlapping magnetic decagon chains form a quasiperiodic pattern. In case of pure dipolar interaction the magnetic pattern is formed on the scale of the tiling constant; i.e., a microscopic pattern is formed. In zero magnetic field this state is degenerate and represents a manifold of quasiperiodic spin configurations. All frustrated systems that have been investigated have either a continuously degenerated, periodic ground state (spins on a honeycomb, a kagome, a triangular, a pyrochlore lattice [12]) or a completely disordered one (spin glasses). The superposition of both types of frustration has not been reported yet. Thus, a magnetic system on a Penrose tiling belongs to a new class of frustrated systems where the degenerated ground state is aperiodic and consists of two parts: ordered decagon rings and disordered spin-glass-like phase inside the decagons.

In the following we will discuss the situation where the exchange coupling is switched on. In the quasiperiodic Penrose tiling with high R, i.e., with the strong exchange interaction, we find a single domain for all cutoff radii $\rho \geq a$. It means that the exchange coupling acting along the two shortest bonds (J and J') is enough to ensure the ferromagnetic order. However, the degree of magnetic order increases with increasing ρ. While the low temperature magnetization is unity for the large exchange cutoff radius $\rho = 1.176a\tau$, it is $\bar{M} = 0.975$ for $\rho = a$ ($R = 10^3$). Hence, the ferromagnetic order in quasicrystals depends on the cutoff radius taken for the exchange interaction. This can cause strong inhomogeneities of the magnetization at the boundaries of laterally confined magnet with quasiperiodic structure.

In finite samples on square and triangular lattices single domain configurations have been found for high R values while in-plane vortex structures dominate for $R \approx 1$ [13]. The vortex phase arises as a result of the influence of the sample boundaries. The dipolar interaction prefers to keep the magnetic moments in the film plane and parallel to the sample edges to avoid formation of magnetic poles. The exchange energy cares for the parallel orientation of the neighboring moments. The interplay of the different contributions leads to formation of the vortex structure with dimensions of the sample size. For the Penrose tiling the situation is completely different. For all R-ratio and cutoff radii the macroscopic vortex configuration is energetically unfavorable with regard to the exchange interaction. When the dipolar energy becomes strong enough to compete with the exchange energy ($R < 0.5$) the microscopic decagonal pattern starts to form (Fig. 3). The decagonal pattern differs from that of the pure dipolar case when exchange interaction is effective. The strong exchange coupling lifts the degeneracy of the decagonal magnetization configuration found for $J = 0$. Magnetic moments are nearly coplanar with the sides of the decagons as in the pure dipolar case. The average magnetization, however, is not zero; i.e., the magnetic moments have some preferential direction [Fig. 3(a)]. We call such magnetization configuration quasiferromagnetic decagonal structure. A

VOLUME 90, NUMBER 13 PHYSICAL REVIEW LETTERS week ending 4 APRIL 2003

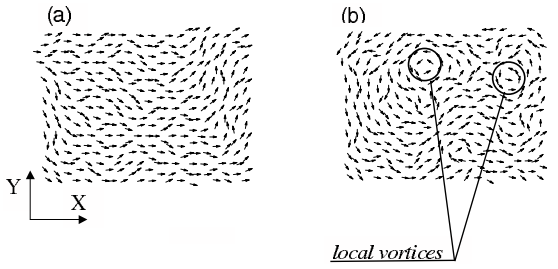

FIG. 3. (a) Top view of the portion of the quasiferromagnetic spin configuration in a sample of finite size for $\rho = 1.176a\tau$ and $R = J/D = 5$. The magnetic moments are nearly coplanar to the sides of the decagons. The X component of the average magnetization is $M_X = 0.85$. (b) An example of a planar spin configuration in the region of transition from the single domain to the decagonal structure for $\rho = 1.176a\tau$ and $R = J/D = 0.4$. The microstructures have been obtained for square and disk-shaped samples of 400 and 10 500 magnetic moments at $J/(k_BT) = 100$. The magnetic moments at the edges are oriented mainly parallel to the boundary as in a conventional vortex structure. However, only local vortices inside the decagons exist.

further decrease of the ratio R leads to an increasing influence of the dipolar interaction on the magnetic microstructure. To minimize the magnetostatic energy the dipoles form lines at the edges of the sample as in conventional vortex structure [Fig. 3(b)]. However, a macroscopic vortex does not form for any shape of the sample. Small local vortices can appear only inside some decagon rings [Fig. 3(b)].

Thus, the influence of the boundaries does not lead to the formation of a macroscopic vortex in a Penrose tiling. The reason for this phenomenon is the spatial variation of the number of nearest neighbors and the exchange interaction strength. As the strength of the exchange interaction decreases exponentially with the distance, J is much stronger for neighbors with $\rho_{ij} \leq a$, i.e., with $J \geq 1$, than for neighbors with $\rho_{ij} > a$. The magnetic moments with $\rho_{ij} \leq a$ are situated mainly on the perimeter of the decagons. It is energetically more preferable to keep these moments parallel than the other ones which causes the appearance of decagonal chains and the local vortices. The formation of macroscopic configurations is suppressed in favor of the microscopic quasiferromagnetic pattern.

In conclusion, the stable magnetization configurations of magnets on a quasiperiodic tiling have been derived theoretically. In contrast to periodic lattices, the formation of macroscopic vortex configuration is suppressed in favor of the microscopic quasiferromagnetic pattern. For low R ratios a new microscopic structure, the quasiferromagnetic decagonal pattern, represents the minimum of the free energy. For pure dipolar interaction the decagonal pattern represents a new class of frustrated systems where the degenerated ground state is aperiodic and consists of two parts: ordered decagon chains and disordered spin-glass-like phase inside the decagons.

The authors thank J. Wille for preparation of the experimental model.

[1] See for a review H. P. Oepen and J. Kirschner, Curr. Opin. Solid State Mater. Sci. **4**, 217 (1999).
[2] Z. Luo, S. Zhang, Y. Tang, and D. Zhao, Scr. Metall. Mater. **28**, 1513 (1993); A. Niikura, A. P. Tsai, A. Inoue, and T. Masumoto, Philos. Mag. Lett. **69**, 351 (1994); A. P. Tsai, A. Niikura, A. Inoue, T. Masumoto, Y. Nishida, K. Tsuda, and M. Tanaka, Philos. Mag. Lett. **70**, 169 (1994).
[3] See for a review U. Grimm and M. Baake, in *The Mathematics of Long-Range Aperiodic Order*, edited by R. V. Moody (Kluwer, Dordrecht, 1997), p. 199.
[4] See for a review K. De'Bell, A. B. MacIsaac, and J. P. Whitehead, Rev. Mod. Phys. **72**, 225 (2000).
[5] R. Penrose, Bull. Inst. Math. Appl. **10**, 266 (1974).
[6] E. Y. Vedmedenko, H. P. Oepen, A. Ghazali, J.-C. S. Lévy, and J. Kirschner, Phys. Rev. Lett. **84**, 5884 (2000).
[7] E. Olive and P. Molho, Phys. Rev. B **58**, 9238 (1998).
[8] S. E. Burkov, Phys. Rev. Lett. **67**, 614 (1991).
[9] P. Gummelt, in *Proceedings of the 5th International Conference on Quasicrystals*, edited by C. Janot and R. Mosseri (World Scientific, Singapore, 1995), p. 84.
[10] P. J. Steinhardt and H. C. Jeong, Nature (London) **382**, 433 (1996); H. C. Jeong and P. J. Steinhardt, Phys. Rev. B **55**, 3520 (1997).
[11] K. W. Urban, Nature (London) **396**, 14 (1998).
[12] P. Schiffer, Nature (London) **420**, 35 (2002).
[13] E. Y. Vedmedenko, A. Ghazali, and J.-C. S. Lévy, Phys. Rev. B **59**, 3329 (1999); J. Sasaki and F. Matsubara, J. Phys. Soc. Jpn. **66**, 2138 (1996).

Ferroelectrics, 305: 129–132, 2004

ISSN: 0015-0193 print / 1563-5112 online
DOI: 10.1080/00150190490462559

Taylor & Francis
Taylor & Francis Group

Quasiperiodic Magnetic Order and Geometrical Frustration on the Penrose Tiling

E. Y. VEDMEDENKO

Institute of Applied Physics, University of Hamburg, Hamburg, Germany

(Received 1 September 2003; accepted 19 September 2003)

The spatial variation of the coordination number on the Penrose tiling leads to suppression of the formation of macroscopic vortex configuration, usual to soft ferromagnetic films on periodic lattices, in favor of microscopic decagonal pattern. That state represents a new class of frustrated systems where the structure is aperiodic and consists of two parts: ordered, stable decagon chains and an unstable, spin-glass phase inside of the decagons. Virgin magnetizing is a two-step process in that system.

Keywords Quasicrystals; magnetic properties of thin films; frustration; classical spin models

1. Magnetic Ordering in Quasicrystals

Recent investigations [1–3] show that a long-range magnetic order can exist in quasicrystals despite their aperiodic atomic structure. Experimentally, antiferromagnetic ordering has been observed in rare-earth-based icosahedral compounds [4]. Theoretically, possible antiferromagnetic ground states have been studied in the framework of the Ising [1], the XY [5, 6] and the quantum Heisenberg model [7]. Ferromagnetic microstructure of a two-dimensional aperiodic film has been derived for three-dimensional Heisenberg spins on a Penrose tiling [3].

In calculations [3] the long-range dipolar interaction, always existing in magnetic and ferroelectric materials, has been taken into account. It has been shown [3] that in ultra-thin film on a Penrose tiling new, decagonal quasiferromagnetic long-range order appears. In the present investigation I will analyze the reasons preventing formation of usual ferromagnetic configurations, such as a vortex structure, on a Penrose tiling. Influence of thermal excitations on the decagonal pattern will be also studied.

2. Energy Considerations

To find out the ground ferromagnetic state on a Penrose tiling we have compared the total energy density of a macroscopic monodomain, a macroscopic vortex and a Monte-Carlo (MC) quasiferromagnetic pattern. The quasiferromagnetic pattern has been obtained by means of MC simulations. The MC procedure is described elsewhere [3]. Two-dimensional films of classical, three-dimensional magnetic moments **S** have been studied. The Hamiltonian

Address correspondence to E. Y. Vedmedenko, Institute of Applied Physics, University of Hamburg, Hamburg, Germany. E-mail: vedmedenko@physnet.uni-hamburg.de

of the problem is given by

$$H = J \sum_{\langle i,j \rangle} \mathbf{S_i} \cdot \mathbf{S_j} + D \sum_{i,j} \left(\frac{\mathbf{S}_i \cdot \mathbf{S}_j}{r_{ij}^3} - 3 \frac{(\mathbf{S}_i \cdot \mathbf{r}_{ij})(\mathbf{S}_j \cdot \mathbf{r}_{ij})}{r_{ij}^5} \right) \tag{1}$$

where J is the exchange coupling constant and $\langle i,j \rangle$ refers to the nearest neighbors, D the dipolar coupling parameter and $\mathbf{r}_{ij}$ the vector between sites i and j. The samples are squares or rectangles containing 400, 2500 and 10500 magnetic moments. I have also used circular areas to crosscheck the results. The vortex and the monodomain configurations have been constructed artificially. Then, in order to take into account effects of the entropy and inhomogeneous magnetization the configurations have been relaxed at low temperature by means of MC procedure. The lowest temperature of the usual MC annealing process $kT = 0.05J \ldots 0.1J$ has been used. At that temperature macroscopic patterns cannot be destroyed by thermal fluctuations while the magnetization is not more homogeneous.

It has been considered in the calculations that the exchange interaction decreases exponentially with the distance between magnetic moments. The strength of the exchange coupling is defined as $J = J_0 e^{(1-\rho_{ij})}$, where $\rho_{ij} = r_{ij}/a$ is the distance between two neighboring moments normalized to the length of the side of Penrose rhombuses a (see Fig. 1). ρ_{ij} takes the lengths of the diagonals of the Penrose rhombuses. The shortest diagonal has a length of $\rho_{ij} = 1/\tau < 1$ with τ- the golden mean. Therefore $J' = J_0 e^{(1-\tau^{-1})}$; i.e., J' is larger than J_0. Further interactions become weaker than J_0 with increasing distance as in that case $\rho_{ij} > 1$. As the magnetic ordering depends on the ratio of the exchange to the dipolar interaction $R = J/D$ and on the radius of the cut-off in the exchange coupling ρ I have performed calculations for different R and ρ. ρ can take one of four values: $\rho = a$, which means that the exchange coupling is considered only along sides and the shortest diagonal of the Penrose rhombuses (see Fig. 1); $\rho = 0.727a\tau$; $\rho = a\tau$ or $\rho = 1.176a\tau$. The latter distances correspond to the interactions along the longer diagonals. R has been varied between 0 ($J = 0$, pure dipolar interactions) and 1000. The energies of different configurations versus R for the maximal value of ρ are presented in Fig. 2. As soon as the energy of the vortex or the quasiferromagnetic structure becomes smaller than the energy of a single domain a crossing of curves will occur. The point of intersection gives a critical ratio R_C where the transition between different configurations happens. We do not find any R and ρ where the macroscopic vortex is preferred. The shaded area separates the phases of the monodomain and the decagonal pattern. The center of the interval where all

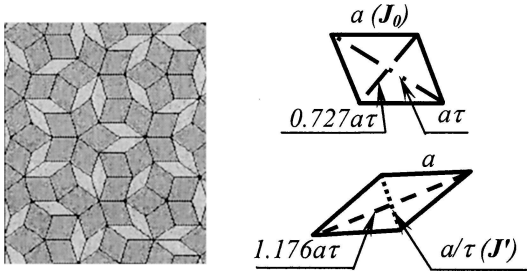

FIGURE 1 A section of the Penrose tiling. The Penrose rhombic tiles are indicated. Five nearest-neighbor distances (the sides and the diagonals of the rhombuses) and their lengths (τ the golden mean) are given. The two strongest exchange bonds according to two shortest nearest-neighbor distances are denoted as J_0 and J'.

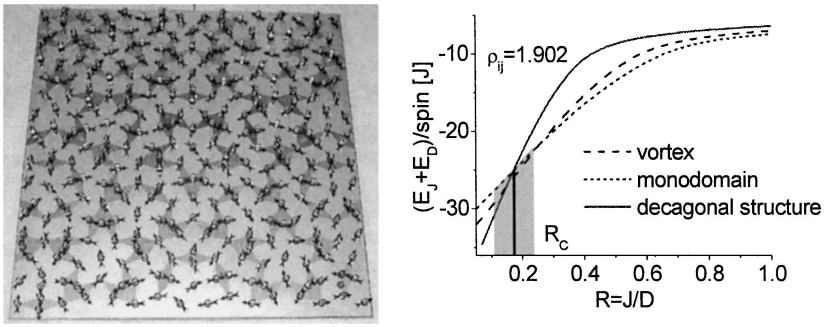

FIGURE 2 (Left) Experimentally obtained dipolar decagonal structure. The red arrows represent the orientation of dipolar moments of magnets fixed onto the nodes of the Penrose tiling. (Right) Total energy per spin for a monodomain, an ideal vortex and a Monte Carlo decagonal structure as a function of $R = J/D$.

three configurations have comparable energy is denoted as R_C. For $R \approx R_C$ the magnetic microstructure consists of ordered regions with the decagonal pattern and local vortices [3]. Thus, the influence of the boundaries does not lead to the formation of a macroscopic vortex in a Penrose lattice. In other words the dipolar energy can compete with the exchange energy only on the scale of the quasiperiodic decagonal microstructure. The reason for this phenomenon is the spatial variation of the number of nearest neighbors and the exchange interaction strength in quasicrystals.

2. Thermal Stability of the Quasiperiodic Decagonal Structure

In the remaining section I will discuss the influence of thermal excitations on the decagonal ordering. To see the time-dependent changes in a microstructure we let run the simulation for several hundred thousand steps per temperature. Extremely slow annealing procedure with 30 temperature steps per MC run has been applied. The results have been compared with an experimental dipolar model made of 309 small magnets on a Penrose tiling. The magnets can freely rotate in the horizontal plane. An example of the experimental magnetic pattern is given in Fig. 2. MC configurations have identical features. The decagonal pattern of pure dipolar system consists of two parts: ordered decagon rings and disordered spins inside of the decagons. The diameters of the closed loops are identical all over the sample. The loops overlap. This overlapping is not accidental but follows the rules of recently proposed "decagonal model" of quasicrystals [8]. Orientations of disordered dipoles are not static at temperatures kT $>$ 0.2 D. They change continuously during the MC run while the decagon chains remain stable and the total energy oscillates around its minimal value. In the experimental model we have simulated the temperature by application of an alternating magnetic field. When a very weak field is applied the magnetic moments inside of the rings begin to oscillate. The moments on the perimeter of decagons, in contrast, remain stable to very high values of the field. In addition to the alternating magnetic field a constant external magnetic field can be also applied to the structure. Even a strongest possible in-plane magnetic field was not enough to destroy the experimental decagonal pattern while the frustrated inner dipoles were immediately aligned. In the simulations the field necessary for the alignment of the chains must be at least 15 times stronger than that needed for the alignment of the frustrated moments. Thus, in the quasiperiodic magnetic structure the stable decagonal pattern coexists with highly frustrated, glass-like phase. That regime corresponds

to the frustration effects in a Penrose tiling found earlier [9]. Virgin magnetization process takes place in two steps: switching of the frustrated phase at a weak external magnetic field and switching of the ordered phase at a higher field.

References

1. See for a review U. Grimm and M. Baake, in *The Mathematics of Long-Range Aperiodic Order*, ed. Moody R.V., Kluwer, Dordrecht, 199–222 (1997).
2. R. Lifshitz, Symmetry of magnetically ordered quasicrystals. *Phys. Rev. Lett*. **80**, 2717–2720 (1998).
3. E. Y. Vedmedenko, H. P. Oepen, and J. Kirschner, *Phys. Rev. Lett*. **90**, 137203(1–4) (2003).
4. B. Charrier, B. Ouladdiaf, and D. Schmitt, *Phys. Rev. Lett*. **78**, 4637–4640 (1997).
5. J. Hermisson, *J. Phys. A: Math. Gen*. **33**, 57–59 (2000).
6. D. Ledue, J. Teillet, J. Carnet, and J. Dujardin, *J. of Non-Crystalline Solids* **153–154**, 403–406 (1993).
7. A. Wessel, A. Jagannathan, and S. Haas, Cond-mat/0209405 (2002).
8. P. Gummelt, in *Proceedings of the 5th International Conference on Quasicrystals*, eds. by C. Janot and R. Mosseri, World Scientific, Singapore, 84–89 (1995).
9. G. G. Naumis, R. A. Barrio, and C. Wang, *Phys. Rev. B* **50**, 9834–9842 (1994).

VOLUME 93, NUMBER 7 PHYSICAL REVIEW LETTERS week ending 13 AUGUST 2004

Noncollinear Magnetic Order in Quasicrystals

E. Y. Vedmedenko,[1] U. Grimm,[2] and R. Wiesendanger[1]
[1]*Institut für Angewandte Physik, Jungiusstrasse 11, 20355 Hamburg, Germany*
[2]*Applied Mathematics Department, The Open University, Walton Hall, Milton Keynes MK7 6AA, United Kingdom*
(Received 5 April 2004; published 13 August 2004)

Based on Monte Carlo simulations, the stable magnetization configurations of an antiferromagnet on a quasiperiodic tiling are derived theoretically. The exchange coupling is assumed to decrease exponentially with the distance between magnetic moments. It is demonstrated that the superposition of geometric frustration with the quasiperiodic ordering leads to a three-dimensional noncollinear antiferromagnetic spin structure. The structure can be divided into several ordered interpenetrating magnetic supertilings of different energy and characteristic wave vector. The number and the symmetry of subtilings depend on the quasiperiodic ordering of atoms.

DOI: 10.1103/PhysRevLett.93.076407 PACS numbers: 71.23.Ft, 75.10.Hk, 75.50.Ee, 75.70.Ak

The last few years have shown a boom in investigations of the spin order in antiferromagnetic films [1,2] motivated by the dramatic changes in the magnetic properties of such systems induced by frustration. In contrast to the rather well studied spin structure of antiferromagnets on periodic lattices, the antiferromagnetic ordering of quasicrystals is the subject of ongoing scientific debate. Whereas an experimental finding of long-range antiferromagnetic order in rare-earth icosahedral quasicrystals [3] turned out to be an artifact [4], theoretical models that deal with magnetism on quasicrystals [5] are known to exhibit long-range magnetic order. Recent inelastic neutron scattering experiments on the Zn-Mg-Ho icosahedral quasicrystal [6] revealed a very peculiar diffuse scattering pattern with icosahedral symmetry at temperatures below 6 K. Such a pattern, in principle, can originate from a noncollinear spin arrangement first suggested by Lifshitz from pure geometrical considerations [7–9]. However, real-space magnetic configurations leading to those long wave-vector correlations remain obscure despite recent interesting results for quantum spins [5]. Thus, the knowledge about the spin structure on quasiperiodic tilings is of basic importance for experiments as well as for theoretical predictions of new phenomena, which can be expected due to nontrivial frustration effects [10].

The patterns found in our theoretical study provide an explanation for the origin of the antiferromagnetic modulations observed experimentally in Ref. [6]. While the spin order in antiferromagnets is usually characterized by a periodic modulation described by wave vectors on the order of inverse atomic distances, the spin order in antiferromagnetic quasicrystals admits three-dimensional noncollinear structures consisting of several interpenetrating subtilings with longer wave vectors. Here we report on the details of the low-temperature antiferromagnetic ordering and the map of the local frustration for the octagonal tiling.

We discuss the antiferromagnetic Hamiltonian

$$H = J_{ij}\sum_{\langle i,j\rangle}\mathbf{S}_i \cdot \mathbf{S}_j - K_1\sum_i (\mathbf{S}_i^z)^2, \qquad (1)$$

where $\mathbf{S}_i$ is a three- or two-dimensional unit vector in the case of classical vector or xy spins, and $\mathbf{S}_i^z$ is equal to ± 1 in the case of Ising spins (so $\mathbf{S}_i^x = \mathbf{S}_i^y = 0$); $\langle i, j\rangle$ denotes the nearest-neighbor pairs. For an antiferromagnetic system, the exchange parameter J_{ij} is positive, and neighboring antiparallel spins contribute a lower energy than parallel neighbors. The coefficient K_1 is the first-order anisotropy constant. Our Monte Carlo simulations have been carried out on finite Ammann-Beenker tilings with free boundary conditions. The procedure is a simulated annealing method with at least 15 successive temperature steps [11]. At each temperature, the convergence of the relaxation process towards equilibrium has been observed for any initial configuration after a few thousand Monte Carlo steps per spin. Hence, the single-spin-update algorithm is efficient in our case. At the end of the cooling down process, the total energy is just fluctuating around its mean equilibrium value. To reduce boundary effects only the core of a tiling has been analyzed. The samples on the octagonal Ammann-Beenker structure, which we concentrate on in what follows, are circular, containing 2193, 11 664 and 53 018 magnetic moments.

The octagonal tiling consists of two motifs: a square and a rhombus of equal edge lengths a [Fig. 1(a)]. The diagonal bonds are, usually, neglected in the calculations [5,12]. We find this disregard physically questionable as the exchange coupling increases exponentially with decreasing interatomic distance. In the present investigation, the short diagonal of the rhombus and the sides of the motifs have been considered as nearest neighbors. We distinguish the two cases $J_d > 2J$ and $J_d < 2J$, where J_d denotes the interaction along the short diagonal and the interaction strength along the sides J is unity. The first case corresponds to a rapid growth of the exchange

VOLUME 93, NUMBER 7 PHYSICAL REVIEW LETTERS week ending 13 AUGUST 2004

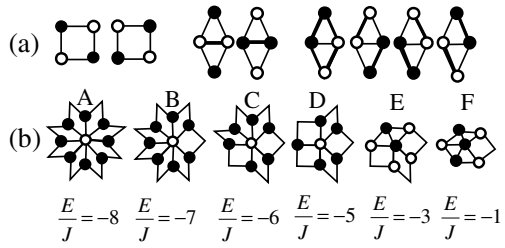

FIG. 1. Configurations for a frustrated Ising antiferromagnet on (a) elementary tiles and (b) six local environments of the Ammann-Beenker tiling. The bold lines denote the frustrated bonds. The open and filled circles represent different spins.

coupling with decreasing interatomic distance. The two nearest-neighbor bonds form six local environments with coordination numbers varying from five to eight as shown in Fig. 1(b). They occur with relative frequencies $\nu_A = 17 - 12\sqrt{2} \approx 2.9\%$, $\nu_B = -41 + 29\sqrt{2} \approx 1.2\%$, $\nu_C = 34 - 24\sqrt{2} \approx 5.9\%$, $\nu_D = -14 + 10\sqrt{2} \approx 14.2\%$, $\nu_E = 6 - 4\sqrt{2} \approx 34.3\%$, and $\nu_F = -1 + \sqrt{2} \approx 41.4\%$ [13]. Taking into account the short diagonals of the rhombic tiles increases the average coordination number of the tiling from 4 (the value without diagonals) to $8\nu_A + 7\nu_B + 6\nu_C + 5(\nu_D + \nu_E + \nu_F) = 8 - 2\sqrt{2} \approx 5.17$.

First we discuss the Ising system. The square tile of the octagonal structure is nonfrustrated as every pair of the moments can be chosen to be antiparallel [Fig. 1(a)]. If we had not taken the short diagonals of the rhombic tiles into account, the same would have been true for the entire tiling, and there would be no frustration, because the rhombic tiling is bipartite. Now, we consider spins on short diagonals as nearest neighbors; the rhombic tiles are always frustrated. If the energy of one nearest-neighbor pair is minimized by having antiparallel spins, the third and fourth spins cannot be chosen to minimize the energy of both of its neighbors [Fig. 1(a)]. The magnetic moment will necessarily be parallel to one of the neighbors. For $J_d < 2J$ two out of six possible configurations have smaller energy as they possess only one pair of parallel nearest neighbors per rhombus instead of two [Fig. 1(a)]. In this case spins can have one of six possible energy values corresponding to different local environments [Fig. 1(b)]. For $J_d > 2J$ the four configurations with the two parallel bonds have the lowest energy as their weight is smaller than that of the strong diagonal coupling. The second case comprises much more different possibilities of energy distribution. To give a quantitative description of the local frustration we introduce a local parameter f,

$$f = \frac{|E_{id}| - |E_i|}{|E_{id}|}, \tag{2}$$

where E_i is an actual energy of a spin i and E_{id} is a ground state energy of a relevant unfrustrated vertex. With this nomenclature, only the central spins of the vertices F and E are magnetically frustrated $f_F = 0.4$ and $f_E = 0.8$ for $J_d = J < 2J$. The Monte Carlo simulations confirm our reasoning based on the analysis of frustration. Figure 2(a) gives the frequency distribution of the exchange energy per atom E for two cases and a top view of a portion of Ising configuration with $J_d > 2J$. The energy distribution for $J_d < 2J$ simply reproduces the frequency of six vertex configurations. The "up" and "down" configurations are perfectly ordered and coincide with the black-and-white model of Niizeki [14]. For large J_d we find eight possible energy values. The up and down subtilings, however, are spatially disordered [see the inset in Fig. 2(a)]. We have calculated the magnetic structure factor

$$S^{zz}(\mathbf{k}) = \frac{1}{N}\sum_{\mathbf{r},\mathbf{r}'} e^{i\mathbf{k}\cdot(\mathbf{r}-\mathbf{r}')}\langle S^z_{\mathbf{r}} S^z_{\mathbf{r}'}\rangle \tag{3}$$

using the Monte Carlo data for different samples. Here $\mathbf{k}$ is the wave vector and $S^z_{\mathbf{r}}$ is a vertical component of a magnetic moment at the position $\mathbf{r}$. The diffraction pattern of the Niizeki configuration coincides with that of

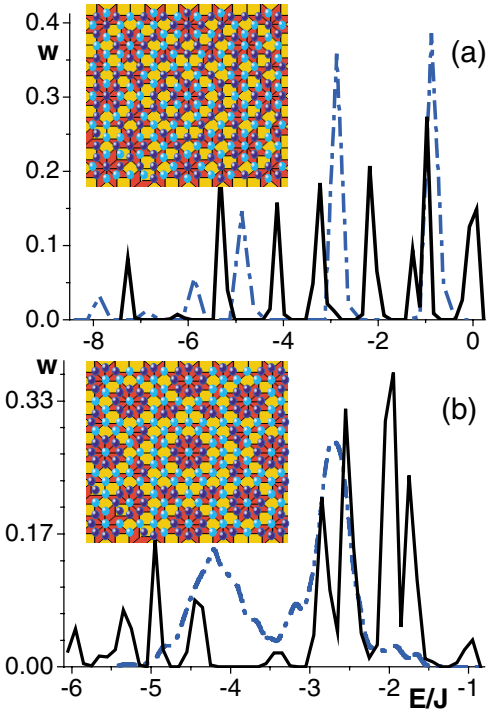

FIG. 2 (color). The frequency distribution of the energy per spin on the octagonal tiling for (a) Ising and (b) vector spins. The solid lines correspond to the case $J_d < 2J$, the dashed lines to $J_d > 2J$. A purely antiferromagnetic interaction at $kT = 0.01J$ is considered. The top views of portions of Monte Carlo configurations with underlying tilings are shown as insets. The light and dark circles represent different spins in (a) and different energies in (b), respectively.

quantum Monte Carlo calculations [Figs. 5(c) and 5(d) of Ref. [5]] and theoretical prediction [9], while the intensity map of the configuration Fig. 2(a) is almost structureless. It means that the Ising solution with $J_d < 2J$ reproduces in essence the antiferromagnetic superstructure, corresponding to a modulation vector $\mathbf{q} = (\frac{1}{2}, \frac{1}{2}, \frac{1}{2}, \frac{1}{2})_{a^*}$ [6] in the octagonal tiling, whereas stronger coupling leads to a spin-glass state.

An exciting question is if the further minimization of the total energy and frustration by means of the noncollinear alignment of magnetic moments is possible. At first glance the magnetic structure of the low-temperature pure antiferromagnetic configuration seems to be rather disordered. The analysis of the local energies, however, reveals several characteristic energetic maxima in the frequency distribution shown in Fig. 2(b). The simple existence of the peaks means that there exist different sorts of magnetic moments having well-defined relative orientation to their nearest neighbors. This orientation, however, is not associated with any absolute direction in space. Therefore, in accordance with the Mermin-Wagner theorem [15], no long-range order exists in two dimensions with continuous symmetry, because thermal fluctuations result in a mean-square deviation of the spins from their equilibrium positions which increases logarithmically with the size of the system. The addition of a very weak anisotropy, which often exists in real samples, does not change the distribution of the exchange energy, but permits one to anchor the absolute spatial orientation of the magnetization. Nevertheless, at first glance the total structure still looks spin-glass-like. In the following, we show that the antiferromagnetic structure of the octagonal tiling is perfectly ordered, but the order is nontrivial and unusual for periodic crystals. We concentrate a further description on 3D vector spins while similar results for xy spins have been obtained.

To obtain an absolute symmetry axis, we apply a very weak out-of-plane anisotropy $K_1 \approx 10^{-3}J$ to the system. The squared vertical component of magnetization $(S^z)^2$ becomes finite. The positions of the energy peaks on the frequency diagram remain unchanged. All maxima are different from those of the Ising model. It means that the angles between the neighboring magnetic moments are not always equal to 180° or 0°; i.e., the magnetic structure is noncollinear. The different number of peaks—eight for $J_d < 2J$ and two for $J_d > 2J$ [Fig. 2(b)]—already tells us that, in contrast to the Ising case, the maxima do not coincide with the six vertices of the tiling. The minimal possible local energy increases from $-8J$ to approximately $-6J$ for $J_d = J$ or $-5.44J$ for $J_d = 2.2J$. The average energy per spin, however, decreases by more than $0.3J$ and reaches the value of $E \approx -2.85J$ and $E \approx -3.30J$, respectively. Hence, the increase of the entropy permits one to minimize the average frustration and the total energy of the system.

Spatial arrangements of the magnetic moments as a function of the exchange energy are given in Fig. 3 for $J_d < 2J$ and in the inset to Fig. 2(b) for $J_d > 2J$. Each configuration of Fig. 3 represents a certain energy range corresponding to one of the eight peaks in the spectrum of Fig. 2(b). Colors represent the x projection of the magnetization. The magnetic moments form eight subtilings of different energy $(E_1, \ldots, E_8)$ which generally do not coincide with a specific vertex type. The splitting of the energy and frustration levels is described in detail in Fig. 3. For example, the vertices B and C (Fig. 1) belong to the same energy maxima E_2 but have different local frustration $f_B = 0.24$, $f_C = 0.11$ (Fig. 3). At the same time the central spin of the vertex D can have either the energy E_3 or E_4 and, therefore, can have two different values of the frustration $f_{D1} = 0.01$ and $f_{D2} = 0.11$ depending on local surroundings. Thus, every configuration of the Fig. 3 can enclose either a part of the atomic places belonging to one vertex type or two different vertex types together. Nevertheless, all structures have a perfect general spatial ordering. Each subtiling can be separated into the energetically degenerate "right" and "left" parts which also have a perfect quasiperiodic arrangement. However, not all right or left moments have identical orientation in space. Figure 4 shows a perspective view of a portion of a typical Monte Carlo configuration and a corresponding energy map. The central magnetic moment has the lowest energy and belongs to the E_1 subtiling. Its eight nearest neighbors have identical energies and correspond to the energy E_7 despite having different sets of mutual angles. The moments forming the next ring have energy E_6. The last ring consists of the alternating E_3 and E_6 spins. Figure 4 shows one of the radially symmetric vertices. However, in the octagonal tiling vertices with a different surrounding can also be found. The energy distribution is then different. Hence, the magnetic structure for $J_d < 2J$ is noncollinear and consists of eight inter-

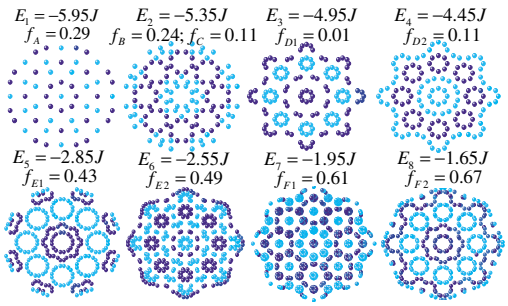

FIG. 3 (color online). Spatial distribution of magnetic moments belonging to eight subtilings of a noncollinear configuration on an octagonal tiling consisting of 2193 spins. $J_d > 2J$. The light and dark circles represent positive and negative x components of the magnetization. The in-plane components are not given for the sake of simplicity. Average values of the exchange energy E and of the local frustration f per spin are indicated.

VOLUME 93, NUMBER 7 PHYSICAL REVIEW LETTERS week ending 13 AUGUST 2004

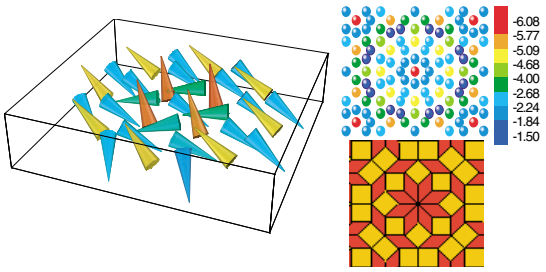

FIG. 4 (color). Perspective view of a portion of a Monte Carlo configuration on an octagonal tiling. The top view of the patch and the energy map are shown as insets. Magnetic moments are represented as cones. The cones are colored according to their vertical magnetization, changing gradually from red for up to blue for down spins. In the energy map inset, the colors encode the energy per moment.

penetrating subtilings. For $J_d > 2J$ we find only two subtilings of different energy.

A frequency distribution of the angle between nearest neighboring moments shows five characteristic angles close to 60°, 80°, 120°, 140°, and 180° for small J_d and a single mutual angle of 110° for large J_d. Because of this noncollinearity the energy of the system is decreased. The diffraction pattern of the whole structure is more complex than that of the Ising or the quantum-mechanical [5] model. As the spin structure is noncollinear, not only the structure factor S^{zz} but also S^{xx} and S^{yy} can be recognized (see Fig. 5). The eightfold S^{xx} and S^{zz} patterns contain additional long wave-vector peaks which could not be identified in the previous investigations [5]. In dependence on the anisotropy (or on the initial random configuration for $K_1 = 0$) new peaks also occur in S^{yy}. The Bragg reflexes found in our study select a subset of the wave vectors given in Ref. [9], where $n_1 + n_2 + n_3 + n_4$ is odd. Peaks with $n_1 + n_2 + n_3 + n_4$ even are extinct. According to the nomenclature of Ref. [9], the following wave vectors can be identified: $(1, 0, 0, 0)$, $(1, -1, 1, 0)$, $(3, -2, 1, 1)$, $(3, -1, -1, 2)$, $(1, 1, -1, 0)$, $(1, 0, 1, -1)$, $(0, 2, -1, 0)$, $(0, 0, 1, -2)$, $(-1, 0, 1, -3)$, $(0, 2, -2, 1)$, $(0, 1, -2, 2)$. Hence, the noncollinearity of the spin structure gives rise to selection

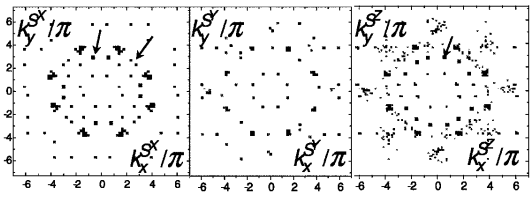

FIG. 5. The calculated Bragg scattering of S^x, S^y, and S^z components of magnetization for the antiferromagnetic superstructure. Reflexes indicated by arrows are new in comparison to previous studies [5].

rules different from those of collinear models [5,7]. With an increasing sample size the peaks become more diffuse and may correspond to the diffuse scattering signal of Ref. [6].

In conclusion, we demonstrate that the frustrated classical Ising system with antiferromagnetic coupling on a quasiperiodic octagonal tiling is perfectly ordered. All spins can be divided into six quasiperiodic (in the 3D physical space) or six periodic (in 6D periodic crystal) subtilings of different energy. Each subtiling corresponds to the one of six vertex types of the Ammann-Beenker structure and is degenerated for up and down magnetic moments. Quantitatively, only two out of six subtilings are frustrated with the local coefficients $f_E = 0.4$ and $f_F = 0.8$. The vector spin system admits a three-dimensional noncollinear magnetic structure. For $J_d < 2J$, the whole structure can be decomposed into eight subtilings of different energy which generally do not coincide with a specific vertex type. All subtilings are frustrated. However, the total degree of frustration and the energy of the system is minimized compared to the noncollinear case. The subtilings are degenerated with respect to the spin direction. The codirectional spins of every subtiling reveal perfect quasiperiodic ordering with a wave vector which is specific for a given subtiling.

We thank R. Lifshitz for helpful comments and indexing of the Bragg peaks. Financial support from the Interdisciplinary Nanoscience Center Hamburg (INCH) is gratefully acknowledged.

[1] Ph. Kurz, B. H. Bihlmayer, K. Hirai, and S. Blügel, Phys. Rev. Lett. **86**, 1106 (2001).
[2] S. Heinze, M. Rode, A. Kubetzka, O. Pietzsch, X. Nie, S. Blugel, and R. Wiesendanger, Science **288**, 1805, (2000).
[3] B. Charrier, B. Ouladdiaf, and D. Schmitt, Phys. Rev. Lett. **78**, 4637 (1997).
[4] T. J. Sato, H. Takakura, A. P. Tsai, and K. Shibata, Phys. Rev. Lett. **81**, 2364 (1998).
[5] S. Wessel, A. Jagannathan, and S. Haas, Phys. Rev. Lett. **90**, 177205 (2003).
[6] T. J. Sato, H. Takakura, A. P. Tsai, K. Shibata, K. Ohoyama, and K. H. Andersen, Phys. Rev. B **61**, 476 (2000).
[7] R. Lifshitz, Mater. Sci. Eng. A **294**, 508 (2000).
[8] R. Lifshitz, Phys. Rev. Lett. **80**, 2717 (1998).
[9] R. Lifshitz, Acta Crystallogr. Sect. A **60**, 167 (2004).
[10] G. G. Naumis, R. A. Barrio, and C. Wang, Phys. Rev. B **50**, 9834 (1994).
[11] E. Y. Vedmedenko, H. P. Oepen, and J. Kirschner, Phys. Rev. Lett. **90**, 137203 (2003).
[12] U. Grimm and M. Baake, in *The Mathematics of Long-Range Aperiodic Order*, edited by R. V. Moody (Kluwer, Dordrecht, 1997), p. 199.
[13] M. Baake and D. Joseph, Phys. Rev. B **42**, 8091 (1990).
[14] K. Niizeki, J. Phys. A **23**, 5011 (1990).
[15] N. D. Mermin and H. Wagner, Phys. Rev. Lett. **17**, 1133 (1966).

Philosophical Magazine,
Vol. 86, Nos. 6–8, 21 February–11 March 2006, 733–739

Taylor & Francis
Taylor & Francis Group

Interplay between magnetic and spatial order in quasicrystals

E. Y. VEDMEDENKO†, U. GRIMM*‡ and R. WIESENDANGER†

†Institut für Angewandte Physik, Universität Hamburg,
Jungiusstr. 11, 20355 Hamburg, Germany
‡Applied Mathematics Department, The Open University,
Walton Hall, Milton Keynes MK7 6AA, UK

(*Received 13 May 2005; in final form 14 September 2005*)

The stable magnetization configurations of antiferromagnets on quasiperiodic tilings are investigated theoretically. The exchange coupling is assumed to decrease exponentially with the distance between magnetic moments. It is demonstrated that the combination of geometric frustration and the quasiperiodic order of atoms leads to complicated non-collinear ground states. The structure can be divided into subtilings of different energies. The symmetry of the subtilings depends on the quasiperiodic order of magnetic moments. The subtilings are spatially ordered. However, the magnetic ordering of the subtilings in general does not correspond to their spatial arrangements. While subtilings of low energy are magnetically ordered, those of high energy can be completely disordered due to local magnetic frustration.

1. Introduction

In contrast to the rather well-studied spin structure of antiferromagnets on periodic lattices, the antiferromagnetic ordering of quasicrystals is the subject of ongoing scientific debate [1–13]. Experimentally, it has been demonstrated that rare earth containing quasicrystals exhibit spin-glass-like freezing at low temperatures [4, 6]. However, this freezing is different from that of conventional spin glasses. The observed dependence of the thermoremanent magnetization on the magnetic field does not follow the spin-glass behaviour and the frequency shift of the freezing temperature lies between those of a canonical spin glass and of a superparamagnet [8]. Hence, the free energy landscape of a rare earth quasicrystal is different from both the highly degenerate distribution of energy barriers in spin glasses and the single global energy minimum in superparamagnets.

Although the atomic and electronic structure of rare earth quasicrystals is not completely understood, it has been postulated [8] that the low-temperature microstructure of such a magnet resembles geometrically frustrated but site-ordered

*Corresponding author. Email: u.g.grimm@open.ac.uk

Philosophical Magazine
ISSN 1478–6435 print/ISSN 1478–6443 online
http://www.tandf.co.uk/journals
DOI: 10.1080/14786430500363569

magnetic systems and consists of weakly interacting magnetically ordered clusters. Another interesting approach is based on recent elastic neutron scattering experiments on a Zn–Mg–Ho icosahedral quasicrystal [7] revealing a very peculiar diffuse scattering pattern with icosahedral symmetry at temperatures below 6 K. In contrast to reference [8], the authors interpret the diffraction pattern as that of several interpenetrating quasiperiodic sublattices, where all spins point in the same direction [11]. Recent theoretical studies of real-space magnetic configurations on the octagonal tiling [9, 11–13] demonstrate that the energy landscape, in accordance with [8], is neither degenerate nor has a single global minimum. All spins can be divided into several quasiperiodic (in the 2D physical space) or periodic (in the corresponding 4D periodic hypercrystal) subtilings of different energy.

In the present investigation, we calculate the low-temperature stable antiferromagnetic configurations on several planar quasiperiodic tilings with tenfold symmetry. In most rare earth intermetallic compounds an oscillatory (RKKY-like) exchange interaction has been observed. To tackle this complicated problem first we concentrate on exponentially decreasing exchange coupling corresponding to a rapid-decaying limit of an oscillatory interaction. It will be demonstrated that the real-space magnetic structure is generally three-dimensional and non-collinear. In disagreement with [8], and in accordance with [7], the magnetic structure consists of several ordered interpenetrating quasilattices with characteristic wavevectors.

2. Simulations and results

We have investigated the magnetic ordering in an antiferromagnet on Penrose, anti-Penrose, Tübingen triangle [14] and Tie–Navette [15] tilings by means of Monte Carlo simulations. Two-dimensional films of classical, three-dimensional magnetic moments $\mathbf{S}$ have been studied. The Hamiltonian of the problem is given by

$$H = J_{ij} \sum_{\langle i,j \rangle} \mathbf{S}_i \cdot \mathbf{S}_j - K_1 \sum_i (\mathbf{S}_i^z)^2 \tag{1}$$

where J_{ij} are the exchange coupling constants and $\langle i,j \rangle$ refers to pairs of spins. Two cases have been explored: $J_{ij} = 1$ for all $r_{ij} \leq 1$ (and $J_{ij} = 0$ for all $r_{ij} > 1$), and an exponential decrease of the exchange interaction with the distance between magnetic moments (which for practical purposes was cut off at distance $r_{ij} > 2$), where r_{ij} denotes the distance between sites i and j (as compared to the edge lengths in the tiling, which are chosen to have length one). The samples are patches of square or rectangular shape, containing some 10 500 magnetic moments. We also used circular areas to check that our results are not affected by the shape of the sample. An extremely slow annealing procedure, with 50 temperature steps per Monte Carlo run, has been applied. To see the time-dependent changes in a microstructure, we ran the simulation for several hundred thousand steps per temperature.

In previous theoretical studies [2, 3, 5] frustrated, two-dimensional structures have been proposed. In accordance with previous publications, we find that the ground state of a system with purely antiferromagnetic exchange interactions is locally frustrated. Under the local frustration f we understand the normalized

difference between an actual energy E_i of a spin i and a ground state energy E_{id} of a relevant unfrustrated vertex with all spins antiparallel to the spin i

$$f = \frac{|E_{id}| - |E_i|}{|E_{id}|}. \tag{2}$$

In contrast to common folklore, the configurations are three-dimensional. Similar to the underlying atomic symmetry, the magnetic structure is quasiperiodic, i.e. it consists of identical units which do not have identical surroundings.

Three-dimensional representations of parts of the low-temperature quasiperiodic patterns observed for the Penrose and the octagonal tiling are shown in figure 1. The corresponding configurations represent the characteristic Penrose and Amman–Beenker 'stars', which are also shown in figure 1 for clarity. On the Penrose tiling, the 'star'-pattern can easily be recognized in the magnetic structure, because the moments belonging to the perimeter of enclosed 'stars' show perfectly antiparallel alignment. On the octagonal tiling, the situation is more complicated. The central magnetic moment is neither parallel nor antiparallel to the neighbouring

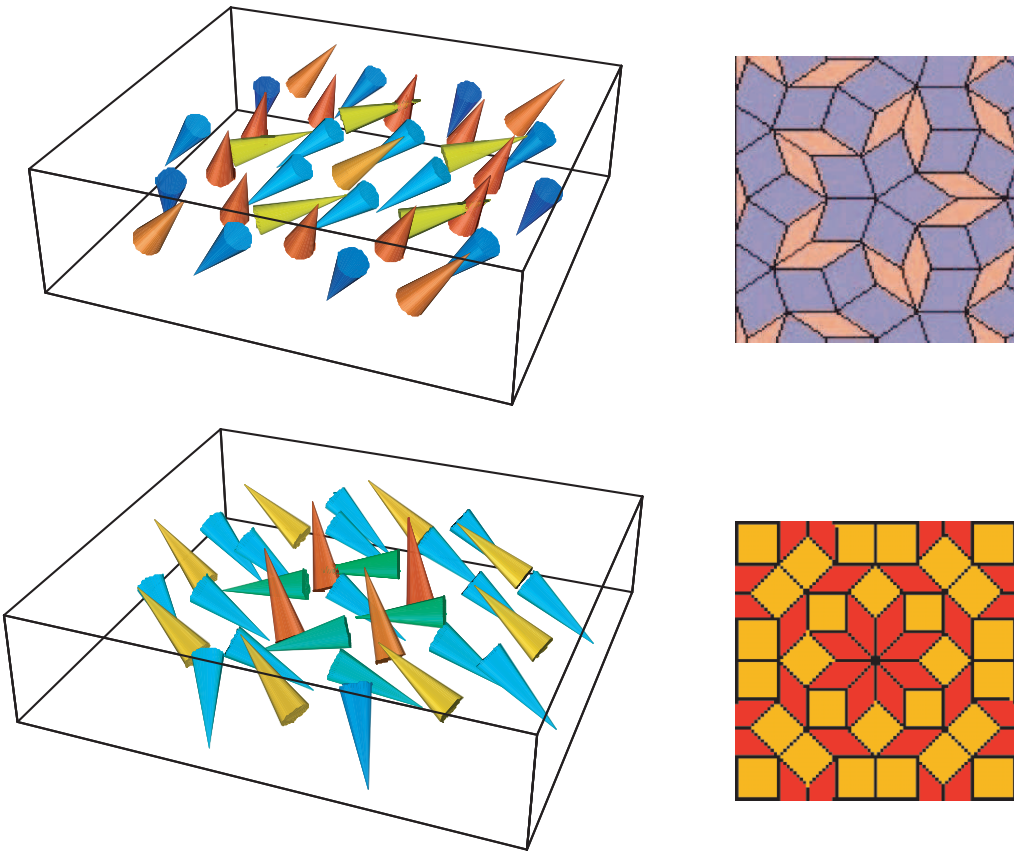

Figure 1. Perspective view of a portion of a Monte Carlo configuration on the Penrose tiling (top) and the octagonal tiling (bottom). Top views of the corresponding patches are shown on the right. The magnetic moments are represented as cones.

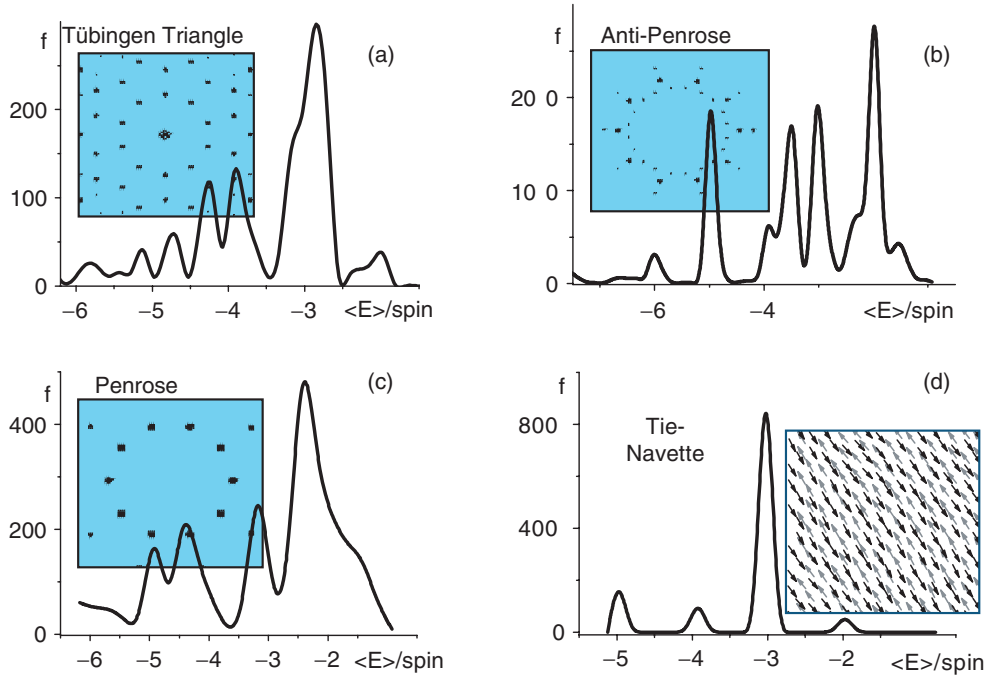

Figure 2. The frequency distribution of the energy per spin on the Tübingen triangle (a), anti-Penrose (b), Penrose (c) and Tie–Navette (d) tilings for classical vector spins. A purely antiferromagnetic interaction J at a temperature $kT = 0.01\,\mathrm{J}$ is considered. The insets in (a)–(c) give the calculated Bragg scattering of the S^y component of the magnetization for subtilings composed of magnetic moments belonging to peaks with $-6 < \frac{\langle E \rangle}{\mathrm{spin}} < -4$. The scale goes from -6 to 6 $k^{S^y}_{x,y}/\pi$. The inset in (d) shows a portion of the stable magnetic configuration on the Tie–Navette tiling as described in the text. Dark and light grey arrows denote antiparallel magnetic moments.

magnetic moments. Its eight nearest neighbours have different sets of mutual angles. The moments forming the next ring have still another orientation with respect to their nearest neighbours. The non-collinear alignment of the neighbouring moments indicates that the system is geometrically frustrated, i.e. there is no possibility to align all neighbours in an antiparallel arrangement. Similar non-collinear antiferromagnetic configurations are formed in the Tübingen triangle and anti-Penrose tilings. Within the examples of tilings considered here, the Tie–Navette tiling represents an exception. The magnetic structure observed for this tiling consists of two antiferromagnetically aligned quasiperiodic sublattices, as shown in figure 2d. This means that every pair of nearest neighbouring moments can be aligned antiparallel, i.e. the antiferromagnetic configuration is not frustrated.

We have calculated the stable low-temperature configurations and the frequency distribution of the exchange energy per atom $\langle E \rangle$ for the Tübingen triangle, anti-Penrose, Penrose and Tie–Navette tilings. The calculations have been performed for an exponentially decreasing exchange coupling and for a short-range exchange coupling $J_{ij} = const = 1$ for all $r_{ij} \leq 1$. The analysis of the local energies reveals several characteristic energetic maxima in the frequency distributions shown in figure 2a–d. The magnetic configurations and the number of the energy peaks for

the same tiling are identical for both choices of exchange couplings ($J_{ij} \propto e^{-r_{ij}}$ and $J_{ij} = 1$ for $r_{ij} \leq 1$). For different tilings, the number and the width of the maxima are different. The simple existence of the peaks means that there exist different sorts of magnetic moments having well-defined relative orientations with respect to their nearest neighbours. These relative orientations depend on the tiling and *not* on the choice of the exchange couplings J_{ij}. For $J(r_{ij} \leq 1) = 1$, however, it can be seen directly from the energy distributions of figure 2 whether the magnetic ordering is collinear or non-collinear. If all nearest neighbours are collinear (parallel or anti-parallel), then the exchange energy per spin should have integral values depending only on the number of the neighbouring moments. This is indeed the case for the Tie–Navette tiling; compare figure 2d. For a non-collinear alignment of neighbouring magnetic moments, $\langle E \rangle$ should be non-integral as the cosines of the angles between the moments are no longer zero or unity. This happens for all other tilings we considered; compare figure 2a–c. The average energy of non-collinear configurations is smaller than the energy of any collinear solution. Hence, the increase of the configurational entropy permits us to minimize the average local frustration and the total energy of the system.

The spatial arrangements of the exchange energies of the magnetic moments are given in figure 3. Each shade of grey in figure 3 represents a certain energy range corresponding to one of the peaks in the spectra of figure 2. The magnetic moments form subtilings of different energies, which generally do not coincide with a tiling obtained by selecting a specific vertex type. The subtilings of low energy $\frac{\langle E \rangle}{\text{spin}} < -3$ are magnetically stable and ordered while those of higher energy $\frac{\langle E \rangle}{\text{spin}} > -3$ are disordered. The disorder can be seen in the portion of the magnetic configuration shown at the bottom of figure 1. The two front moments belonging to the subtiling of a large energy have angles which deviate considerably from those of the other moments in the ring while the moments in the inner rings with lower energy have collinear orientations. With increasing temperature the magnetization of subtilings of large energy is fluctuating while the magnetization of low-energy subtilings is still stable. The spatial quasiperiodic ten-fold symmetry of the ordered subtilings can be seen from the calculated magnetic Bragg scattering given in the insets to figure 2. While the atomic ordering of the unstable subtilings can be seen in the Fourier space their magnetic reflexes are extinct because of disorder.

3. Summary

In conclusion, we demonstrate that a vector spin system with antiferromagnetic coupling on different quasiperiodic tilings is locally frustrated. All spins can be divided into several quasiperiodic (in our two-dimensional physical space) or periodic (in the corresponding four-dimensional periodic hypercrystal) subtilings of different energy, which generally do not coincide with a specific vertex type. The vector spin system admits a three-dimensional non-collinear magnetic structure. The non-collinearity of the magnetic configuration permits us to minimize the degree of frustration and the total energy of the system in comparison with the collinear case. The co-directional spins of every subtiling reveal quasiperiodic ordering with a wavevector which is specific for a given subtiling. The Tie–Navette tiling is not

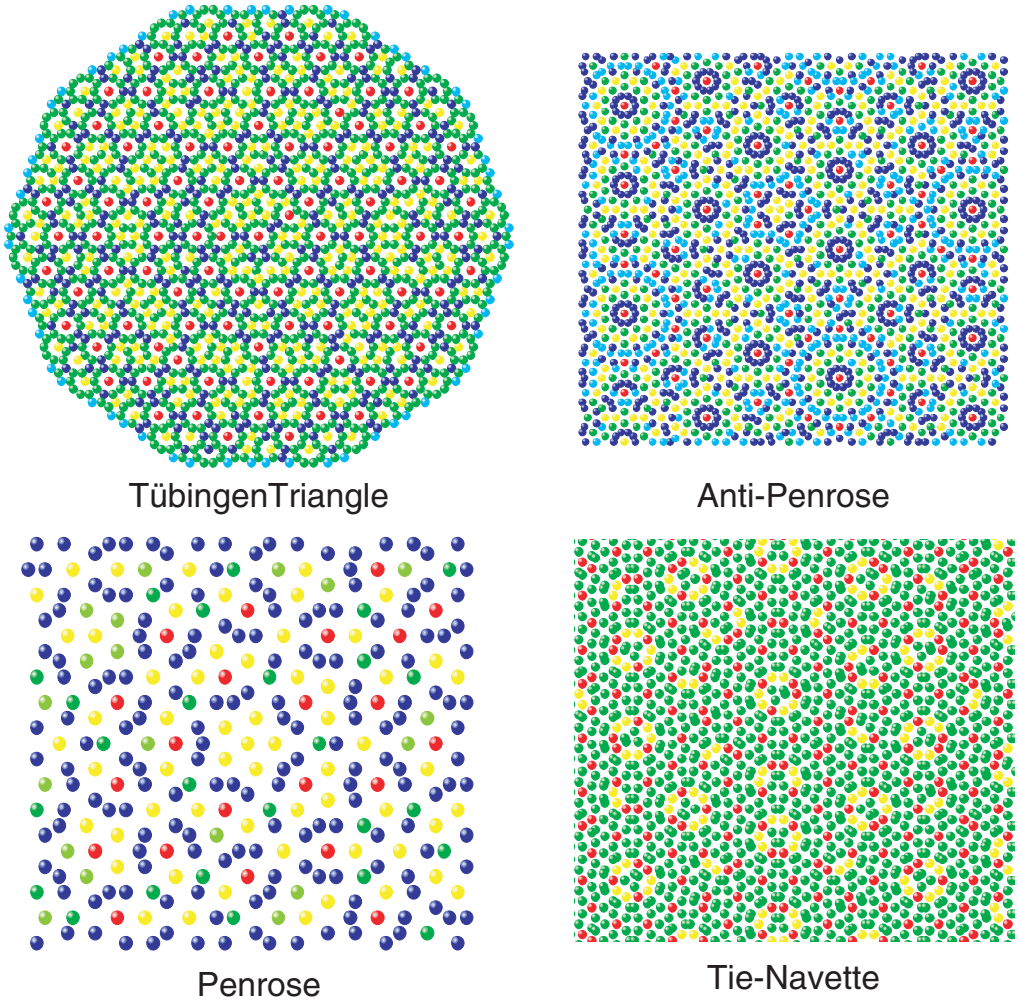

Figure 3. Energy maps for classical vector spins on Tübingen triangle (a), anti-Penrose (b), Penrose (c) and Tie–Navette (d) tilings. The circles give positions of magnetic moments. Different shades of grey denote different energies corresponding to the peaks in figure 2. Purely antiferromagnetic interaction with $J = 1$ for all $r_{ij} \leq 1$ at $kT = 0.01$ J is considered.

frustrated and admits collinear magnetic configurations. For the short-ranged exchange interaction, this arises as a consequence of the bipartiteness of the graph formed by connecting interacting pairs of spins; however, we observe that the antiferromagnetic order persists for the case of a long-range, exponentially decreasing exchange interaction.

References

[1] C. Godrèche, J.M. Luck and H. Orland, J. Stat. Phys. **45** 777 (1986).
[2] D. Ledue, J. Teillet, J. Carnet and J. Dujardin, J. Non-Cryst. Solids **153** 403 (1993).

[3] R. Lifshitz, Quasiperiodic spin space groups, in *Proceedings of the 5th International Conference on Quasicrystals*, edited by C. Janot and R. Mosseri (World Scientific, Singapore, 1995), pp. 43–46.
[4] Z. Islam, I. R. Fisher, J. Zarestky, P. C. Canfield, C. Stassis and A.I. Goldman, Phys. Rev. B **61** R11047 (1998).
[5] J. Hermisson, J. Phys. A: Math. Gen. **33** 57 (2000).
[6] M. Scheffer and J.-B. Suck, Mat. Sci. Eng. A **294** 629 (2000).
[7] T.J. Sato, H. Takakura, A.P. Tsai, K. Shibata, K. Ohoyama and K.H. Andersen, Phys. Rev. B **61** 476 (2000).
[8] J. Dolinšek, Z. Jagličić, T.J. Sato, J.Q. Guo and A.P. Tsai, J. Phys.: Condens. Matter **15** 7981 (2003).
[9] S. Wessel, A. Jagannathan and S. Haas, Phys. Rev. Lett. **90** 177205 (2003).
[10] E.Y. Vedmedenko, H.P. Oepen and J. Kirschner, Phys. Rev. Lett. **90** 137203 (2003).
[11] E.Y. Vedmedenko, U. Grimm and R. Wiesendanger, Phys. Rev. Lett. **93** 076407 (2004); cond-mat/0406373.
[12] A. Jagannathan, Phys. Rev. Lett. **92** 047202 (2004).
[13] A. Jagannathan, Phys. Rev. B **71** 115101 (2005).
[14] M. Baake, P. Kramer, M. Schlottmann and D. Zeidler, Int. J. Mod. Phys. B **4** 2217 (1990).
[15] R. Lück and K. Lu, J. Alloys Compd. **209** 139 (1994).

Publication List

Thesis

E.Y. Vedmedenko (1993): The optical and electrical properties of some micellar structures of biological origin. PhD Thesis: Kiev, Ukraine, Physics Institute of Academy of Sciences. 201 pp.

Reviews and books

1. E. Y. Vedmedenko and R. Wiesendanger (2006): Anisotropic domain walls in magnetic Nanostructures. In John V. Chang (Ed.) *New Topics in Condensed Matter Research*, Nova Publishers, New York, in production.

2. E. Y. Vedmedenko (2006): Magnetic ordering of the Spin Reorientation Transition in Nanostructures. In A. Ghazali, and J-C.S. Levy (Eds.) *Magnetism of Surfaces and Nanostuctures*, Transworld Research, Kerala, ISBN: 81-308-0115-9.

3. E. Y. Vedmedenko (2005): Non-collinear Magnetism in Quasicrystals, Modern Physics Letters B, 19, N27, 1-20.

4. E. Y. Vedmedenko (2005): Quasicrystals: Magnetism. In: *Encyclopedia of Materials: Science and Technology Updates*, Elsevier, Oxford, ISBN: 0-08-043152-6.

5. E. Y. Vedmedenko (2005): Oberfläche zwingt zur Ordnung, Physik Journal, 4, 81-85.

Papers

1. M. Bode, E.Y. Vedmedenko, K. von Bergmann, A. Kubetzka, P. Ferriani, S. Heinze, and R. Wiesendanger (2006): Atomic spin structure of antiferromagnetic domain walls, Nature Materials, in press.

2. K. von Bergmann, S. Heinze, M. Bode, E.Y. Vedmedenko, G. Bihlmayer, S. Blügel, and R. Wiesendanger (2005): Observation of a complex magnetic mosaik structure in a hexagonal Fe monolayer, Phys. Rev. Lett., in press.

3. J. Kötzler, D. Görlitz, M. Kurfiß, L. von Sawilski, and E.Y. Vedmedenko (2006): Vortex fluctuations and ordering of dipolar-coupled granular moments in thin ferromagnetic films, Phys. Rev. B, submitted.

4. E.Y. Vedmedenko, U. Grimm, and R. Wiesendanger (2006): Interplay between magnetic and spatial order in Quasicrystals, Phil. Mag. 86, 733-739.

5. E.Y. Vedmedenko, N. Mikuszeit, H.P. Oepen, and R. Wiesendanger (2005): Multipolar Ordering and Magnetization Reversal in Two-Dimensional Nanomagnet Arrays, Phys. Rev. Lett. 95, 207202 1-4. The paper has been selected for the November 21, 2005 issue of Virtual Journal of Nanoscale Science & Technology.

6. N. Mikuszeit, E.Y. Vedmedenko, R. Wiesendanger, and H.P. Oepen (2005): Multipole moments of the in-plane magnetized nanodiscs, J. Appl. Phys. 97, 10J502-505.

7. E. Y. Vedmedenko, K. von Bergmann, H.P. Oepen, and R. Wiesendanger (2005): Lattice dependent anisotropy in the orientation of magnetic domain walls, J. Magn. Magn. Mater 290-291, 746-749.

8. N. Mikuszeit, E.Y. Vedmedenko, and H.P. Oepen (2004): Multipole Interaction of polarized Single-Domain Particles, J. of Phys. C: Condenced Matter 16, 9037-9047.

9. E.Y. Vedmedenko, U. Grimm, and R. Wiesendanger (2004): Noncollinear magnetic order in Quasicrystals, Phys. Rev. Lett. 93, 076407 1-4.

10. E.Y. Vedmedenko (2004): Quasiperiodic magnetic Order and geometrical Frustration on the Penrose Tiling, Ferroelectrics 305, 129-132.

11. E.Y. Vedmedenko, A. Kubetzka, K. von Bergmann, O. Pietzsch, M. Bode, H.P. Oepen, J. Kirschner, and R. Wiesendanger (2004): Domain Wall Orientation in magnetic nanowires, Phys. Rev. Lett. 92, 077207 1-4. The paper has been selected for the March 8, 2004 issue of the Virtual Journal of Nanoscale Science & Technology.

12. E.Y. Vedmedenko, H.P. Oepen, and J. Kirschner (2003): Decagonal Quasiferromagnetic microstructure on the Penrose tiling: Phys. Rev. Lett. 90, 137203 1-4.

13. Y. Millev, E.Y. Vedmedenko, and H.P. Oepen (2003): Dipolar Magnetic Anisotropy Energy of Laterally Confined Ultrathin Ferromagnets: Multiplicative Separation of Discrete and Continuum Contributions: J. of Phys. D: Applied Physics 36, 2945-2949.

14. E.Y. Vedmedenko, H.P. Oepen, and J. Kirschner (2003): Size-dependent spin reorientation transition in nanoplatelets, Phys. Rev. B. 67, 012409 1-4. The paper has been selected for the February 10, 2003 issue of the Virtual Journal of Nanoscale Science & Technology.

15. E.Y. Vedmedenko, H.P. Oepen, and J. Kirschner (2003): Size-dependent magnetic properties in nanoplatelets, J. Magn. Magn. Mater. 256, 237-242.

16. E.Y. Vedmedenko, H.P. Oepen, and J. Kirschner (2002): Microstructure of the spin reorientation transition in second-order approximation of magnetic anisotropy, Phys. Rev. B 66, 214401 1-6.

17. E.Y. Vedmedenko, H.P. Oepen, and J. Kirschner (2001): Magnetic microstructure of the spin reorientation transition, J. Appl. Phys. 89, 7145-7146.

18. E.Y. Vedmedenko, H.P. Oepen, A.Ghazali, J-C.S. Lévy, and J. Kirschner (2000): Magnetic microstructure of the spin reorientation transition: A computer experiment. Phys. Rev. Lett. 84, 5884-5887.

19. J-C.S. Lévy, A. Ghazali, and E.Y. Vedmedenko (2000): Magnetic structures in ultrathin films and nanostructures: simulation. Acta Physica Polonica A 97, 431-434.

20. E.Y. Vedmedenko, A. Ghazali, and J-C.S. Lévy (1999): Magnetic vortices in ultrathin films. Phys. Rev. B 59, 3329-3332.

21. E.Y. Vedmedenko, A. Ghazali, and J-C.S. Lévy (1998): Magnetic structures of Ising and vectors spins monolayers by Monte-Carlo simulations. Surf. Science 402-404, 391-395.

22. E.Y. Vedmedenko, M.V. Kurik (1997): Influence of an electric field on the structure of saliva crystals. Technical Physics 42, 1440-1442 .

23. E.Y. Vedmedenko (1996): Charge transfer and crystallization features of micellar structures of biological origin. Proceedings of International Conference *Actual aspects of morphology*, Ternopil, Ukraine, 6-7 May; Vol.III, 776-778.

24. E.Y. Vedmedenko, M.V. Stuchinskaya, I.N. Kuvichka, M.V. Kurik (1994): Electrical conductivity of blood serum. Tech. Phys. Lett. 20, 578-580.

25. E.Y. Vedmedenko, I.N. Kuvichka, M.V. Kurik (1993): Interrelation between electrokinetic phenomena and interphase interactions with open surface. Ukranian Journal of Physics 38, 733-736.

26. E.Y. Vedmedenko (1993): Phenomena of charge transfer in solid micellar structures of biological origin. Proceedings of International congress of Physics in Ukraine, Kiev, Ukraine, 22-27 June; vol.: *Statistical Physics and Phase Transitions*, 162-165.

27. E.Y. Vedmedenko (1993): Crystallization features of micellar biostructures in the external electrical field. Proceedings of International congress of Physics in Ukraine, Kiev, Ukraine, 22-27 June; vol.: *Statistical Physics and Phase Transitions*, 165-169.

28. E.Y. Vedmedenko, I.N. Kuvichka, M.V. Kurik (1992): Correlation between the presence of micells in biomedia and their fractal crystallization. Tech. Phys. Lett. 18, 154-156.

29. A.N. Lebed, E.Y. Vedmedenko (1991): A small-chamber thermostat for the crystallization of biological media Laboratornoe delo (Laboratory affairs) 6, 57-59 (in Russian).

30. E.Y. Vedmedenko, I.N. Kuvichka, M.V. Kurik (1991): The influence of the external electrical field on the ordered liquid structures crystallization. Tech. Phys. Lett. 17, 19-21.

Patents

1. Y.V. Gavrushenko, E.Y. Vedmedenko (1996): Device for the determination of surface tension of liquids. Patent of Ukraine N°4940692, IKI G 01 N 5/05 .

2. E.Y. Vedmedenko, Y.V. Gavrushenko (1995): Method of surface tension determination and equipment for its realization. Patent of Russia, N ° 2035034, IKI G 01 N 5/05 .

3. V.I. Putincev, E.Y. Vedmedenko, Y.V. Gavrushenko (1993): Method of surface tension determination and equipment for its realization. Patent of the Soviet Union, SU 1835068 A3, IKI G 01 N ° 5/05 .